



Provided by the author(s) and NUI Galway in accordance with publisher policies. Please cite the published version when available.

Title	Planet engulfment and the planetary nebula morphology mystery
Author(s)	Boyle, Laura
Publication Date	2018-04-13
Publisher	NUI Galway
Item record	<a href="http://hdl.handle.net/10379/7281">http://hdl.handle.net/10379/7281</a>

Downloaded 2022-07-03T04:05:45Z

Some rights reserved. For more information, please see the item record link above.





**NUI Galway**  
**OÉ Gaillimh**

# **Planet engulfment and the planetary nebula morphology mystery**

*Thesis submitted by*

**Laura A. Boyle**

*In partial fulfillment of the requirements for the degree of*  
**Doctor of Philosophy**

**Supervisor: Dr. Matt P. Redman**

Centre for Astronomy  
School of Physics  
College of Science  
National University of Ireland, Galway

**April 2018**



# Abstract

This thesis presents an investigation into the galactic population of planetary nebulae (PNe) whose progenitors have evolved through the engulfment of massive planets during the asymptotic giant branch (AGB) phase of their evolution. The objective of this research was to investigate the hypothesis that planet engulfment can aid in explaining the observed non-spherical planetary nebula (PN) population, as a complementary shaping mechanism to the binary hypothesis. This was performed by the design and development of a new research tool, **SIMSPLASH** (SIMulationS for the PLAnet Shaping Hypothesis), which was developed for the specific purpose of conducting, for the first time, a population synthesis of planet engulfment in planetary nebula progenitors.

The first step in this investigation involved modelling the tidal evolution of planets orbiting PN progenitor stars to determine the importance of the adopted initial conditions and input physics in the stellar models and their effects on the orbital evolution of star-planet systems. The next step was to determine the probabilities of stars having and engulfing massive planets as a function of stellar mass and metallicity. This was achieved by combining the tidal evolution treatment with both the known exoplanet populations, as well as theoretical planet populations, and the occurrence rates of massive planets.

Finally, taking into consideration the results from the analyses described above, a PN population synthesis was performed using the star formation history and metallicity evolution of the galaxy as well as varying forms of the initial mass function and planetary nebula formation constraints. The population of visible PNe in the present-day galaxy was calculated to consist of a total of  $16,500 \pm 2,200$  PNe, of which  $240 \pm 20$  PNe ( $\simeq 1.5\%$ ) have evolved from the engulfment of a massive planet on the AGB and  $3,300 \pm 200$  PNe are the result of binary interactions ( $\simeq 20\%$ ), translating to an expected non-spherical population of  $\simeq 21.5\%$  of all PNe currently visible in the galaxy. The overall conclusion

---

from this work is that while planet engulfment can explain a small fraction of the observed population of non-spherical PNe ( $\simeq 7\%$ ), the hypothesis is not capable of resolving the mystery of the unexplained population of non-spherical planetary nebula morphologies. This conclusion adds support to the emerging view that not all low-to-intermediate mass stars can form visible PNe.

# Acknowledgements

It goes without saying that this thesis would not have materialised without the patience, help and encouragement of my supervisor, Dr. Matt Redman. From the initial stages of securing a scholarship, to the final stages of preparing this thesis (and all of the panic-y bits in between!), Matt has provided exceptional supervision and I was very lucky to have had his guidance over the past 4 years. I am also grateful to the members of my GRC - Dr. Gary Gillanders, Dr. Marie Coggins and Dr. Mark Lang - for taking the time to evaluate my progress and offering advice along the way.

I am grateful to Peter Behroozi for providing the star formation history and Shigeru Ida for providing the synthetic exoplanet populations, which were so important for this research. Also discussions with the following people provided much enlightenment: David Jones, Eva Villaver, Jason Nordhaus, Niyas Alikutty Madappattu, Noam Soker and Orsola De Marco, to name a few. Thanks also to all of the conference buddies I've met over the years - the planetary nebula community in general contains such a friendly and welcoming bunch of people and I'm really glad I've had a chance to be a part of that.

To the NUIG physics postgrads there really is no better gang to go for a *quiet pint* with, which provided a much needed respite at various points through the years. To my non-astronomy friends: Caroline, Ciara, Emily, Lorraine, Shane and the Abbey/Tuam girls: thanks for being there and a special thanks to Aine and Patrick for accommodating me and showing me around Beijing after the conference. Special thanks to Anne Lynch for giving me that pre-viva pep-talk (it really helped!) and for all the other support yourself and Michael offered as well.

To the two people who raised me with the tenacity required to get a PhD - my mom and dad- thank you both for having taught me that I can persevere through anything and to not give up and always giving me the encouragement I needed to do this. I couldn't

---

have done it without you both, and I'm dedicating this thesis to ye. Also to my siblings for respecting the quiet-time all those times I was studying, and especially Marguerite for all your help in the lead up to submitting and viva and lending me your laptop when my hard drive failed!

Last but absolutely not least - thank you so much, Sean. You have been by my side throughout this whole process and I would not have finished this thing if it wasn't for your understanding, your encouragement to keep going but most importantly your love and support at the most difficult times. I will never be able to accurately convey to you how thankful I really am, you have been beyond amazing.

# Abbreviations and acronyms

<b>ADF</b>	Abundance discrepancy factor
<b>AGB</b>	Asymptotic giant branch
<b>ALMA</b>	Atacama large millimetre array
<b>AU</b>	Astronomical unit
<b>CE</b>	Common envelope
<b>CSPN(e)</b>	Central star(s) of a planetary nebula(e)
<b>bCSPN(e)</b>	Binary central star(s) of a planetary nebula(e)
<b>E-AGB</b>	Early asymptotic giant branch
<b>EHB</b>	Extreme horizontal branch
<b>FLIER</b>	Fast low-ionisation emission region
<b>GISW</b>	Generalised interacting stellar winds
<b>HB</b>	Horizontal branch
<b>HST</b>	Hubble space telescope
<b>IMF</b>	Initial mass function
<b>ISM</b>	Interstellar medium
<b>ISW</b>	Interacting stellar winds
<b>LIS</b>	Low ionisation structure

---

<b>MASH(HASH)</b>	Macquarie (Hong Kong)/AAO/Strasbourg H $\alpha$
<b>MASER</b>	Microwave amplification by the stimulated emission of radiation
<b>MESA</b>	Modules for experiments in stellar astrophysics code
<b>MHD</b>	Magneto-hydrodynamics
<b>MIST</b>	Mesa Isochrones and Stellar Tracks (Database)
<b>MLT</b>	Mixing length theory
<b>MS</b>	Main sequence
<b>OGLE</b>	Optical gravitational lensing experiment
<b>PN(e)</b>	Planetary nebula(e)
<b>PPN(e)</b>	Proto-planetary nebula(e)
<b>RGB</b>	Red giant branch
<b>SIMSPLASH</b>	Simulations for the planet shaping hypothesis code
<b>SFR</b>	Star formation rate
<b>SSP</b>	Simple stellar population
<b>TP-AGB</b>	Thermal-pulsing asymptotic giant branch
<b>ZAMS</b>	Zero age main sequence

# **List of publications**

## **Talks**

- Women in Physics Ireland- Conference (2014), Queens University Belfast, Ireland; “Planet Destruction and the Shaping of Planetary Nebulae”
- Irish National Astronomy Meeting (INAM) (2015), Queens University Belfast, Ireland; “Planet Destruction and the Shaping of Planetary Nebulae”
- International Astronomical Union Symposium 323, Planetary Nebulae: Multi-Wavelength Probes of Stellar and Galactic Evolution (2016); “Planet Destruction and the Shaping of Planetary Nebulae”

## **Posters**

- Institute of Physics in Ireland - Spring Meeting (2015), Cork, Ireland; “Planet Destruction and the Shaping of Planetary Nebulae”

## **Papers**

- Boyle & Redman (2017), “Planet Destruction and the Shaping of Planetary Nebulae”, Proceedings of the International Astronomical Union Symposium 323, Planetary Nebulae: Multi-Wavelength Probes of Stellar and Galactic Evolution



# **Declaration**

The work in this thesis is based on research carried out at the Centre for Astronomy, School of Physics, National University of Ireland, Galway. No part of this thesis has been submitted elsewhere for any other degree or qualification and it is all my own work unless stated otherwise within the text.



# Contents

<b>Abstract</b>	<b>iii</b>
<b>Acknowledgements</b>	<b>v</b>
<b>Abbreviations and acronyms</b>	<b>vii</b>
<b>List of publications</b>	<b>ix</b>
<b>Declaration</b>	<b>xi</b>
<b>List of figures</b>	<b>xvi</b>
<b>List of tables</b>	<b>xix</b>
<b>1 An overview of planetary nebulae</b>	<b>1</b>
1.1 Introduction . . . . .	2
1.2 Historical advancements . . . . .	3
1.3 Planetary nebula formation . . . . .	5
1.3.1 Stellar evolution of planetary nebula progenitors . . . . .	5
1.3.2 Asymptotic giant branch mass-loss and the planetary nebula . . . . .	9
1.4 Morphologies of planetary nebulae . . . . .	11
1.4.1 Global morphological structure . . . . .	14
1.4.2 Secondary morphological structure . . . . .	17
1.5 The origin of aspherical symmetries . . . . .	22
1.5.1 Stellar rotation . . . . .	22
1.5.2 Magnetic fields . . . . .	23
1.5.3 The binary hypothesis . . . . .	25

---

1.6	Planets and planetary nebulae . . . . .	33
1.7	Thesis overview . . . . .	37
<b>2</b>	<b>Theoretical formalism, methodology and techniques</b>	<b>41</b>
2.1	Introduction . . . . .	41
2.2	Tidal evolution of planetary orbits . . . . .	42
2.2.1	Tidal dissipation and the role of turbulent convection . . . . .	45
2.3	Stellar evolution models . . . . .	47
2.3.1	Stellar evolution with MESA . . . . .	47
2.3.2	The MESA Isochrones and Stellar Tracks (MIST) database . . . . .	48
2.4	The populations of exoplanets . . . . .	50
2.4.1	The Exoplanet Orbit Database and the known exoplanets . . . . .	50
2.4.2	Synthetic planet distributions . . . . .	52
2.5	Planetary nebula population synthesis . . . . .	56
2.5.1	Star formation history . . . . .	57
2.5.2	The initial mass function . . . . .	57
2.6	SIMSPFLASH: SimulationS for the PLAnet Shaping Hypothesis . . . . .	60
2.6.1	Orbital mode . . . . .	60
2.6.2	Single-epoch population mode . . . . .	61
2.6.3	Multi-epoch population mode . . . . .	62
<b>3</b>	<b>Planet engulfment by progenitors of planetary nebulae</b>	<b>63</b>
3.1	Introduction . . . . .	64
3.2	SIMSPFLASH in Orbital mode: Calculating the engulfment zones for planets around PN progenitors . . . . .	66
3.2.1	Semi-major axis evolution . . . . .	66
3.2.2	The MESA Isochrones and Stellar Tracks Database (MIST): Input physics . . . . .	68
3.2.3	MESA stellar models . . . . .	73
3.2.4	Interpolation . . . . .	73
3.3	Results: The engulfment zones of planetary nebula progenitors . . . . .	74
3.3.1	Non-rotating, solar metallicity stars and the effects of a conservative RGB mass-loss coefficient . . . . .	74

---

3.3.2	The effects of rotation . . . . .	83
3.3.3	The effects of varying initial composition . . . . .	87
3.4	Summary and conclusions . . . . .	91
<b>4</b>	<b>The engulfment probabilities of PN progenitors</b>	<b>95</b>
4.1	Introduction . . . . .	96
4.2	SIMSPLASH in Single-epoch population mode: planet engulfment in a PN progenitor population . . . . .	98
4.2.1	Orbital evolution of planet populations . . . . .	99
4.2.2	The occurrence rates of massive planets . . . . .	102
4.2.3	The probability of planet engulfment . . . . .	104
4.2.4	The distribution of stellar masses . . . . .	106
4.2.5	Determination of the planet-fraction of the planetary nebula progenitor population . . . . .	107
4.3	Results: The planet-fraction of PN progenitor populations . . . . .	110
4.3.1	The PN progenitor star population . . . . .	110
4.3.2	The PN progenitor planet-fraction from the known exoplanets . .	111
4.3.3	The PN progenitor planet-fraction from synthetic exoplanet populations . . . . .	121
4.4	Summary and conclusions . . . . .	128
<b>5</b>	<b>Population synthesis of planet engulfment by planetary nebula progenitors</b>	<b>133</b>
5.1	Introduction . . . . .	134
5.2	SIMSPLASH in Multi-epoch population mode: Calculating the planet-fraction by PN population synthesis . . . . .	137
5.2.1	Star formation history . . . . .	137
5.2.2	Metallicity evolution of the Milky Way . . . . .	140
5.2.3	The number of visible present-day galactic PNe from each epoch	141
5.2.4	Models, assumptions and approximations . . . . .	142
5.3	Results: The present-day population of galactic planetary nebulae . . .	147
5.3.1	The total number of PNe and the planet-fraction . . . . .	147
5.3.2	Comparison with earlier estimates and observations . . . . .	151
5.3.3	Model limitations . . . . .	154

5.4	The consequences of planet engulfment on the evolution of PN progenitors	156
5.5	Summary and conclusions	162
<b>6</b>	<b>Summary and conclusions</b>	<b>167</b>
6.1	Introduction	167
6.2	Summary	168
6.2.1	SIMSPLASH: A new tool for exploring the effect of planet engulfment on the PN population	168
6.2.2	Exploring the engulfment zones of planetary nebula progenitors	169
6.2.3	The planet-fractions of planetary nebula progenitor populations	170
6.2.4	The planet-fraction of planetary nebulae in the Milky Way	171
6.3	Future work	173
6.3.1	The future of the known exoplanets: Re-calculating the planet-fraction with discoveries from Gaia	173
6.3.2	Proposed updates to SIMSPLASH	174
6.3.3	PN MyCn 18: A planet-shaped planetary nebula?	175
<b>A</b>	<b>Deterministic models of planet formation</b>	<b>177</b>
	<b>Bibliography</b>	<b>179</b>

# List of Figures

1.1	M 27, The Dumbell Nebula . . . . .	1
1.2	NGC 6543, The Cat’s Eye Nebula . . . . .	4
1.3	Evolutionary track for a $1 M_{\odot}$ star . . . . .	6
1.4	The AGB thermal pulse cycle . . . . .	7
1.5	A montage of planetary nebulae . . . . .	10
1.6	NGC 6543 with varying degrees of observed structural detail . . . . .	13
1.7	The global morphologies of planetary nebulae . . . . .	15
1.8	Planetary nebulae with multiple shells . . . . .	18
1.9	The Helix Nebula, an example of a planetary nebula with knotty structures	20
1.10	Planetary nebulae with low ionisation structures and hypersonic knotty outflows . . . . .	21
1.11	Hen 2-104 and MyCn18: The striking similarity between symbiotic nebulae and PNe . . . . .	26
1.12	R Sculptoris, an AGB star with a spiral in the wind . . . . .	27
1.13	The possible outcomes of a common envelope . . . . .	29
1.14	The binary period distribution . . . . .	32
2.1	The tidal torque in a two body system . . . . .	43
2.2	The basic work-flow of a synthetic planet population model . . . . .	55
2.3	Comparisons between models for the average star formation history for a Milky Way mass galaxy . . . . .	58
2.4	Schematic workflow diagram of SIMSPLASH . . . . .	61
3.1	An artist’s impression of planet undergoing engulfment . . . . .	63
3.2	The MIST models: Stellar structure properties for a $2 M_{\odot}$ star . . . . .	70

---

## LIST OF FIGURES

---

3.3	The MIST models: The maximum RGB and AGB radii as a function of star mass . . . . .	72
3.4	The semi-major axis evolution of a $1M_J$ planet orbiting a $1M_\odot$ star with varying initial semi-major axes . . . . .	75
3.5	The semi-major axis evolution of a $1 M_J$ planet orbiting a $1.5 M_\odot$ star with varying initial semi-major axes . . . . .	76
3.6	The semi-major axis evolution of a $1 M_J$ planet orbiting a $3 M_\odot$ star with varying initial semi-major axes . . . . .	77
3.7	The semi-major axis evolution of a $1 M_J$ planet orbiting a $5 M_\odot$ star with varying initial semi-major axes . . . . .	78
3.8	The semi-major axis evolution of a $10 M_J$ planet around a $1.5 M_\odot$ star with varying initial semi-major axes . . . . .	79
3.9	The RGB and AGB engulfment zones as a function of planet mass . . . . .	79
3.10	The semi-major axis evolution of a $1 M_J$ planet orbiting a $1.5 M_\odot$ star with varying initial semi-major axes and typical mass-loss rates . . . . .	82
3.11	The difference in RGB engulfment zone boundaries between a non-rotating and rotating $2 M_\odot$ star with a $1 M_J$ planet . . . . .	84
3.12	Engulfment zone boundaries as a function of star mass for a $1 M_J$ planet orbiting rotating and non-rotating stars . . . . .	86
3.13	RGB engulfment zone boundaries for varying stellar masses and metallicities and a $1 M_J$ planet. . . . .	90
3.14	AGB engulfment zone boundaries for varying stellar masses and metallicities and a $1 M_J$ planet. . . . .	90
4.1	Semi-major axis vs. mass scatter plot of the known exoplanets including Kepler candidates . . . . .	95
4.2	The occurrence rates of massive planets as a function of host star mass and metallicity . . . . .	103
4.3	Histogram of host star masses from the Exoplanet Orbit Database sample. .	104
4.4	Semi-major axis vs. mass scatter plot of the known exoplanets after mass cuts . . . . .	112

4.5	Histogram displaying the resulting number of planet engulfment of the known exoplanets as a function of stellar mass . . . . .	114
4.6	RGB engulfment probabilities from the known exoplanets . . . . .	115
4.7	AGB engulfment probabilities from the known exoplanets . . . . .	115
4.8	Interpolated probabilities for RGB engulfment as a function of host-star mass and metallicity (the known exoplanets) . . . . .	119
4.9	Interpolated probabilities for AGB engulfment as a function of host-star mass and metallicity (the known exoplanets) . . . . .	119
4.10	Semi-major axis vs. mass scatter plot of the synthetic planet population after mass cuts . . . . .	122
4.11	RGB engulfment probabilities from the synthetic planet populations . .	124
4.12	AGB engulfment probabilities from the synthetic planet populations . .	124
4.13	Interpolated probabilities for RGB engulfment as a function of host-star mass and metallicity (synthetic planet population) . . . . .	126
4.14	Interpolated probabilities for AGB engulfment as a function of host-star mass and metallicity (synthetic planet population) . . . . .	126
4.15	Bar plot of the numbers of PN progenitors with RGB and AGB engulfments in each mass bin for the $Z_* = 0.025$ model . . . . .	128
5.1	Galactic distribution of all currently known PNe . . . . .	133
5.2	Schematic diagram of the Multi-epoch population mode of SIMSPLASH . .	138
5.3	Summary plot of the total number of visible PNe resulting from the population synthesis models . . . . .	148
5.4	The total number of visible PNe emanating from each epoch for a range of models . . . . .	150
5.5	The possible outcomes of a planet engulfment . . . . .	157

---

## LIST OF FIGURES

# List of Tables

3.1	AGB engulfment zones: rotating vs. non-rotating stellar models . . . . .	88
3.2	RGB engulfment zone boundaries for varying masses and metallicities and a $1 M_J$ planet. . . . .	89
3.3	AGB engulfment zone boundaries for varying masses and metallicities and a $1 M_J$ planet. . . . .	91
4.1	Stellar population summary . . . . .	110
4.2	PN progenitor population summary . . . . .	110
4.3	Population engulfment results summary for the grids of stellar models employed. . . . .	113
4.4	PN progenitor population from the known exoplanets evolved with mea- sured metallicity . . . . .	116
4.5	PN progenitor population proportions from the known exoplanets evolved with measured metallicity . . . . .	116
4.6	PN progenitor population from the known exoplanets evolved with five different metallicities . . . . .	120
4.7	PN progenitor population proportions from the known exoplanets evolved with five different metallicities . . . . .	120
4.8	Population engulfment results summary for the grids of stellar models employed. . . . .	123
4.9	PN progenitor population from the synthetic planet population evolved with five different metallicities . . . . .	125
4.10	PN progenitor population proportions from the synthetic planet popula- tion evolved with five different metallicities . . . . .	127

---

## LIST OF TABLES

---

5.1	The best fit parameters for the galactic stellar-mass-metallicity relationship	141
5.2	The present-day planetary nebula population . . . . .	149
5.3	The PN population synthesis models . . . . .	164

# Chapter 1

## An overview of planetary nebulae



Figure 1.1: A modern bi-colour image of M 27, The Dumbbell Nebula. M 27 was the first documented planetary nebula, discovered by Charles Messier in 1764. The term planetary nebula was coined by William Herschel as a reflection of the colourful, disk-like appearance of M 27. North is up and East is to the left. Image credit: Bill Snyder.

## 1.1 Introduction

The planetary nebula (PN) represents the short-lived ionisation phase in low-to-intermediate mass stars, occurring shortly after an asymptotic giant branch star expels its circumstellar envelope. It is during the PN phase that much of a stars mass is recycled back into the interstellar medium, enriching the galaxy with an abundance of heavy elements such as carbon and oxygen, which eventually become the building blocks for planets. Thus, studies of planetary nebulae (PNe) are not only crucial for understanding the full life cycle of sun-like stars, but also for our understanding of galactic evolution as a whole, including the formation and evolution of our home solar system. The vast majority of PNe exhibit morphological structures which cannot be explained by the evolution of a single star. While it is becoming ever more clear that binary evolution plays a substantial role, the progenitor binary-fraction is unable to account for the large fraction of PNe which deviate from spherical symmetry. A promising idea, however, is that the binary companion need not be stellar in nature, but that even a massive planet can produce some of the morphologies which are so often observed.

The aim of the research presented within this thesis is to investigate to what extent massive planets can explain the population of non-spherical planetary nebulae. This is performed by modelling the tidal evolution of star-planet systems in theoretical planet populations in order to determine the probabilities of PN progenitor stars engulfing planets on the asymptotic giant branch, as a function of the progenitors main sequence mass and metallicity. The probabilities are then incorporated into a PN population synthesis to determine the present-day population of PNe which have evolved through such an event. The novelty of this work is the use of theoretical planet populations to uncover the distribution of planets which cannot yet be known from observation. Furthermore, planet engulfment as an evolutionary channel for planetary nebulae has not yet been thoroughly considered in any PN population synthesis study. Finally, the development of the new research tool to perform this research is a useful contribution in terms of its potential for future work on the topic.

In this introductory chapter, the focus will be on the general background of PNe, including the historical triumphs, physical characteristics and the effects that stellar binaries and planets can have on evolving PN progenitors.

## 1.2 Historical advancements

The inadvertent discovery of the first planetary nebula occurred in 1764. Charles Messier had been compiling a list of fixed, diffuse objects in order to aid astronomers in differentiating them from the highly sought-after transient observations of comets (Today this compilation is known as the Messier Catalogue). The 27th entry to this list (M 27), which is commonly known as the Dumbell nebula today, is now famous as the first documented observation of a PN. The designation of the term planetary nebula, which contains the Latin meaning *planet-like cloud*, is owed to William Herschel, who coined the term shortly after, as he believed that the Dumbell nebula resembled the planet Uranus due to its apparent disk-like shape and colourful hue as viewed through a small telescope. A modern bi-colour narrow-band image of the Dumbell nebula is shown in figure 1.1.

Full comprehension of the underlying physics, structure and emission involved in planetary nebulae was far beyond the reach of astronomers at the time of their discovery. In fact, it was widely believed that nebulous objects were merely star clusters which appeared diffuse because the magnification needed to resolve the stars individually was lacking. Herschel was the first to suggest otherwise when his observations of the planetary nebula NGC 1514 showed evidence of a link between the nebulosity comprising most of the object and the bright star at its centre (Herschel 1791). Nonetheless, it was not until 100 years after their discovery, in 1864, when the first spectral study of a PN was performed. The early spectroscopic observations would begin to expose the true, and notoriously cryptic, nature of these objects.

Huggins & Miller (1864) found that the spectrum of NGC 6543, the Cat's Eye nebula shown in figure 1.2, consisted of a single emission line rather than the strong stellar continuum and absorption features that were expected from the stars which they believed they were observing. Follow up observations and analysis revealed that the emission could be resolved into three lines, the strongest was that of the Balmer line of hydrogen ( $H\beta$ ). But, what was most extraordinary was that the other two emission lines were of wavelengths which could not be identified as any of the known elements. They believed they had stumbled upon a new element, *nebulium*.

The correct interpretation of these observations was put forward by Bowen (1928), who argued that the source of the inexplicable emission lines was not a new element, but

rather they are due to transitions which are only possible in an extremely low-density gas. In the favourably low-density conditions, bound electrons can be excited to higher energy levels within the ground state via collisions. Provided that they are not quickly de-excited again by subsequent collisions, the electrons will eventually drop back down to the bottom level, emitting photons in the process. Such conditions cannot be replicated on Earth, and so these transitions were inconceivable at the time. These seemingly impossible transitions give rise to what are now known as *forbidden lines*, and they dominate the spectra of PNe where densities are typically lower than  $10^4 \text{ cm}^{-3}$  and so collisional de-excitation is rare. Further investigations led by Perrine (1929) showed that the emission



Figure 1.2: NGC 6543, The Cat’s Eye Nebula. North is towards the top of the image and East is towards the left. Image credit: NASA, ESA, HEIC, and The Hubble Heritage Team (STScI/AURA).

lines observed in PNe tend to be broad and in some cases split, giving a clear indication of an expanding gas. The exact nature and origin of the expanding gaseous cloud was still a mystery until the late 1950s, when a comparison between the velocity of the expansion and the escape velocity of giant stars showed a striking correlation (Shklovsky 1957). This correlation led to a similar conclusion to that of Deutsch (1956), who derived the mass-loss rates of the supergiant  $\alpha$  Her using Doppler shifts of absorption lines. The conclusion being that giant stars must eject their envelopes as they reach the end of their lives, with Shklovsky (1957) proposing that the ejected envelope of a stellar giant would later become the ionised gas observed around PNe.

## 1.3 Planetary nebula formation

### 1.3.1 Stellar evolution of planetary nebula progenitors

Stars with initial masses in the range of  $\sim 0.8\text{--}8 \text{ M}_\odot$  will eventually become PNe. The evolutionary track for a  $1 \text{ M}_\odot$  star is shown in figure 1.3. As is the case for all stars, the progenitors of PNe begin their lives through the collapse of a cold molecular cloud, forming a protostar which is powered through the release of gravitational potential energy. Once the protostar reaches the temperature and pressure requirements for nuclear reactions to ensue, the star is on the main sequence where it will spend the majority of its life converting hydrogen to helium.<sup>1</sup>

Hydrogen fusion takes place via either the proton-proton chain (for stellar masses  $M_* \lesssim 2 \text{ M}_\odot$ ), or the CNO cycle (for  $M_* \gtrsim 2 \text{ M}_\odot$ ). Regardless of the hydrogen burning process utilised, the result of the reactions is that as the main sequence progresses the abundance of hydrogen in the centre of the star is slowly depleted, while a helium core grows. At this stage the star cannot meet the temperature requirements for helium fusion and the temperature gradient in the core disappears ( $dT/dr = 0$ ). This, together with the continuous growth of the helium core, begins to become problematic for the star. Hydrostatic equilibrium is temporarily interrupted once a critical mass is reached (the Schönberg-Chandrasekhar limit), as the outward pressure can no longer support the weight of the surrounding envelope, and the core begins to contract and heat. Hydrogen fusion, which is now occurring in a layer adjacent to the core, accelerates with the rising core temperature. Consequently, the envelope expands, decreases its effective temperature and moves towards the right on the H-R diagram (figure 1.3). At this point the star is beginning its ascent on the red giant branch (RGB).

During the RGB ascent the star is still in a state of core contraction and envelope expansion. Opacity increases as a direct result of the rising luminosity, triggering the onset of a fully convective envelope. As the convection penetrates the deep interior of the star, nucleosynthesised elements are brought to the surface, in a process known as the *first dredge-up*. Meanwhile, because of the larger radius, the gravitational binding

---

<sup>1</sup>The majority of the theory behind the stellar lifecycle presented in the following can be found in Prialnik (2009), unless otherwise referenced.

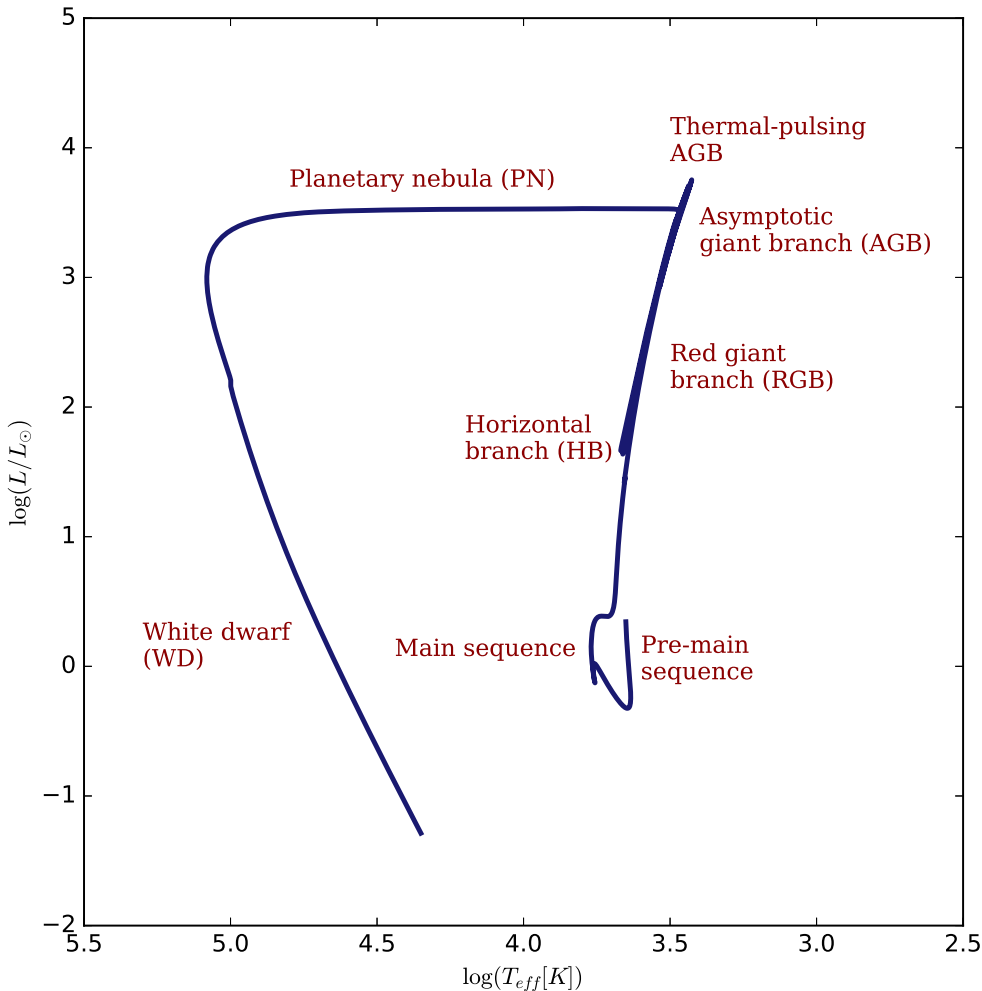


Figure 1.3: Evolutionary track for a  $1 M_\odot$  star. This figure was constructed by the author using data from the Mesa Isohrones and Stellar Tracks (MIST) project (Choi et al. 2016).

energy of the outer layers is greatly diminished, and so the stellar wind is more capable of accelerating atoms in the photosphere beyond the escape velocity. This stellar mass-loss is important for the star as it helps to ensure that the resulting white dwarf core never reaches the Chandrasekhar mass limit ( $1.4 M_\odot$ ).

The end of the RGB is brought about as the continuous core contraction eventually leads to core temperatures which can facilitate triple- $\alpha$  reactions, whereby three helium nuclei fuse to produce carbon, marking the transition from the RGB to the horizontal branch (HB). Stars with masses  $M_* \lesssim 2 M_\odot$  however will have developed electron degenerate helium cores. Thus, the high temperatures associated with the ignition of helium

and an inability to expand and cool results in a thermonuclear runaway event known as the *helium flash*. The extreme rise in temperature from the helium flash acts to remove the degeneracy of the electrons and finally the core can expand. For a star with mass  $M_* \gtrsim 2 M_\odot$ , the core temperature required for helium fusion is reached before electron degeneracy can occur and so it can forgo the helium flash, having a much more peaceful HB transition (Marigo 2001; Karakas & Lattanzio 2014). The HB is analogous to the main sequence, although instead of hydrogen burning, helium is fused steadily producing carbon and subsequently oxygen.

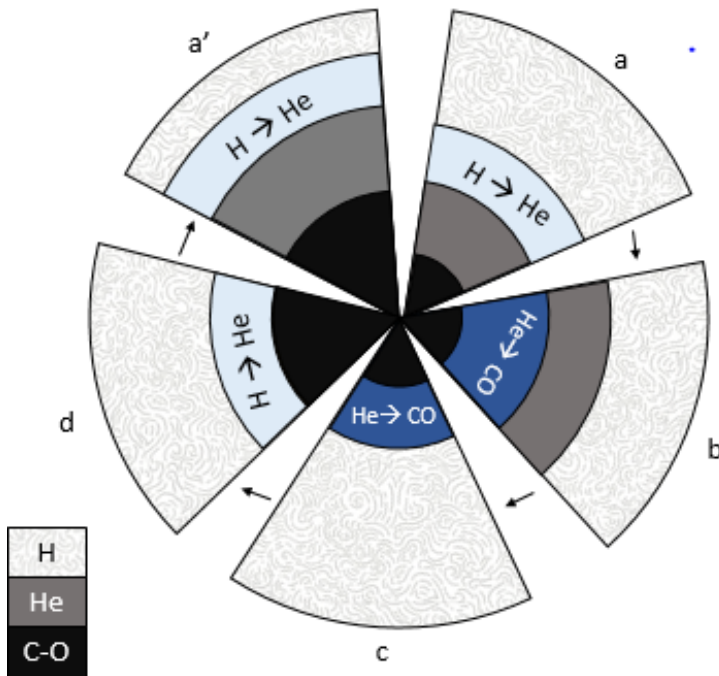


Figure 1.4: The AGB thermal pulse cycle as depicted in Prialnik (2009), redrawn by Mary Geer Dethero (as part of her undergraduate student internship). Hydrogen shell burning occurs during stages a and d, while helium shell burning takes place in stages b and c. In stage c, the outer convective zone extends inwards beyond the helium burning shell's boundary, and nucleosynthesised elements are dredged-up to the surface. Stage a' is the same as a, with the only difference that the carbon-oxygen core has grown.

Core helium fusion continues until, once more, the core is depleted of its energy source. As was the case at the end of the main sequence, the core contracts and heats, and in response the envelope expands, cools and becomes redder. It now resumes its journey upwards on the H-R diagram as an asymptotic giant branch (AGB) star, the final nuclear burning phase and the immediate progenitor of a PN (Herwig 2005). Again, con-

vection sets in throughout the hydrogen envelope. Intermediate mass stars ( $M_* \gtrsim 3 M_\odot$ ) are capable of a convective envelope which extends down to the hydrogen burning layer, bringing its fusion products to the surface in a *second dredge-up*. During this early AGB phase (E-AGB), the star consists of a degenerate carbon-oxygen (C-O) core surrounded by a thin helium burning shell, beneath the hydrogen envelope. The helium burning shell continues to add mass to the C-O core while advancing outwards, eventually becoming close enough to the envelope to restart hydrogen burning in a second shell. However, the two nuclear burning shells cannot continue to proceed simultaneously because the pressure generated by a non-degenerate helium burning shell results in expansion and cooling, essentially quenching itself as the temperature drops. However, the stable hydrogen reactions occurring just beneath the stellar envelope, act to increase the mass of the helium layer which then contracts, heats and begins fusion once again. This time, much like the helium flash at the end of the RGB, the ignition of helium occurs in a ferocious runaway thermonuclear reaction, known as a thermal pulse. A rapid increase in luminosity quickly expands the envelope, extinguishing the burning hydrogen. This cycle, in which periods of quiescent hydrogen shell burning are disrupted by the abrupt ignition of helium, is known as the thermal-pulsing AGB phase (TP-AGB). Figure 1.4 illustrates the structure of the AGB star throughout the thermal pulse cycle.

Each thermal pulse is succeeded by the inwards movement of the convective zone boundary (see figure 1.4), which acts to mix the products of the helium shell burning, predominantly carbon, throughout the envelope in a *third dredge-up* process. It is this process which facilitates the transition from its initial oxygen-rich atmosphere ( $C/O < 1$ ) to that of a carbon star ( $C/O > 1$ ) (Herwig 2005). The full cycle of thermal pulses and mixing events will occur multiple times until the end of the AGB allowing further synthesised products, namely heavy elements such as  $^{14}\text{N}$ ,  $^{22}\text{Ne}$ ,  $^{18}\text{O}$ , to be mixed into the outer layers. Additionally, subsequent thermal pulses allows further reactions of synthesised elements which release neutrons (e.g.  $^{22}\text{Ne} \rightarrow ^{25}\text{Mg}$  in the most massive AGB stars, and  $^{13}\text{C} \rightarrow ^{16}\text{O}$  for a lower mass AGB). The flux of neutrons facilitates the enrichment of the star with what are known as slow neutron capture (s-process) elements (Karakas & Lattanzio 2014). The amount of chemical enrichment that can arise from the dredge up of both carbon enhancement and the s-process depends on the number of thermal pulses and third dredge up events the AGB star is capable of having.

### 1.3.2 Asymptotic giant branch mass-loss and the planetary nebula

Throughout the TP-AGB, as the outer layers expand, the outer regions become cool enough for atoms to coalesce into molecules and form dust particles. The dust particles can then be accelerated by radiation pressure, dragging gas with them via friction, ultimately ejecting mass into dusty circumstellar shells. As mass is continuously removed from the star in this way, the hydrogen burning shell moves ever closer to the surface and the core temperature, radiation pressure, and the mass-loss rate continues to rise. At this point, the rate at which mass is lost on the AGB can reach  $10^{-4} \text{ M}_\odot \text{ yr}^{-1}$  (Delfosse et al. 1997) with velocities of  $10 \text{ km s}^{-1}$  at the tip of the AGB; this is known as the *super-wind*. Such high mass-loss rates can result in the star losing at least 50% of its initial mass in a relatively short period of time. The envelope ejection timescale is now much shorter than the cooling timescale of the core, and so when the envelope mass falls below  $10^{-3} - 10^{-4} \text{ M}_\odot$ , the hot core becomes exposed. Once the core is exposed, the mass-loss rate decreases dramatically to  $10^{-8} \text{ M}_\odot \text{ yr}^{-1}$  as the wind begins to reach velocities of  $10^3 \text{ km s}^{-1}$ . This fast, tenuous wind quickly catches up to the previously ejected slow, dense wind. At the interface between the two winds, the mean free path of an atom coming from the central star is very small compared with the dimensions of the system, thus it cannot diffuse through the previously ejected material and a shell of condensed gas will be produced from a collision at the interface of the winds. This is known as the interacting stellar winds theory (ISW), first proposed by Kwok et al. (1978). Once the core temperature exceeds 25,000 K the circumstellar material becomes ionised and the star shines as a PN (Balick & Frank 2002). The timescale for the complete ejection of a typical PN envelope (based on a mass-loss rate of  $3 \times 10^{-5} \text{ M}_\odot \text{ yr}^{-1}$ ) is of the order of  $\simeq 6 \times 10^3$  yrs and, in general, the timescale for ionisation of the ejected material to occur is  $\simeq 5 \times 10^3$  yrs (Wood & Faulkner 1986). The continuous wind from the central star pushes the ionised shell outwards, until eventually the planetary nebula completely dissipates, and is no longer visible, as the circumstellar material including the nucleosynthesised products, is returned to the ISM. The typical PN visibility time is  $\simeq 20,000 - 30,000$  yrs (Moe & De Marco 2006), during which time it can be observed across a broad range of wavelengths. Ambient temperatures in PNe range from 10 – 20 K in molecular gas (Bujarrabal et al. 2001) to as high as  $1 \times 10^5$  K in the atmospheres of their central

stars (Werner 2012) and due to the ionising radiation of their central stars they emit in all wavelength regimes (with the exception of gamma radiation). Thus they are ideal observational candidates for probing the stellar, and galactic, evolution theories. Furthermore, their observed characteristics make them one of the most interesting types of object in the galaxy. A vast majority of PNe have a high degree of asphericity (see figure 1.5) which casts doubt on the ISW theory which is unable to explain the departure of spherical symmetry. For this reason the morphologies and shaping of PNe has been the focus of PN research for decades. In the following section the morphological classification of commonly observed traits is discussed, where yet unanswered questions with regards to their formation are introduced.

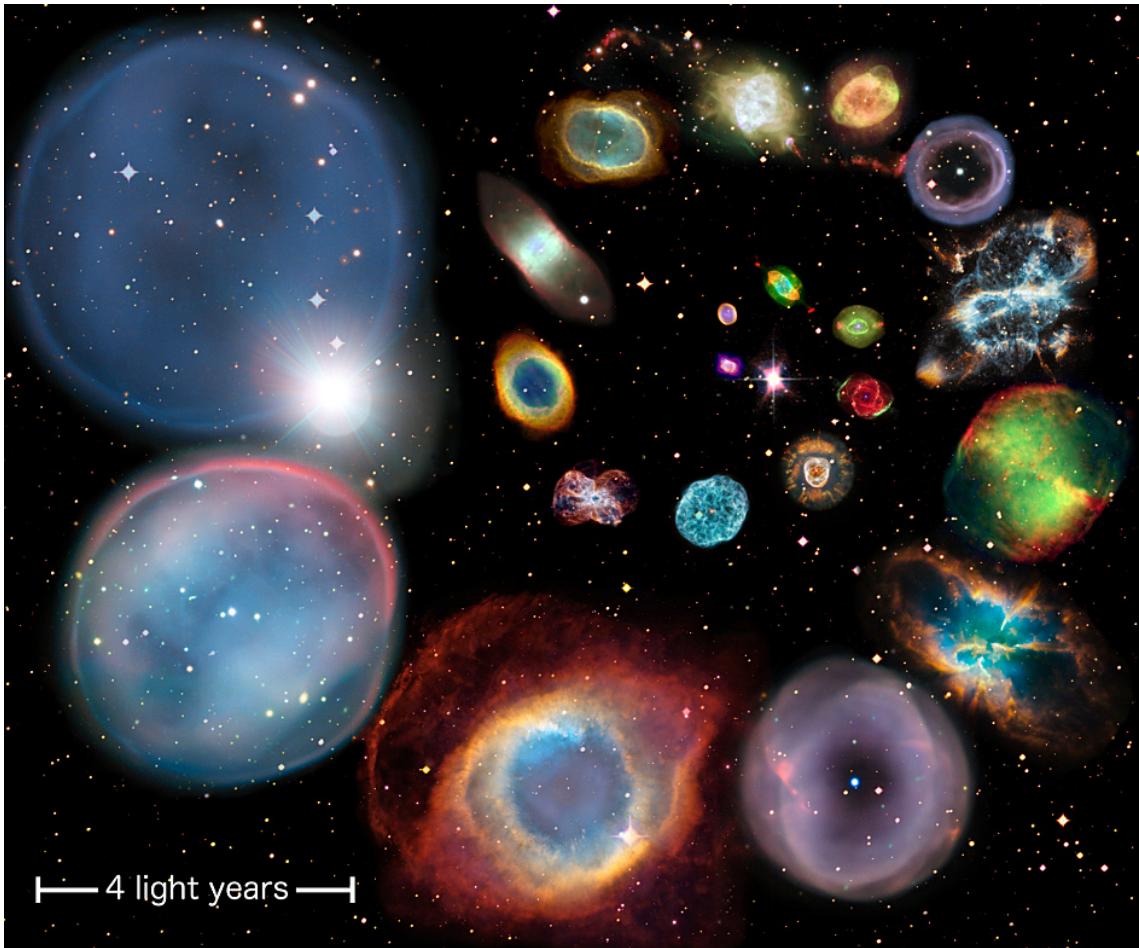


Figure 1.5: A montage of planetary nebulae arranged according to their physical size.  
Image Credits: ESA/Hubble & NASA, ESO, Ivan Bojicic, David Frew, Quentin Parker.

## 1.4 Morphologies of planetary nebulae

Morphological studies enhance our understanding of astrophysical objects. In particular, the intricate structures observed in many planetary nebulae can reveal clues to evolution processes undergone by their progenitors, while also uncovering recurrent patterns which are then used to classify them. Curtis (1918) was the first to make vast strides in studying the morphology of PNe with a view of understanding the dynamics of these objects. Since then, many attempts have been made at a morphological classification scheme for PNe, usually based on their apparent morphologies using optical imaging.

However, morphological inferences drawn from observation must be done with care. PNe consist of ionised, atomic and molecular matter, all of which may have different geometries. To identify the varying components they need to be observed with different techniques and at multiple wavelengths. Shaw (2012) highlighted the importance of observational considerations, such as varying the degree of exposure and observing in multiple wavelengths, using PN NGC 6543 (figure 1.6). Clearly, while optical imaging can reveal morphological structures such as halos, shells and lobes, adjusting the angular resolution on such images by a factor of 10 has an enormous impact on the identification of these structures. Similarly, there is much to be gained from the process of combining narrow-band images which clearly reveal ionization stratification and jets protruding from the central star, neither of which are detectable from the ground based image (the ground-based image in comparison with the Hubble Space Telescope (HST) image, in the upper left and right of figure 1.6, respectively). The deep HST image with compressed dynamic range, in the lower left of figure 1.6, reveals concentric rings displaying the importance of dynamic range and exposure depth, while the lower right of the image shows an X-ray observation, which is key to understanding the effects of pressure from hot gas on the nebula. The large central image is the result of deep, multi-band imaging and reveals the interaction of the far-reaching AGB wind with the interstellar medium. Another argument in favour of the need for multi-wavelength imaging of PNe is the difference in information gained through optical imaging versus mid-infrared imaging, where the former can suggest the existence of a dusty torus, but the latter aids in determining a torus' properties, such as its size and orientation. PNe are also often studied using radio continuum images and sub-mm observations, which offer information on the overall morphology and

dust emission mapping, respectively. Finally, high spatial and spectral resolution interferometric observations of cold/warm gasses performed in the mm/sub-mm regime are particularly useful for probing molecular regions in PNe which cannot be identified using optical imaging. For example, early optical observations of the pinched waist of PN NGC 6302 hinted at the existence of a hidden circumstellar structure near the central star of the nebula which was later confirmed to consist of a massive, expanding molecular torus by Peretto et al. (2007). The distribution and physical properties of these molecular components in PNe were largely unknown until recent advancements in mm/sub-mm technologies. Such observations allow for the comparison of distributions between ionised, molecular and dusty regions and thus a better understanding of the full physical structure of the nebula (e.g., Kwok 2007). The majority of molecular observations in PNe are of the CO molecule (carbon monoxide) since it is more capable of surviving photodissociation due to its high abundance (and thus acts as self-shielding from the UV radiation) and molecular stability in comparison to other molecules. Young planetary nebulae (as well as post-AGB objects or pre-planetary nebulae) have a richer variety of molecules which comprise most of the nebular mass and so molecular observations in these objects are paramount in determining their morphologies, while more evolved nebulae suffer from strong UV radiation from their central stars, as well as the interstellar UV field, which act to destroy many molecular species (see e.g., Bujarrabal 2016).

Another major challenge facing the development of classification schemes based on observed morphologies lies in the projection effects that enshroud astronomical observations (Frank et al. 1993). Deciphering the true morphology of PNe is difficult because we can only see a 2-dimensional representation on the sky. For example, a bipolar PN could be mistakenly classified as elliptical if the waist and lobes of the nebula are too faint to be detected, or if observed from an angle other than edge-on (Kwok 2010). Some examples of PNe which have an apparent ring-like morphology but have been reclassified as bipolar include NGC 3132 and NGC 6720 (Monteiro et al. 2000; Kwok et al. 2008). To circumvent this problem morpho-kinematic modelling is often used to decipher the true shape of the nebula (e.g., Santander-García et al. 2004, 2010; Jones et al. 2010; Clyne et al. 2015). These studies are performed using long-slit spectroscopy to measure the Doppler shifts in various nebular regions and thus constrain the kinematical components of the nebula, and when combined with multi-wavelength imagery it is possible to determine the true PN

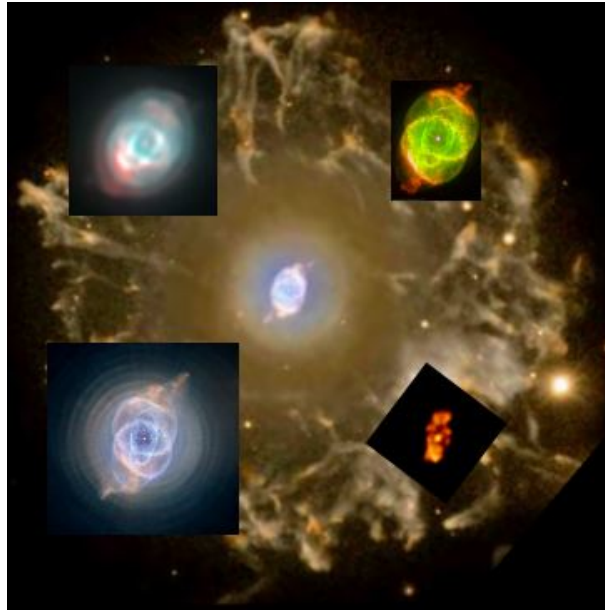


Figure 1.6: NGC 6543 with varying structural detail displaying that differing observational technique and wavelength range can result in an incorrect classification. *Centre*: Deep multi-band image (R. Corradi/IAC), *Upper left*: amateur ground based image, *Upper Right*: Multi-band HST image (J.P. Harrington and K.J. Borkowski, and NASA), *Lower left*: Deep HST image with compressed dynamic range (NASA, ESA, HEIC, and The Hubble Heritage Team (STScI/AURA)), *Lower right*: X-ray image from CXC (Chu et al. and NASA). Figure is as depicted in Shaw (2012).

structure. In order to harness some of the vast potential of modern telescopes (such as the Atacama Large Millimetre/Submillimetre Array), recent advancements have combined morpho-kinematic modelling with observations of molecular regions in PNe, revealing even more information on their physical conditions and morphologies (Santander-García et al. 2015). Santander-García et al. (2017) recently revisited the molecular region of the PN NGC 6302 (mentioned previously) by utilising their technique of morpho-kinematic modelling combined with molecular line observations. Their study not only recovered a deeper understanding of the morphology of the previously studied molecular component (e.g., Peretto et al. 2007), but revealed a previously undetected ring of molecular gas near the central star of the PN.

Hence, there is much importance placed on thorough observations of PNe, and in particular on the determination of their true morphologies such that a robust classification scheme can be continuously adhered to. PN morphologies can be organised in terms of their overall, *global*, morphology or in terms of the presence of finer, *secondary*, structures, or a combination of both.

### 1.4.1 Global morphological structure

PN morphological types are usually classified based on the overall outline of the spatially resolved nebula. This scheme, which was first developed by Balick (1987), consists of the three main morphological types: round, elliptical and bipolar, examples of which are shown in figure 1.7. The scheme also takes into account the rare occurrence of those PNe which do not fit into any of the three main classes (known as irregular PNe). Bipolar PNe, which can be further organised as bi-lobed (two outer lobes connected to the central star) or butterfly (the centre consists of a tightly-pinched waist), have the hottest central stars of all morphological classes. Furthermore, Stanghellini et al. (1993) and Corradi & Schwarz (1995) found that bipolar PNe tend to have lower galactic scale heights (130 pc, which is consistent with the scale heights of stars with  $M_* > 1.5 M_\odot$ ) and higher abundances of neon, nitrogen and helium than elliptical PNe. Such scale heights and metallicities suggest that bipolar PNe form from higher mass progenitors than their round and elliptical counterparts, which have average galactic scale heights of 320 pc (consistent with the galactic latitudes of stellar masses  $M_* < 1.5 M_\odot$ ).

Round PNe generally have low abundances of metals and are classified as a central star surrounded by a spherical bubble which can be viewed as a thin rim with sharp outer edges; thus a round morphology is the prototype for the ISW theory. However, despite the prediction of round PNe from the ISW theory, a vast majority of PNe lay within the elliptical and bipolar classes. Approximately 70% of all PNe are elliptical and bipolar, with only  $\simeq 10\%$  of PNe having spherical morphologies according to morphological surveys (the remaining PNe are irregular or multi-polar) (Parker et al. 2006). In order to explain the formation of elliptical and bipolar PNe, a revised version of the ISW paradigm was defined. The generalised interacting stellar winds (GISW) model (Kahn & West 1985; Icke 1988; Icke et al. 1989; Mellem & Frank 1995; García-Segura et al. 1999) predicts that enhanced densities in the equatorial plane, formed during the slow mass-loss phase on the AGB, can facilitate the formation of elliptical and bipolar PNe (where the equator-to-pole density ratio,  $q$ , is larger than unity). Mild density enhancements ( $1 < q < 2$ ) would result in a slightly higher wind velocity in the polar directions than in the equatorial plane resulting in elliptical PNe. Intermediate equator-to-pole density ratios ( $2 < q < 5$ ) are capable of producing bipolar lobes, an example of such lobes

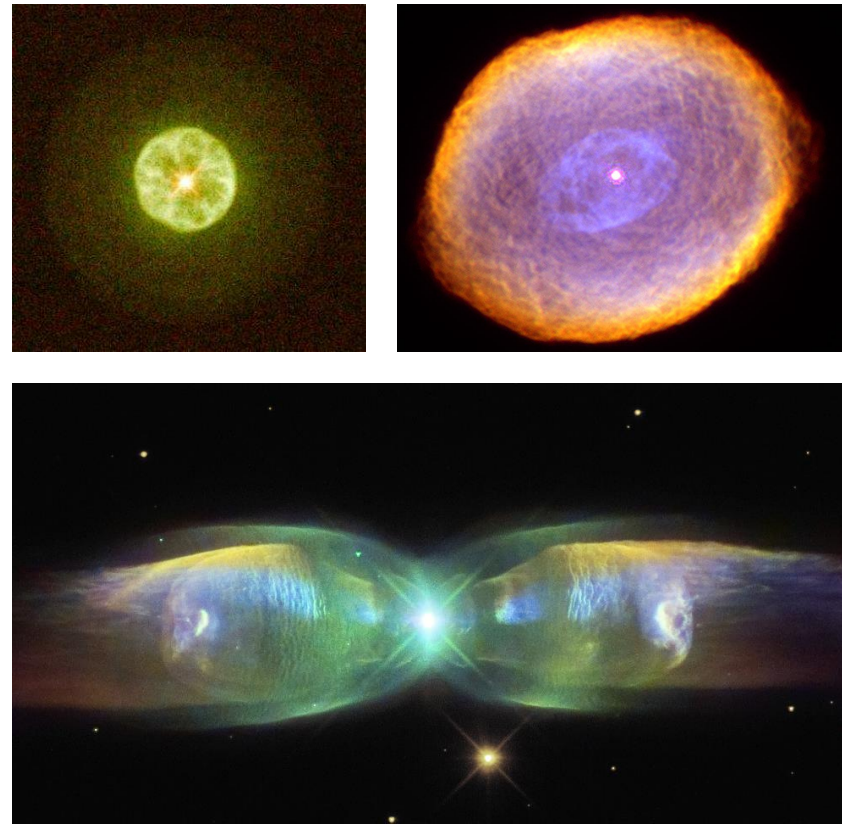


Figure 1.7: The global morphological types of PNe. *Upper left*: PN IC 3568, the Lemon Slice Nebula, is classified as a spherical PN (Image credits: Howard Bond (STScI), Robin Ciardullo (Penn. State U.), NASA/ESA). *Upper right*: PN IC 418, the Spirograph Nebula, is classified as an elliptical PN (Image credits: Sahai (JPL) et al., Hubble Heritage Team (STScI / AURA), NASA). *Bottom*: PN M2-9, the Wings of a Butterfly Nebula, is a bipolar PN (Image credits: B. Balick (U. Washington) et al., WFPC2, HST, NASA). North is towards the top and East is towards the left in all images.

can be seen in the PN Menzel 3 (depicted in the right-hand side of figure 1.10, pg. 21) whereas an extreme equatorial density enhancement ( $q > 5$ ) would be needed to form highly collimated objects, for example the highly collimated bipolar PN M2 9 depicted in the bottom panel of figure 1.7 (Balick 1987; Mellem & Frank 1995). Classification schemes should be capable of incorporating the majority of planetary nebula structures into well-defined morphological classes. Observationally, the distinction between classes can be quite subtle when considering the mildly elliptical in comparison to round PNe and likewise the comparison between extremely elliptical objects in comparison to bilobed, which of course makes classification difficult. Thus, complementary classification types such as axial-symmetries, reflection-symmetries and point-symmetries are sometimes employed (e.g., Corradi & Schwarz 1995; Manchado 2004; Parker et al. 2006). To

be classed as axial-symmetric a PN must be symmetrical about any axis, whereas reflection symmetry is defined as having symmetry about the polar axis only. Point symmetric PNe represent some of the most intriguing of all PNe as they often tend to be S-shaped, fulfilling the requirement of symmetry through the central nebula. Thus far the GISW model fails to adequately describe the existence of point symmetric PNe (Soker 1990, 1997). A remarkable variation on point symmetric PNe are those which show multiple point symmetric features, such as the lobes associated with bipolar PNe, with respect to different axes. These PNe are known as multi- and quadru- polar PNe, where each pair of lobes defines its own equatorial plane perpendicular to the lobe axes (Manchado et al. 1996). The existence of two or more pairs of lobes indicates that the symmetry axis must have changed between the mass-loss events that formed the PN.

While the attention of most classification schemes is focused solely on PNe for the purpose of understanding their morphologies and formation mechanisms, Sahai et al. (2011) argue that a more reliable determination of morphological trends can be sought by devising classifications based on young PNe and proto-planetary nebulae (or pre-planetary nebulae, PPNe), where the PPN represents the short-lived phase occurring between the AGB-tip and the PN (typical timescale for the PPN phase is less than  $10^3$  yrs). While morphological classification schemes based on PPNe suffer disadvantages in the fact that they are compact sources whose central stars are not yet hot enough to photoionise the nebula, the PPNe are more likely to have retained information and signatures of the mechanisms by which they formed (Sahai 2002). With this in mind, Sahai et al. (2011) devised a new classification scheme from a HST survey using only young PNe and PPNe in order to shed light on the primary formation mechanisms before the PNe develop instabilities. The instabilities can occur from interactions with the ISM and the fast central star winds and become subject to the passing of photonisation fronts, both of which may obscure underlying geometries which are evident early on. Another advantage of the new classification scheme is that, in contrast to earlier ground-based morphological surveys (e.g., Corradi & Schwarz 1995), the HST not only gives better angular resolution of objects to aid in classification (typical ground-based angular resolution is  $> 1''$ ), but a larger number of objects are visible leading to better statistics. The classification scheme consists of seven primary classes (round, elliptical, bipolar, irregular, point-symmetric, spiral-arm and multi-polar).

The classification scheme for PPNe of Sahai et al. (2011) revealed that the vast majority of these objects are extremely elliptical and bipolar, with only  $\approx$ 3 - 4% displaying round morphologies. Furthermore, many of the observed bipolar and multi-polar PPNe are accompanied by fast collimated outflows and jets. Such outflows are generally cold, and thus observed via molecular lines, and tend to exhibit a puzzling excess in linear momentum which cannot be explained by radiation pressure (Bujarrabal et al. 2001; Sahai et al. 2008).

As observational capabilities for both PNe and PPNe continue to improve, our understanding of PN morphological trends naturally advance with them. Compilations of modern catalogues such as the Macquarie (Hong Kong)/AAO/Strasbourg H $\alpha$  Planetary Nebula Catalogue (MASH/HASH) (Parker et al. 2006; Parker et al. 2016) have allowed for the identification of false positives in PNe, along with revised classification of some objects based on the ever mounting multi-wavelength data, and thus the improvement of PN statistics. However, despite these improvements, a recurrent theme persists; the vast majority ( $\gtrsim$  80%) of PNe deviate (to some degree) from spherical symmetry (Corradi & Schwarz 1995; Manchado 2004; Parker et al. 2006; Parker et al. 2016; Sahai et al. 2011).

### 1.4.2 Secondary morphological structure

PN Morphologies can be further classified based on the presence of a number of secondary structures which may contain information on the mechanisms by which the PN was formed. Extended halos, which are most readily observed in [OIII] and hydrogen- and helium- recombination lines, are often a characteristic of elliptical and spherical PNe but tend to surround a much brighter, often aspherical, central nebula (Balick & Frank 2002). Hydrodynamic modelling has demonstrated that the density distributions of PN halos are consistent with mass lost towards the end of the AGB expanding into an isotropic medium (Frank et al. 1990). Such a result certainly adds weight to the ISW paradigm of Kwok et al. (1978). However, the fact that halos often surround a structured inner PNe is indicative of an abrupt change in the nature of stellar mass-loss before the onset of the PN phase. The mechanisms responsible for the shift from an isotropic spherical expansion into a complex asymmetrical wind is highly uncertain. A special case of halo morphology is that of multiple shelled PNe like those observed in NGC 7027 and CRL 2688 (figure

1.8 left and right, respectively). The shells occur as almost perfectly circular with relatively uniform separations. In the case of a PN with a double shell, the ISW paradigm may also provide a reasonable explanation as the inner dense part of the shell becomes optically thin, allowing the ionising radiation to reach and illuminate the outer tenuous mass more easily. Multiple shells are thought to originate via episodic mass-loss/multiple ejections from the central star during the AGB with separations between shells having periods from a few hundred to a thousand years (Kaler 1974; Terzian & Hajian 2000) and, as with halos, they are often observed to surround a highly complex and structured PN.

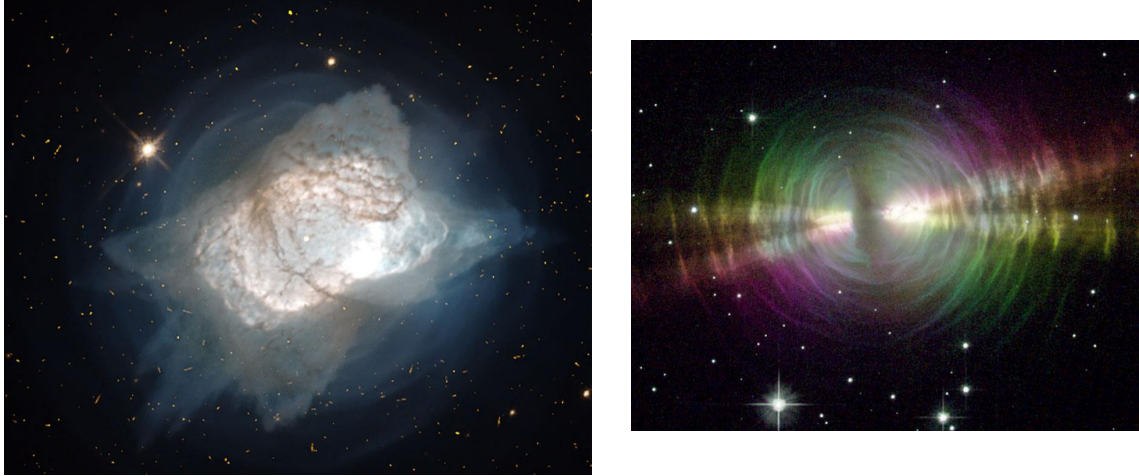


Figure 1.8: Multiple shelled PNe. *left*: NGC 7027, Image credit: Hubble Legacy Archive, ESA, NASA *right*: CRL 2688, the Egg nebula, Image credit: W. Sparks, R. Sahai, JPL, NASA, Hubble Heritage Team (STScI/AURA).

An early attempt at classification of PN shell/halo morphologies by Kaler (1974) consisted of classes based on photographic estimates of the relative shell brightness. A PN was classed as having an extended halo (or so called *giant halo nebula*) if the ratio of the outer to inner radii was greater than 5. These criteria for multiple shelled PNe were later found to be unreliable since the shell sizes and brightness ratios are most likely dependent on how evolved the system is (Chu et al. 1987). Instead Chu et al. (1987) determined a classification which they argue would better indicate the mechanism by which they initially formed. Their classification scheme consists of type I, wherein the multiple shelled PNe consist of detached shells where the outer to inner shell ratio is less than 2. The

diameters of type I PNe range from 0.5 pc to larger than 1 pc, and the outermost shells are limb brightened while the surface brightness profiles show deep dips between the shells. Conversely, type II PNe shells are attached to the primary shell with outer to inner radii ratios larger than 2. Type II multiple shelled PNe have a change in slope between shells but do not have deep dips in their brightness profile.

In addition to shells and halos, around 50% of PNe possess small-scale morphological structures, which are arguably more difficult to explain by classical PN formation theories than the shells and haloes discussed previously. These small-scale structures, such as jets, knots and filaments, are most often observed in lines of low-ionisation, predominantly [NII], [SII], [OII] and [OI], and were thus grouped by Gonçalves et al. (2001) within the blanket-term *Low-ionisation structures* (LIS). In general, structures with an aspect ratio close to 1 are referred to as knots, while filaments have an aspect ratio larger than 1. One of the most well-known PNe, NGC 7293 (the Helix nebula, figure 1.9 (left)), is a prime example of the presence of knots in PNe. The high resolution image NGC 7293 (shown in the right inset of figure 1.9) reveals the presence of elliptical knots with long radial tails pointing away from the central star (which has earned them the nickname “cometary-knots”) suggesting that winds from the central star sweep into the dense knots which are being slowly evaporated, with the evaporated gas being swept backwards (O’Dell et al. 2000). Other examples of PNe exhibiting such tail-like structures include the Dumbbell nebula (see figure 1.1) and Abell 30. In general knots in PNe are thought to contain a significant fraction of the total nebular mass which is trapped into molecular zones (O’Dell & Handron 1996), many of which present themselves in groups which have perplexingly organised patterns (Balick & Frank 2002). It is not at all clear how the knots form in such large, organised groups nor is it entirely certain how the individual knots form to begin with. Some suggestions include that they may be formed via Rayleigh-Taylor instabilities either at the main ionisation front (Capriotti 1971) or as an instability resulting from the fast wind overtaking the slow wind at the onset of the PN phase (Vishniac 1994), which is consistent with such a large fraction of nebular mass being contained within the knot (Capriotti 1973). They may also be primordial in nature, having originated as condensations in the cool atmosphere of the progenitor AGB (Dyson et al. 1989; Matsuura et al. 2009). High velocity pairs of remote knots found on opposing sides of the nebula, usually located along the major axes of PNe in a point-symmetric fashion, are also commonly ob-



Figure 1.9: Knots in a PN: NGC 7293, The Helix Nebula. *Left*: Spitzer Space Telescope image displaying the global elliptical morphology of the Helix nebula Image credits: JPL-Caltech, NASA *Right*: Striking view of some of the thousands of “cometary knots” residing within the inner ring of the nebula. Colour mapping: [O III]=blue, H $\alpha$  =green, [N II]=red. Image credits: C. R. O’Dell and K. Handron, NASA (O’Dell and Handron 1996).

served structures. Dubbed as ‘fast low-ionisation emission regions’ (FLIERs, also known as ansae) (Balick et al. 1993), due to their extremely high speeds (ranging from  $\pm 25$  -  $200$  km s $^{-1}$ ), they are thought to originate as an ejection directly from the central star as their kinematic age is usually younger than the surrounding nebula. Flieres are usually small ( $10^{15}$  -  $10^{16}$  cm), dense ( $n_e = 10^3$  -  $10^4$  cm $^{-3}$ ) and have a tendency towards nitrogen enrichment. High abundances in nitrogen also indicates a high-velocity ejection emanating from the PN central star. They appear to be most common in elliptical PNe, occurring in about half of the objects within this class (Balick et al. 1998). NGC 6826 is one of the many PNe exhibiting Flieres and is displayed in figure 1.10 (left). A similar, yet distinct, manifestation is the presence of hypersonic ( $\simeq 500$  km s $^{-1}$ ) knotty outflows such as those observed in PN Menzel 3 (figure 1.10 (right)) (Redman et al. 2000; Guerrero et al. 2004).

Flieres and knotty outflows are often an accompaniment of highly collimated outflows/filaments with aspect ratios much larger than unity, known as jets. Jets appear in pairs emanating from either side of the central star and have much larger velocities than the surrounding nebulae (Gonçalves et al. 2001), and are linked with the onset of extreme

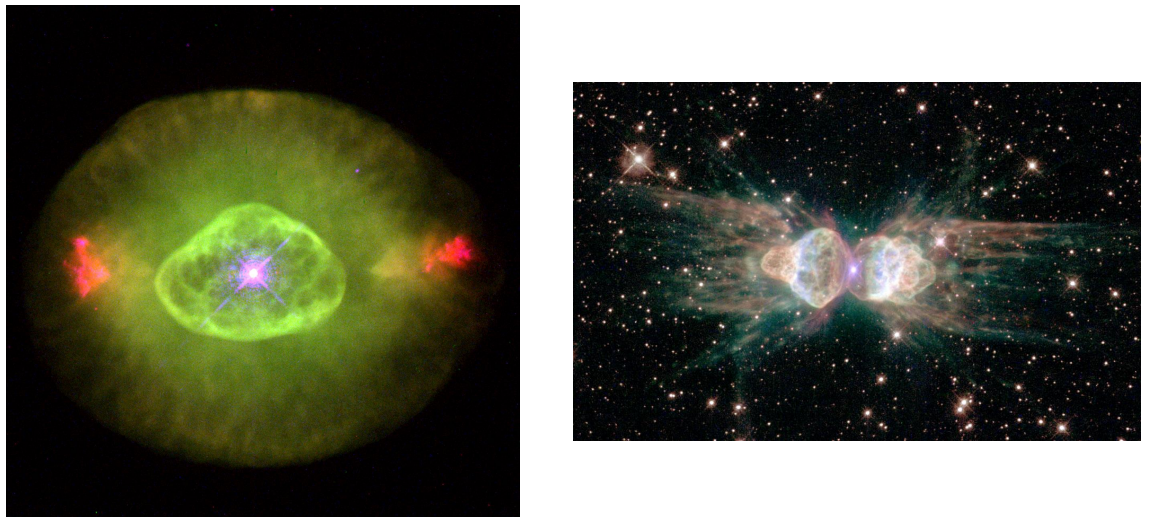


Figure 1.10: High speed LIS.*Left:* Hubble Space Telescope image of NGC 6826, The Blinking Eye nebula, an excellent example of an elliptical PN with fast low-ionisation emission regions (FLIERs). Image credits: Bruce Balick, NASA *Right:* Hubble Space Telescope image of Menzel 3, the Ant nebula, an example of a bipolar PN with hypersonic knotty outflows Image credits: R. Sahai, Hubble Heritage Team, ESA, NASA, JPL.

bipolarity in PNe (Nordhaus & Blackman 2006). However, it is suggested that most jets are the direct result of accretion disks (Soker & Livio 1994) and/or magnetic fields, and as we shall see in the following sections, the origin of such accretion disks and magnetic fields is unclear.

## 1.5 The origin of aspherical symmetries

The ISW, and in particular the generalised ISW, models established a much greater understanding of the formation of PNe. However, many questions still remain as neither theory can adequately explain the secondary structures, such as the high-speed knots, jets and Fliers, outlined in the previous section. Furthermore, the biggest concern is that even though it is clear that an equatorial density enhancement is needed to shape the AGB winds into elliptical and bipolar PNe, the origin of such an enhancement is still a matter of conjecture. Generally there are three main sources of an equatorial density enhancement or wind collimation that are considered in the literature: fast rotation, magnetic fields and binarity, albeit with each having its own caveat. But, as will become evident later in this section, the three shaping theories are most likely intertwined (Soker 1997).

### 1.5.1 Stellar rotation

Soker (1997) defined PNe as being shaped by rotation if the cause of asymmetry is a direct result of the centrifugal force. If the star is capable of having a rotational velocity higher than some critical rotational value, which is determined by the terminal wind velocity and the local escape velocity, the star will have a lower escape velocity at its equator. Thus, the star will ultimately experience an increase in the wind density towards the equatorial plane and decreased wind density in the polar regions (Bjorkman & Cassinelli 1993; Ignace 1996). Should this happen, a disk will naturally form in the equatorial plane and when the star blows its fast winds, bipolar lobes will form since mass can escape more readily in the polar direction. However, it has been shown that as a star evolves to the giant phases, either RGB or AGB, conservation of angular momentum means that it must rotate at a much lower rate than it was capable of on the main sequence. While modest rotation rates may be capable of producing very mild asymmetries, it is generally accepted that single stars cannot rotate at the velocities required for producing the majority of axis-symmetric and bipolar structures (Garcia-Segura et al. 2014). A binary companion can provide this source of angular momentum to spin up the AGB envelope (Nordhaus & Blackman 2006).

### 1.5.2 Magnetic fields

Magnetic fields have been postulated as a shaping agent in planetary nebulae long before observational evidence of such an effect surfaced (e.g., Pascoli 1987). The presence of magnetic fields in evolved stellar objects are usually confirmed through observations of polarised masers (microwave amplification by stimulated emission of radiation). As such, magnetic fields detected in the circumstellar envelopes of AGB stars (Vlemmings et al. 2001, 2002; Etoka & Diamond 2004; Vlemmings et al. 2005), post-AGB objects (Amiri et al. 2011) and PPNe (Sabin et al. 2014) have supported and prompted many theoretical investigations to explore the shaping of PNe by magnetic fields (García-Segura et al. 1999, 2005; Blackman et al. 2001b). Remarkably, reports of evidence for the presence of magnetic fields in the central stars of PNe (Jordan et al. 2005) and also well-aligned toroidal fields in PNe themselves by submillimetre imaging polarimetry (Greaves 2002; Sabin et al. 2007), have continually invigorated investigations into the idea.

However, while observational signatures present astounding evidence for magnetic field presence in PNe, the origin of the fields is not entirely clear. Blackman et al. (2001a) suggest that a dynamo in the AGB envelope can generate the required magnetic field strengths to collimate the winds as the envelope is ejected. Since contraction of the AGB core causes an increase in core rotation, the interface between the core and the differentially-rotating convective envelope of the AGB star is a natural breeding ground in which to produce such a dynamo. They tested the theory by combining the estimated rotation profile of a typical AGB star with a non-linear dynamo model and concluded that the strength of the magnetic fields generated from the highly magnetised core not only have the potential to collimate the wind from the AGB, but that the surface magnetic field could produce coronal mass ejections facilitating the formation of knotty structures. Upon further investigation, magneto-hydrodynamic (MHD) simulations confirmed that when combined with stellar rotation the dipolar field can take on a toroidal geometry, where hoop stresses act to collimate the flow by drawing material towards the axis during the post-AGB wind. This scenario is known as the magnetised wind bubble model and is believed to be responsible for collimation and jets, resulting in elliptical, bipolar and point-symmetric PNe (Chevalier & Luo 1994; García-Segura et al. 1999; Blackman et al. 2001b; García-Segura et al. 2005). The creation of- and shaping by jets is unsurprising,

since jets have been known to shape outflows in other rotating astrophysical disk systems such as active galactic nuclei and young stellar objects. Since jets in PNe are also a possible source of secondary morphological characteristics such as FLIERs and high speed knots along the symmetry axes, an extension of magnetic field shaping is the production of these characteristics. Furthermore, observations of H<sub>2</sub>O masers tracing a jet protruding from an AGB star indicate that a magnetic field was the source of the jet (Vlemmings et al. 2006).

Still, the idea of shaping planetary nebulae by magnetic fields is subject to strong doubts surrounding its feasibility. While MHD models have been successful in determining the plausibility of magnetic fields in shaping a planetary nebula, (e.g., Blackman et al. 2001b), the models are based on the assumption that the magnetic field already exists intrinsically or can be generated and sustained by a dynamo seeded by rotation. The dynamo models of Blackman et al. (2001a) do produce a sufficiently strong field for magnetic shaping but the authors note that they have exaggerated the differential rotation that may develop in the star and do not take into account loss of angular momentum through, for example, magnetic braking. Furthermore, even in the case that a magnetic field is successfully generated by a dynamo, its long-term sustainability is doubtful. In order to shape a planetary nebula, the scale of the magnetic field required would be much larger than single-star rotation can sustain and any large-scale magnetic field will actually halt differential rotation in the circumstellar envelope and subsequently be the source of its own dissolution too soon to be able to effect the geometry of the mass-loss (Soker 2006; Nordhaus et al. 2007). In that case, the presence of a magnetic field also excludes any chance of shaping by rotation alone. Nonetheless, it is still a possibility that magnetic fields (and therefore rotation) are linked to the nebular shaping process in a single star, but only if the required angular momentum can be extracted from an external source such as an interaction with an orbiting companion. The companion can either be a stellar binary or substellar (planet or brown dwarf), as long as the companion can offer enough angular momentum to the primary star to induce rotation. Although in that case it can be argued that the underlying source of PNe shaping is ultimately due to the presence of a companion. In fact Soker (2006) suggests that if a stellar binary is indeed present, the shaping effect caused by the binary interaction itself will play a much larger role in shaping than a magnetic field can. For this reason the general consensus in the field is

that magnetic fields are certainly an important source of shaping but rotation, magnetic fields and binarity should not be considered as mutually exclusive and, as demonstrated by Garcia-Segura et al. (2014), binarity must be considered as the leading cause of the vast majority of non-spherical PNe.

### 1.5.3 The binary hypothesis

The *binary hypothesis* refers to the argument that most planetary nebulae are the result of a binary interaction (De Marco 2009). A binary interaction not only provides a natural symmetry axis by means of the orbital plane, but can also provide the angular momentum required to increase rotation and/or generate magnetic fields, as discussed in the previous sections (see De Marco & Izzard 2017; Jones & Boffin 2017, for recent reviews of the impact of binaries on stellar evolution and planetary nebulae).

Observational evidence supporting the binary hypothesis has achieved impressive calibre since the first confirmation of a binary central star of a PN in 1976 (PN Abell 63, Bond 1976). In particular, a plethora of binary central stars of PNe (bCSPNe) have been discovered within just a couple of decades (De Marco et al. 2004; Miszalski et al. 2009; Boffin et al. 2012; Corradi et al. 2014; Jones et al. 2014, 2015; Sowicka et al. 2017). Recently, Hillwig et al. (2016) presented a remarkable correlation between the symmetry axes of bipolar PNe with binary central stars being aligned to the orbital plane of the system, providing the most convincing evidence to date for the binary hypothesis and confirming the connection between binary evolution and some of the morphologies of PNe. A similar, yet distinct, class of nebulae which are believed to have had their morphologies influenced via the presence of a binary interaction are known as symbiotic nebulae and are often misclassified as PNe. In such systems, the primary has already evolved past the PN phase leaving behind a hot WD core which later ionises the mass being ejected from the secondary, which is now a Mira-type giant (e.g., Santander-García et al. 2008). While symbiotic systems are not technically PNe, the fact that they are inherently a binary phenomenon and bear a striking resemblance to PNe in terms of their morphologies provides strength to the binary hypothesis in PN shaping. An intriguing example of the similarities between PNe and symbiotic nebulae can be seen in figure 1.11 in which the inner hourglass morphology of the symbiotic nebula Hen 2-104 closely resembles the

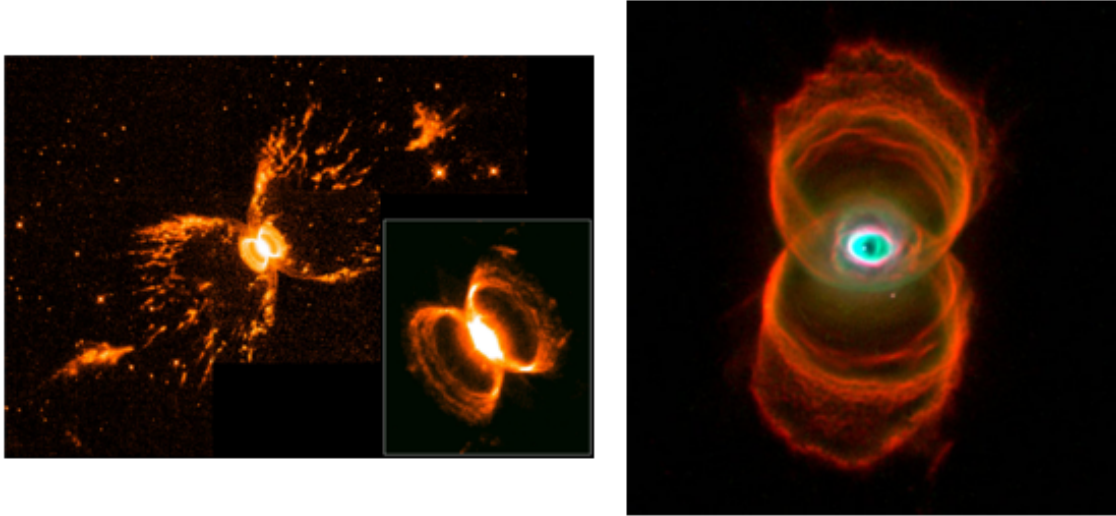


Figure 1.11: Hen 2-104 and MyCn18: The striking similarity between symbiotic nebulae and PNe. Image credits: (*left*) R. Corradi (*right*) R. Sahai and J. Trauger (JPL), WFPC2, HST, NASA

hourglass morphology of PN MyCn 18.

There are a number of ways in which a stellar binary companion can shape a PN and, in general, the influence of a binary interaction on the resulting PN depends on the orbital parameters and mass ratio of the binary system. Soker (1997) proposed a simple categorisation for the varying types of binary interactions based upon the varying degrees of binary separations, under which the morphology of a PN being influenced by non-single star evolution is defined by having at least one property of the primary being determined by an orbiting body. Consequently, PNe resulting from stellar binarity are usually organised into interactions arising in extremely wide binaries, moderately wide binaries and close binaries.

Extremely wide binary systems, refer to systems where the orbital period,  $T_{\text{orb}}$ , is much longer than  $\tau_{\text{PN}}$ , the PN lifetime ( $\tau_{\text{PN}} \ll T_{\text{orb}}$ ), and are only capable of accounting for nearly negligible morphological structures, such as small blobs or bubbles inside the nebula, but not for any prominent secondary or global morphological changes. On the other hand, moderately wide binaries, in which case the orbital period is comparable to the PN lifetime ( $\tau_{\text{PN}} \sim T_{\text{orb}}$ ), can produce density enhancements in the orbital plane, and thus asymmetries, as a result of mass transfer if the orbital velocity of the secondary is comparable to the rate of mass-loss of the AGB (Boffin 2015). Observations using

the Atacama Large Millimetre/Submillimetre Array (ALMA) of the mass-losing AGB star, R Sculptoris (depicted in figure 1.12) revealed an excellent example of the type of structure which can result from such an interaction (Maercker et al. 2012). The spiral structures produced via mass transfer in AGB binary systems such as R Sculptoris had been previously predicted by hydrodynamic simulations which strongly suggested that the mass transfer in a wide binary system would produce a spiral in the winds (Mohamed & Podsiadlowski 2012).

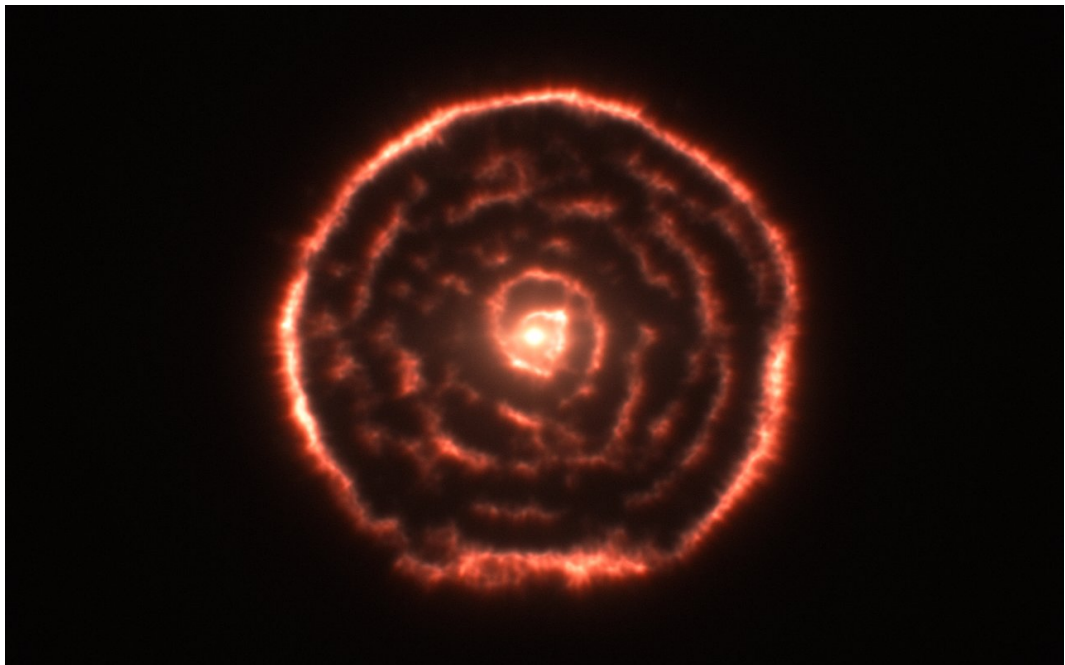


Figure 1.12: Using the Atacama Large Millimetre/Submillimetre Array (ALMA) Maercker et al. (2012) discovered a large spiral structure in the wind of R Sculptoris. Such a structure is likely the result of a wide binary interaction. Image credits: Maercker et al. (2012), ESO.

Close binaries produce the most pronounced and broad range of shaping effects in PNe. A close binary can produce asymmetries by means of gravitational interactions, and also tidal forces (Soker 1995), which may act to increase the rotation of the AGB envelope and enhance stellar mass-loss (Tout & Eggleton 1988). For example, a binary with an eccentric orbit would enhance the mass-loss periodically resulting in displacement of the nebula from the centre of mass of the system (Soker et al. 1998). Close binaries can also result into accretion onto the secondary, leading to high mass-loss rates in the equatorial plane. There is a possibility that the density enhancement brought on by accretion onto the secondary could be linked to another interesting shaping possibility, the formation

of quadrupolar PNe by the precession of a close companion (Manchado et al. 1996). Interestingly quadrupolar PNe tend towards high N/O abundances, and the correlation of high abundances of N/O between bipolarity, and high mass progenitors ( $\gtrsim 2.4 M_{\odot}$ ) suggests that PNe with high N/O ratios form from higher mass stars. Thus this indicates that quadrupolar PNe may have formed from progenitors in this mass range which is consistent with suggestions that higher mass progenitors are more likely to be a binary (Soker 1998a).

A subset of close binary progenitor systems will undergo a common envelope (CE), a scenario which further enhances the shaping opportunities for the resulting PNe, and are likely to be the catalysts for the most extreme PN morphologies. PNe in which their progenitor system evolved through a CE are often referred to as post-CE PNe. The ingredients for a CE scenario in a PN progenitor binary system are generally two stars with differing masses, where the most massive of the pair has evolved off the main sequence and has obtained a deep convective envelope, as in an RGB or AGB star, while the less massive star still resides on the main sequence. When the AGB primary overfills its Roche lobe it begins a dynamical mass transfer onto the secondary which quickly loses thermal equilibrium if it is unable to accrete the mass as quickly as it is being transferred (Paczynski 1976). This configuration is highly unstable and tends to result in the companion star filling its own Roche lobe and spiralling into the envelope of the primary, where it settles into a tight orbit around the core (Iben & Livio 1993; Rasio & Livio 1996; Ivanova et al. 2013).

Nordhaus & Blackman (2006) described three shaping outcomes predicted for a CE interaction, shown schematically in figure 1.13. The first, depicted as (a) in figure 1.13, is the removal of mass from the envelope in the orbital plane or equatorial region of the system. As the companion enters into a CE with the primary, angular momentum and energy will be transferred from the orbit into the AGB envelope as the companions orbit shrinks. Supplying a sufficient amount of angular momentum to the primary in this way can increase the rotation of the primary, and ultimately enhance mass-loss in the equatorial region. Alternatively, if the deposited orbital energy is sufficient, the companion can unbind the stellar envelope which will be ejected into the orbital plane. The enhanced mass-loss then provides the density enhancement necessary for the generalised ISW model to produce a non-spherical PN. A failure to eject the envelope persists in the

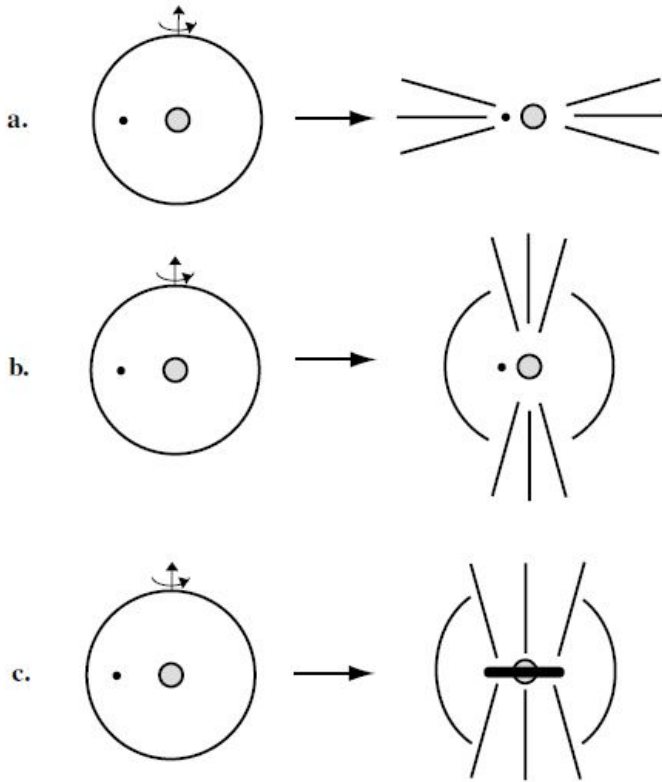


Figure 1.13: The outcomes of a binary common envelope scenario proposed by Nordhaus & Blackman (2006). (a): The removal of mass from the envelope in the orbital plane, or equatorial region, of the system. (b): An alpha-omega dynamo generation of a magnetic field as a result of the differential rotation between the secondary and the AGB envelope. (c): the destruction of the companion near the core of the AGB star, formation of an accretion disk, and a disk-driven outflow.

many attempts that have been made at simulating this scenario via 3-D hydrodynamic models, however (e.g., Passy et al. 2012; Iaconi et al. 2017; Iaconi et al. 2017). Models typically find that while the envelope is inflated, or lifted away from the system, only a small amount of mass becomes unbound. While recent models including recombination energy have been able to eject the envelope (Nandez & Ivanova 2016), there is still a debate on how much of this energy is in fact available for the process since it is possible that the majority of it may be radiated away (De Marco & Izzard 2017; Sabach et al. 2017).

The second possible outcome of a CE interaction described in Nordhaus & Blackman (2006), (b) in figure 1.13, refers to an alpha-omega dynamo generation of a magnetic field as a result of the differential rotation between the secondary and the AGB envelope. As already mentioned earlier, angular momentum will be injected into the AGB as a result of the in-spiral of the companion and the onset of a CE. Such an external source of angular

momentum can sustain the differential rotation required to produce and sustain a magnetic dynamo.

Finally, the third possible outcome from a CE interaction, (c) in figure 1.13, describes the destruction and accretion of the companion near the core of the AGB. Once the system is within a CE, the orbital separation of the binary system is expected to decrease very rapidly (on a timescale of hundreds of days, De Marco & Izzard 2017) due to drag forces between the envelope and the companion. In the case that the companion does not provide enough orbital energy to the envelope for scenario (a), and thus continues to spiral-in towards the core, it will reach a critical point where it will be destroyed (or *shredded*) by tidal forces, resulting in its remnant-mass forming an accretion disk around the core of the primary. If shredding occurs, and an accretion disk forms, a disk-driven outflow similar to those seen in young stellar objects and active galactic nuclei is likely.

From the discussion on the possible role of binarity in PN shaping presented in the previous paragraphs it is clear that there are many theoretical avenues through which a binary system can evolve to produce a non-spherical PN via enhanced rotation, magnetic activity or otherwise. However, it can be argued that we are still far from explicitly determining the exact nature of the role of binarity in PN shaping. Furthermore, if binarity is the leading cause of PN shaping then it should be expected that the progenitor binary distribution should correlate with the non-spherical PN population, but in reality this is not the case.

Miszalski et al. (2009) utilised the high cadence and sensitivity of the Optical Gravitational Lensing (OGLE) survey to search for photometric variability in the central stars of a number of PNe which were included in the survey sample. The results of that work provided the most accurate observational (that is, the only bias was that only PNe which were photometrically detectable and observable by the OGLE survey were included) binary-fraction to date. The binary-fraction from this survey was  $\simeq 15 - 20\%$ . While this is considered to be a lower limit, and is only representative of close binaries, there is still cause for some concern regarding this as the binary-fraction. Firstly, the observed binary-fraction is obviously far lower than the observed fraction of non-spherical PNe ( $\simeq 80\%$ , Parker et al. 2006). This fraction, however, contains all PNe with at least some degree of asphericity, even if the deviations are very small. Since close binary interactions are thought to produce the most extreme PNe, those with bipolar morphologies and other

large deviations from spherical symmetry, the observed post-CE fraction of PNe might indeed correlate adequately with the morphological classifications (where the fraction of bipolar PNe is  $\approx 15\%$ ). However, when taking into account elliptical and extremely elliptical PNe, which account for  $\approx 55\%$  of all PNe and still require an explanation from a binary origin, along with all other non-spherical morphologies (irregular/quadrupolar,  $\approx 10\%$ ), the fraction of PNe which need to be explained by a binary interaction, including both wide and close binaries, increases again to 80% of the entire stellar population. According to the period distribution of binaries from Raghavan et al. (2010), shown in figure 1.14, where the fraction of stars in a binary system is  $\approx 50\%$  of the total PN progenitor population, binaries with separations which could shape a PN, either mildly or extreme, is only around 30% of the entire stellar population. There are simply not enough PN progenitors in a binary system to account for the high numbers of non-spherical PNe.

Population synthesis models and tidal evolution calculations of binary systems provide another source of perplexity in the binary hypothesis in comparison to the binary progenitor population. Madappatt et al. (2016) recently calculated that the binary-fraction of post-CE PNe should only be around 2.5% of all PNe, according to their tidal evolution model and the period distribution of binary systems, indicating that the observed post-CE binary-fraction is too high to compare with the stellar population. Furthermore, taking into account that some of these CE binaries could also lead to an event where the companion and the core of the primary merge rather than forming a binary central star means that the prediction of 2.5% of all central stars of PNe being post-CE binaries is actually an upper limit. Such a low estimate for the fraction of post-CE PNe provides further support to the postulation that perhaps binary interactions are actually responsible, or are even *required*, for producing all PNe and that single stars which do not interact at all produce non-visible PNe (Soker & Subag 2005; Moe & De Marco 2006; Moe & De Marco 2012; Madappatt et al. 2016). In any case, there is still a lot of uncertainty on the true binary-fraction of CSPNe. While there is no doubt that binarity is extremely important and can account for a high number of non-spherical PNe, it is still not entirely clear that all PNe are the result of a stellar binary interaction.

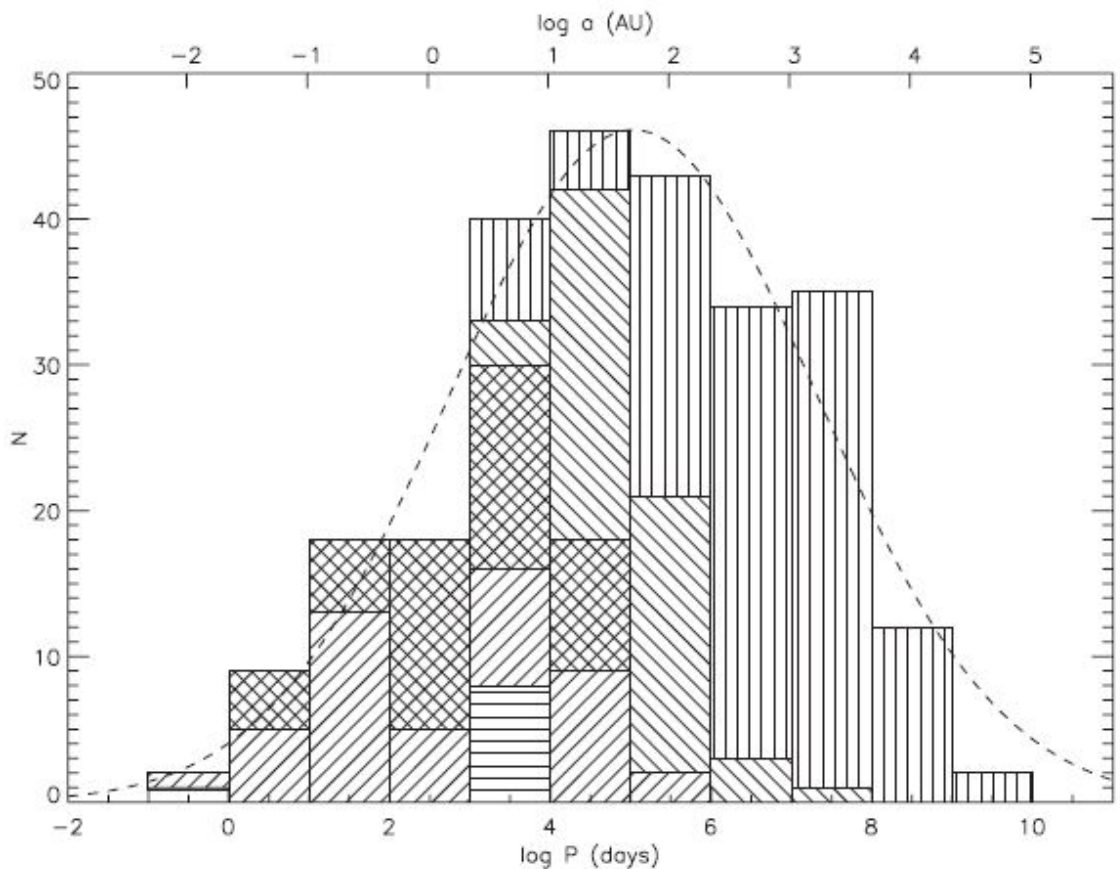


Figure 1.14: The period distribution of binary stars from the survey of Raghavan et al. (2010), where differing patterns depict the various detection methods of the systems. Horizontal line shading corresponds to detection by proper-motion accelerations; the forward-sloped lines correspond to spectroscopic binaries; back-sloped lines are visual binaries; the cross-hatchings depict binaries which were discovered by both spectroscopic and visual methods; vertical lines are binaries with common proper-motion.

## 1.6 Planets and planetary nebulae

In the previous sections we have seen that the transition from a spherical AGB star to a non-spherical planetary nebula is still something of a mystery. According to the generalised ISW theory, to form a non-spherical PN there needs to be a mechanism which can produce a density enhancement in the equatorial region of a mass-losing AGB star, or a mechanism by which the mass-loss is collimated as the fast wind blows. Fortunately, the formation of non-spherical PNe can be explained by a combination of stellar rotation, magnetic fields and binaries. It is clear that binarity plays the most major role in facilitating the shaping mechanisms. However, as discussed in the previous section, there are discrepancies between the stellar binary progenitor population and the population of non-spherical PNe. There is even speculation that without the presence of a binary, a PN may be too faint to detect or may not even be formed at all, and thus skewing the observed morphologies towards a non-spherical majority. Generally, studies of binary interactions in PNe assume that the companion is stellar. In virtue of the discrepancy between observed morphologies and the progenitor population, a new hypothesis emerged in that the companion does not necessarily need to be stellar in nature and that the definition of a binary interaction in the shaping of PNe can be extended to include brown dwarfs and, as is the subject of this thesis, massive planets (Soker 1996b, 1997; Nordhaus & Blackman 2006).

The ways in which a planet can influence the morphology of a PN is not very different to that of the binary hypothesis. In fact, in the Soker (1997) definition of binarity, the classes of orbiting bodies which influence PNe also include those that are substellar in nature. Furthermore, Nordhaus & Blackman (2006) proposed that the various channels for PN shaping by a binary, outlined in the previous section and depicted in figure 1.13, are also possible with a massive planet. In the past two decades the numbers of planets known to be orbiting sun-like stars has increased greatly, adding support to the argument that some non-spherical PNe may be of planetary origin. Furthermore, simulations of the orbital evolution of planets orbiting evolving stars suggest that planets often undergo a process commonly known as *engulfment* as the star ascends either the RGB or AGB (Villaver & Livio 2007, 2009; Villaver et al. 2014). As we will see later on, in chapter 3, whether or not a planet is engulfed depends on the evolution of the stellar structure,

and thus the adopted input physics in stellar models. Determining the conditions for engulfment is an active area of research, and is an important subject in this work. The engulfment process can be described as similar to a binary CE in that the planet enters the envelope of its expanding host as it becomes an RGB or AGB star. Once the planet enters the stellar envelope, drag forces cause the planet orbit to decrease very rapidly. During the engulfment and spiral-in process, its orbital energy and angular momentum are dumped into the stellar envelope, and if the engulfment takes place on the AGB and depending on the initial conditions of the system, it can result in one of the three Nordhaus & Blackman (2006) shaping scenarios.

Also relevant to the planet shaping hypothesis is the idea that planet engulfment can effectively enhance mass-loss on the RGB, causing it to lose most of its envelope (Soker 1998b; Nelemans 2010; Bear & Soker 2011). The result of such mass-loss on the RGB is that the star cannot evolve to the AGB which in turn prevents the formation of the planetary nebula, instead it will evolve as an extreme horizontal branch star (EHB), eventually becoming a helium white dwarf (Dorman et al. 1993). Originally, stellar binary interactions on the RGB had been suggested to be the cause of an RGB star to undergo such an evolutionary path (see, e.g., Han et al. 2002, 2003, and references therein). However, not all of these objects have a stellar companion. Nelemans & Tauris (1998) investigated the ingestion of a planet to explain the discovery of under-massive single helium white dwarfs. The only other plausible explanation for the formation of such a white dwarf would have been a double-degenerate merger, but that scenario predicted higher rotational velocities in the remnants than what was observed. Recent discoveries of planets orbiting extreme horizontal branch stars support the idea further (Geier et al. 2009; Charpinet et al. 2011). If the RGB engulfment of a planet can halt the evolution of a single star in such a way, then there may also be a subset of single stars in the progenitor populations which do not become PNe at all, further reducing the number of single-stars and spherical PNe in the observed PN population.

Given the ever growing number of known planet hosting stars, planet shaping could account for a substantial fraction of elliptical PNe, and in some cases may even be responsible for producing extremely elliptical/bipolar PNe. Although there has, as of yet, been no direct observational link between planets and the shaping of planetary nebulae, support for the planet hypothesis is slowly mounting and the idea is beginning to gain traction

within the PN community. For example, Clyne et al. (2014) suggested that the extreme bipolar morphology of PN MyCn 18 and its enigmatic hypersonic knotty outflows could be the result of a planet engulfment, destruction and shaping event. A most recent observation in support of the planet hypothesis is the detection of an inclined, young ring of molecular gas with a mass comparable to a Jupiter-like planet by Santander-García et al. (2017), who suggested that the origin of the ring could possibly be the engulfment and destruction of a massive planet.

The planet shaping hypothesis has not been immune to scrutiny however, with some suggestions that planets cannot offer enough orbital energy or angular momentum to cause any long lasting, visible, shaping effect. This opposition is based on the results of hydrodynamic simulations of Staff et al. (2016), who found that the in-spiral of a planet within the AGB envelope was not capable of ejecting the envelope; the envelope becomes inflated somewhat, but only a small fraction of mass is removed. However, as discussed earlier, the same problem has presented itself in hydrodynamic simulations of binary common envelopes. Thus, the ejection of the envelope in terms of both binaries and planets can still be considered as an open ended debate. Furthermore, the planet shaping hypothesis is not only limited to the scenarios previously discussed in relation to the binary hypothesis. Soker (2004) suggested that the deposition of orbital energy and/or angular momentum by a planet entering the stellar envelope may not be the only effect a planet can have on its host and describes a number of *non-linear* ways in which a planet engulfment can alter the evolution such that the resulting PN is non-spherical (See also Bear & Soker 2011). A non-linear effect refers to an effect that is very sensitive to even very small changes induced by the engulfment of a planet. When a planet enters the envelope of a star with a convective envelope it can excite pressure waves (p-waves). The p-waves, even if they are initially very small-scale oscillations, increase in amplitude as they propagate outwards; the effect will naturally be strongest in the orbital plane and increases linearly with the mass of the planet (see also Soker 2017, for a recent discussion). Such oscillations act to enhance the mass-loss, producing the desired density enhancement for the generalised ISW model. Furthermore, as the planets orbit decreases within the envelope, the effect of the p-waves increases. The effect of p-waves in itself could lead to a non-spherical PN, but an even more powerful scenario would be the combination of such with the spiral-in and shredding of a companion and the formation of an accretion disk around the core,

giving rise to an energetic bipolar outflow.

Another non-linear way in which a planet can alter the host stars evolution is by the deposition of angular momentum, increasing the rotational velocity of the star, even by a very small amount. Carlberg et al. (2009) found that the engulfment of a planet can indeed increase the rotation rate of an RGB star. The non-linear effect of rotation in the sense of shaping the AGB wind, however, is not the same as discussed previously; instead it has an effect on the formation of cool magnetic spots on the stellar surface (Soker 1998c; Soker & Clayton 1999). Such magnetic spots can enhance dust formation near the stellar surface, and thus increases the mass-loss rate. Should the planet increase the rotation slightly in the orbital plane, inducing small-scale/weak dynamo activity, the magnetic spots will form near the equator increasing the mass-loss rate in the equatorial region with respect to the polar regions (Nordhaus & Blackman 2006).

Thus from a theoretical (as well as a possible slowly-emerging observational) standpoint, it is apparent that planet shaping is capable of accounting for a proportion of non-spherical PNe. Unfortunately we are still far from determining to what extent planet shaping does count towards the population of non-spherical PNe by any observational means. Nonetheless, since there is still no explanation for such a large majority of observed PNe with non-spherical morphologies, and because evidence towards the role of planets in a few example PNe is beginning to gain momentum, it is now timely to consider the likely frequency of planet shaping and how it fits in with the PN morphological classifications, the progenitor population and the PN population as a whole. If planet engulfment can explain a substantial fraction of non-spherical PNe, this may alleviate the mystery surrounding PN morphologies and the lack of stellar binaries available to produce them.

## 1.7 Thesis overview

The aim of the research presented in this thesis is to investigate the hypothesis that planet engulfment is responsible for the morphologies in a subset of non-spherical planetary nebulae, with the overall aim of calculating the *planet-fraction* of PNe (the fraction of PNe whose morphologies were influenced by the engulfment of a planet during the AGB phase). This is achieved by modelling the orbital evolution of exoplanet systems to determine the conditions for engulfment for various PN progenitors, and apply the same treatment to entire populations of planet-hosting stars in order to determine the probability of planet engulfment by the AGB progenitors of PNe, as a function of main-sequence mass and metallicity. To calculate the number of PNe we can expect to have undergone a planet-shaping scenario in the galaxy, a population synthesis was performed and is presented in this thesis. In order to carry out the work presented here a new tool was developed, **SIMSPLASH** (SIMulationS for the PLAnet-Shaping Hypothesis). **SIMSPLASH** contains three modes of operation: *Orbital* mode, which handles the orbital evolution of individual star-planet systems, *Single-epoch population* mode, which determines the probabilities of stars engulfing massive planets as a function of stellar mass and metallicity and applies this information to the current stellar population; and *Multi-epoch population* mode, which performs PN population synthesis calculations. Each mode of operation provides a different task/analysis and their details are provided in their respective chapters. The following is an overview of the content contained within each chapter and its context to the thesis as a whole.

**Chapter 2** provides the details of the technical theory and methods employed throughout this thesis. This includes the theoretical formalism for the tidal evolution of an exoplanet orbit in response to an evolving star and the theory of tidal dissipation, which will be exploited throughout chapters 3, 4 and 5. This chapter also describes the databases, external software and methods which were utilised to develop the **SIMSPLASH** tool, including the background theory for the standard techniques involved in performing population synthesis calculations, such as the forms of the stellar initial mass functions. Finally, a brief description of **SIMSPLASH** is presented, although full details of each mode of operation are included in chapters 3, 4 and 5.

**Chapter 3** describes the contents of the SIMSPLASH Orbital mode, which is then used to determine the RGB and AGB *engulfment zones* of planet-hosting stars; the range of semi-major axes within which a planet will be engulfed during the RGB and AGB, respectively. This analysis is performed on example star-planet systems with various stellar models, planet masses and initial semi-major axes to highlight the conditions for engulfment to occur and to investigate which stellar properties have important effects on engulfment zone calculations. Since one of the first steps in determining the plausibility of the planet shaping hypothesis must lie in the orbital evolution of the planet during the red giant branch and asymptotic giant branch, determining the orbital evolution and conditions for the engulfment of planets is a crucial aspect of the hypothesis being investigated in this thesis. The chapter begins with a description of the formulae for the semi-major axis evolution. The semi-major axis evolution of a planet orbiting an evolving star is a balance of mass-loss and tides, where the tidal formula is a direct extension of the tidal theory described in chapter 2. The orbital evolution is then calculated by integrating the semi-major axis evolution with the stellar evolution models which are also outlined within the chapter. It is demonstrated that SIMSPLASH, when run in Orbital mode, agrees well with the current knowledge of planet engulfment by comparing the results to those previously presented in the literature. New results stemming from the inclusion of rotation and a modest mass-loss coefficient in the stellar models used are also presented here.

**Chapter 4** presents, for the first time, a method to determine the probabilities of planet engulfment by PN progenitors as a function of a stars main-sequence mass and metallicity. This work utilises SIMSPLASH in its single-epoch population mode; an option for evolving and analysing an entire population of exoplanets. For a given sample of exoplanets, SIMSPLASH reads in all relevant information for each star-planet system in the sample and determines the number of systems in which an engulfment occurs and at what stage in the evolution. The chapter begins by introducing the populations being investigated in the chapter which are the known exoplanets from the Exoplanet Orbit Database, and synthetic populations of exoplanets provided by Shigeru Ida. By combining the results of the engulfment calculations of a particular population with the occurrence rates of massive planets, SIMSPLASH performs a statistical analysis and the probabilities of planet

engulfment are determined as a function of stellar mass and metallicity. Finally, a simple calculation to determine the number of main sequence PN progenitors *currently* in the galaxy which will undergo a planet engulfment scenario is presented and used to draw some conclusions on the formation of the current population of PNe.

**Chapter 5** presents, for the first time, a planetary nebula population synthesis which includes the effects of planet engulfment on the population of PNe visible in the galaxy today, using `SIMSPLASH` in its Multi-epoch population mode. The chapter begins by outlining the main ingredients of the population synthesis model within `SIMSPLASH` which includes the star formation history, galactic metallicity evolution and the determination of the number of visible PNe in the current galactic population. Following this, the adopted assumptions and approximations in the presented models are outlined. This includes binary and stellar statistics and the use of the engulfment probability results from chapter 4 to determine the number of PN progenitors formed within each population which will evolve through the engulfment of a massive planet. An inventory of the PN formation history is calculated and compared to previous estimates of the PN population, and the expected planet-fraction of PNe is thus presented. Finally, a discussion of planet engulfment as a shaping mechanism, and possible sources of evidence of the scenario already existing in the literature, is presented.

**Chapter 6** marks the concluding chapter of this thesis. Here, a summary of the results and conclusions presented in chapter 3 through chapter 5 will be presented, and the overall conclusions for the prospect of the shaping of planetary nebulae stemming from this thesis will be highlighted. Lastly, suggestions for future work related to the contents of this thesis are proposed.



# **Chapter 2**

## **Theoretical formalism, methodology and techniques**

### **2.1 Introduction**

This chapter describes the methods and background theory which form the basis for the work presented in this thesis. Since the aim of this research is to investigate the hypothesis that planet engulfment can explain a proportion of the non-spherical morphologies in PNe, a crucial aspect is to model the orbital evolution of planets around evolving stars. The orbital evolution depends on the tidal evolution of the semi-major axis and also the response of the semi-major axis to stellar mass-loss, and so an understanding on how tides are raised and their effects on the orbital evolution is important, as is the use of stellar evolution tracks. The standard tidal theory is thus presented in the next section along with the adopted formalism for turbulent dissipation of energy of Zahn (1977, 1989). Following this, the `MESA` Isochrones and Stellar Tracks database (MIST) of Choi et al. (2016), as well as the `MESA` code itself, both of which have been extensively utilised in this work, are introduced in section 2.3. Other important aspects of this research are the properties of exoplanets, stellar distributions and the PN population synthesis technique, which are addressed in sections 2.4 and 2.5, respectively. Finally, an introduction to `SIMSPLASH`, the code developed for this research, is outlined in section 2.6.

## 2.2 Tidal evolution of planetary orbits

A well-known phenomenon in orbital mechanics is that in a two-body system tides will be raised on one body by the other as a result of the variation of the gravitational force across the body, causing the system to evolve dynamically, all the while conserving angular momentum (Darwin 1879). A familiar example of this is the Earth-Moon system; the gravitational force experienced by the side of the Earth closest to the moon is much larger than that experienced by the side farthest away from the Moon, leading to a deformation commonly known as a *tidal-bulge*. The response of the Moon to the tide it has raised, and the continuous dissipation of kinetic energy as a result of friction, results in the evolution of the orbital period of the Moon and the rotation of the Earth. This effect has indeed been determined for the Earth-Moon system, in which the semi-major axis of the Moon has been calculated to be slowly increasing, and as a consequence of the conservation of angular momentum the rotation rate of the Earth is slowing down (Murray & Dermott 2000).

Just like the Earth-Moon system, the tidal phenomenon is observed in star-planet systems, where the star will experience a tide raised by a closely orbiting planet, resulting in two opposing tidal bulges on the star. This is drawn schematically in figure 2.1, where the planet of mass  $M_{\text{pl}}$  and star of mass  $M_*$  are separated by a distance,  $a$ , and  $f_1$  and  $f_2$  are the forces applied to the near and far bulges, respectively. Referring to the same figure, the orbital velocity of the planet is faster than the rotational velocity of the star (and so the orbital frequency of the planet,  $\omega_{\text{pl}}$ , is larger than the rotational frequency of the star,  $\Omega_*$ ), thus the bulges are said to *lag* behind the orbiting planet (characterised by a lag-angle,  $\alpha$ ) which ultimately results in the dynamical evolution of the system. This configuration is described in more detail in the following, where the description of tides in star-planet systems is largely adapted from Zahn (2008). Note that circular orbits are assumed.

If the rotation of the star is synchronised with the orbit of the planet the tidal bulges will be aligned with the line connecting the centre of the star to the centre of the planet; a stable configuration. However, when the orbit is not synchronised with the rotation the system is unstable. According to the equilibrium tide model, in the absence of dissipation mechanisms, the system will evolve towards a stable equilibrium state of minimum kinetic energy in which the equatorial planes of the two bodies coincide with the orbital plane

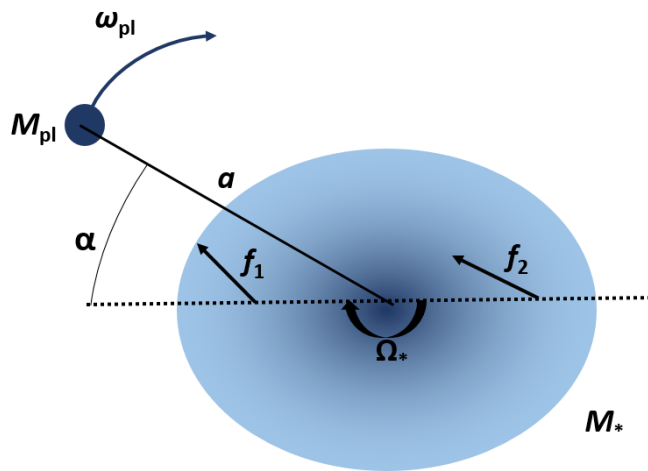


Figure 2.1: The tidal torque in a two body system: A star will experience a tide raised by a closely orbiting planet, resulting in two opposing tidal bulges on the star, where the planet of mass  $M_{\text{pl}}$  and star of mass  $M_*$  are separated by a distance,  $a$ , and  $f_1$  and  $f_2$  are the forces applied to the near and far bulges, respectively. If the orbital velocity of the planet,  $\omega_{\text{pl}}$ , is faster than the rotational velocity of the star,  $\Omega_*$ , the bulges become misaligned with the line connecting the two bodies, and a torque arises in the primary (the dotted line through the bulged region of the star) acting to spin up the star until an equilibrium can be reached. The misalignment is characterised by a lag-angle,  $\alpha$ . Consequently, angular momentum is exchanged from the orbit to the spin rate of the star, leading to the dynamical evolution of the system. Image redrawn by author following Zahn (2008)

(coplanarity), circular orbits, and where the rotation frequency of the star is equal to the orbital frequency of the planet. Considering the case of where the orbital velocity of the planet is faster than the rotational velocity of the host star, dissipation of energy due to tidal friction results in the tidal bulges to be misaligned with, and lag behind, the orbiting planet. This lag is characterised by the lag-angle,  $\alpha$ , which tends to zero as the rotation of the star tends towards the orbital velocity of the planet. Consequently, the star experiences a torque which facilitates the increase in rotation in order to reach the equilibrium state. Taking the relative height of the tidal bulge as  $\delta R_*/R_*$  (where  $R_*$  is the stellar radius), which is approximated as equal to the ratio of the differential acceleration (tidal force) exerted on the bulges to the surface gravity,  $g$  (the binding force), such that

$$\frac{\delta R_*}{R_*} \simeq \frac{GM_{\text{pl}}R_*/a^3}{GM_*/R_*^2} = \frac{M_{\text{pl}}}{M_*} \left(\frac{R_*}{a}\right)^3. \quad (2.1)$$

By undertaking the approximation that the density of the star is constant, the mass contained in either bulge can be easily estimated as  $\delta M_* = (\delta R_*/R_*)M_*$ , the torque is then given by

$$\Gamma \simeq (f_2 - f_1)R_* \sin \alpha \simeq -\delta M_* \left[ \frac{GM_{\text{pl}}R_*}{a^3} \right] R_* \sin \alpha = -\frac{GM_{\text{pl}}^2}{R_*} \left( \frac{R_*}{a} \right)^6 \sin \alpha. \quad (2.2)$$

A torque of equal magnitude will also act on the planet and, due to the continuous dissipation of energy, results in the exchange of angular momentum from the planetary orbit to the stellar rotation.

The *weak friction approximation* describes the lag-angle as being proportional to the difference in the rotational velocity of the star and the orbital angular velocity of the planet ( $\Omega_* - \omega_{\text{pl}}$ ). But it also depends on the efficiency of the processes that are responsible for the dissipation of kinetic energy. The dissipation of kinetic energy negates the work done by the torque, ultimately facilitating the continuous reduction of angular momentum from the planetary orbit. The efficiency of the mechanism for dissipation of energy is measured by its characteristic time  $\tau_{\text{diss}}$ , such that the lag-angle is given by

$$\alpha = \frac{(\Omega_* - \omega_{\text{pl}})}{t_{\text{diss}}} \frac{R_*^3}{GM_*}, \quad (2.3)$$

where  $\alpha$  has been made dimensionless by introducing the dynamical (or free-fall) time,

and so the tidal torque is then:

$$\Gamma \simeq -\frac{(\Omega_* - \omega_{\text{pl}})}{t_{\text{diss}}} q^2 M_* R_*^2 \left( \frac{R_*}{a} \right)^6, \quad (2.4)$$

where  $q = M_{\text{pl}}/M_*$ . If the equilibrium cannot be reached the planetary orbit will continue to decrease and will eventually collide with the star; this is the basis for planet engulfment defined in chapter 1.

### 2.2.1 Tidal dissipation and the role of turbulent convection

It is clear from the previous section that the orbital evolution depends on magnitude of the tidal torque, which itself depends on the lag-angle, and ultimately the strength of the physical processes that are responsible for the dissipation energy and the associated dissipation timescale. Identifying the physical processes that facilitate tidal dissipation is one of the main difficulties in tidal theory.

Zahn (1977) studied these processes with regards the equilibrium tide and recognised that turbulent viscosity is the dominant dissipation mechanism. Turbulence, a result of the convection in the envelopes of RGB and AGB stars, causes the formation of eddies in the atmosphere, enhancing the rate of energy and momentum exchange between particles. Such an energy exchange can be explained by considering the Kolmogorov theory of turbulence, in which kinetic energy constrained in the large scale flow of the tides cascades down from large scale structures to small scale structures and, as a result of the enhanced viscous friction, dissipates into heat. Zahn (2008) described this process as the tidal flow being acted on by a force emanating from the turbulent viscosity,  $\nu_t$ , which is of the order of  $\nu_t = v\ell$ , where  $v$  is the r.m.s vertical velocity of the turbulent eddies and  $\ell$  is their vertical mean free path, or mixing length. If most of the thermal energy is transported through the star by convection the dissipation timescale can then be expressed as proportional to the global convective timescale ( $\tau_{\text{diss}} \propto \tau_{\text{conv}}$ ).

Verbunt & Phinney (1995) tested the turbulent viscosity theory of Zahn (1977, 1989) using a sample of wide binaries in which one component of the binary was a giant star, and measured the eccentricities and circularisation timescales, and found turbulent viscosity to be consistent with observations. In doing so they introduced a dimensionless scale factor,  $f$ , such that

$$\frac{1}{\tau_{\text{diss}}} = \frac{f}{\tau_{\text{conv}}}, \quad (2.5)$$

where  $f$  is determined by integrating the viscous dissipation across the entire convective zone. The value of  $f$  is a subject of debate however, and the prescription for this factor has been described as the *Achilles heel* of tidal theory. Most studies are in agreement with Verbunt & Phinney (1995), who found that  $f = 1$  is consistent with observations provided that  $\tau_{\text{conv}} \ll P$ , where  $P$  is the orbital period. For example, Zahn (1989) adopted a value of  $f = 1.01(\alpha_{\text{MLT}}/2)$ , where  $\alpha_{\text{MLT}}$  is the mixing length parameter and assuming standard mixing length theory, where  $\alpha_{\text{MLT}}$  is constrained between 1.6 and 2,  $f \approx 1$ . However, when the convective turnover time exceeds the orbital period, a so called fast-tide, the precise value of  $f$  is uncertain, but it is often assumed that  $f \propto (P/\tau_{\text{conv}})^n$ , where  $n$  is suggested as being within 1-2 (Zahn 2008), and is dependent on the contribution of the eddies to the overall tidal dissipation (Goldreich & Nicholson 1977). In his early work, Zahn (1966) suggested that when the convective timescale exceeds the tidal period, that the mean free path should be replaced by the distance that the convective eddies have travelled in a half period, thus determining the value of the turbulent viscosity defined above. However it was later found by Goldreich & Nicholson (1977), that only small scale eddies are able to contribute to the tide, and that large scale eddies are unable to exchange energy with the tidal flow on this timescale, and a value of  $n = 2$  was suggested to further dampen the tide.

With regards to the uncertainty in the exact prescription for the turbulent viscosity described above, and thus the introduction of this uncertainty into the orbital evolution of exoplanets and planet engulfment studies, Kunitomo et al. (2011) incorporated different values of  $n$  for their orbital evolution models and naturally found that as  $n$  increases tidal dissipation does indeed become less efficient. However, as Villaver et al. (2014) pointed out, this is only an appreciable uncertainty when the orbital period is smaller than  $\tau_{\text{conv}}$ , and in such a case these very short-period planets would be engulfed very early on in the evolution regardless, and so the value of  $n$  should not present such a large uncertainty in engulfment studies.

## 2.3 Stellar evolution models

For this research, stellar evolution tracks are key to obtaining the results of chapters 3, 4 and 5. For example, in order to calculate the tidal evolution of a star-planet system and the response of the planet to the evolution of its host star as described in the previous section, the full stellar structure of the star needs to be calculated with respect to time such that the time-dependent properties of the star are known at each point in the evolution. This allows us to model the onset of convection and calculate the convective timescale which is vital for the tidal evolution of the system. The evolution of the stellar structure can vary largely as a function of star mass, but also as a function of other initial conditions and input physics such as the initial metallicity and also mass-loss coefficients employed. It is therefore important to have access to a grid of stellar evolution tracks. Two sets of stellar models were employed in this thesis, both calculated with the Modules for Experiments in Stellar Astrophysics (`MESA`)<sup>1</sup> code (Paxton et al. 2011, 2013, 2015). One grid of stellar models are the `MESA Isochrones and Stellar Tracks` (`MIST`) models of Choi et al. (2016), and a second smaller grid calculated by the author.

### 2.3.1 Stellar evolution with `MESA`

`MESA` was developed by Bill Paxton in collaboration with others over a 6 year period before its first official release in 2011, with the objective of providing a stellar evolution tool for education, outreach and scientific research. `MESA` is a 1D open-source community software which boasts efficient libraries and the use of sophisticated numerical methods such as adaptive mesh refinement and high-order interpolation schemes. Because `MESA` was designed to run on most modern computers, but can also be deployed on multi-core systems, it allows for the quick determination of the aforementioned stellar properties. `MESA` can be run on most modern laptops with Mac or Linux operating systems. The minimum requirements for `MESA` are a 64-bit processor, at least 4 GB of RAM and 10 GB of free space.

Once `MESA` is installed, a directory is created that contains all of the modules from which the stellar models are built. The individual modules contain various micro- and

---

<sup>1</sup>`MESA` can be downloaded from <http://mesa.sourceforge.net/>

macro- physical properties (for example the *rates* module which handles the thermonuclear reaction rates within `MESA`) and numerical algorithms (such as the *interp\_1d* module which handles interpolation). A full description of the modules which `MESA` is comprised of can be found in the Paxton et al. (2011, 2013, 2015) `MESA` release papers. As discussed in the release papers, the most important of these modules is the *star* module, which employs all of the other modules to calculate any single star evolution. The star module reads the input files (known as *inlist* files in `MESA`) which must be configured by the user. The *inlist* files provide the necessary information for the star module to initialise the input physics modules which create a nuclear reaction network and access the equation of state and opacity data. The star module then performs a stellar evolution calculation in one step and then uses a self-suggested timestep to advance to the next state in the evolution. The timesteps are extremely important for a stellar evolution calculation as they need to be large enough for the evolution to complete in an efficient manner but small enough for the models to converge. The suggested timestep is computed by re-meshing the model if appropriate, adjusting the model to reflect changes in, for example mass -loss or -gain, and solving the new structure and composition of the star with a Newton-Raphson solver, and then estimating the next timestep. Once the new timestep is estimated, a range of tests are performed to determine if the timestep should be reduced. Finally, the `MESA` output is saved to a `LOGS` directory, where the stellar structure is logged to a history file at each timestep. This history file thus contains the temporal evolution of the star's structure such as radius, luminosity and mass-loss rates, which are needed to compute the orbital evolution of star-planet systems.

### 2.3.2 The `MESA` Isochrones and Stellar Tracks (MIST) database

The stellar evolution tracks utilised extensively in the research presented in this thesis are adopted from the `MESA` Isochrones and Stellar Tracks database (MIST) of Choi et al. (2016). The MIST project<sup>2</sup> began in 2012 as an effort to create a large grid of single-star evolution models using `MESA`. The MIST database was created by Jieun Choi (Harvard), Aaron Dotter (ANU), Charlie Conroy (Harvard), Matteo Cantiello (UCSB/KITP) (Dotter 2016; Choi et al. 2016). The MIST stellar evolution tracks have been used throughout

---

<sup>2</sup><http://waps.cfa.harvard.edu/MIST/>

this research since the database contains a wide range of pre-calculated stellar models covering an appropriate range of star masses and metallicities across all phases of stellar evolution important for this research. Full details of the initial conditions and adopted physics of the models employed are provided, where applicable, in the respective chapters.

## 2.4 The populations of exoplanets

An obvious factor to consider in exploring the planet shaping hypothesis is the prevalence of massive planets around main sequence PN progenitor stars. According to recent surveys, exoplanets are common around sun-like stars. In fact, it has been suggested that the occurrence rate of planets orbiting stars with masses of between  $0.5\text{--}1.2 M_{\odot}$  is  $\approx 1$  (Winn & Fabrycky 2015). To arrive at the planet-fraction of planetary nebulae it is necessary to account for the proportions of PN progenitors which have planets capable of shaping a PN. To do this, knowledge of the semi-major axis and mass distributions of exoplanets is needed as well as an orbital evolution model described already in section 2.1.

In this section the origin of the planet samples used throughout this thesis (the samples are utilised explicitly in chapter 4, and implicitly in chapter 5) are described. Two planet samples are used to arrive at the planet-fraction; the observed *known exoplanets* from the Exoplanet Orbit Database, and a *synthetic* planet sample obtained from planet formation models. The following is a brief description of the Exoplanet Orbit Database, the pitfalls of the known exoplanets (and thus the need for synthetic planet populations) and an introduction to the theory behind planet formation models.

### 2.4.1 The Exoplanet Orbit Database and the known exoplanets

This research has made use of the Exoplanet Orbit Database and the Exoplanet Data Explorer at [exoplanets.org](http://exoplanets.org). The Exoplanet Orbit Database<sup>3</sup> is an online compilation of exoplanet data, including Kepler candidates, which was developed by extending the first comprehensive lists of known exoplanets from Butler et al. (2002) and Fischer & Valenti (2005) in order to keep track of the rapidly growing numbers of discoveries. It has since been continuously updated and maintained by Wright et al. (2011) and, more recently, by Han et al. (2014). The goal of the database was to provide a well-documented account of the orbital parameters of all the known exoplanets and also the properties of their host stars. It is freely available and allows users to easily access, download and explore its entire contents. The upper limit for the definition is the Exoplanet Orbit Database is  $24 M_J$ , which the developers admit is a rather generous definition. The quality of

---

<sup>3</sup><http://exoplanets.org/>

the data contained in the database however is paramount, as only the most robust orbital parameters for exoplanet detections in the literature are included in the database. From the measured orbital parameters (period, semi-amplitude, eccentricity, time and periastron), the planet mass and the orbital semi-major axis are calculated in the database for every planet. The detection method determines which parameters are known for a given system, which in turn determines how the best estimate for the planet mass is derived (Han et al. 2014). Thus the Exoplanet Orbit Database is an invaluable resource for this research and provides the data needed as input to explore the fates of massive planets around PNe hosts according to the distributions of planet masses and semi-major axes of the known exoplanets, as well as the properties of their host stars.

A related ingredient, and one which is derived from the same planet searches from which the data contained in the Exoplanet Orbit Database is comprised of, is the massive planet occurrence rates among PN progenitors. Winn & Fabrycky (2015) recently provided a thorough review of the state of the art of exoplanet occurrence studies. It has long since been known that there is a metallicity correlation for stars hosting massive planets (Fischer & Valenti 2005; Johnson et al. 2010a). The theoretical explanation for such an observation is that planets forming in metal-rich environments experience a higher dust-to-gas ratio in the primordial disk. A high dust-to-gas ratio facilitates condensation and accelerates the growth of proto-planets via accretion, and if the growth rate is high enough the proto-planet core can reach a sufficient mass to begin to accrete the surrounding gas before it is lost from the disk. The runaway accretion of gas leads to the formation of a gas giant; this is known as the core accretion paradigm and is the prevalent formation theory for gas giant formation (Pollack et al. 1996). With increasing evidence for the massive planet-metallicity correlation, Fischer & Valenti (2005) proposed that the massive planet-metallicity correlation could be ascribed to a power law. Other independent studies revealed that not only does a correlation appear between stellar metallicity and planet occurrence, but also for stellar mass (Johnson et al. 2007; Gaidos & Mann 2014). As of now, the relationship between massive planet occurrence and host star mass is relatively well-known for FGK stars. In particular, stars with masses of around  $1 M_{\odot}$  are the perfect candidates for Doppler surveys in comparison to their more massive counterparts since they are numerous, have slower rotational velocities and cooler atmospheres as described by Johnson et al. (2010a) and references therein. Unfortunately, predicting the

occurrence rates of massive planets for intermediate mass stars ( $>1.5 M_{\odot}$ ) is challenging for a number of reasons. The fact that there are fewer intermediate mass stars means that there are fewer of these targets in surveys. Furthermore, in transit surveys, the photometric variability in such a system is smaller and thus more difficult to detect and confirm as a planet transit. On the other hand, radial velocity detections of such stars poses problems in its own right, since more massive stars, and thus hotter and having higher rotational velocities, have fewer absorption lines and so the accuracy of radial velocity measurements is reduced. In an attempt to determine the occurrence rates of planet-hosting stars above  $1.5M_{\odot}$ , some studies (e.g., Bowler et al. 2010; Johnson et al. 2010b) observe these stars at later stages in their evolution (sometimes dubbed as *retired A stars* in the literature). Since RGB and AGB stars rotate more slowly, are quieter/have less jitter and are cooler, radial velocity measurements are more accurate in these stars, and thus by the use of stellar isochrones the main sequence mass of the stars can be determined. However this solution has been met with criticism, since the initial masses derived from observations of an RGB/AGB mass is dependent on metallicity and the stellar models used, as argued by Lloyd (2013). Nonetheless, despite attempts at radial velocity measurements of evolved intermediate mass stars, the numbers of known planet-hosting stars in such a mass range is still relatively low in comparison to low-mass stars, and is a selection bias which should be kept in mind. Similarly, due to the nature of the Doppler and transit detections, a detection bias also exists in the known exoplanets; giant, inner planets were more readily detected in past surveys. Fortunately, there is much optimism for the future of astrometric detections in exoplanet searches, a technique which up to now has not been on the forefront of exoplanet discoveries. In particular, the emergence of the Gaia mission is expected to return thousands of new massive planets in wider orbits than those already known, and also uncover planets orbiting many different types of stars, including intermediate and high mass stars (Winn & Fabrycky 2015).

### 2.4.2 Synthetic planet distributions

Due to the biases inherent in the known exoplanets mentioned previously, adopting the mass and semi-major axis distributions of the known exoplanets introduces uncertainties in the calculation of the planet-fraction of planetary nebulae. In order to alleviate some

of this uncertainty, synthetic planet populations are employed in this research. Since the simulation of such populations are beyond the scope of the present study, they have been generously provided by Shigeru Ida (Private communication, 2017). The populations were generated using a planet formation and evolution model which is based on a series of studies spanning over a decade which began with the pioneering core-accretion planet formation models outlined in Ida & Lin (2004a). The original model of Ida & Lin (2004a) was the first of its kind with regards to utilising planet formation theory to construct a full population of synthetic planets in order to be compared to the known exoplanets, which remarkably consisted of only about 100 planetary systems at the time. By making this comparison between the semi-major axis and mass distributions of the synthetic population and that of the known exoplanets, it was possible to further constrain the formation theories from which the synthetic populations were simulated. For interested readers, full details of the physical models of planet formation used to produce the planet populations for this research can be found in a number of works by Shigeru Ida and Douglas Lin (Ida & Lin 2004a,b, 2005, 2008a,b, 2010; Ida et al. 2013).

In general, a planet formation and evolution model begins with the structure and evolution of the proto-planetary disk and its planetesimals, where the disk properties are drawn from probability distributions obtained from observations of proto-planetary disks. Proto-planets are then seeded within the disk as the starting point for the accretion of gasses and solids. The accretion is followed throughout the formation of the planet, along with N-body interactions between the proto-planets themselves and between the proto-planets and the disk, in order to follow the motion of the proto-planets until the system settles into its final configuration. Hence the full formation model is built from a series of sub-models containing the physics and initial conditions described above (Benz et al. 2014). For each set of initial conditions the model will calculate the final outcome, which is a planet with a defined mass and semi-major axis. When this is performed a large number of times, a synthetic planet population is built. The synthetic population can then be compared to the known exoplanets by applying the same observational biases that limit real exoplanet detections. Figure 2.2 shows the typical work-flow for generating a synthetic planet population and determining whether the synthetic population is in agreement with those observed (Mordasini et al. 2015). If a statistical agreement between the known exoplanets distributions and the synthetic planet populations is not found, this indicates that

the planet formation models contain incorrect physics and/or initial conditions, prompting a re-evaluation of the entire model and thus improvements in planet formation theories on the whole, which was the original goal of the technique developed by Ida & Lin (2004a). The technique is displayed schematically in figure 2.2.

On the other hand, if an agreement between the known exoplanets distribution and the synthetic planet distribution is found with the observational bias applied, then inferences about the full synthetic planet population can begin to be suggested. In particular, it can be assumed that the full synthetic planet population should now contain the true underlying, unobservable, semi-major axis and mass distributions of exoplanets. The planet formation and evolution models are thus a key ingredient in the determination of the probabilities of massive planets forming within the engulfment zones of their host stars. Furthermore, since the essence of planet formation models is to unite the proto-planetary disk properties with the resulting planets themselves, it has been possible to compute the synthetic populations of planets orbiting stars of varying masses by adopting the observed properties of proto-planetary disks for intermediate mass stars (T Tauri and Herbig Ae/Be star disks) (see Ida & Lin 2005, for details on planet formation models around stars of various masses). For this reason in particular, the data provided by the planet formation models is an extremely valuable asset for this research in terms of revealing the population of planets orbiting the stars with masses of which very few observations exist.

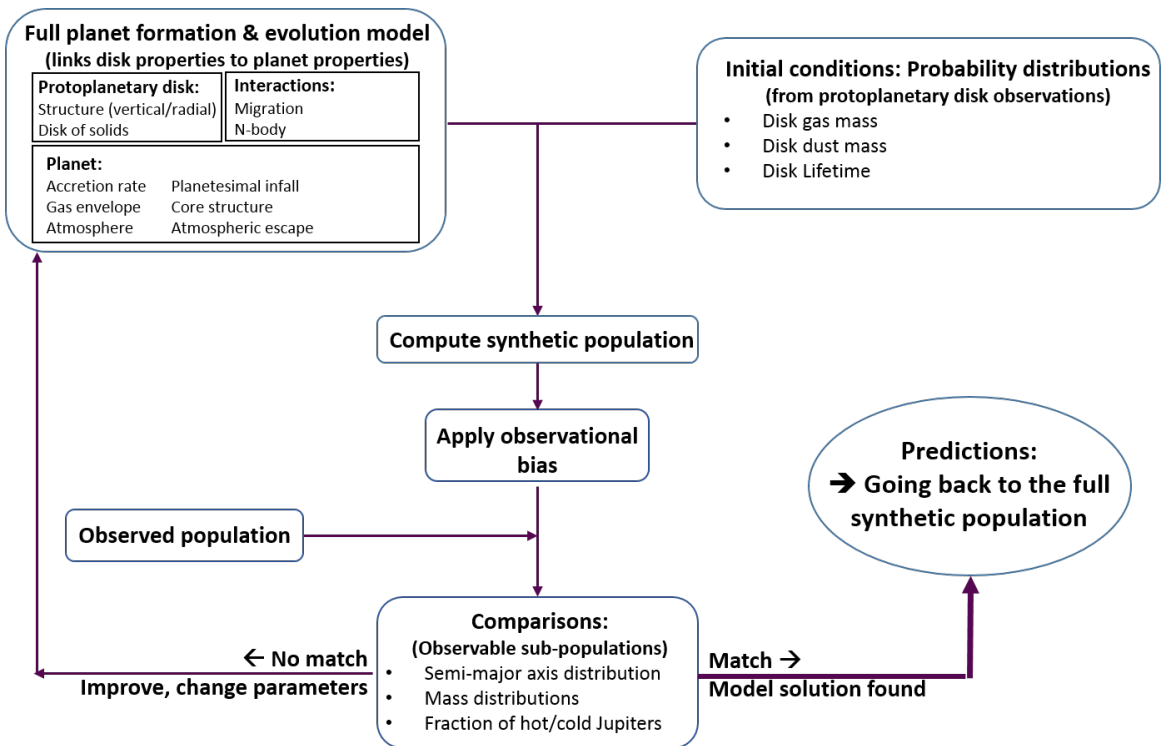


Figure 2.2: The basic work-flow of building synthetic planet populations: A population of planets is generated, where each planet is simulated according to a full planet formation model and proto-planetary disk properties. Once an observational bias is applied to the synthetic population it is compared to the observed distribution of exoplanets. If a statistical agreement is found between the synthetic population and the observed population, the synthetic population can be used to make inferences. Image re-drawn by author as depicted in Mordasini et al. (2015).

## 2.5 Planetary nebula population synthesis

Because the overall goal of this research is to determine the current planet-fraction of planetary nebulae it is necessary to conduct a planetary nebula population synthesis of the Milky Way. The adopted method for such a population synthesis is similar to that which was outlined in Moe & De Marco (2006); Moe & De Marco (2012) who presented a similar calculation, but their goal was to predict the whole population of PNe, and in particular those which evolved from binary progenitors. Moe & De Marco (2006) describes how the total number of PNe in the galaxy can be accounted for by following the evolution of planetary nebula progenitors through from their formation at various galactic epochs to the present-day.

The basis of this type of model stems from the fact that a galaxy is essentially a composite stellar population. That is, it is constructed by the summation of the evolution of many simple stellar populations coming from all epochs during a star formation history. Thus the galaxy includes young stars, old stars and stellar remnants such as planetary nebulae. Where a simple stellar population is defined as a coeval population of stars forming with the same metallicity Conroy (2013) (the most basic example is a star cluster). If the galaxy is modelled as a series of epochs of star formation, each epoch represents one simple stellar population. Accordingly, stars which are born at a given galactic age such that they have had sufficient time to evolve to the PN phase, and still be visible in the present-day, make up the current population of planetary nebulae. By taking into account the PN progenitor binary-fraction in each epoch, Moe & De Marco (2006); Moe & De Marco (2012) determined the fraction of PNe which evolved through binary interactions.

In general, the basic elements of a population synthesis are the star formation history, the stellar initial mass function and the metallicity history of the galaxy. In this research, the formation and evolution of planets during the star formation history is obviously imperative as well. The following gives a general outline of each of the basic elements which, in chapter 5, are combined with the results of the orbital evolution modelling of planet formation model populations, described in section 2.3, to arrive at the planet-fraction.

### 2.5.1 Star formation history

In order to determine the number of stars forming at each epoch, the star formation rate as a function of time,  $\psi(t)$ , must be known. The star formation rate, as the name suggests, is the total mass of stars forming per year and a model of the evolution of the star formation rate as a function of time gives the star formation history. A typical way to model the star formation rate is to adopt the decaying exponential fitting formula

$$\psi(t) \propto \exp\left(-\frac{t}{\tau_{\text{SFR}}}\right), \quad (2.6)$$

where  $\tau_{\text{SFR}}$  is the star formation rate decay timescale. However, by linking galaxies of differing redshifts, but with the same cumulative number densities to trace the build-up of stellar masses, Behroozi et al. (2013) determined that an exponentially decaying star formation history is in fact only a good fit to the most massive galaxies, not for those with comparable masses to the Milky Way. This is evident from figure 2.3, where the solid black line depicts the average star formation history for a Milky Way mass galaxy, and the green and blue dashed lines are the star formation histories as determined by Behroozi et al. (2013) and the decaying model, respectively. For this reason the star formation history adopted in this work is the average star formation history calculated and provided by Peter Behroozi of Behroozi et al. (2013).

Finally it is noted that since planet formation and also the stellar lifetime are dependent on the metallicity, it is important to include a metallicity relationship in a star formation history model, since the continuous formation of stars and their eventual destruction means that the abundance of metals in the galaxy is not constant in time. Adopting a star formation history such as that of Behroozi et al. (2013), allows for a simple relationship between metallicity, stellar mass and redshift (e.g., Maiolino et al. 2008).

### 2.5.2 The initial mass function

The initial mass function (IMF) describes the distribution of stellar masses in a population of stars in a given volume of space (Salpeter 1955). Since the first quantification by Ed Salpeter in 1955, it has remained as one of the most powerful tools in any stellar or galactic population study. By using the relations between the present-day luminosity

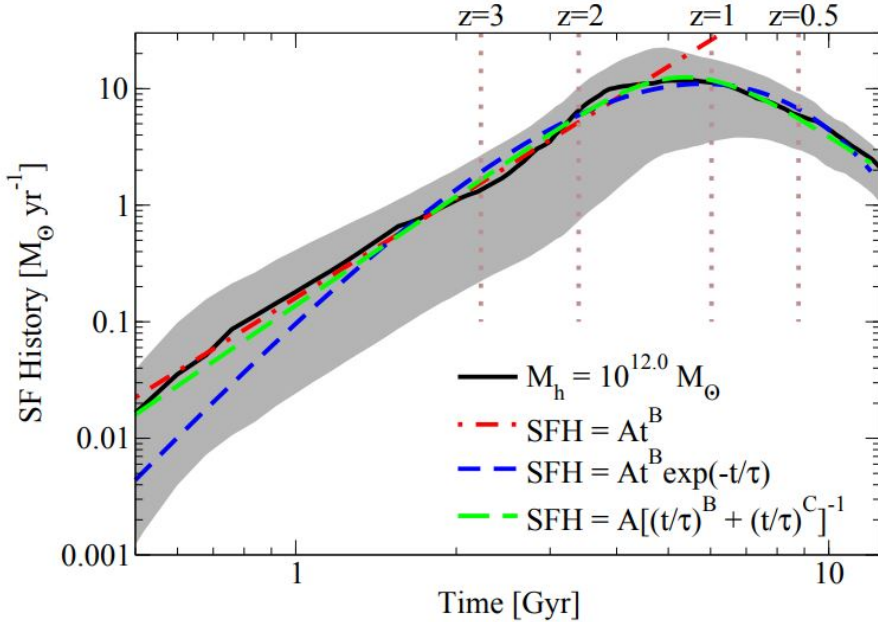


Figure 2.3: Comparison between different forms of the average star formation history for a Milky Way mass galaxy. The solid black line is the average star formation history for a Milky Way mass galaxy, while the broken lines depict the average star formation histories resulting from the use of various fitting formulae (Behroozi et al. 2013).

function and the mass-luminosity relationship, Salpeter (1955) determined a present-day mass function which could then be extrapolated backwards using stellar evolution considerations to determine the IMF. He showed that the IMF followed a declining power-law for stars with masses between  $0.4$  and  $10 M_{\odot}$ . The IMF is especially important to the population synthesis study presented here, where in each epoch of the planetary nebula population synthesis, the masses must be binned into increments of  $0.1 M_{\odot}$ , and the fraction of stars forming in each mass bin must be determined. It is necessary to determine the numbers of stars forming in a given time-interval with masses such that their lifetimes are equal to the age of that interval and are thus visible as planetary nebulae in the present-day galactic population.

The IMF can describe the stellar mass distribution by number,  $\phi(M_*)$ , or by the mass locked up in stars,  $\xi(M_*)$ , in a given mass interval.  $\phi(M_*)$  is defined such that the number of stars formed in the range  $(M_*, M_*+dM_*)$  is  $\phi(M_*)dM_*$ , and is given by

$$\phi(M_*) = c_1 M_*^{-\alpha}. \quad (2.7)$$

Similarly the IMF by mass,  $\xi(M_*)$ , is defined as

$$\xi(M_*) = c_2 M_*^{-\alpha+1}, \quad (2.8)$$

where  $c_1$  and  $c_2$  are normalisation constants and  $\alpha$  is the power-law index, for which Salpeter determined a value of  $\alpha = 2.35$ .

Other forms of the IMF have since been suggested, such as the widely adopted IMF of Kroupa (2001) who proposes that the Salpeter slope does not hold for low mass stars and instead fits a broken power law with the values for  $\alpha$  varying as

$$\begin{aligned} \alpha_0 &= 0.3, & 0.01 \leq M_* < 0.08 \\ \alpha_1 &= 1.3, & 0.08 \leq M_* < 0.5 \\ \alpha_2 &= 2.3, & 0.5 \leq M_*. \end{aligned} \quad (2.9)$$

Another well-known and widely used form of the IMF is the log-normal fit of Chabrier (2003)

$$\xi(M_*) \propto \begin{cases} \exp\left[-\frac{(\log M_* - \log(0.22))^2}{2(0.57)^2}\right], & \text{if } M_* \leq 1 M_\odot \\ M_*^{-1.3}, & \text{if } M_* > 1 M_\odot \end{cases} \quad (2.10)$$

The choice of IMF is important in a population synthesis study since the difference in adopting a Kroupa (2001) versus a Chabrier (2003) IMF is that the fraction of stars in the PN mass range ( $0.8 - 8 M_\odot$ ) varies from 12.3% to 19.4% of all stars, respectively. The difference is a consequence of the fact that the Kroupa (2001) yields a higher fraction of stars on the low-mass end ( $< 0.8 M_\odot$ ) than the Chabrier (2003) IMF. Both the Kroupa (2001) and Chabrier (2003) IMFs are adopted in this research to determine the distribution of stellar masses forming during each epoch of star formation, where the minimum and maximum stellar masses are taken as 0.08 and  $120 M_\odot$ . For computational ease, the GNU IMF library, LIBIMF, of Pflamm-Altenburg & Kroupa (2006), is adopted in this work as a facility within the SIMSPLASH code developed for this work (which is introduced in the next section).

## 2.6 SIMSPLASH: SimulationS for the PLAnet Shaping Hypothesis

SIMSPLASH (shown schematically in figure 2.4) is a new tool developed by the author specifically to carry out the work in this thesis by combining all of the theory, data and techniques discussed in the previous sections to explore the process of planet engulfment and ultimately to calculate the planet-fraction of planetary nebulae<sup>4</sup>. It is written in C with PYTHON bindings (MATPLOTLIB, NUMPY, PANDAS, SCIKIT-LEARN), employs the GNU Scientific Library (GSL) interpolation functions, the GNU IMF library (LIBIMF) of Pflamm-Altenburg & Kroupa (2006) and incorporates a thorough database of pre-calculated stellar models<sup>5</sup>. All of the results presented in chapters 3, 4 and 5 were obtained using SIMSPLASH and so the results presented in this thesis can be efficiently reproduced with the code. SIMSPLASH contains three modes of operation which are selected by the user upon running. The three modes are Orbital mode, Single-epoch population mode and Multi-epoch population mode. Any mode can be selected by simply editing the configuration file in the working directory. The following sections provide details on which features are available for selection in each mode, how to setup experiments in SIMSPLASH and what needs to be specified for a simulation.

### 2.6.1 Orbital mode

The results presented chapter 3 were obtained with the Orbital mode of SIMSPLASH. When run in Orbital mode, SIMSPLASH calculates the orbital evolution of a planet as the host star evolves. It employs the tidal dissipation theory described in section 2.1 and the MIST stellar models of Choi et al. (2016), and determines whether a planet will be engulfed or not, for a given set of initial conditions. The default model contains a  $1 M_{\odot}$  main sequence star of solar metallicity ( $Z = 0.014$ ), with a  $1 M_J$  planet to be evolved for a range of test initial semi-major axes from 0.5-3 AU in increments of 0.05 AU. Other models are easily specified by changing the initial conditions in the configuration file. For example, if the user wishes to evolve a system with just a single initial semi-major axis, they simply

---

<sup>4</sup>SIMSPLASH is available at [https://github.com/simsplash/simsplash\\_code](https://github.com/simsplash/simsplash_code)

<sup>5</sup>SIMSPLASH also contains a MESA wrapper to calculate new evolution tracks on the fly. However, in the present study this facility has not been tested thoroughly and so is not utilised here.

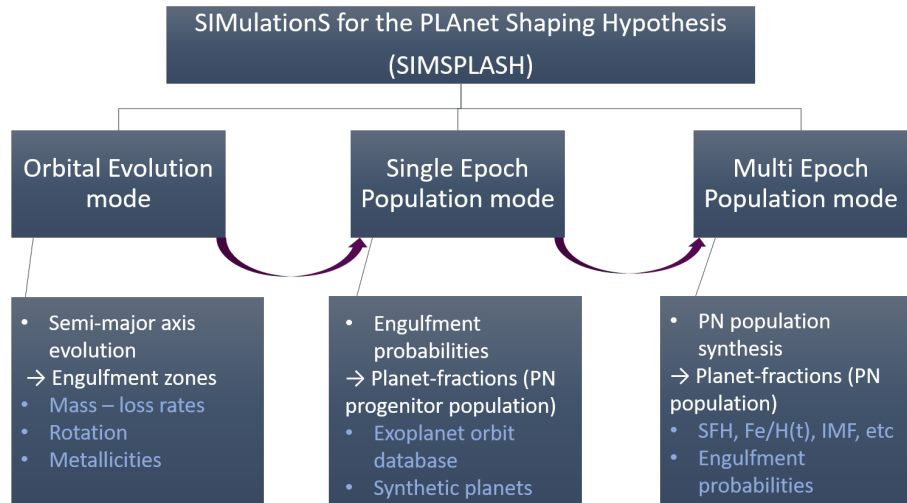


Figure 2.4: Schematic workflow diagram of SIMSPLASH

choose this option in the configuration file before running and input the initial semi-major axis. Running a model in this way makes it easy to test different stellar initial conditions for a star-planet system at a specific semi-major axis. On the other hand, running a range of semi-major axes is best utilised for determining the engulfment zones of particular systems and investigating the effects of various initial conditions on such.

Any stellar model included in the stellar database can be selected for the evolution. Once an Orbital model has finished running, SIMSPLASH prints a summary of the evolution and whether or not a planet is engulfed. If a range of semi-major axes is selected, it outputs the RGB and AGB engulfment zone boundaries, and the width of the AGB engulfment zone. Finally, it saves and plots the resulting evolution files in a results directory for further analysis.

## 2.6.2 Single-epoch population mode

The results of chapter 4 were obtained using the Single-epoch population mode of SIMSPLASH. The Single-epoch population mode determines the numbers of RGB and AGB engulfments given a population or sample of star-planet systems. Any planet sample can be evolved in this way by placing the file containing the information on the star-planet systems in the *planets\_database* directory, and specifying the name of the file in the configuration script. It then separately evolves each star-planet system in the sample, as in

Orbital mode, and tracks the results with a 0, 1 or 2 coding for systems where there was no engulfment, an RGB engulfment or an AGB engulfment, respectively. After running, a file is saved containing the summary statistics of the sample and the numbers of RGB and AGB engulfments.

The user must specify whether each star-planet system in the population should be evolved according to the host-star metallicity reported for each system, or whether to evolve each star-planet with the same metallicity which must also be specified. After the sample has been evolved, if the chosen sample was either the exoplanets.org or synthetic planet sample (detailed in section 2.4.2), `SIMSPLASH` proceeds to perform a statistical analysis on the results and returns the probabilities of engulfment as a function of stellar mass and metallicity. Finally, by employing a user-specified initial mass function for the distribution of star masses and the formula for the occurrence of stars hosting massive planets, the population of PNe which would evolve from such a population is determined. Further details will be provided later in chapter 4.

### 2.6.3 Multi-epoch population mode

The results of chapter 5 were calculated with the Multi-epoch population mode of `SIM-SPLASH`. The Multi-epoch population mode determines the current planet-fraction of planetary nebulae in the Milky Way. Given an average star formation and metallicity history of the galaxy it conducts a population synthesis by calculating the number of PN progenitors formed and calling on the functions in Single-epoch population mode for each epoch and utilising the metallicity history, it can determine the numbers of planets forming and being engulfed by planetary nebula progenitors during that epoch. Once the population of PN progenitors are formed in that population it uses the stellar lifetimes to determine the number of which are visible as planetary nebulae today, and most importantly the fraction of that number which have engulfed a massive planet. Thus by performing the calculation for each epoch and summing all to the present-day, the planet-fraction of planetary nebulae is calculated.

# Chapter 3

## Planet engulfment by progenitors of planetary nebulae

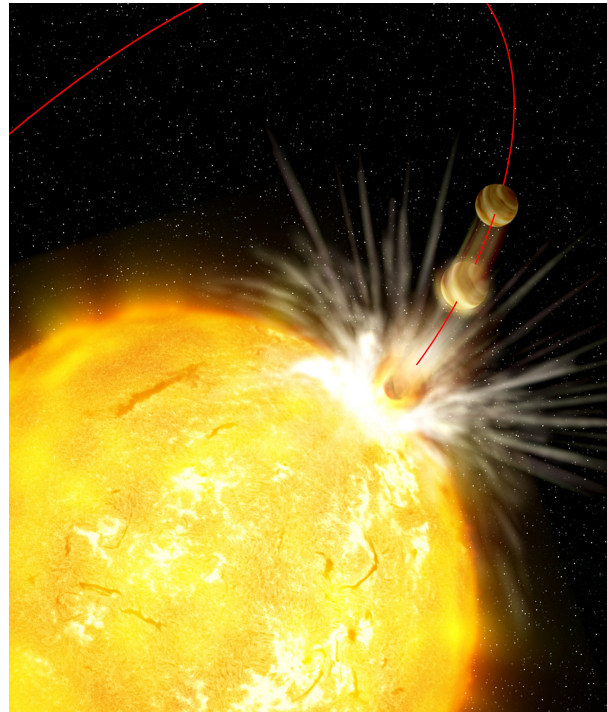


Figure 3.1: An artist's impression of a planet undergoing engulfment by its host star.  
Image credit: Gabi Perez /IAC, ESO.

### 3.1 Introduction

An important, and persistently challenging, central objective in the field of planetary nebulae (PNe) research is to establish a characterisation of the shaping mechanisms behind the array of morphologies observed. Keeping in mind that the aim of this thesis is to investigate the claim that a subset of non-spherical planetary nebulae may be a result of the interaction of planets with single asymptotic giant branch stars (Soker 1996b; Nordhaus & Blackman 2006), the basis of the work in this chapter is the argument that one of the first steps in determining the plausibility of planet shaping of planetary nebulae must lie in the orbital evolution of the planet during the red giant branch (RGB) and asymptotic giant branch (AGB).

Given the correct combination of stellar mass, planet mass and initial semi-major axis, tidal forces can draw a planet into the envelope of its expanding host (e.g., Mustill & Villaver 2012). In the event that a planet is engulfed on the AGB, its angular momentum and orbital energy will be deposited into the stellar envelope while the planet spirals-in towards the core of the star, spinning up the envelope in the orbital plane and inducing differential rotation and/or enhanced mass-loss in the plane (Soker 1996b, 1997; Nordhaus & Blackman 2006). Either of which may ultimately result in a non-spherical PN. Or if the planet is destroyed within the envelope, for example, its remnants may be deposited onto the stellar core, leading to a shaping event by jets, as demonstrated by the semi-analytic calculations of Nordhaus & Blackman (2006). Such a scenario was suggested by Clyne et al. (2014) to explain the extreme bipolar morphology of PN MyCn 18 and its enigmatic hypersonic knotty outflows.

On the other hand, a planet entering the envelope of an RGB star may have significant consequences as well, as it may impede the evolution of its host, ultimately preventing the formation of a PN at all (Nelemans 2010; Bear & Soker 2011). In any case, whether the planet enters the envelope on the RGB or the AGB is crucial, since only an AGB engulfment can result in the shaping of PNe. Determining whether planets are more likely to undergo an engulfment on either evolutionary phase is useful as it raises the question of whether planet engulfment is in fact a mechanism which tends towards the prevention of the formation of a PN, rather than a mechanism which aids in shaping them, or whether it causes both. Hence it is important to address the engulfment of planets on the RGB also.

Interest in the orbital evolution of a planet in response to the post-MS evolution of its host star dates back to over three decades ago in the work of Vila (1984). At that time, and without any evidence for the existence of extra-solar planets, the motive was to determine the survival of the Earth and the other terrestrial planets in our Solar System. Vila simply compared the predicted maximum extent of the stellar envelope of the sun to the semi-major axis of the Earth and concluded that it will be destroyed on the red giant branch. Further studies simulated the scenario including the effects of mass-loss and determined that the Earth would be pushed out to safety as a result of the conservation of angular momentum (e.g., Sackmann et al. 1993). With the discovery of exoplanets, interest in orbital evolution modelling has been revived, this time with much more detail with regards to the effects of tides and mass-loss. But, while the fate of the Earth is still said to be inconclusive, since it is highly dependent on the parameterisation of the tides and stellar models, (see, e.g., Rasio et al. 1996, for a discussion), much has since been learned about the response of a planetary orbit to an evolving star (Villaver & Livio 2007, 2009; Nordhaus et al. 2010; Kunitomo et al. 2011; Mustill & Villaver 2012; Nordhaus & Spiegel 2013; Villaver et al. 2014; Privitera et al. 2016; Madappatt et al. 2016). These studies, in which the orbital evolution of planets around evolving stars is calculated, have yielded crucial insights into the effects of mass-loss and stellar tides on a planets survival.

Despite the fact that the orbital evolution of exoplanets around evolved stars is relatively well studied, there is no open source orbital evolution code available for such studies<sup>1</sup>. Furthermore, while most studies are somewhat similar in the overall approach to modelling the orbital evolution, many models differ in terms of the input physics of stellar models and initial conditions (such as the initial stellar metallicity) leading to a variety of results for the engulfment zones of particular systems. As a result, combining all results coherently into one bigger picture is not straightforward since the reproduction of, and thus comparisons between, previous studies is a time consuming process. For this reason, a secondary aim associated with the development of the Orbital mode of SIMSPLASH was to provide a basis for any type of orbital evolution calculations of planets, and has been written such that it is easily modifiable, particularly in terms of the stellar models employed. However, the main aim of the production of the Orbital mode of SIMSPLASH is

---

<sup>1</sup>The POET: Planetary Orbital Evolution Due to Tides code of Penev et al. (2014) exists but it uses a more simplified treatment of tides (the so-called *Q-formalism*), and the stellar tracks included in their database do not evolve past the main sequence, so it is largely unsuitable for this work.

to determine the engulfment zones of planet hosting stars which is needed for calculating the planet-fraction of planetary nebulae, and will remain the main subject of this chapter, where the RGB engulfment zone refers to the range of initial semi-major axes that result in engulfment during the RGB, and the AGB engulfment zone refers to the range of initial semi-major axes that result in an engulfment on the AGB. In the following, a detailed description of the simulations provided in the Orbital mode is described.

## 3.2 SIMSPLASH in Orbital mode: Calculating the engulfment zones for planets around PN progenitors

Beginning on the main sequence with the planet at an initial semi-major axis the specified stellar evolution track is loaded into the code from the *stellar\_database* in SIMSPLASH. New stellar models can be added to the stellar database at any time, as any MESA stellar model is compatible with SIMSPLASH. It is then passed to the orbital evolution function which cycles through the stellar track for each data entry, or time-step, evolving the host star. In each time-step, a function to calculate the new semi-major axis is called. If the semi-major axis changes significantly at any point (either increasing or decreasing), an interpolation function is called to compute finer time-steps for the stellar evolution in the vicinity of that point and the evolution is calculated again using the interpolated stellar track. Whether the planet is engulfed or not, and at which point in the evolution this occurs, is returned to the output. The entire evolution is then saved and plotted for further analysis.

### 3.2.1 Semi-major axis evolution

In general, the semi-major axis evolution of a planet orbiting an evolving star is defined as the balance between mass-loss, which will act to increase the semi-major axis, and tides which will cause a reduction in the semi-major axis

$$\frac{da}{dt} = a \frac{\dot{M}_*}{M_* + M_{pl}} + \frac{da}{dt}_{(tides)}, \quad (3.1)$$

where  $M_{pl}$ ,  $M_*$ ,  $\dot{M}_*$  are the planet and stellar masses and the stellar mass-loss rate, respectively, and  $a$  is the semi-major axis of the planet. The first term in equation 3.1 represents

the evolution due to mass-loss of the star. The second term in equation 3.1 is the tidal evolution term. Some studies, for example Villaver & Livio (2007, 2009), include the effect of frictional and gravitational drag forces due to accretion of mass by the planet on the planetary orbit. However, Villaver & Livio (2009) concluded that the effects of frictional and gravitational drag forces are negligible for the orbital evolution, so these terms are not included in the calculations presented here, and the planet mass is always held constant. Furthermore, as in Nordhaus et al. (2010) and Villaver & Livio (2009), all planetary orbits are taken to be circular as the initial value of eccentricity has little effect on the orbital decay rate. Kunitomo et al. (2011) further confirmed the viability of neglecting eccentricity evolution and found it to have little-to-no effect on their conclusions in their investigation into planet engulfment as an explanation for the apparent gap in short-period massive planets.

The standard treatment for the tidal evolution of a planet in response to an evolving star is the tidal dissipation theory of Zahn (1977) (See section 2.1 for a description of the background theory) and the following formula for the semi-major axis evolution

$$\frac{da}{dt_{\text{(tides)}}} = -f \frac{a}{\tau_{\text{conv}}} \frac{M_{\text{env}}}{M_*} \left(1 + \frac{M_{\text{pl}}}{M_*}\right) \frac{M_{\text{pl}}}{M_*} \left(\frac{R_*}{a}\right)^8 \left(1 - \frac{\Omega_*}{\omega_{\text{pl}}}\right), \quad (3.2)$$

where  $M_{\text{env}}$ ,  $M_{\text{pl}}$  and  $R_*$  refer to the mass of the stellar envelope, the mass of the planet and the stellar radius, respectively.  $\omega_{\text{pl}}$  and  $\Omega_*$  are the planet orbital frequency and the stellar rotation frequency, respectively.  $\tau_{\text{conv}}$  is the convective turnover timescale and is defined as

$$\tau_{\text{conv}} = \left(\frac{M_{\text{env}} R_{\text{env}}^2}{3L_*}\right)^{\frac{1}{3}}, \quad (3.3)$$

where  $L_*$  is the stellar luminosity and  $R_{\text{env}}$  is the radius of the convective envelope. The radius of the convective envelope is approximated as  $R_{\text{env}} = R_*$ . All orbits are assumed to be circular ( $e = 0$ ). The term  $f$  in equation 3.2 is the dimensionless tidal dissipation factor, taken to be  $f = (P/2\tau_{\text{conv}})^2$  when  $\tau_{\text{conv}} > P/2$ . If  $\tau_{\text{conv}} > P/2$ ,  $f = 1$  (Villaver & Livio 2009), where  $P$  is the orbital period. Tides raised on the planet are not considered in the orbital evolution calculations since the primary is a post- main-sequence star, the orbit decays almost entirely due to tides raised on the star and those raised on the planet are negligible since it is a compact companion. Furthermore, as a planet orbit is circularised

any tides raised on a planet decrease and ultimately vanish for circular orbits and since we only consider circular orbits this is a reasonable assumption (Nordhaus et al. 2010).

For each star-planet system, equation 3.1 is integrated numerically using a Runge-Kutta solver. In each time-step of the integration the stellar parameters are loaded from the stellar models, and the new semi-major axis is calculated until such point that an engulfment occurs or the orbit increases to such an extent that an engulfment is no longer viable.

### 3.2.2 The MESA Isochrones and Stellar Tracks Database (MIST): Input physics

The evolution of the host star is the most important part of the orbital evolution. Looking at equation 3.1, and in particular equation 3.2 with its large dependence on stellar radius, each step in the orbital evolution is dependent on the stellar structure of the host star and so good stellar evolution models are imperative. Indeed one of the major differences between orbital evolution models across the literature is the use of a variety of different stellar evolution codes and their input physics such as, for example, the mass-loss coefficient and the inclusion/exclusion of overshooting and/or rotation.

`SIMSPLASH` contains a library of pre-calculated stellar evolution tracks. The default tracks in `SIMSPLASH` are the `MESA` Isochrones and Stellar Tracks (MIST) grid of models (Choi et al. 2016; Dotter 2016). The MIST models are computed with the stellar evolution code `MESA` (Modules for experiments in stellar astrophysics) of Paxton et al. (2011, 2013, 2015) and were adopted here because they consist of a large database of single stellar evolutionary tracks across all evolutionary phases for all masses and relevant metallicities.

Some of the important properties of the MIST models are highlighted in the following. Interested readers are encouraged to consult the aforementioned papers for further information about `MESA`<sup>2</sup> and the MIST project<sup>3</sup>.

---

<sup>2</sup>The `MESA` website: <http://mesa.sourceforge.net/>.

<sup>3</sup>The MIST website <http://waps.cfa.harvard.edu/MIST/>.

### Mass-loss rates

Mass-loss rates in MIST are modelled using the standard prescriptions of Reimers (1975) (equation 3.4) and Bloecker (1995) (equation 3.5) for the RGB and AGB, respectively.

$$\dot{M}_R = 4 \times 10^{-13} \eta_R \frac{(L_*/L_\odot)(R_*/R_\odot)}{(M_*/M_\odot)} M_\odot \text{ yr}^{-1}, \quad (3.4)$$

$$\dot{M}_B = 4.83 \times 10^{-9} \eta_B \frac{(L_*/L_\odot)^{2.7}}{(M_*/M_\odot)^{2.1}} \frac{\dot{M}_R}{\eta_R} M_\odot \text{ yr}^{-1}. \quad (3.5)$$

where  $\eta_R$  and  $\eta_B$  are the Reimers and Bloecker mass-loss coefficients, and are set at 0.1 and 0.2 respectively, in order to reproduce the initial to final mass relationship and AGB luminosity functions in the Magellanic clouds. They turn on Reimers mass-loss at the beginning of the evolution since only a negligible amount of mass is lost during the MS ( $10^{-13} M_\odot \text{ yr}^{-1}$  for a solar metallicity  $1 M_\odot$  star). The total mass-loss rate is capped at  $10^{-3} M_\odot \text{ yr}^{-1}$  in all MIST models to prevent convergence issues in `MESA` (Choi et al. 2016).

### Rotation

The MIST models are available with and without rotation, both of which are included as options for use in the orbital evolution code. In the MIST models the standard stellar structure equations are modified by centrifugal acceleration in terms of the presence of rotation. More details on the implementation of rotation can be found in Choi et al. (2016) and Paxton et al. (2013). It should be noted that the MIST models do not include rotation for stars of  $M_* < 1.2 M_\odot$  in order to reproduce the slow rotation rates observed in the sun and other low mass stars. This is because evolutionary models suggest that low-mass stars have strong differential rotation profiles at ZAMS and magnetic fields, which induce magnetic breaking in such stars, are not included in `MESA` calculations. The models which do include rotation ( $1.2 M_\odot < M_* < 8 M_\odot$ ) have rotation profiles of  $\Omega_{\text{ZAMS}}/\Omega_{\text{CRIT}} = 0.4$ , where  $\Omega_{\text{ZAMS}}$  and  $\Omega_{\text{CRIT}}$  are the initial and critical (sometimes referred to as the break up rotation frequency) surface rotation frequencies, respectively. Example plots for the evolution of the RGB and AGB radii and the helium core mass of a  $2 M_\odot$  star, for rotating (plotted in blue) and non-rotating (plotted in black) MIST models, are illustrated in figure 3.2.

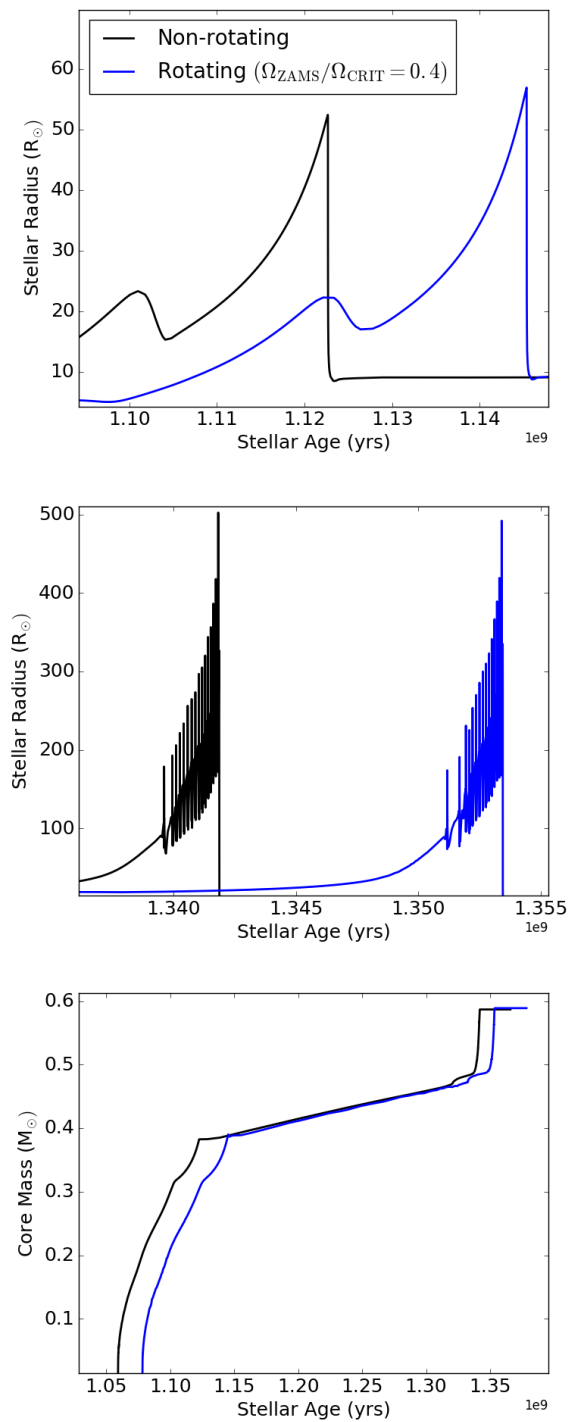


Figure 3.2: The MIST models of Choi et al. (2016): Stellar structure properties for a rotating (plotted in blue) and non-rotating (plotted in black)  $2 M_{\odot}$  star. Upper panel: RGB radius evolution. Middle panel: AGB radius evolution. Lower panel: Helium core mass evolution.

### Convective mixing and overshoot

Mixing length theory (MLT) describes the convective transport of energy in the stellar interior. According to standard mixing length theory, the mixing length parameter,  $\alpha_{\text{MLT}} = l_{\text{MLT}}/H_p$ , is a parameterisation of how efficient convection is. A large  $\alpha_{\text{MLT}}$  means that a fluid parcel can travel a large distance, ( $l_{\text{MLT}}$ ), before it deposits its energy into the ambient medium with local scale pressure height  $H_p$ . The MLT adopted in MIST is a modified version of Henyey et al. (1965), with  $\alpha_{\text{MLT}} = 1.82$ .

Mixing occurring at convective boundaries is known as overshoot. MIST follows the parameterisation of Herwig (2000) to account for overshooting, and adopt overshoot parameters of  $f_{\text{ov,core}} = 0.0160$  for the core and  $f_{\text{ov,env}} = 0.0174$  for the envelope of the star.

### Abundances

Choi et al. (2016) note that the definition of solar metallicity has been revised to  $Z=0.014$  (see, e.g., Caffau et al. 2011, for a discussion). The MIST models adopt protosolar abundances as the reference scale for all metallicities, where  $[Z/H]$  is computed with respect to  $Z = Z_\odot = 0.014$ . The solar abundance scale therefore follows  $X_\odot = 0.7154$ ,  $Y_\odot = 0.2703$  and  $Z_\odot = 0.014$ . The metallicities included in the stellar model database in SIMSPLASH are  $Z= 0.008, 0.005, 0.014, 0.025, 0.04$ . The maximum radii as a function of star mass, for the range of metallicities included from the MIST models included within SIMSPLASH are plotted in figure 3.3.

### Convergence issues

Choi et al. (2016) note that there is a subset of the MIST stellar models which do not run to completion due to convergence issues, a problem which was also encountered by the author and reported by Madappatt et al. (2016). Madappatt et al. (2016), for example, suggested that artificially increasing the mass-loss rate on the upper AGB can overcome such an issue as it forces the star to complete its evolution more quickly to avoid reaching a point where structural changes become unphysical. Despite this attempt, they were still unable to converge some models. The MIST models have sufficiently fine mass sampling such that they sidestep this problem by interpolating between complete and incomplete tracks; another reason why the MIST models are employed.

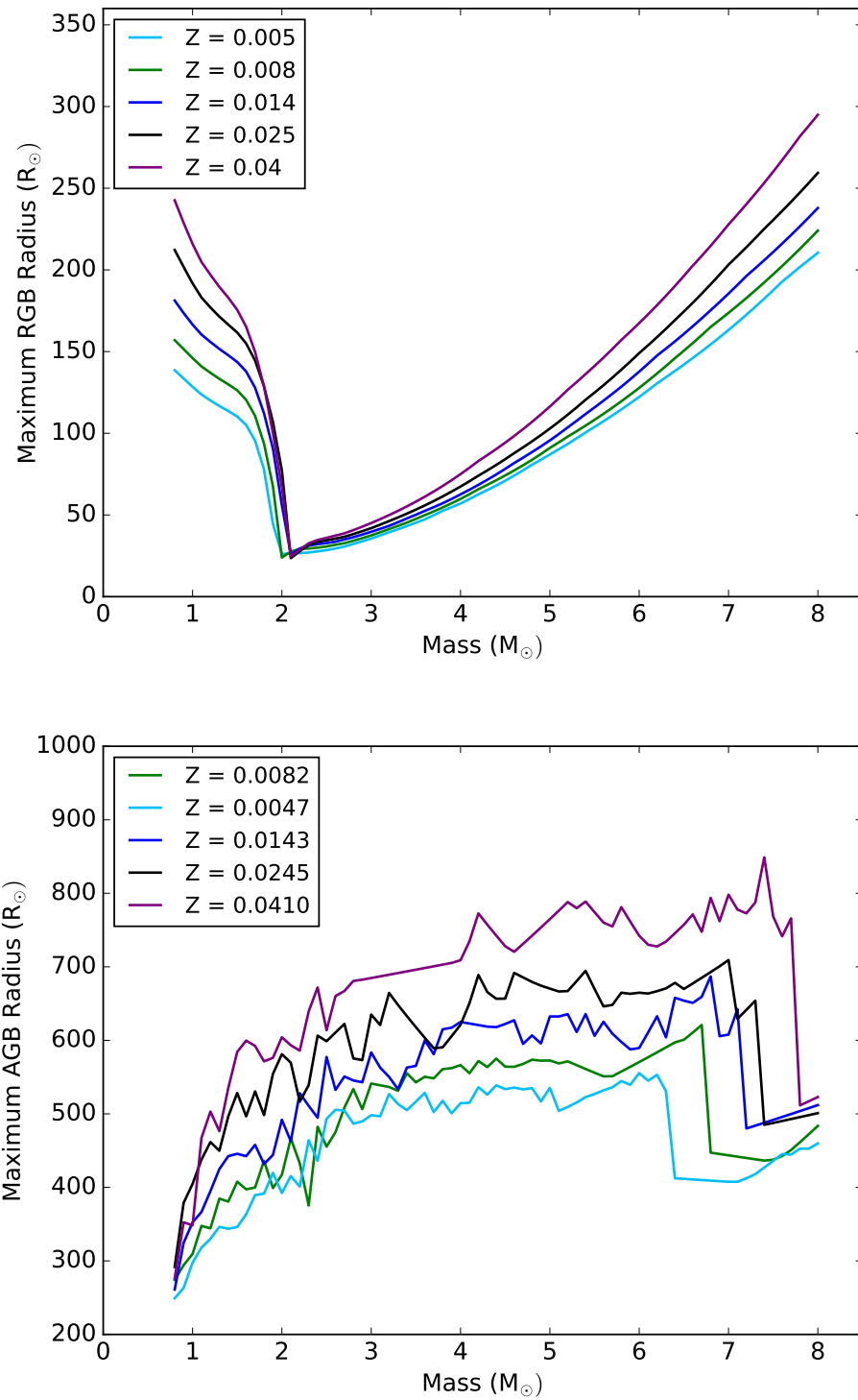


Figure 3.3: Example plots of the MIST models of Choi et al. (2016): The maximum RGB and AGB radii as a function of star mass for the range of metallicities adopted in this code. Data shown here is for a rotating star since the relative change in maximum radius as a function of metallicity is the same for rotating and non-rotating stars.

### 3.2.3 MESA stellar models

SIMSPLASH also contains a grid of stellar evolution tracks calculated by the author, also calculated with `MESA` (Paxton et al. 2011, 2013, 2015), but with different input physics to the MIST models of Choi et al. (2016). The grid currently contains non-rotating stellar evolution tracks for initial metallicities of  $Z = 0.01$  and  $Z = 0.02$  with masses ranging from  $0.8\text{--}8.0 \, M_{\odot}$  in increments of  $0.1 \, M_{\odot}$  calculated with the default input physics outlined in the `MESA` instrument papers. The main difference in the two grids are the Reimers (1975) (equation 3.4) and Bloecker (1995) (equation 3.5) mass-loss coefficients for the RGB and AGB, respectively. In these models,  $\eta_R$  and  $\eta_B$  are fixed at 0.5 and 0.1, respectively.

### 3.2.4 Interpolation

Since the time-steps in stellar evolution models tend to be very large `SIMSPLASH` checks for any significant changes in semi-major axis at each step in the integration. If the orbit increases or decreases by 10% of its initial value the integration is stopped and an interpolation function is called to interpolate between 10 steps before and 10 steps after that point. This is necessary because the semi-major axis is extremely sensitive to the expanding stellar radius, and even a small change in stellar radius can cause the semi-major axis of the planet to transition from a relatively stable orbit to plunging into the stellar envelope and surpass the core in one time-step. This leads to a ‘negative’ semi-major axis being calculated by `SIMSPLASH`, which is obviously a nonsensical output and is an artefact of the time-steps being too large. The user can choose to change the interpolation resolution by changing the points within which the interpolation will be performed and how many interpolated points should be added within these. The interpolation function used in `SIMSPLASH` is the 1-dimensional monotonic interpolation function of Steffen (1990) provided within the GNU scientific library.

### 3.3 Results: The engulfment zones of planetary nebula progenitors

In the following, the engulfment zones are presented for some example systems. As discussed earlier, the AGB engulfment zone is defined as the range of semi-major axes,  $a$ , within which a planet will avoid engulfment on the RGB but undergo an engulfment on the AGB. Planets that do not survive the RGB are defined as being in the RGB engulfment zone. Planets which are not engulfed on either the RGB or the AGB are said to be at a safe semi-major axis. The semi-major axis which marks the transition from that of which engulfment occurs on the RGB, and that of which engulfment occurs on the AGB, will be referred to as the RGB engulfment zone boundary. Likewise the semi-major axis marking the transition from the AGB engulfment zone to the safe semi-major axes will be referred to as the AGB engulfment zone boundary. In all figures depicting the evolution, each coloured line represents the semi-major axis evolution of a planet of a given mass starting at a different distance from the host star. Models in which the initial semi-major axis was within the RGB engulfment zone are illustrated in red, those within the AGB engulfment zone are in green, and those which are at a safe initial semi-major axis are in blue. The stellar radius, on the same plot, is the thick black line. In models depicting the entire evolution (from the end of the main sequence to the end of the AGB), the first ‘spike’ in the stellar radius indicates that the star is on the RGB, and the second, larger, spike indicates that the star is on the AGB.

#### 3.3.1 Non-rotating, solar metallicity stars and the effects of a conservative RGB mass-loss coefficient

Figure 3.4 shows the evolution of a  $1 M_{\odot}$  non-rotating star from the end of the main sequence to the end of the AGB, and the semi-major axes evolution of a  $1 M_J$  planet beginning at varying initial distances from the star, where  $1 M_J$  is the mass of the planet Jupiter ( $9.5 \times 10^{-4} M_{\odot}$ ). The stellar metallicity of this model is solar and the Reimers and Bloecker mass-loss coefficients are  $\eta_R = 0.1$  and  $\eta_B = 0.2$ , respectively. The evolution was calculated for initial semi-major axes between  $0.5 - 3$  AU ( $\sim 105 - 645 R_{\odot}$ ) in

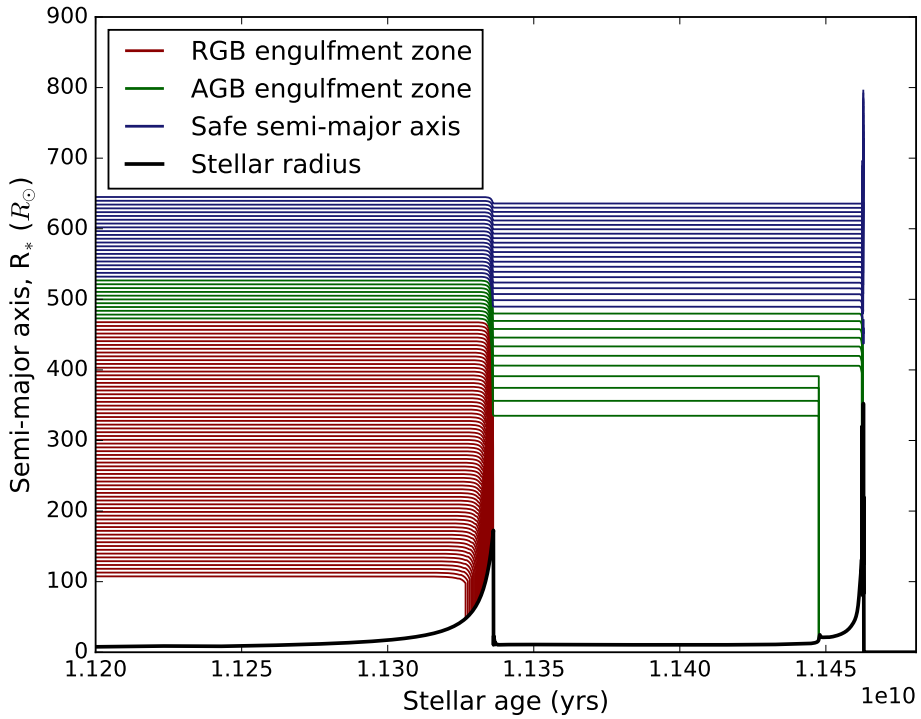


Figure 3.4: The orbital evolution of a  $1 M_J$  planet around a  $1 M_\odot$  star with varying initial semi-major axes. Red lines depict the range of semi-major axes in the RGB engulfment zone, the green lines depict the AGB engulfment zone and the blue lines represent the safe initial semi-major axes. The thick black line is the stellar radius.

increments of 0.025 AU ( $\sim 5 R_\odot$ ).<sup>4</sup>

Examining figure 3.4, it is clear that as the stellar radius on both the RGB or the AGB begins to expand, the evolution of the semi-major axis of those planets within the respective engulfment zones decreases very suddenly and continues to decrease until the planet is engulfed by the star (the point at which the semi-major axis meets the stellar radius). The sudden decrease in semi-major axis emphasises the strength of the tide at these phases in the stars evolution. Recall from chapter 1, as the star ascends the RGB the core is contracting, while the envelope begins to expand and increase in opacity due to the rising luminosity. As a result of the rising opacity the envelope becomes fully convective. Since the efficiency of the tides is dependent on convection for the dissipation of kinetic energy in the envelope (see chapter 2), the sudden increase in radius, and thus sudden onset of convection, results in a rapid increase in the strength of the tides and a rapid

<sup>4</sup>SIMSPFLASH takes semi-major axis input in astronomical units (AU), and semi-major axes are converted to solar units in the calculations. Results are reported in, and rounded to the nearest,  $1 R_\odot$ . For reference,  $1 \text{ AU} \approx 215 R_\odot$ .

in-fall of the planet towards the star. This relationship is contained in the  $(R_*/a)^8$  term in equation 3.2; the evolution of the semi-major axis evolution has a very high dependence on the stellar radius. Because of the tides, the  $1 M_\odot$  star can engulf a planet as far away as  $470 R_\odot$ , almost 3 times the extent of its maximum radius on the RGB ( $166 R_\odot$ ). The expansion of the stellar envelope and onset of convection during the AGB ascent has the same effect, but on a larger scale. However, the AGB engulfment zone appears to be quite conservative in comparison to that of the RGB for the  $1 M_\odot$  star. This does not mean that the tides are less effective on the AGB (in fact they are stronger); the modest extent of the AGB engulfment zone in comparison to that of the RGB is due to the strong, competing, effects of the mass-loss that the star experiences at the tip of the AGB. For this reason the star can engulf planets only  $\simeq 1.5$  times farther than the maximum extent of its AGB radius, up to  $530 R_\odot$ . In the case of the  $1 M_\odot$  star in figure 3.4, there is a  $\simeq 60 R_\odot$  wide region within which  $1 M_J$  planets must be in order to be capable of shaping a PN.

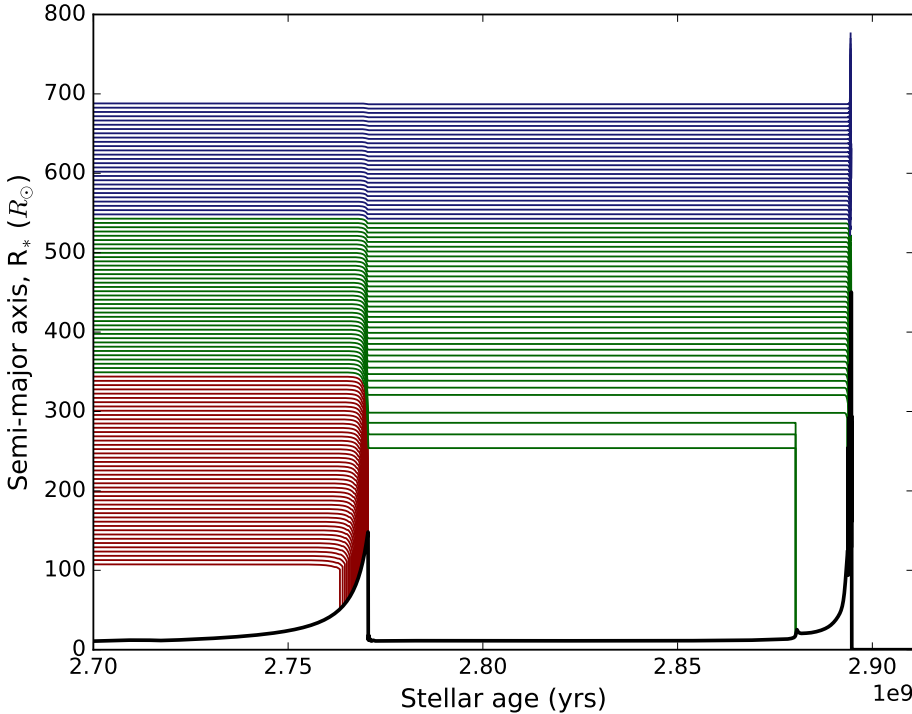


Figure 3.5: Same as figure 3.4 but for a  $1.5 M_\odot$  star and  $1 M_J$  planet. As before, red lines depict the range of semi-major axes in the RGB engulfment zone, the green lines depict the AGB engulfment zone and the blue lines represent the safe initial semi-major axes. The thick black line is the stellar radius

Using the same treatment as described above, but for a non-rotating,  $1.5 M_\odot$  star

### 3.3. RESULTS: THE ENGULFMENT ZONES OF PLANETARY NEBULA PROGENITORS

---

and a  $1 M_J$  planet, in figure 3.5, we see that the AGB engulfment zone is between  $345$  and  $540 R_\odot$ , over 3 times as wide as for the  $1 M_\odot$  star. This is due to the difference in maximum RGB and AGB radii reached by the two stars. The  $1.5 M_\odot$  star reaches a maximum radius of  $143 R_\odot$  on the RGB, and since it does not expand to the same extent as that of a  $1 M_\odot$  star, more planets can surpass the RGB unscathed but be engulfed later on. Furthermore, the maximum AGB radius is larger for the  $1.5 M_\odot$  star, resulting in more planets being engulfed at larger semi-major axes. Again, notice that the star is capable of engulfing planets more than twice the maximum extent of its envelope during the RGB, while during the AGB the effect of stellar mass-loss results in a more modest engulfment zone in relation to the maximum extent of the envelope.

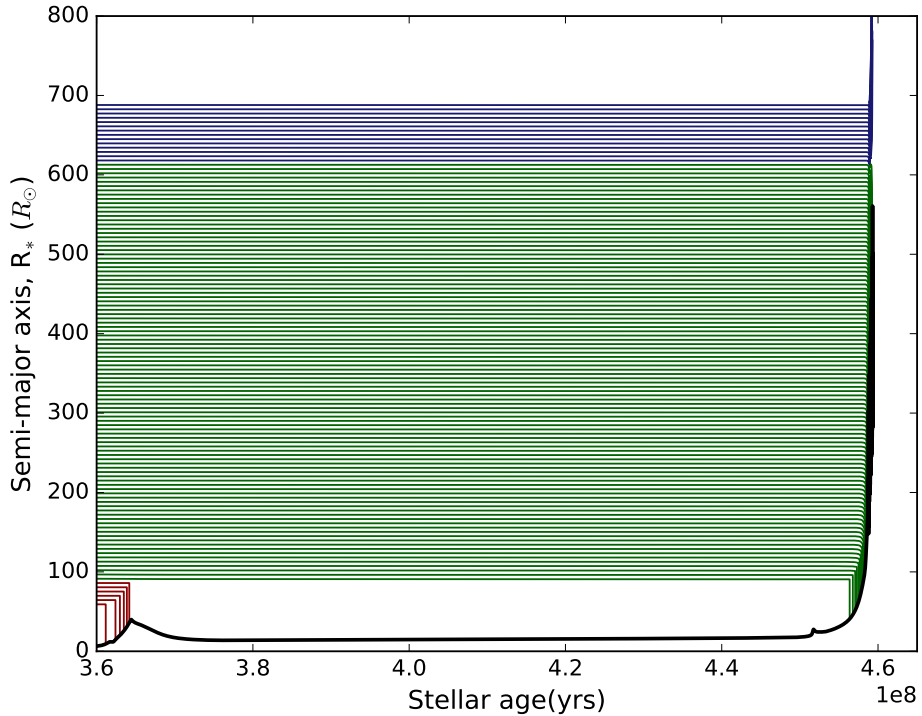


Figure 3.6: Same as figure 3.4 but for a  $3 M_\odot$  star.

The differing widths of the AGB engulfment zone are even more noticeable for the  $3$  and  $5 M_\odot$  stars (figures 3.6 and 3.7, respectively). Stars with masses larger than  $\simeq 2 M_\odot$  do not reach electron degeneracy in their helium cores prior to the horizontal branch. As noted by Villaver et al. (2014) and Kunitomo et al. (2011), stars which do develop electron degeneracy have much larger and luminous envelopes during the RGB and undergo rapid expansion during the helium flash, while the higher mass stars RGB phase ends be-

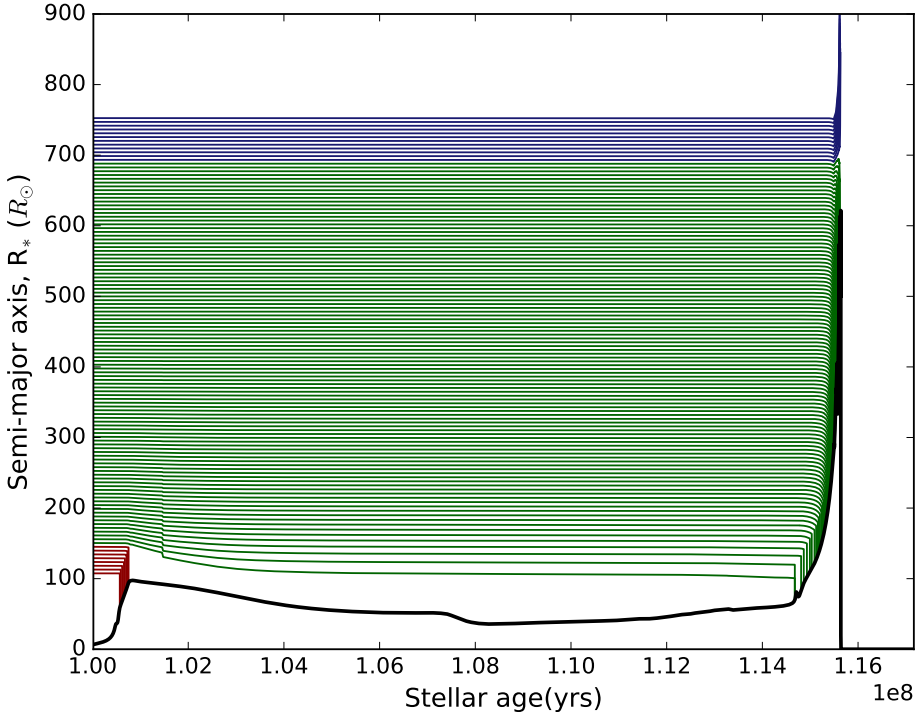


Figure 3.7: Same as figure 3.4 but for a  $5 M_{\odot}$  star.

fore electron degeneracy can be reached, as discussed in chapter 1, such that their RGB envelopes do not expand to the same extent as the 1 and  $1.5 M_{\odot}$  stars.

Re-focusing our attention again to a  $1.5 M_{\odot}$  star, but this time with a  $10 M_J$  planet (figure 3.8), we see that the extent of the RGB engulfment zone has increased (from  $345 R_{\odot}$  to  $530 R_{\odot}$ ), but so has the AGB engulfment zone boundary (from  $540$  to  $740 R_{\odot}$ ), in other words the AGB engulfment zone is shifted upwards and increases by  $\simeq 7\%$ . Figure 3.9 provides a summary of the upward shift in engulfment zones with increasing planet mass for the  $1.5 M_{\odot}$ . Such a shift in engulfment zone boundaries is expected and was noted in many planet engulfment studies (e.g., Villaver & Livio 2009).

Up to this point, all of the orbital evolution calculations presented were calculated with the MIST stellar models of Choi et al. (2016), which have Reimers (1975) (equation 3.4) and Bloecker (1995) (equation 3.5) mass-loss coefficients for the RGB and AGB, respectively, set to  $\eta_R = 0.1$  and  $\eta_B = 0.2$ . Firstly, with regards to the mass-loss coefficient on the RGB, the value of the RGB mass-loss coefficient is usually set to  $\eta_R = 0.5$  in orbital evolution modelling which was the case, for example, in recent calculations by Madappatt et al. (2016), where the value of  $\eta_R = 0.5$  was chosen in order to be consistent with the recently

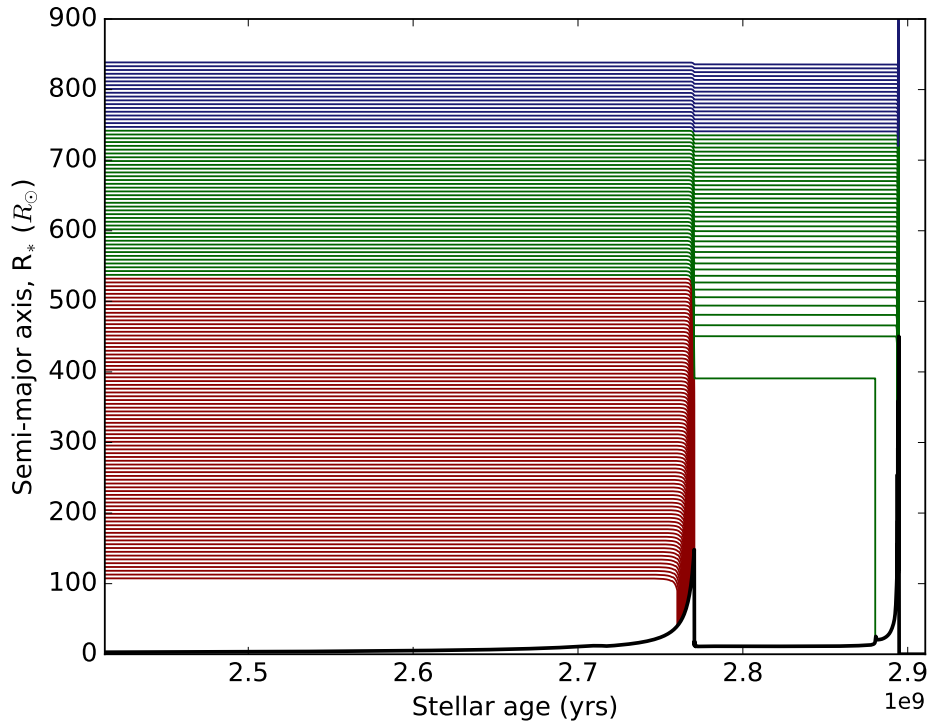


Figure 3.8: Same as figure 3.5 but with a  $10 M_J$  planet orbiting a  $1.5 M_\odot$  star. Red lines depict the range of semi-major axes in the RGB engulfment zone, the green lines depict the AGB engulfment zone and the blue lines represent the safe initial semi-major axes. The thick black line is the stellar radius.

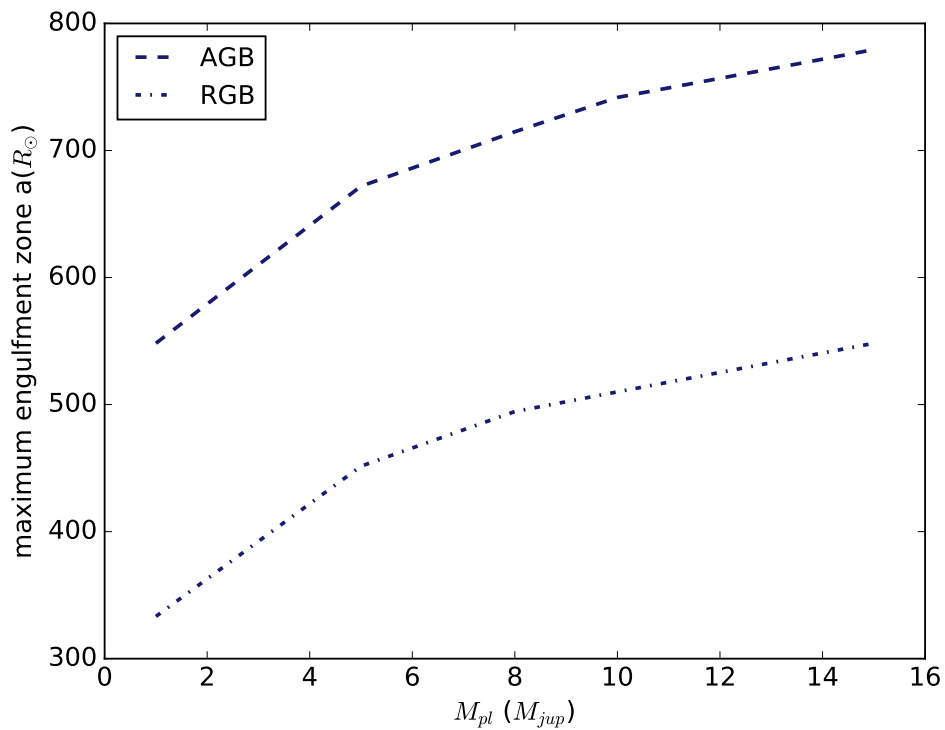


Figure 3.9: Comparison of the RGB and AGB engulfment zones as a function of planet mass for a  $1.5 M_\odot$  star.

calculated value by McDonald & Zijlstra (2015) and also Ekström et al. (2012). However, mass-loss, and its parametrisation, is a notoriously uncertain phenomenon. According to Choi et al. (2016), the validity of assuming the mass-loss coefficients they employ in their models can be sought from initial-to-final mass relations observed in clusters. Choi et al. (2016) report that  $\eta_R = 0.1$  was chosen for the MIST models based on the asteroseismic observations of open cluster stars of Miglio et al. (2012), who found that adopting a value of  $\eta_R = 0.1$  fits accordingly when studying the cluster NGC 6791. Nonetheless, the topic remains a source of debate, and thus a subject of uncertainty in modelling of the orbital evolution. One important difference in adopting a lower value for the RGB mass-loss coefficient is that it renders a lower mass-loss rate for the RGB, which translates to the strength of the tide being effective for further semi-major axes at the RGB engulfment zone boundary, meaning less close-in planets would survive past RGB evolution.

To highlight the difference in the adopted mass-loss coefficients in the MIST models and those usually adopted in orbital evolution calculations, figure 3.10 shows the orbital evolution of a  $1.5 M_\odot$  solar metallicity ( $Z = 0.014$ ) star and  $1 M_J$  planet evolved with stellar models calculated by the author and adopting the same input physics as the MIST models but with Reimers (1975) and Bloecker (1995) mass-loss coefficients,  $\eta_R$  and  $\eta_B$ , fixed at 0.5 and 0.1, respectively. The colours on this plot were changed in order to indicate that a different set of stellar models were used in this calculation, where purple lines depict the range of semi-major axes in the RGB engulfment zone, the cyan lines depict the AGB engulfment zone and the blue lines represent the safe initial semi-major axes. As before, the thick black line is the stellar radius. In this model, the RGB and AGB engulfment zone boundaries are  $290 R_\odot$  and  $470 R_\odot$ , respectively; values which are  $\approx 10\%$  and  $\approx 15\%$  (respectively) lower than the engulfment zone boundaries presented for the MIST models which would result in more planets being available for engulfment on the AGB near the RGB engulfment zone boundary, but less planets being engulfed near the AGB engulfment zone boundary. The effect of adopting either mass-loss prescription on the population of planetary nebulae being shaped by planets, however, will largely depend on the semi-major axis and mass distributions of exoplanets.

Recently Sabach & Soker (2018) suggested that the typical mass-loss rates used in many of the previous orbital evolution studies (e.g., Madappatt et al. 2016), are actually the result of enhanced mass-loss from the presence of a stellar binary, and that single stars

would have a much lower mass-loss rate, perhaps as low as 10-20% of the canonical one (in their paper they adopt the mass-loss coefficient of  $\eta_R = 0.5$  as the typical value, and the lower rate to be  $\eta_R = 0.07$ ). While Sabach & Soker (2018) do not perform a full tidal calculation in their work, they do present an interesting discussion on the topic of adopting a lower RGB mass-loss coefficient, which adds strength to the value adopted in the MIST models. They argue that the observationally constrained higher mass-loss rates would only be plausible in a single star after the injection of angular momentum, say from engulfing a planet on the RGB first. Otherwise, a lower RGB mass-loss rate would be more fitting and would result in a maximum AGB envelope extending to as much as twice the extent it would have with the canonical value. Since the companion masses that are considered in binary shaping, and thus in the study by Madappatt et al. (2016), in determining the population of post common envelope binary PNe, are sufficient to enhance mass-loss *before* a common envelope can occur, then the high mass-loss coefficient would likely be most valid for their study. Since a planet mass companion would not be capable of enhancing mass-loss until *after* engulfment, the mass-loss coefficient adopted in the MIST models would be a valid prescription if the speculation of Sabach & Soker (2018) was true, since it is assumed that no engulfment has occurred by the star prior to the semi-major axes evolution carried out here. However, their view is still considered speculative. Nonetheless, in order to constrain the uncertainty in the mass-loss prescription on planet, both prescriptions should ideally be adopted in a population synthesis.

In essence, the RGB mass-loss prescription is an uncertainty inherent in all orbital evolution models and needs to be carefully considered, and may even depend on whether the companion mass is stellar or planetary in nature, for orbital evolution calculations. The subject of uncertainty as a result of the value for the RGB mass-loss coefficient has been visited previously by Villaver et al. (2014) who investigated the effect of the parameterisation of RGB mass-loss on their engulfment models by comparing three different prescriptions, with the most notable differences being between values of  $\eta_R = 0.2$  and  $\eta_R = 0.5$ . They also find that the engulfment zone is sensitive to the mass-loss coefficient with the resulting difference in the RGB engulfment zone boundary being  $\simeq 13\%$  between the modest mass-loss rate and the higher value. They do not model the evolution of the semi-major axis along the AGB in this paper, or comment on the knock-on effect for the resulting AGB engulfment zone, however. The consequence of adopting a lower value for

the Reimers RGB mass-loss coefficient on the resulting AGB engulfment zone boundary is that, since the mass-loss rate is lower on the RGB, the envelope and core masses are larger when the star reaches the AGB, prolonging the life of the star, and allowing the stellar envelope to extend to larger radii. However, while a difference between the extent of the AGB engulfment zone boundary between models calculated with  $\eta_R = 0.1$  and  $\eta_R = 0.5$  is found in this work, it must be noted that it is not entirely due to the effect of  $\eta_R$  since the AGB mass-loss coefficient is different between the two models, making such a comparison difficult, where the MIST models adopted a value of  $\eta_B = 0.2$  for the AGB mass-loss coefficient, again to reproduce the initial-final-mass relation in the Magellanic clouds. Madappatt et al. (2016) report that increasing  $\eta_B$  from 0.1 to 0.2, decreases the maximum AGB radius by 10%.

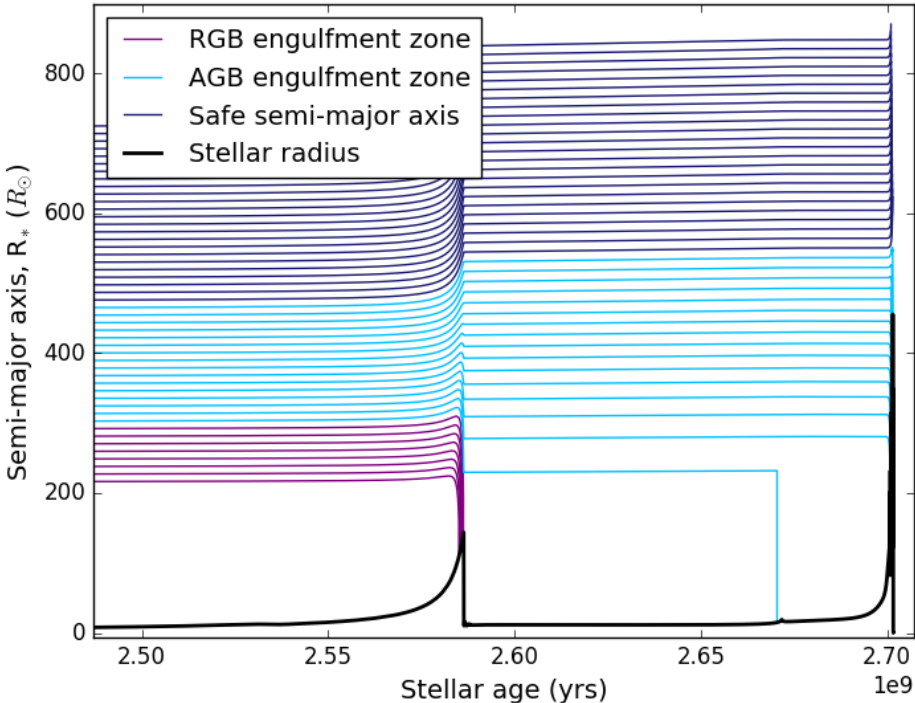


Figure 3.10: The orbital evolution of a  $1.5 M_\odot$  star and  $1 M_J$  planet evolved with stellar models calculated by the author with Reimers (1975) and Bloecker (1995) mass-loss coefficients,  $\eta_R$  and  $\eta_B$ , fixed at 0.5 and 0.1, respectively. Purple lines depict the range of semi-major axes in the RGB engulfment zone, the cyan lines depict the AGB engulfment zone and the blue lines represent the safe initial semi-major axes. As before, the thick black line is the stellar radius.

### 3.3.2 The effects of rotation

The effects of rotation on the orbital evolution of planets around RGB stars was recently incorporated in the calculations of Privitera et al. (2016). Their objective was to more accurately investigate whether planet engulfment could account for the population of rapid red giant rotators, in comparison to the previously calculated models of Carlberg et al. (2009) who did not account for the initial rotation of their host stars. Privitera et al. (2016) make the argument that rotation alters the stellar structure of the star, and hence will affect the boundary of the RGB engulfment zone, and state that the inclusion of rotation in stellar models must have a non-negligible impact on the conditions for planet engulfment. This is true, and as they describe, the most noticeable difference in stellar structure occurs during the main sequence where rotational mixing causes an increase in core mass and MS lifetime (Choi et al. 2016). But, as they also note, the difference in luminosity on the RGB between rotating and non-rotating models is very slight. Nonetheless, it is important to determine the effect of rotation in stellar models on the engulfment zones since stars do rotate, however slowly in the mass ranges considered, and any changes in the stellar structure that are a result of that should be accounted for in the orbital evolution model. Furthermore, Privitera et al. (2016) did not follow the evolution through to the AGB phase. However, it is noted that the exchange of angular momentum from the planet orbit to the star (the spin-up of the star) is not modelled here. This is reasonable since the increase in rotational frequency of the star as a result of the exchange is not large enough to have a significant effect on the semi-major axis evolution, as found by Privitera et al. (2016), where the most extreme effect would be if the star was spun-up enough such that the  $(1-\Omega_*/\omega_{pl})$  term in equation 3.2 became negative and essentially increases the semi-major axis. Thus the investigation here is purely into the effect of rotation on the stellar structure and how that impacts the orbital evolution.

In this section the MIST models of Choi et al. (2016) are employed to investigate the effect of rotation on the RGB and AGB engulfment zones. Figures 3.11 depicts the semi-major axes evolution of a rotating ( $\Omega_{ZAMS}/\Omega_{CRIT} = 0.4$ )  $2 M_\odot$  star with a  $1 M_J$  planet calculated, as in the previous section, for varying initial semi-major axes, zoomed in on the RGB. The models were run with narrow increments of initial semi-major axes of 0.01 AU ( $\simeq 2 R_\odot$ ). The resulting RGB engulfment zones are 105 and  $110 R_\odot$  for

the non-rotating and rotating stars (left and right panels of figure 3.11), respectively; an increase of  $\simeq 5\%$  when calculating with rotation. Interestingly, Privitera et al. (2016) reported a much larger difference in their models of a 20% *decrease* in the RGB engulfment zone boundary between a slow rotating ( $\Omega_{\text{ZAMS}}/\Omega_{\text{CRIT}} = 0.1$ ) model and a fast rotating ( $\Omega_{\text{ZAMS}}/\Omega_{\text{CRIT}} = 0.5$ ) model. Figure 3.12 summarises the RGB engulfment zone boundaries for a range of star masses calculated by Privitera et al. (2016) (depicted in grey) and those calculated in this work, where the dashed lines represent results obtained using rotating stellar models and solid lines represent those of non-rotating stellar models.

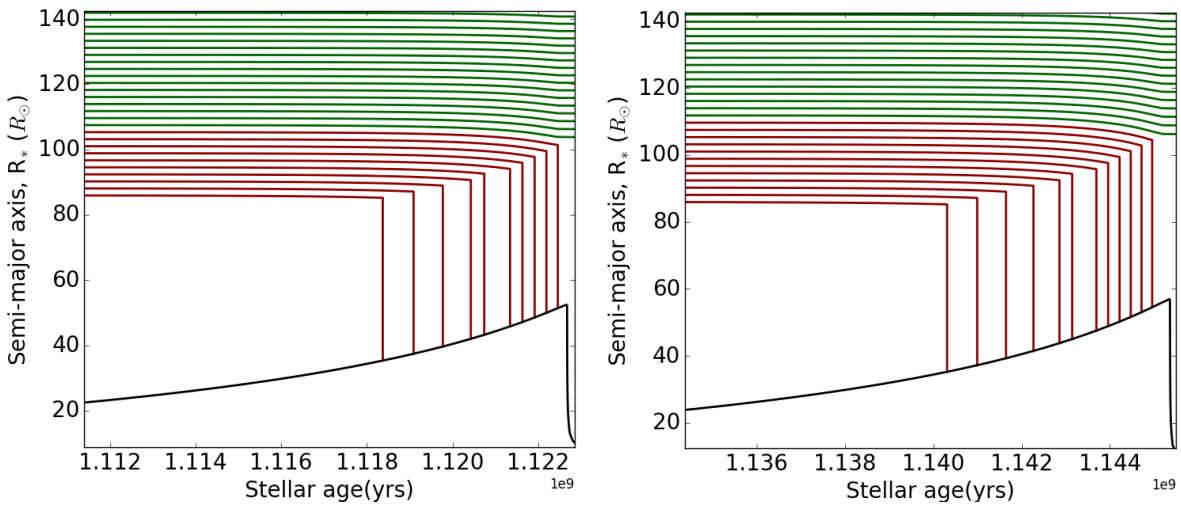


Figure 3.11: The difference in RGB engulfment zone boundaries between a non-rotating (left image) and rotating (right image)  $2 M_{\odot}$  star with a  $1 M_J$  planet (zoomed in on the RGB engulfment zone in order to illustrate the change in the RGB engulfment zone boundary). The red lines depict the initial semi-major axes which result in an RGB engulfment while the green lines depict those which are not engulfed on the RGB, but are later engulfed on the AGB.

The discrepancy in the direction in which the RGB engulfment boundary moves towards is due to the fact that the faster rotating stellar model used in the calculations of Privitera et al. (2016) results in a slightly lower value for the maximum extent of RGB radius than that of the more slowly rotating model, while the rotating MIST model produces a slightly higher maximum RGB radius than the non-rotating model (see figure 3.2). The reason their faster rotating model reaches lower luminosities, and the MIST models reach higher luminosities, stems from rotationally induced mixing and how it increases the mass of the core during the main sequence. If core growth during the main sequence is efficient enough, the core mass needed to ignite helium on the RGB is reached before degeneracy

### 3.3. RESULTS: THE ENGULFMENT ZONES OF PLANETARY NEBULA PROGENITORS

---

can occur resulting in no helium flash and so the star reaches a lower maximum luminosity before turning onto the horizontal branch. In their slower rotating model, since lower rotation rates means less core growth during the main sequence, their star reaches the temperature for helium ignition when the core has reached a semi-degenerate state, resulting in a larger maximum luminosity reached before leaving the RGB. The stellar models used by Privitera et al. (2016) are a modified version of Ekström et al. (2012), which have more efficient rotational mixing than the MIST models (see Choi et al. 2016), resulting in relatively less enhancement of main sequence core growth. Because of the lower core growth on the main sequence in the rotating MIST models in comparison to the non-rotating model, the difference in core mass is not sufficient to shift the core from a state of semi-degeneracy to a non-degenerate state. Thus the rotating stars in MIST reach the temperatures required for helium burning while in a semi-degenerate state, just as the non-rotating star does, but with a slightly higher core mass and slightly higher luminosity. In essence, whether or not rotation produces an increase or decrease in the RGB engulfment zone boundary by altering the thermal state of the core, depends on the efficiency of rotational mixing.

The large difference, in general, of the extent of the RGB engulfment zone boundaries between the results presented here and that of Privitera et al. (2016) is, as discussed previously, due to the efficiency in rotational mixing of the Ekström et al. (2012) stellar models. Choi et al. (2016) note that, in general, the rotating Ekström et al. (2012) models are hotter and more luminous than the MIST models due to rotational mixing, and because Privitera et al. (2016) adopt a *slowly rotating* model and compare it to a fast rotating model, while here the comparison is between a *non-rotating* model and a relatively fast rotating model, their models will result in larger radii on the RGB in general since they are both rotating, even if slowly. If the stellar models used here were instead using the exact same rotation rates as adopted in Privitera et al. (2016), the conclusion would be the same, due to the less efficient rotational mixing, and likewise if non-rotating Ekström et al. (2012) models were adopted the results would likely agree with those in this work. Choi et al. (2016) note that both the MIST models and those of Ekström et al. (2012) are comparable to observations despite these differences. Thus, this has revealed another source of uncertainty in tidal evolution modelling as a result of the stellar models employed.

With regards to the AGB, the maximum radius reached by the  $2 \text{ M}_\odot$  star on the AGB

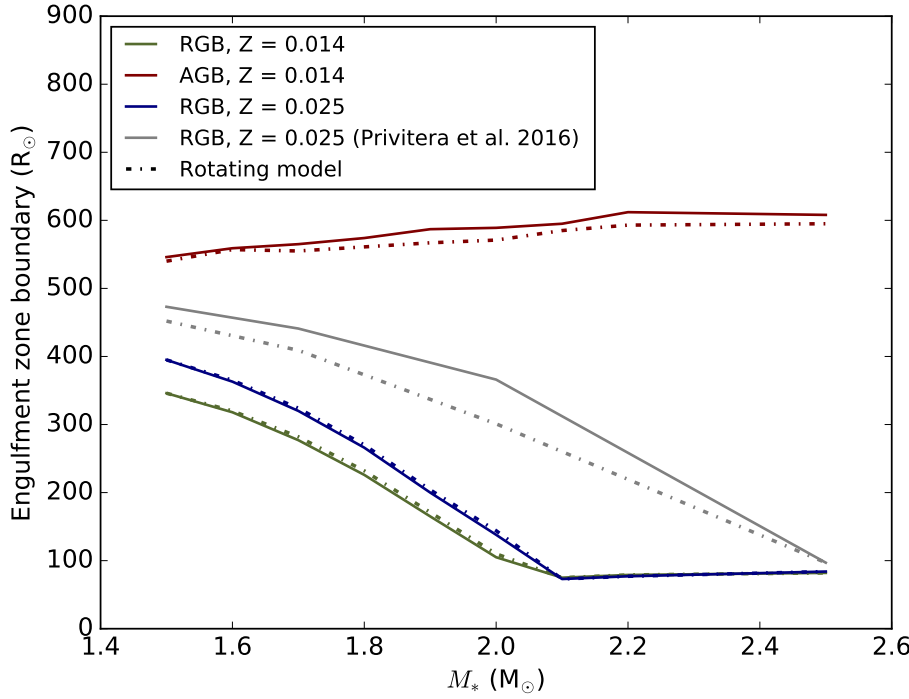


Figure 3.12: Engulfment zone boundaries for a  $1 M_J$  planet orbiting rotating (dashed lines) and non-rotating (solid lines) stars as a function of star mass. The RGB engulfment zone boundaries calculated for a star with metallicity  $Z = 0.025$  is depicted in blue, while those of Privitera et al. (2016) for the same metallicity are shown in grey. In contrast to the Privitera et al. (2016) model, it is found here that the RGB engulfment zone boundary increases, although very slightly, when rotation is included. The green and red models illustrate the effect of rotation for a star with  $Z = 0.014$  for the RGB and AGB, respectively.

is slightly lower in the rotating model in comparison to the non-rotating model (see figure 3.2). This causes the boundary for non-rotating and rotating models to decrease from 589 to  $571 R_\odot$ , an  $18 R_\odot$  decrease ( $\approx 3\%$ ) in the upper boundary of the AGB engulfment zone. The small decrease in the maximum AGB radius in the rotating model is due to rotationally enhanced mass-loss, which is enhanced by a very small amount for low-to-intermediate mass stars (Paxton et al. 2013; Choi et al. 2016), resulting in the envelope being ejected at a slightly lower luminosity. The small enhancement in mass-loss also means the tides are slightly less effective.

The results for the rotating and non-rotating AGB engulfment zones for a range of star masses ( $1.5, 1.6, 1.7, 1.8, 1.9, 2.0, 2.1, 2.2$  and  $2.5 M_\odot$ ) at solar metallicity ( $Z = 0.014$ ), with a  $1 M_J$  planet are summarised in table 3.1. Across the range of masses tested here, it is found that for all models calculated, the AGB engulfment zone decreases in width

by a small amount due to the RGB engulfment zone boundary increasing by a small amount for rotating models, and the AGB engulfment zone boundary decreasing by a small amount for rotating stellar models. In comparing the widths of the AGB engulfment zones, one can see that the rotating model results in a decrease, on average, by only  $\simeq 5\%$ , meaning that less planets would be capable of shaping a planetary nebula according to the rotating models. However, the decrease is small, validating the assumption made by Madappatt et al. (2016) that stellar models calculated with or without rotation will not have a large effect on the overall result. In fact, going back to the case of the  $1.5 M_{\odot}$  star and semi-major axis evolution of a  $1 M_J$  planet, the resulting RGB engulfment zone boundary remains the same between the rotating and non-rotating model, while the AGB engulfment zone boundary is only lowered by  $\simeq 1\%$ , indicating that the prescription for mass-loss dominates over rotation in determining the conditions for engulfment.

Comparing the results of the RGB engulfment zone boundaries calculated using the rotating and non-rotating models for metallicities of  $Z = 0.014$  and  $Z = 0.025$  in figure 3.12 it is clear that the effect of rotation is the same regardless of the adopted metallicity. With that said, the difference in the RGB engulfment zone boundaries between the  $Z = 0.014$  and  $Z = 0.025$  metallicity models indicate that metallicity plays a strong role in the extent of the RGB engulfment zone boundary for stars which form a helium degenerate core. Since there is evidence for a strong metallicity correlation on the formation of exoplanets, the effect of host star metallicity on the semi-major axis evolution will be demonstrated in the next section.

### 3.3.3 The effects of varying initial composition

In the previous section, the range of masses within which the transition mass for a star reaching a semi-degenerate state and a non-degenerate state was explored to determine the effect that rotation can have on the RGB engulfment zone boundary. In contrast to the findings of Privitera et al. (2016) it was shown that, unless rotationally induced mixing processes are very efficient, rotation does not affect the transition mass between thermal states in the core. Nonetheless, from the aforementioned discussion, as well as the stark contrast between the engulfment zone boundaries of, for example a  $1 M_{\odot}$  and a  $3 M_{\odot}$  star shown in figures 3.4 and 3.6, respectively, it is obvious that whether or not a

AGB engulfment zone ranges ( $R_\odot$ )		
$M_*(M_\odot)$	Non-rotating	Rotating
1.5	346-546	346-540
1.6	318-559	320-557
1.7	277-565	282-555
1.8	226-574	232-561
1.9	165-587	171-567
2.0	105-589	110-571
2.1	75-595	75-585
2.2	79-612	79-593
2.5	82-608	82-595

Table 3.1: The AGB engulfment zones for rotating and non-rotating stellar models for a range of star masses with a  $1 M_J$  planet. The metallicity of the star in these calculations is  $Z = 0.014$ .

star develops an electron degenerate helium core is a critical aspect for the RGB engulfment zone boundary. A very important determining factor for a star transitioning from semi-degeneracy to non-degeneracy is its initial composition, as was demonstrated by (Kunitomo et al. 2011; Villaver et al. 2014). The exact mass where the transition between the degenerate and non-degenerate core is uncertain, though it is dependent on the initial chemical composition and occurs somewhere around  $\simeq 2 M_\odot$ . Increasing the initial heavy-element abundance, i.e., increasing the metallicity, will lead to higher transition mass for degeneracy, while lowering the metallicity will result in a more subdued transition to triple-alpha burning with less expansion on the RGB due to lower opacity in the atmosphere (less cooling) and low efficiency of the CNO-cycle of the hydrogen burning shell.

The left and right hand panels of figure 3.3 illustrates the maximum radius reached as a function of star mass on the RGB and AGB, respectively, for the range of initial metallicities,  $Z$ , included in the SIMSPLASH stellar database. Unsurprisingly, the RGB engulfment zone boundary is sensitive to star mass, and star mass becomes especially important near the transition mass between stars which go through the helium flash and those which do not. This is evident in figures 3.13 and 3.14, where the differences in the RGB and AGB

### 3.3. RESULTS: THE ENGULFMENT ZONES OF PLANETARY NEBULA PROGENITORS

---

$M_*(M_\odot)$	RGB engulfment zone boundaries ( $R_\odot$ )				
	0.04	0.025	0.014	0.008	$Z_*$
1.5	426	395	346	297	252
1.6	383	365	320	273	230
1.7	329	324	282	236	198
1.8	262	270	232	187	155
1.9	187	204	171	129	97
2.0	125	144	110	75	75
2.1	75	73	75	77	75
2.2	75	77	79	77	75
2.5	79	84	82	80	77
3.0	86	90	88	86	84
5.0	170	155	150	142	138
8.0	376	331	305	288	271

Table 3.2: RGB engulfment zone boundaries for varying masses and metallicities and a  $1 M_J$  planet.

engulfment zone boundaries, respectively, as a function of mass, varies in accordance with the adopted metallicity. This relationship was noted in previous studies also (e.g., Kunitomo et al. 2011; Villaver et al. 2014). We do not observe the same engulfment zone boundaries as they do, however, due to the differing mass-loss rate coefficients employed and the inclusion of rotation in the models presented here (although, as demonstrated already, the effect of rotation is likely to be small).

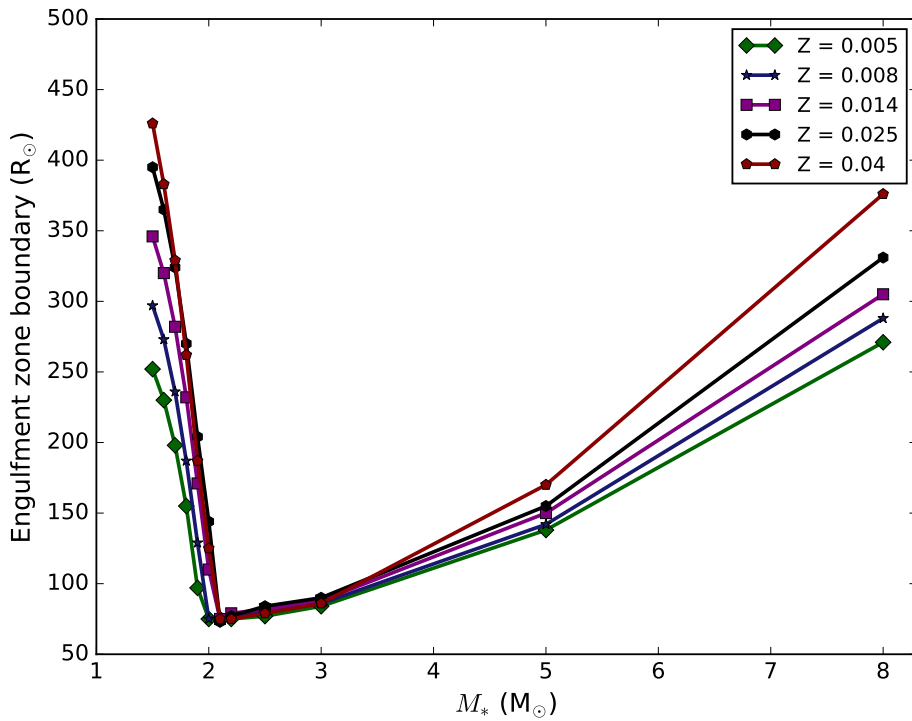


Figure 3.13: RGB engulfment zone boundaries for varying stellar masses and metallicities and a  $1 M_J$  planet.

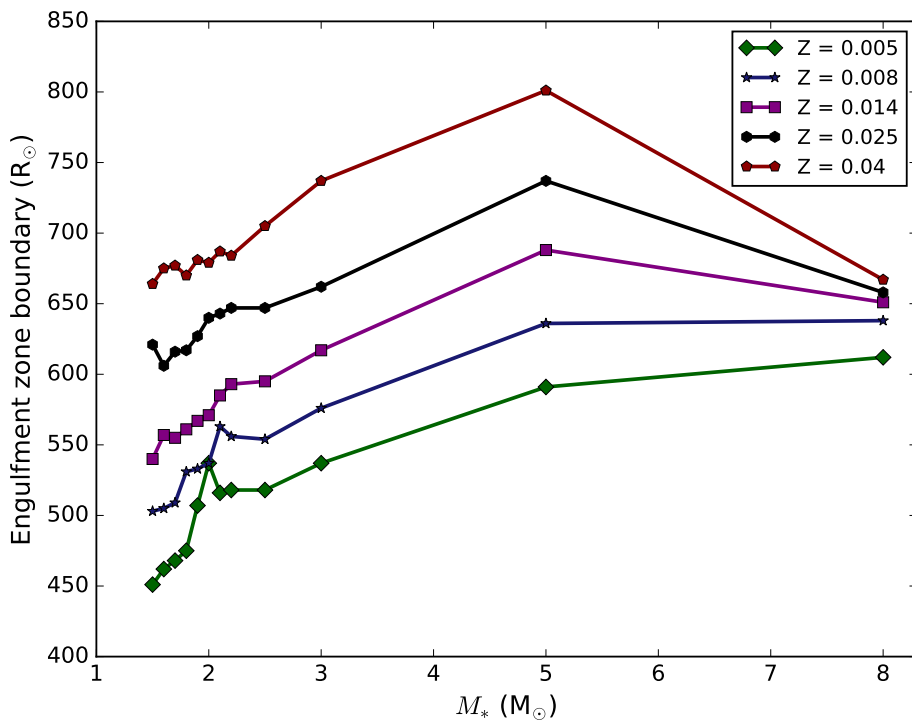


Figure 3.14: AGB engulfment zone boundaries for varying stellar masses and metallicities and a  $1 M_J$  planet.

$M_*$ ( $M_\odot$ )	AGB engulfment zone boundaries ( $R_\odot$ )					
	$Z_*$	0.04	0.025	0.014	0.008	0.005
1.5	664	621	540	503	451	
1.6	675	606	557	505	462	
1.7	677	616	555	509	468	
1.8	670	617	561	531	475	
1.9	681	627	567	533	507	
2.0	679	640	571	537	537	
2.1	687	643	585	563	516	
2.2	684	647	593	556	518	
2.5	705	647	595	554	518	
3.0	737	662	617	576	537	
5.0	801	737	688	636	591	
8.0	667	658	651	638	612	

Table 3.3: AGB engulfment zone boundaries for varying masses and metallicities and a  $1 M_J$  planet.

## 3.4 Summary and conclusions

In this chapter, the `SIMSPLASH` Orbital mode was presented and used to explore the conditions for, and to calculate, the engulfment zones of planetary nebula progenitors. Noting the fact that the conditions required for planet engulfment are sensitive to the input physics and initial conditions of stellar models, `SIMSPLASH` was written to be easily modifiable and is capable of evolving stars using the pre-calculated stellar models from `MESA` and the `MIST` project of (Choi et al. 2016).

In the work presented here, the `MIST` stellar models were used in the orbital evolution of a range of star-planet systems to study the effects of rotation and initial composition of the host stars, in order to constrain the conditions under which planetary nebula progenitor stars will engulf massive planets. The effect of the low RGB mass-loss coefficient in the `MIST` models was also addressed by comparing with models with the typical mass-loss coefficients. A summary of the findings from the models presented is as follows:

- Engulfment zone boundaries are sensitive to star mass. The star mass is particularly

important around the mass that marks the transition from stars which develop electron degenerate helium cores and undergo the helium flash and those that do not. Stars which do develop electron degenerate helium cores, are more likely to engulf a planet on the RGB than on the AGB, since the RGB envelope is more luminous and extends to larger radii. Since on the AGB the orbit suffers the effects of strong mass-loss, the AGB engulfment zone boundary cannot therefore extend to larger values in comparison to the RGB, despite a much larger envelope. It was demonstrated briefly that since the mass which marks the transition from a star developing degeneracy, and stars that do not, is sensitive to the initial composition of the star, the resulting engulfment zone boundaries are also sensitive to the same effect, in accordance with previous findings in the literature.

- Engulfment zone boundaries are also sensitive to planet mass. Both the RGB and AGB engulfment zone boundaries shift to larger semi-major axes with increasing planet mass, with the overall width of the AGB engulfment zone increasing by a few percent. The effect this has on the PN progenitor star population depends on whether more massive planets are likely to be found close to, or far away, from their host stars, and so knowledge of the mass and semi-major axis distributions of exoplanets is important in determining the population of planetary nebulae which could have evolved through the engulfment of a massive planet.
- The effect of using a conservative value for the RGB mass-loss coefficient, as in the MIST stellar models, in comparison to the typically adopted mass-loss coefficient was demonstrated to have a large impact on the RGB engulfment zone boundary, in agreement with Villaver et al. (2014). Furthermore, the effect that a modest RGB mass-loss rate has on the extent of the AGB engulfment zone boundary was discussed. Since the star evolves to the AGB with more mass, the AGB envelope can extend to larger radii, extending the AGB engulfment zone boundary, meaning the planets farther out can be engulfed on the AGB. On the other hand, a modest mass-loss on the RGB translates to the strength of the tides extending to larger semi-major axes, effectively extending the RGB engulfment zone also. Whether or not a modest mass-loss coefficient on the RGB provides a more conducive environment for engulfment, and thus planetary nebula shaping, in comparison to the typically

adopted mass-loss coefficients, will largely depend on the semi-major axis and mass distributions of the planets.

- Upon investigating the effect of rotation in the models presented here, a disagreement was found between the direction of change in the RGB engulfment zone boundary to that of Privitera et al. (2016), who found that rotation increases the main sequence core mass to such an extent that it shifts the transition from a semi-degenerate core to a non-degenerate core, leading to a decrease in the RGB engulfment zone boundary. In the stellar models employed here, no such effect was observed. It was argued here that the discrepancy is caused by different rotational mixing efficiencies during the main-sequence, such that in the models used here the increase in core mass is just large enough to produce a noticeable change in luminosity at all stages in the evolution, but not large enough to change the thermal state of the core. Thus a new source of uncertainty in the tidal evolution modelling of star-planet systems, which include rotation, has been uncovered, since a higher rotational mixing efficiency in stellar models results in a more luminous and extended RGB phase in comparison to models with similar rotation frequencies and lower rotational mixing efficiencies.



# Chapter 4

## The engulfment probabilities of PN progenitors

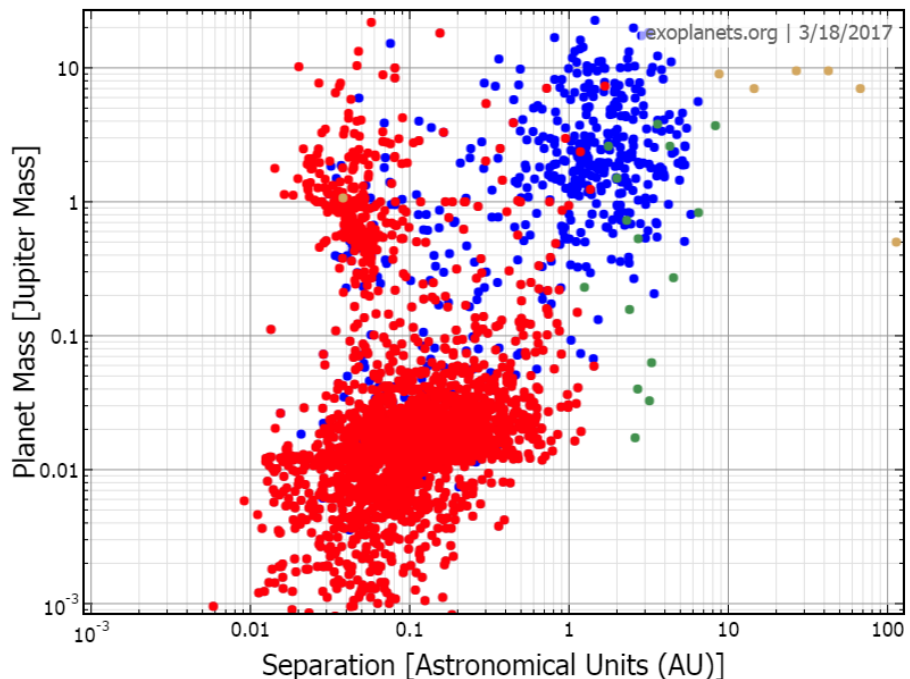


Figure 4.1: Separation (semi-major axis) vs. mass scatter plot of the known exoplanets including Kepler candidates as of 18/03/2017. Plot generated on exoplanets.org. Planets depicted in red are those which were discovered via the transit method, blue planets are radial velocity discoveries and those depicted in green are micro-lensing discoveries.

## 4.1 Introduction

Despite strong evidence for binarity as the origin of non-spherical PNe (e.g., Miszalski et al. 2009; Corradi et al. 2014; Jones et al. 2015; Hillwig et al. 2016), the period distribution of binary progenitor systems suggests that binary shaping is insufficient to account for the total population of non-spherical planetary nebulae (Raghavan et al. 2010) (See chapter 1 for a discussion). An encouraging idea, and that which is being investigated in this thesis, is that a proportion of the non-spherical population of PNe may be the result of the engulfment of a planet by the AGB progenitors of PNe. In this chapter a method to calculate the planet-fraction in populations of planetary nebula progenitors is demonstrated using the distributions of the known exoplanets and synthetic planet populations.

Since the first discovery of exoplanets in 1995 (Mayor & Queloz 1995), we have seen an explosion of exoplanet discoveries with nearly 3000 confirmed planets to date (see figure 4.1), with a further 2500 unconfirmed Kepler candidates<sup>1</sup>. The successes of exoplanet surveys have spurred an interest into many characteristics of exoplanet systems with an interesting and varied array of research ranging from the occurrence rates of hot-Jupiters and super-Earths, to the habitable zone and the search for extra-terrestrial life. Undeniably, the most pertinent exoplanet studies to the work presented in this thesis are the investigations into the dynamical evolution of planetary orbits in response to the post main-sequence evolution of the host star, and the subject of engulfment. Planet engulfment studies are often an attempt to explain seemingly unrelated phenomena such as lithium overabundance (Adamów et al. 2012; Reddy & Lambert 2016) and rapid rotation (Siess & Livio 1999; Carlberg et al. 2009; Privitera et al. 2016) in red giant branch stars, and also the formation of under-massive, single, helium white dwarfs (Nelemans & Tauris 1998). In a similar fashion to such studies, the first step to investigate planet-shaping in planetary nebulae was to determine the conditions which are favourable to planet engulfment around stars in the PN progenitor mass range, as was presented in chapter 3. With this knowledge in hand, it is now timely to investigate the population of PN progenitors with massive planets that will result in an engulfment, and thus shaping of the subsequent PN.

---

<sup>1</sup>From exoplanets.org.

Recently, Madappatt et al. (2016) conducted a study of tidal interactions on the orbital evolution of companions to PN progenitors with the aim of determining the fraction of post-common envelope binary central stars of PNe. While they determined the engulfment conditions for companions with masses as low as that of planets and brown dwarfs in their paper, they did not determine how planet engulfment, and shaping, could affect the population of PNe in their investigation. Nordhaus & Spiegel (2013) conducted a tidal model for planet engulfment with the known exoplanets at that time. However, they did not consider the effect of the adopted initial stellar metallicity in their models, nor did they attempt to infer the PN population from their findings. Up to now, the planet-fraction for planetary nebulae, based on the thorough treatment of tides in the evolution of planets around evolving stars and knowledge of the distribution of exoplanet systems, has not been attempted.

The aim of the work presented in this chapter is to determine the probabilities of PN progenitors engulfing massive planets on either the RGB or AGB, as a function of main sequence mass and metallicity. To do this, the Single-epoch population mode of SIMSPLASH was developed which contains tools to obtain, filter, evolve and analyse data of both the known exoplanets and synthetic planet populations. It is argued here that based on the knowledge of the currently known exoplanets, planet formation theories, and the conditions for planet engulfment, it is possible to calculate the probability of a star having a planet with the combination of mass and semi-major axis such that the planet will be engulfed. Furthermore, knowing the probability that a star will engulf a massive planet, it is shown how to determine an estimate on the fraction of star-planet systems in a population which will undergo an AGB engulfment, and thus lead to a non-spherical PN. In the following sections, the method to determine the probabilities of planet engulfment as a function of host-star mass and metallicity is demonstrated. From these probabilities the total number of main-sequence stars with planets currently in the galaxy, which would produce a non-spherical morphology from this scenario, is calculated.

## 4.2 SIMSPLASH in Single-epoch population mode: planet engulfment in a PN progenitor population

Beginning with a population of planets and their host stars, SIMSPLASH evolves each planet individually, according to the Orbital mode of SIMSPLASH presented in chapter 3, to determine the number of systems in a population with an engulfment on the RGB, AGB or no engulfment. In order for a planet engulfment to be the cause of PN shaping, the engulfment needs to take place during the AGB phase. The planet also needs to be capable of offering enough angular momentum to the star to induce shaping when it is engulfed. The required angular momentum to shape a PN is not calculated here. Rather, the aim is to predict how often such an engulfment, and thus shaping, scenario is likely to occur by considering the populations of planets orbiting PN progenitors. This is achieved by assuming that any AGB engulfment of a planet with mass,  $M_{\text{pl}}$ , larger than  $1 M_J$  can produce any shaping effect, either mild or severe. The first step in finding the planet-fraction of planetary nebulae is then to determine the probability of a star with mass  $0.8 M_\odot < M_* < 8 M_\odot$ , hosting a planet with  $M_{\text{pl}} > 1 M_J$ , within the range of semi-major axes where it will avoid an engulfment on the RGB and will be engulfed on the AGB. It is also important here to consider the stars which have planets within the RGB engulfment zone since there is speculation that the engulfment of a massive planet on the RGB can thwart the evolution of the host star, preventing the star from reaching the AGB phase and evolving to a PN (Nelemans & Tauris 1998; Bear & Soker 2011).

Upon the determination of the numbers of planets in a population being within the AGB and RGB engulfment zones, SIMSPLASH fits a regression model to the results and extracts the probabilities of a planet being within either engulfment zone as a function of host-star mass. The results are then combined with the occurrence rates of massive planets to determine the fraction of stars having and engulfing massive planets, which are then used to determine the planet-fraction of the PN progenitor population. In the following sections the various components of the Single-epoch population mode of SIMSPLASH are described in more detail.

### 4.2.1 Orbital evolution of planet populations

Single-epoch population mode employs the Orbital mode of SIMSPLASH for each star-planet system in a sample. See chapter 3 for information regarding the orbital evolution of star-planet systems and the stellar models employed.

There are currently two population options in the SIMSPLASH *Planets.Database* directory to experiment with: The Exoplanet Orbit Database and the synthetic planet populations provided by Shigeru Ida, both introduced briefly in chapter 2 and discussed further in the following sections.

#### The Exoplanet Orbit Database

The Exoplanet Orbit Database was described in chapter 2 (section 2.3). If the user specifies to calculate the planet-fraction using the known exoplanets, SIMSPLASH will check its *Planets.Database* for the *exoplanets.csv* file, which contains the entire Exoplanet Orbit Database. If the file does not exist, or if the existing version is older than 14 days, a more recent version will be downloaded, in order to keep account of future additions to the Exoplanet Orbit Database. Once the data is obtained SIMSPLASH is programmed to make cuts to only include systems where the planet mass, host star mass and semi-major axis are reported, and of those, only systems which are relevant to this research. It is also programmed to handle missing metallicity values and multi-planet systems in an appropriate way. The relevant data cuts and treatments are outlined below:

- **Planet mass**

The Exoplanet Orbit Database has a limit of  $\approx 24 M_J$  for the maximum mass of a planet (Han et al. 2014), which as the authors admit is likely a generous limit. SIMSPLASH adopts the International Astronomical Union value of  $13 M_J$  as the limiting mass for the differentiation between a planet and a brown dwarf, since this mass has been calculated as the minimum mass required for the fusion of deuterium in the core (Boss et al. 2007). On the other hand, since planet shaping of planetary nebulae requires a massive planet, only planets with  $M_{pl} > 1 M_J$  are included.

- **Host star mass**

Host star masses in the sample are rounded to the nearest  $0.1 M_\odot$ , since the stellar

models in `SIMSPLASH` range from  $0.8$  to  $8\text{ M}_\odot$  in increments of  $0.1\text{ M}_\odot$ . The largest host star mass in the Exoplanet Orbit Database is  $3.2\text{ M}_\odot$ . On the other hand, the lowest host star mass is  $\simeq 0.01\text{ M}_\odot$ . Since only planetary nebula progenitors are of interest in this study, only systems where the star mass was  $M_* > 0.75\text{ M}_\odot$  are kept in the sample (since these systems will be rounded up to  $0.8\text{ M}_\odot$ ).

- **Host star metallicity**

The effect of the host star metallicity on the orbital evolution and thus the RGB and AGB engulfment zone boundaries were demonstrated in chapter 3. Thus it is important to evolve the host star according to its reported metallicity. However, this requires an extensive grid of stellar models. While `SIMSPLASH` contains a reasonably well dispersed range of metallicities, it may not have the exact metallicity for each host star. For this reason, where applicable, host star metallicities are rounded to the nearest metallicity for which there is a stellar model available. Where the metallicity of the host star in the Exoplanet Orbit Database is unknown, the mean metallicity of the stars in the Exoplanet Orbit Database for the range of star-planet systems considered,  $Z = 0.017$ , is adopted. Host star metallicities are reported in the Exoplanet Orbit Database as [Fe/H], and are converted to  $Z_*$  using the following relationship

$$[\text{Fe}/\text{H}] = \log\left(\frac{Z_*}{Z_\odot}\right). \quad (4.1)$$

- **Systems with multiple planets**

The Orbital mode of `SIMSPLASH` is currently only capable of evolving two-body systems. Thus approximations need to be made in order to handle the population of multiple-planet systems. Firstly, it is assumed that systems in the Exoplanet Orbit Database which are marked as having multiple planets, but where only one planet remains after the planet mass cut is performed (that is, the other planets in the system have  $M_{\text{pl}} < 1\text{ M}_J$ ), can be treated as single planet systems.

Secondly, for the remaining multiple-planet systems, where two or more planets remain after the planet mass cut is made, the systems are separated from the full sample. `SIMSPLASH` then performs the orbital evolution for each planet and its host star as if it were a two-body system and then determines, for each host star, which

of the planets are engulfed and whether they are engulfed on the RGB or the AGB. Host stars with multiple-planet systems in which none of the planets are engulfed are added back to the full population as one system with no engulfment. In the case that more than one planet is engulfed for a given host star and at least one of those planets is engulfed on the RGB, SIMSPLASH counts the system as an RGB engulfment. Finally, systems where all planets are engulfed on the RGB or AGB are appropriately counted as a single planet system with an RGB or AGB engulfment.

- **Planets in binary star systems**

Since the Orbital mode of SIMSPLASH is currently only capable of evolving two-body systems, planets in a binary system are discarded from the sample. Furthermore since a planet in a binary system would be more likely to contribute to the binary-fraction of planetary nebulae, and the interest of this research is to determine the planet-fraction, the population of planets in binary systems is not of much interest here.

### Synthetic planet populations

Planet formation and evolution models were introduced in section 2.4.2. The synthetic models used in this work were provided by Shigeru Ida, and were generated with the Ida & Lin planet formation and evolution models. The planet populations used in this research were generated for star masses 0.8, 1.0, 1.5, 2.0, 3.0 and 5.0  $M_{\odot}$  in order to cover a wider range of PN progenitor masses than the host-stars of the known exoplanets. Further details on the ingredients involved in generating planet population models are provided in appendix A, and interested readers are encouraged to consult the Ida & Lin papers (Ida & Lin 2004a,b, 2005, 2008a,b, 2010; Ida et al. 2013).

For each star mass, there are 3000 disk systems, where each disk system corresponds to a single star having multiple planets with a range of masses and semi-major axes. SIMSPLASH performs the same mass cuts to the data as performed on the Exoplanet Orbit Database planets. With regards to treatment of multiple planet systems in the synthetic planet populations, SIMSPLASH evolves each planet separately as with the Exoplanet Orbit Database planets. However, the treatment of multiple planet systems in which there is both an RGB and AGB engulfment must be handled with care. On one hand there is

speculation that an RGB engulfment will prevent further evolution and thus cancel out any subsequent evolution and hence any AGB engulfment. On the other hand since it is intended that the engulfment probabilities calculated here will be used in a PN population synthesis, adopting this scenario while calculating the engulfment probabilities prevents the exploration of the PN population synthesis in the case where an RGB engulfment *does not* prevent subsequent evolution to the AGB phase, which is important since it is still unknown what effect a massive planet engulfment on the RGB can have. In order to avoid adopting this assumption in calculating the engulfment probabilities, multiple systems in which there is a combination of RGB, AGB and no engulfments, each system is counted as a single system evolving separately in the final population. By handling these systems in this way, these systems are naturally counted as inconclusive systems, which indeed they are.

Finally, it must be noted the disk properties used to generate planet populations for stars  $\gtrsim 3 M_{\odot}$  are not yet well understood and can only be obtained by an extrapolation of the mass dependence known for the relatively well understood T Tauri and Herbig Ae/Be stars. Furthermore, as discussed in section 2.4.2, planet formation models are strengthened by comparison to the observed distribution of exoplanets, of which there are currently no observations of planets orbiting stars above  $3.2 M_{\odot}$ . The synthetic planet population for the  $5 M_{\odot}$  stars is thus subject to uncertainty due to the uncertainties in the initial conditions (i.e., the proto-planetary disk properties) (Shigeru Ida, private communication).

### 4.2.2 The occurrence rates of massive planets

As discussed in chapter 2, there appears to be a strong correlation between the occurrence of massive planets and the mass and metallicity of their hosts. To determine the probability of a star having and engulfing a planet, the occurrence rates of massive planets as a function of host star mass and metallicity must be determined. The massive planet occurrence rate of Gaidos & Mann (2014) is adopted such that the fraction of stars having mass,  $M_*$ , and metallicity, [Fe/H], hosting a massive planet is given by

$$f_{\text{GP}}(M_*, [\text{Fe}/\text{H}]) = f_0 10^{a[\text{Fe}/\text{H}]} M_*^b, \quad (4.2)$$

where  $f_0$  is a constant estimated as 0.07. The factors  $a$  and  $b$  are the metallicity factor and the mass correlation parameter, respectively. Gaidos & Mann (2014) determined a value for  $a$  of  $1.80 \pm 0.31$  for FGK stars and assume  $b = 1$ . Figure 4.2 illustrates the relationship between the occurrence of massive planets and host star mass and metallicity. According to figure 4.2 the occurrence rates of massive planets for stars with masses of  $\approx 1 M_\odot$  ranges from just a few percent to around 60 percent depending on the metallicity. Intermediate mass stars with solar metallicity have an occurrence rate of  $\lesssim 10$  percent. While it is unknown, due to lack of observations for such, whether this occurrence rate holds for host star masses  $\gtrsim 1.5 M_\odot$ , it is assumed here that it can be extrapolated to higher masses. In order to avoid calculating a fraction larger than unity for higher star masses at the highest metallicities,  $f_{GP}$  is capped at 1.0 where applicable in calculations.

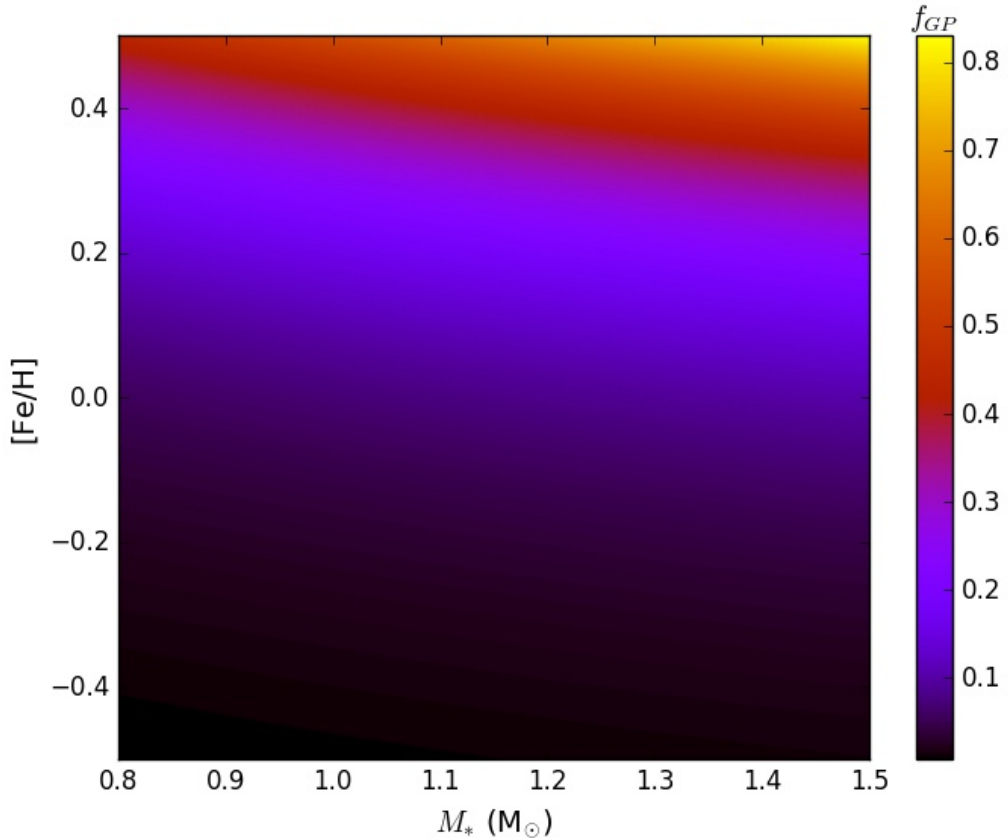


Figure 4.2: The occurrence rates of massive planets as a function of host star mass and metallicity plotted using the relationship of Gaidos & Mann (2014).

### 4.2.3 The probability of planet engulfment

In chapter 3 it was demonstrated that the engulfment zones are sensitive to stellar mass. Therefore, when calculating the planet-fraction, it would be ideal if the population of planet hosting PN progenitors were separated into mass bins in order to determine the fraction of stars in each bin that will engulf their planets. However, for both the known exoplanets and the synthetic planet populations described in the previous section, this treatment is not possible since there are only a few observations in each mass bin for the known exoplanets, and there are only six synthetic planet populations available (one population for each host star mass).

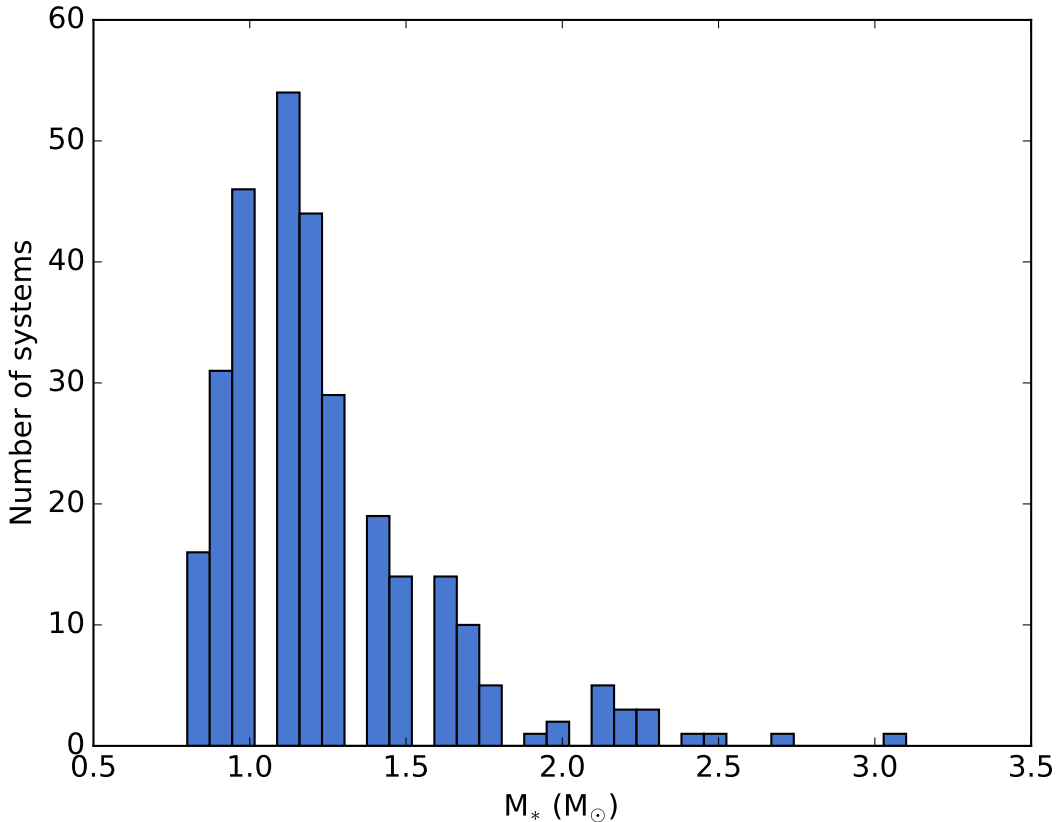


Figure 4.3: Histogram of host star masses from the Exoplanet Orbit Database sample.

Figure 4.3 shows the histogram of masses of the planet hosting stars in the reduced exoplanet sample. Obviously, there is a large inconsistency of sample sizes for the various mass bins, where the mean star mass in the sample is  $1.2 M_\odot$  and a standard deviation of is  $0.3 M_\odot$ . Thus determining the fraction of stars engulfing their planets of any star mass

is not possible by binning the data according to host star mass. In order to determine the fraction of stars engulfing planets then, a simple logistic regression is performed on the known exoplanet engulfment data in order to compute the probabilities of engulfment (for both the RGB and AGB) across all star masses. Using the star mass as the input variable, SIMSPLASH utilises the PYTHON package SCIKIT-LEARN to fit the logistic regression model to the results of the orbital evolution of the known exoplanets and the synthetic planet populations and thus computes the probabilities for both RGB and AGB engulfment in massive planet hosting stars (denoted as  $P_{\text{RGB}}$  and  $P_{\text{AGB}}$ , respectively).

Logistic regression is a generalised linear model and is a similar statistical procedure to the well-known, and widely used, linear regression, but rather than predicting a continuous, normally distributed response variable, given an input variable,  $X$ , the logistic regression predicts the probability that the input variable belongs to a particular category,  $Y$ , by utilising the logistic function

$$\ln\left(\frac{p(Y)}{1 - p(Y)}\right) = \beta_0 + \beta_1 X, \quad (4.3)$$

where  $p(Y)$  is the probability that the outcome is in the category  $Y$ , for a given input  $X$ . The values  $\beta_0$  and  $\beta_1$  are obtained by maximising the log-likelihood of the binomial distribution, and determines the best fitting model between the input variable (star masses) and the observed outcomes (a planet is engulfed on the RGB/AGB or it is not). The probabilities of engulfment as a function of star mass can then be extracted from the model. Interested readers can consult a recent series of papers by de Souza et al. (2016) describing the logistic regression method and its potential for astronomical statistical inference, and explains that while it is often over-looked in astronomy it is a powerful technique for classification and prediction. It should be noted that, since there are three possible outcomes (the RGB engulfment zone, AGB engulfment zone or a safe semi-major axis), this is technically a multinomial problem. However, the problem is easily separated into two *one-vs.-all* (e.g., AGB engulfment zone vs. all other outcomes) logistic regression models; one for the probabilities associated with the RGB engulfment zone and one for the AGB engulfment zones.

#### 4.2.4 The distribution of stellar masses

The Kroupa (2001) IMF is employed in this chapter to determine the number of stars in each mass bin, which are calculated in `SIMSPLASH` by utilising the built-in `LIBIMF` initial mass function library of Pflamm-Altenburg & Kroupa (2006). Other forms of the IMF exist and are available for use in this library, such as that of Chabrier (2003), and can be selected in the Single-epoch population mode of `SIMSPLASH`. However, for the purpose of exploring the present-day PN progenitor population and the associated planet-fraction in this chapter, the Kroupa (2001) IMF is sufficient, since the main objective is to calculate the probabilities of planet engulfment on which the IMF does not have any effect.

### 4.2.5 Determination of the planet-fraction of the planetary nebula progenitor population

By utilising the methods described throughout the previous sections, the current population of PN progenitors and the respective fraction of stars engulfing planets on the RGB and AGB is calculated to gain a general understanding of the populations that the current population of PNe evolved from. Given the total mass,  $M_T$ , locked up in stars in the population of interest (e.g., the present-day Milky Way) SIMSPLASH determines the number of stars,  $N_T$ , and the distribution of their masses according to the stellar binary-fraction and the Kroupa (2001) IMF. The Raghavan et al. (2010) stellar binary-fraction ( $f_B$ ) of 50% for FGK stars is adopted as representative of the entire population.

Consider the total population of PN progenitors,  $N_T$ , obtained by normalising the IMF to the total mass of the entire stellar population. To get the total number of PN progenitor *systems*, each star in a binary system counts as a one star in  $N_T$ , such that the number of *stars* in binary systems is  $N_B = 0.67N_T$ , and the total number of stars in single systems is  $N_S = 0.33N_T$  (since the stellar binary-fraction is taken as 50%). The total number of systems in the PN progenitor population is then

$$N_{\text{syst}} = (N_B/2) + N_S. \quad (4.4)$$

In the same way, the number of stars in a particular mass bin is  $N_i [M_i, M_i + dM]$  (where the subscript  $i$  denotes the bin), and the number of PN progenitor systems is

$$N_{i,\text{syst}} [M_i, M_i + dM] = (N_{i,B} [M_i, M_i + dM]/2) + N_{i,S} [M_i, M_i + dM], \quad (4.5)$$

where, just as before,  $N_{i,B} = 0.67N_i [M_i, M_i + dM]$  and  $N_{i,S} = 0.33N_i [M_i, M_i + dM]$ .  $dM$  is taken to be  $0.1 M_\odot$  in order to split the population of stars into sufficiently small mass bins to combine with the fraction of stars of a given mass engulfing planets.

For binary PN progenitor systems in each mass bin it is taken that  $\simeq 28\%$  of binaries have orbital separations of  $a \lesssim 3$  AU and thus interact on the RGB (denoted as  $N_{i,B(\text{RGB})}$ ),  $\simeq 32\%$  have a separation of  $3 \lesssim a \lesssim 30$  AU, resulting in a strong interaction the AGB, ultimately shaping the PN (denoted as  $N_{i,B(\text{AGB})}$ ), and the remaining binaries do

not interact at all, leading to a spherical PN (following the prescription from De Marco & Soker 2011). It is noted that symbiotic binary systems in which the planetary nebula of the primary has already dissipated and the Mira-type secondary (D-type symbiotic systems) can interact (even at very wide separations with periods of hundreds of years) to produce non-spherical morphologies, the resulting nebulae are classified as symbiotic nebulae rather than PNe and so it is reasonable to neglect them from the population of PNe resulting from binary interactions in this work since they are not included in PN morphological surveys (see e.g., Parker et al. 2006, for a discussion of the contaminants removed from PN classification surveys). In this work it is taken to be true that a binary RGB interaction will prevent the formation of a PN (see, e.g., Han et al. 2002; Bear & Soker 2011, for a discussion on how binary interactions can cause extreme enhanced mass-loss and thus prevents PN formation).

The number of single stars in a mass bin, with planets of mass  $M_{\text{pl}} > 1M_J$  and within the RGB and AGB engulfment zones of those stars are given by the following two equations, respectively

$$N_{i,\text{Pl(RGB)}} [M_i, M_i + dM] = N_{i,S} [M_i, M_i + dM] \times f_{i,\text{GP}} f_{i,\text{RGB}} \quad (4.6)$$

$$N_{i,\text{Pl(AGB)}} [M_i, M_i + dM] = N_{i,S} [M_i, M_i + dM] \times f_{i,\text{GP}} f_{i,\text{AGB}} \quad (4.7)$$

where  $f_{i,\text{GP}}$  is the occurrence rate of massive planets as a function of  $M_i$  and  $[\text{Fe}/\text{H}]$  described in the previous section.  $f_{i,\text{RGB}}$  and  $f_{i,\text{AGB}}$  are obtained from the probability distributions described in section 4.2.3 (assuming the fraction of AGB/RGB engulfments can be approximated as the probability, i.e.,  $f_{\text{RGB/AGB}} \equiv P_{\text{RGB/AGB}}$ ). While stars with planets within the RGB engulfment zone will not result in non-spherical planetary nebulae it is important to consider them as there is speculation that an engulfment scenario can alter the subsequent evolution of the star. A planet engulfment or a binary interaction on the RGB might be capable of effectively enhancing mass-loss to such an extent that it loses most of its envelope (Nelemans 2010; Bear & Soker 2011), the result being that the star cannot evolve to the AGB which in turn prevents the formation of the planetary nebula. In such an event it would instead evolve as an extreme horizontal branch star, eventually becoming a helium white dwarf (e.g., Dorman et al. 1993). However, it is still uncertain to what extent this is accurate for planets. For this reason, the planet-fraction is calculated

both with RGB planet engulfment considerations and without (in which case an engulfment on the RGB is treated as if the star evolves normally as a single star). The total number of PN progenitors with planets within the RGB and AGB engulfment zones is thus obtained by summing across all PN progenitor masses.

The resulting *non-spherical* PN population can be broken up into systems which are shaped by binary interactions during the AGB, and systems which are shaped by planet engulfment on the AGB. Single stars without planets in the engulfment zone and binary stars with a separation that is too large for any shaping to occur are considered here to evolve as single-star systems and result in spherical PNe (denoted by  $N_{i,Sph}$ ). Considering again the full population of stars that make PNe, after summing across all masses, the total number of PN progenitors in the present-day population is then comprised of .

$$N_{\text{prog}} = \sum_i^k (N_{i,\text{Pl(AGB)}} + N_{i,\text{B(AGB)}} + N_{i,\text{Sph}} + N_{i,\text{pl(RGB)}}), \quad (4.8)$$

where  $k$  is the number of mass bins. When considering the case in which a planet engulfment on the RGB alters the stars evolution and prevents the PN,  $N_{i,\text{Pl(RGB)}}$  is simply taken to be zero in equation 4.8.

By making the, albeit very simplified, approximation that the present-day population of PN progenitor stars is a good representation of the population from which the present-day population of PNe evolved from, then the planet-fraction,  $f_{\text{planet}}$ , and the binary-fraction,  $f_{\text{binary}}$ , of planetary nebulae are estimated by

$$f_{\text{planet}} = \frac{\sum_i^k N_{i,\text{Pl(AGB)}}}{N_{\text{prog}}}, \quad (4.9)$$

$$f_{\text{binary}} = \frac{\sum_i^k N_{i,\text{B(AGB)}}}{N_{\text{prog}}}, \quad (4.10)$$

respectively, and their sum is taken as equal to the total fraction of non-spherical PNe. Finally, the total number of non-spherical PNe is simply  $N_{\text{Pl(AGB)}} + N_{\text{B(AGB)}}$ , and so the fraction of the non-spherical PN population as a result of shaping by planets,  $f_{\text{NS(Pl)}}$  is

$$f_{\text{NS(Pl)}} = \frac{\sum_i^k N_{i,\text{Pl(AGB)}}}{\sum_i^k N_{i,\text{Pl(AGB)}} + N_{i,\text{B(AGB)}}}. \quad (4.11)$$

## 4.3 Results: The planet-fraction of PN progenitor populations

### 4.3.1 The PN progenitor star population

In order to calculate the planet-fraction of PN progenitors, it is necessary to first calculate the number of PN progenitors in total in a population, and also the number of single and binary star progenitor systems. This was obtained by normalising the IMF to the total luminous galactic mass (see, e.g., Moe & De Marco 2006). Adopting a total luminous galactic mass,  $M_T^{\text{MW}}$ , of  $7.5 \times 10^{10} \text{ M}_\odot$  (see, e.g., Dehnen & Binney 1998) yields  $1.3 \times 10^{11}$  stars in the Milky Way according to the (Kroupa 2001) IMF. As discussed in section 4.2.4, binary systems count as two stars and single stars count as one star, so this results in  $8.6 \times 10^{10}$  progenitor systems, of which  $4.3 \times 10^{10}$  are binary systems and the same number are single-star systems (a 50% progenitor binary-fraction). These values are summarised in table 4.1.

$M_T^{\text{MW}}$	$N_T^{\text{MW}}$	$N_{\text{syst}}^{\text{MW}}$	$N_S^{\text{MW}}$	$N_B^{\text{MW}}$	$f_{\text{PN}}^{\text{MW}}$
$7.5 \times 10^{10} \text{ M}_\odot$	$1.3 \times 10^{11}$	$8.6 \times 10^{10}$	$4.3 \times 10^{10}$	$4.3 \times 10^{10}$	12.3%

Table 4.1: Calculation summary for the total mass and number of stars currently in the galaxy according to adopting a total luminous galactic mass of  $7.5 \times 10^{10}$ . The superscript *MW* is to denote that this is for all stars across all masses in the Milky Way. 12.3% of stars have masses in the PN progenitor mass range.

$M_T$	$N_T$	$N_{\text{syst}}$	$N_S$	$N_B$
$2.9 \times 10^{10} \text{ M}_\odot$	$1.6 \times 10^{10}$	$1 \times 10^{10}$	$5 \times 10^9$	$5 \times 10^9$

Table 4.2: Results summary for the present-day PN progenitor population and its respective numbers of systems.

12.3% of all stars will have masses in the PN progenitor mass range. Table 4.2 presents a summary of the PN progenitor population calculated using the IMF. The total mass of stars in the PN progenitor mass range,  $M_T$ , and the total number of PN progenitor stars in the Milky Way,  $N_T$ , is  $2.9 \times 10^{10} \text{ M}_\odot$  and  $1.6 \times 10^{10}$  stars, respectively. This results in

a total of  $\simeq 1 \times 10^{10}$  PN progenitor systems currently in the Milky Way. Adopting this information and combining it with the analysis outlined in the previous section allows us to determine the planet-fraction of PN progenitors in the following.

### 4.3.2 The PN progenitor planet-fraction from the known exoplanets

The Exoplanet Orbit Database was accessed with `SIMSPLASH` on the 25/06/2017 and contained a total of 5287 planets orbiting 4345 stars. After the appropriate cuts were made to the data (see section 4.2.1 for details), the sample consisted of 300 star-planet systems and a further 56 planets in multiple planetary systems. Each planet flagged as being in a multiple planet system was first evolved with the Orbital mode and either discarded or kept according to the criteria in section 4.2.1. Figure 4.4 shows the distribution of planet masses and semi-major axes of all 356 planets. Planets in multiple systems are shown in red in figure 4.4 to denote that they may or may not be removed from the sample later, depending on the orbital evolution of each planet in the system.

The MIST stellar models of Choi et al. (2016), with rotation turned on, are adopted for this analysis and the known exoplanet population is evolved firstly using the measured metallicity corresponding to each host star. Secondly, in order to determine the effect of evolving the entire population using a single metallicity for each host star (for example the mean metallicity of the sample), the known exoplanets are also evolved with stellar models of the five different metallicities available in `SIMSPLASH`. Table 4.3 presents the number of engulfments corresponding to the population being evolved with each available metallicity.

Each star-planet system in the exoplanet orbit database was first evolved with an initial stellar metallicity corresponding to the measured metallicity of the host-star (rounded to the nearest metallicity model available in `SIMSPLASH`). The remaining planet sample, after the cuts described in the previous section were made, was evolved with the Orbital mode of `SIMSPLASH`. After taking the multiple planet systems into account according to their engulfment as described in section 4.2.1, the final sample consisted of 327 star-planet systems (300 data points with a single planet, and a further 27 which were in multiple planet systems), where 262 planets were found to be in the RGB engulfment zone of their host, 37 in the AGB engulfment zone, and 28 were at a safe semi-major axis.

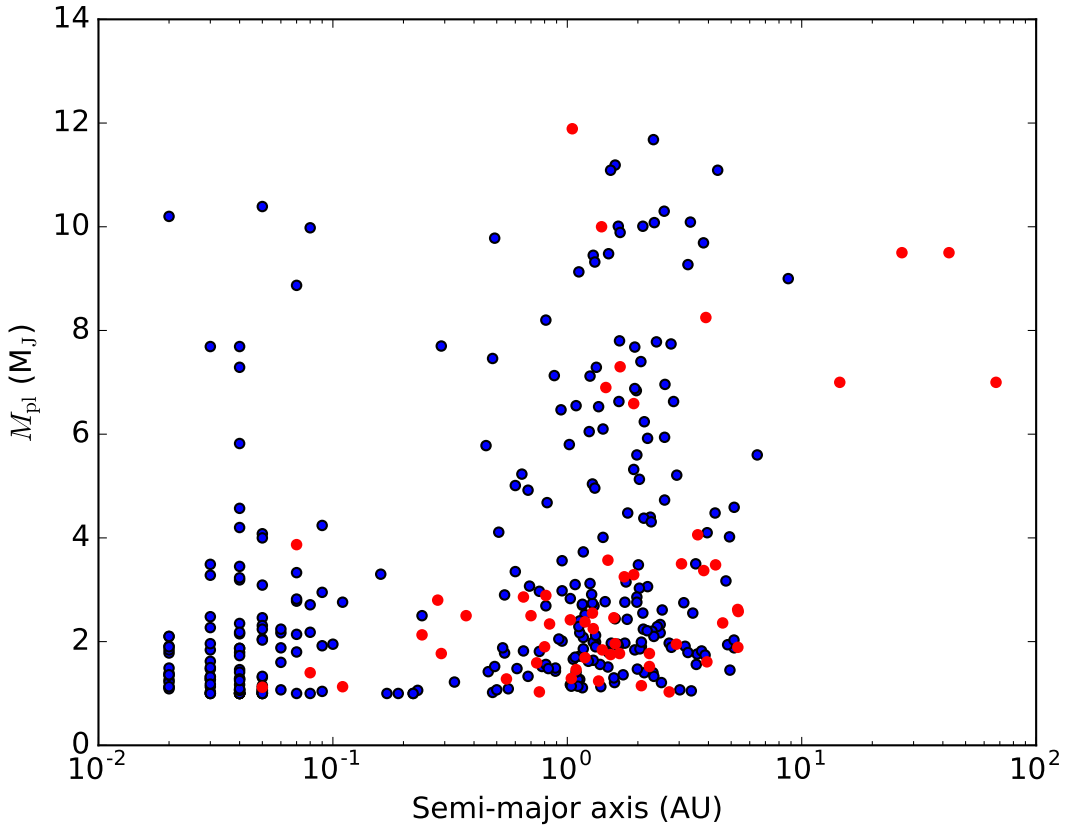


Figure 4.4: Semi-major axis vs. mass scatter plot of the known exoplanets from the Exoplanet Orbit Database, after mass cuts were made to the data. Planets in multiple systems are shown in red to denote that some of them may be removed from the sample later, depending on which planets in those systems are engulfed.

Figure 4.5 shows the number of planets in the respective engulfment zones as a function of host star mass when evolved with an initial metallicity according to the (rounded) measured host star metallicity. It appears that higher mass stars are more likely to host a massive planet within the AGB engulfment zone than lower mass host stars, which isn't particularly surprising given that in chapter 3 (section 3.3.1) we saw that the RGB engulfment zone is much larger than the AGB engulfment zone for the  $1 M_\odot$  star in contrast to the  $1.5 M_\odot$  star which had a significantly larger AGB engulfment zone. However this is also likely to be a result of the observational bias inherent in the radial velocity method - close-in massive planets around solar mass stars are the easiest to find, and so they contaminate the sample with planets which will be engulfed during the RGB. However, it is still interesting to investigate the probability of a star engulfing a massive planet based on these results, keeping in mind that the following methods may need to be replicated,

$Z_*$	$N_{\text{SAMPLE}}$	$N_{\text{AGB}}$	$N_{\text{RGB}}$	$N_{\text{SAFE}}$
$Z_{\text{host-star}}$	327	37	262	28
0.005	327	58	224	45
0.008	327	41	243	43
0.014	327	38	256	33
0.025	327	34	266	27
0.04	327	30	271	26

Table 4.3: Population engulfment results summary for the known exoplanets population evolved with the five metallicity grids of stellar models employed and also the population as evolved with the measured metallicity of the host-star ( $Z = Z_{\text{host-star}}$ ).

and the results updated in future, as the sample of exoplanets becomes more complete in terms of larger semi-major axes and host-star masses.

To quantify the results displayed in figure 4.5 further, a logistic regression is fit to the population engulfment data in order to compute the probability of a star engulfing a massive planet as a function of its mass. The logistic regression is performed within `SIMSPLASH` by utilising the `PYTHON` package `SCIKIT-LEARN` which computes the probabilities by estimating the parameters in equation 4.3 using maximum likelihood estimation techniques. The purple curve in figure 4.6 displays a plot of the computed probabilities of an RGB engulfment as a function of host star mass. In order to estimate the confidence intervals and thus gauge the goodness of fit, the data was bootstrapped and the logistic regression was fit to each subset of the data. The bootstrapped models are also plotted in figure 4.6 (the grey shaded regions) and the 95% confidence intervals are shown as the dashed black lines. As expected from looking at 4.5, the probability of an RGB engulfment decreases with increasing host-star mass. These probabilities assume that the star has a planet in the first place, however. Thus, in order to determine the probability of a star *having and* engulfing a massive planet, the probability of engulfment is multiplied by the massive planet occurrence rates calculated using the relation of Gaidos & Mann (2014) in equation 4.2, and adopting the mean metallicity of the sample. The resulting probabilities of stars having and engulfing a massive planet are also plotted in figure 4.6 (the dark blue curve).

Similarly, the purple curve in figure 4.7 displays the plotted probabilities of a star engulfing a massive planet on the AGB (assuming the star has a massive planet in the first

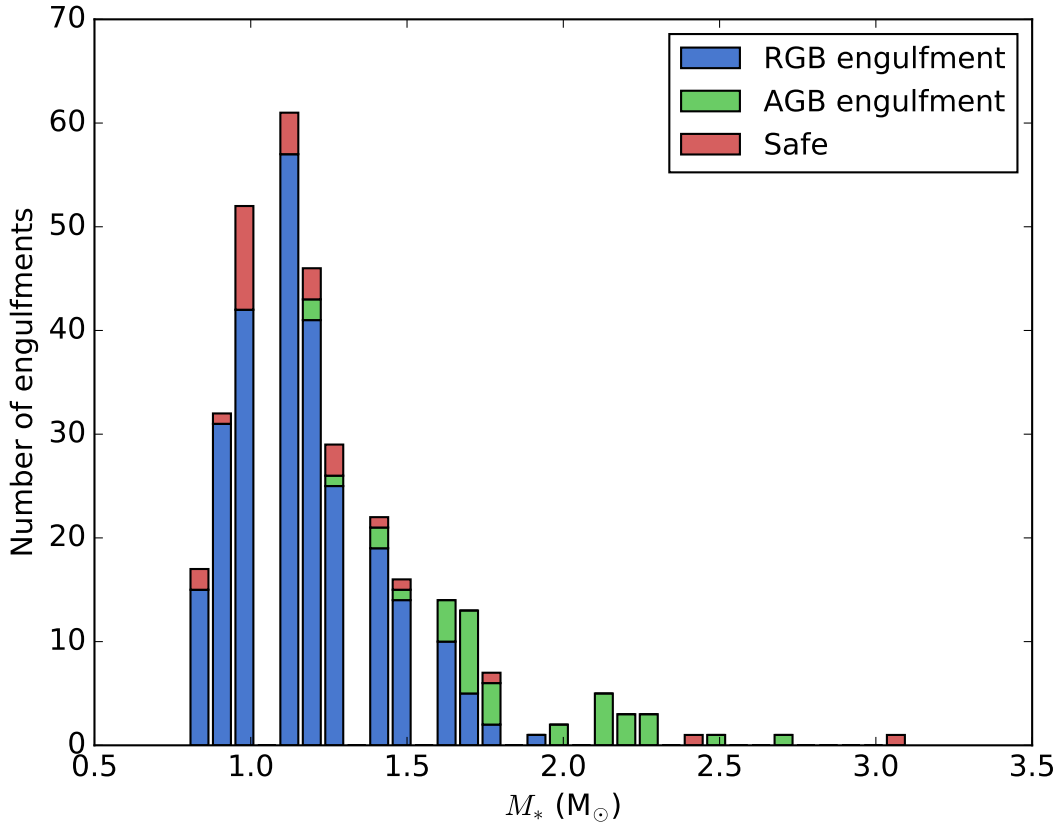


Figure 4.5: Histogram displaying the resulting number of planet engulfment of the known exoplanets as a function of stellar mass. In this model, each star-planet system is evolved using stellar models with the measured metallicity of the host star.

place) and the purple curve in the same figure is a plot of the probabilities of a star *having and engulfing* a massive planet, respectively, as a function of host star mass. As before, the grey shaded regions in figure 4.7 represent the bootstrapped models and the dashed black lines represent the bounds of the 95% confidence limits. Perhaps unsurprisingly, the confidence intervals for the engulfment probabilities increase as the host star mass increases. This is due to the known exoplanets small sample size, particularly for intermediate mass stars. Nonetheless, the computed probabilities agree with figure 4.5; as the host star mass increases, so too does the probability of an engulfment on the AGB.

To determine the planet-fraction, the IMF and the information provided in table 4.2 was employed to split the population of planetary nebula progenitors in the galaxy into mass bins of  $0.1 M_\odot$  and calculate the number of stars in each bin, as in equations 4.6 and 4.7. By combining the number of single stars in each mass bin with the respective probabilities of planet engulfment as a function of star mass in figures 4.6 and 4.7, the number

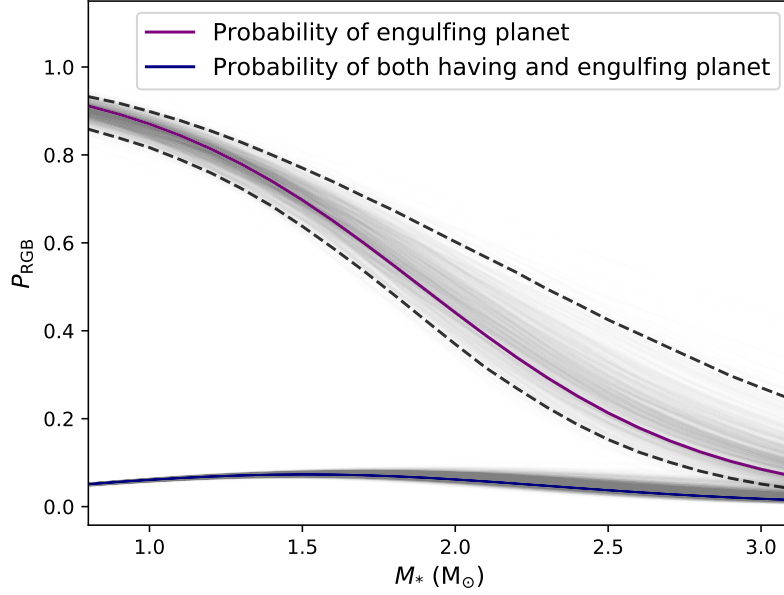


Figure 4.6: The probabilities of massive planet engulfment on the RGB as a function of star mass from the known exoplanets and adopting the measured metallicities of the host stars, fit with a logistic regression. The purple curve represents the probability of engulfment of a massive planet assuming the star has a planet in the first place. The dark blue curve represents the combined probability of a star both having and engulfing a planet, by adopting the massive planet occurrence rate of Gaidos & Mann (2014) with a mean metallicity of  $Z_* = 0.014$  in equation 4.2. The grey shaded regions represent the bootstrapped models and the dashed black lines represent the bounds of the 95% confidence limits.

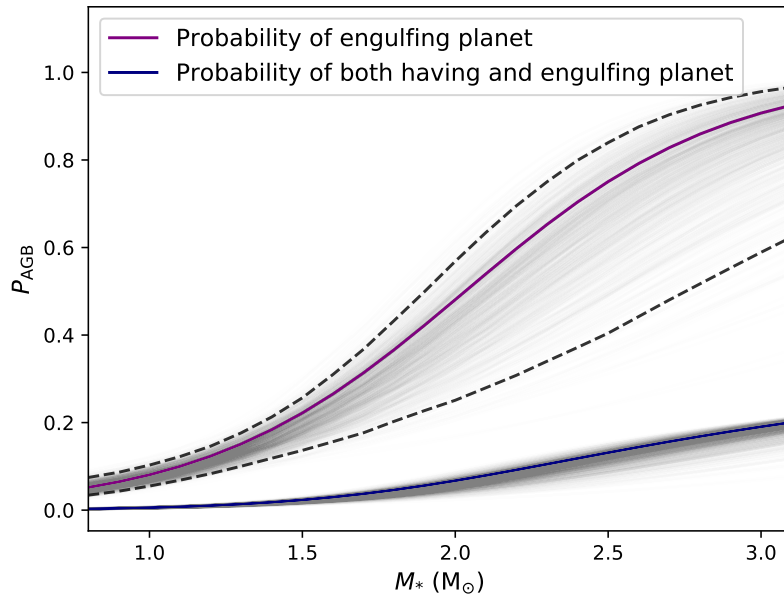


Figure 4.7: Same as figure 4.6, but for the probabilities of engulfment on the AGB.

of RGB and AGB planet engulfs in each bin, along with the number of binary interactions and stars evolving as single systems as described in section 4.2.5, were computed. The probabilities of engulfment for star masses above  $3.1 M_{\odot}$  were simply taken to be the same as for  $3.1 M_{\odot}$ , since no data exists for planets around stars in this mass range to date. The planet-fraction, the binary-fraction and the fraction of stars which will evolve to a spherical PN were then obtained, by summing all bins and using equations 4.8 to 4.11. These results are summarised in tables 4.4 and 4.5. This analysis was performed assuming that a planet engulfment interaction on the RGB can prevent the star from ever becoming a planetary nebula, and also without that assumption. However, while the total number of PNe is shifted downwards by this assumption, the resulting planet, binary and spherical fractions remained relatively unchanged ( $< 0.01$  difference) and so they are not reported in the table.

	$N_{\text{prog}}$	$\sum_i^k N_{i,\text{Pl(AGB)}}$	$\sum_i^k N_{i,\text{Pl(RGB)}}$	$\sum_i^k N_{i,\text{B(AGB)}}$	$\sum_i^k N_{i,\text{Sph}}$
(Excl. RGB planet engulfment)	$8.9 \times 10^9$	$2.6 \times 10^8$	$2.8 \times 10^8$	$1.7 \times 10^9$	$6.9 \times 10^9$
(Incl. RGB planet engulfment)	$9.1 \times 10^9$				$7.1 \times 10^9$

Table 4.4: The resulting PN progenitor population numbers when adopting the probabilities of engulfment according to the known exoplanets evolved with stellar models according to the measured metallicity of each host star. Where  $N_{\text{prog}}$ ,  $\sum_i^k N_{i,\text{Pl(AGB)}}$ ,  $\sum_i^k N_{i,\text{Pl(RGB)}}$ ,  $\sum_i^k N_{i,\text{B(AGB)}}$  and  $\sum_i^k N_{i,\text{Sph}}$  respectively refer to the total number of PN progenitors, the total number of PN progenitors expected to engulf planets on the AGB and RGB, the total number expected to have a binary interaction on the AGB and the total number expected to evolve as single systems to form spherical PNe.

$f_{\text{planet}}$	$f_{\text{binary}}$	$f_{\text{single}}$	$f_{\text{NS}}$	$f_{\text{NS(PI)}}$
0.03	0.19	0.78	0.22	0.14

Table 4.5: The resulting PN progenitor population proportions when adopting the probabilities of engulfment according to the known exoplanets evolved with stellar models according to the measured metallicity of each host star. The planet and binary fractions of PN progenitors are denoted as  $f_{\text{planet}}$  and  $f_{\text{binary}}$ , respectively, while the fraction of PN progenitors which will evolve as single stars to form spherical PNe (i.e., single stars without a planet engulfment, and binary systems which do not interact) is denoted as  $f_{\text{single}}$ . The predicted fraction of non-spherical PNe,  $f_{\text{NS}}$  is 22%, of which 14% of the non-spherical population are expected to be the result of a planet engulfment ( $f_{\text{NS(PI)}}$ ).

According to the distribution of the known exoplanets then, the fraction of PN progenitor stars which will engulf a planet on the AGB is only around 3%. However, if planet engulfment and binary interactions are responsible for all non-spherical planetary nebulae, this means that  $\simeq 15\%$  of all *non-spherical* PNe evolving from a population similar to the current PN progenitor population of the Milky Way would be shaped by planets. This is a non-negligible proportion, particularly considering that 80% of the observed population of PNe are non-spherical. Accordingly, one should expect that of the observed non-spherical population of PNe,  $\simeq 11\%$  would have been shaped by planet engulfment and 69% shaped by binary interactions. This still does not account for the discrepancy between the observed non-spherical and spherical fractions and those calculated to evolve via single-star evolution. However, as stated previously, the current sample of the known exoplanets is incomplete for intermediate mass stars and biased towards close-in planets, so this analysis will need to be repeated in the future as the sample of the known exoplanets is updated, particularly with the promising capabilities of the ongoing Gaia mission which is expected to uncover thousands of massive planets orbiting intermediate mass stars out to wider semi-major axes (Perryman et al. 2014). Fortunately, as the sample of the known exoplanets becomes more complete, repeating the above experiment in the future will be a relatively efficient process now due to the development of SIMSPLASH.

Recalling from chapter 3, it was demonstrated that the effect of host-star metallicity on the maximum radius reached by the stars, and thus both the RGB and AGB engulfment zone boundaries, was substantial. In order to demonstrate the effect of the adopted host-star metallicity for each star-planet system over an entire population, the number of engulfs were calculated again, but this time by evolving each star-planet system in the population with a common metallicity rather than that which was reported in the Exoplanet Orbit Database. Each of the five different metallicities available in SIMSPLASH were adopted, and thus five population models were calculated in the same way as described previously.

As before, the number of engulfs in the population resulting from the orbital evolution models, for each of the five different stellar metallicity models, were fit with a logistic regression to determine the probabilities of stars engulfing a planet on either the RGB or AGB as a function of host-star mass. The probabilities from the five regression models were then interpolated with respect to metallicity to compute a finer grid of en-

gulfment probabilities as a function of both mass and metallicity. The resulting grids were then combined with the occurrence rates of massive planets of Gaidos & Mann (2014) to determine the probability of having and engulfing planets, for all metallicities between 0.005 and 0.04. The probabilities of having and engulfing planets on the RGB and AGB, as a function of mass and metallicity, are plotted in figures 4.8 and 4.9, respectively.

Inspecting figures 4.8 and 4.9 reveals that the overall range of probabilities of RGB engulfs are lower than that of AGB engulfment. This may seem counter intuitive at first considering that in all models, the number of RGB engulfs are much higher than the number of AGB engulfs (table 4.3). However this can be explained by again considering the distribution of engulfs in figure 4.5 and also the Gaidos & Mann (2014) occurrence rates of massive planets. The majority of RGB engulfs in the sample lay within the  $\simeq 0.8$  and  $1.2 M_{\odot}$  host-star mass bins in the histogram. According to figure 4.2, the occurrence rates of massive planet of stars in this mass range for all metallicities are very low, but particularly at low metallicities where the occurrence rate is less than 10%. Since the occurrence rates of massive planets for low mass host stars and metallicities never exceeds 50-60%, the probability of a star having and engulfing a planet on the RGB remains below 60%. On the other hand, since the majority of AGB engulfs are by stars with masses  $\gtrsim 1.2 M_{\odot}$ , and the occurrence rates of massive planets in this host-star mass range is much higher, the range of probabilities of a star having and engulfing a planet on the AGB reflects this.

Clearly, the probability of having and engulfing a planet for a given mass varies largely depending on the mean metallicity of stars in a population, demonstrating that high metallicity environments are more conducive for planet shaping of planetary nebulae. Indeed performing the analysis on the PN progenitor population described previously, the results of which are displayed in tables 4.6 and 4.7, we see the planet-fraction ranges between  $\simeq 1\% - 13\%$  for the low and high metallicity models, respectively. Furthermore, because the numbers of RGB engulfs increases dramatically for low-mass stars with increasing metallicity, the relative numbers of PN progenitors in the population decreases. Finally, the effect of adopting a metallicity of  $Z_* = 0.014$  vs.  $Z_* = 0.025$  for the mean metallicity of planet-hosting stars, is that the planet increases from 3%-9%, resulting in the fraction of *non-spherical* PNe to be just more than doubled from 14-30%, respectively. Based on the mean metallicity of *all* planet hosting stars (Maldonado et al. 2013), the typ-

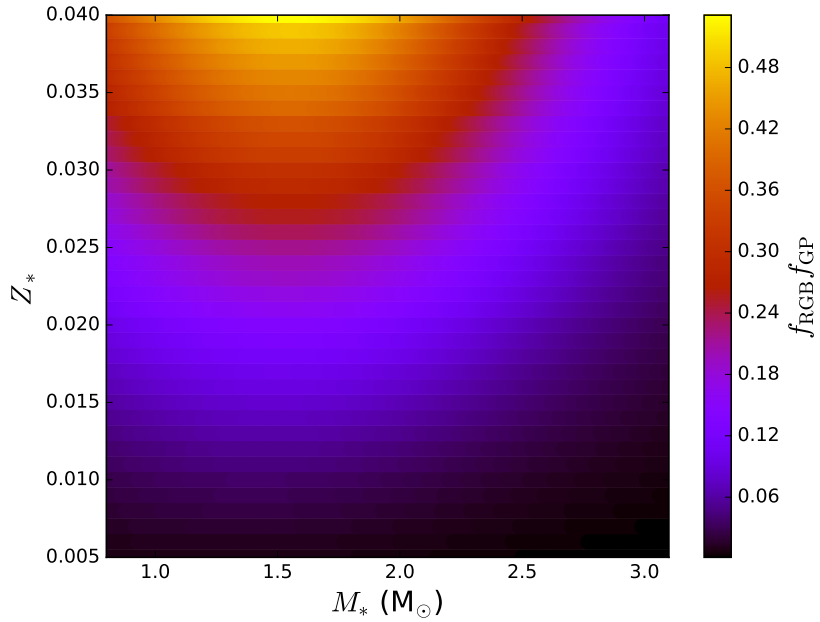


Figure 4.8: The probabilities of a star having and engulfing a massive planet on the RGB as a function of host star mass and metallicity according to the known exoplanets, interpolated between results from all five metallicity models available in SIMSPLASH.

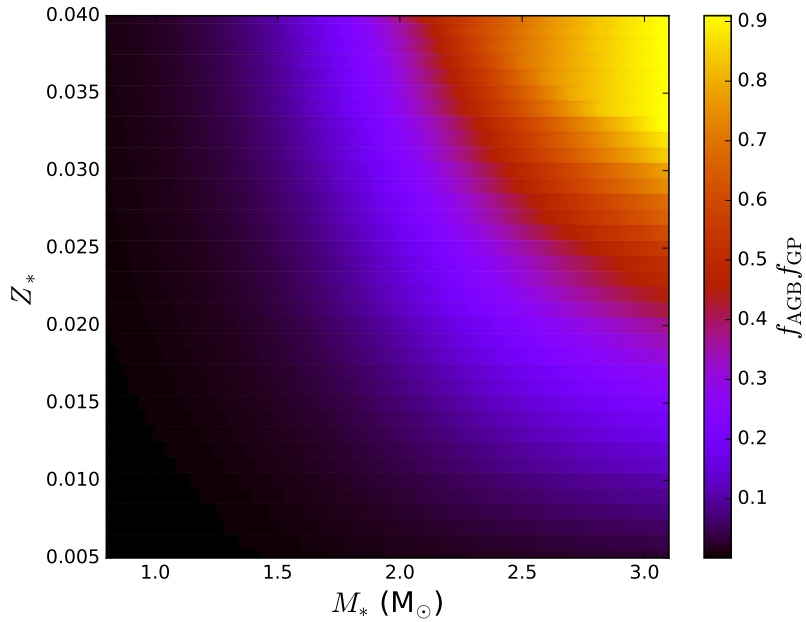


Figure 4.9: The probabilities of a star having and engulfing a massive planet on the AGB as a function of host star mass and metallicity according to the known exoplanets, interpolated between results from all five metallicity models available in SIMSPLASH.

ical prescription for the metallicity in orbital evolution models is  $Z_* = 0.02$  (Villaver et al. 2014; Privitera et al. 2016).

$Z_*$	$N_{\text{prog}}$	$\sum_i^k N_{i,\text{Pl(AGB)}}$	$\sum_i^k N_{i,\text{Pl(RGB)}}$	$\sum_i^k N_{i,\text{B(AGB)}}$	$\sum_i^k N_{i,\text{Sph}}$
0.005	$9.1 \times 10^9$	$4.6 \times 10^7$	$3.6 \times 10^7$	$1.7 \times 10^9$	$1.8 \times 10^9$
0.008	$9.0 \times 10^9$	$1.0 \times 10^8$	$9.4 \times 10^7$	$1.7 \times 10^9$	$7.2 \times 10^9$
0.014	$8.9 \times 10^9$	$2.6 \times 10^8$	$2.8 \times 10^8$	$1.7 \times 10^9$	$6.9 \times 10^9$
0.025	$8.3 \times 10^9$	$7.1 \times 10^8$	$8.4 \times 10^8$	$1.7 \times 10^9$	$5.9 \times 10^9$
0.04	$7.3 \times 10^9$	$9.5 \times 10^8$	$1.8 \times 10^9$	$1.7 \times 10^9$	$4.6 \times 10^9$

Table 4.6: The resulting PN progenitor population numbers when adopting the probabilities of engulfment according to the known exoplanets evolved with five different metallicity stellar models.

$Z_*$	$f_{\text{planet}}$	$f_{\text{binary}}$	$f_{\text{single}}$	$f_{\text{NS}}$	$f_{\text{NS(PI)}}$
0.005	0.01	0.19	0.80	0.20	0.05
0.008	0.01	0.19	0.80	0.20	0.05
0.014	0.03	0.19	0.78	0.22	0.14
0.025	0.09	0.21	0.70	0.30	0.30
0.04	0.13	0.23	0.64	0.36	0.36

Table 4.7: The resulting PN progenitor population proportions when adopting the probabilities of engulfment according to the known exoplanets evolved with five different metallicity stellar models.

### 4.3.3 The PN progenitor planet-fraction from synthetic exoplanet populations

The synthetic planet data described in section 4.2.1 consisted initially of 3000 disk systems for each of the star mass populations. After the appropriate cuts were made to the data as described earlier, the number of planet star systems per mass was reduced significantly as was the total number of systems. Figure 4.10 displays the mass vs. semi-major axis scatter plot of the reduced data, with data from the known exoplanets overlaid in order to illustrate the comparison between the two distributions. Clearly the synthetic population produces far more planets on wider orbits.

Each star-planet system was evolved as described previously to determine the number of RGB and AGB engulfs, using the reported metallicity for each host star. The remaining sample consisted of 3994 star-planet systems. Table 4.8 is a summary of the number of star-planet systems, after data cuts were made, and the number of engulfment on either the RGB or AGB per star mass, as well as the total population combined. The first thing to notice about the data in table 4.8 is that the number of star-planet systems in a sample for a given mass increases with increasing star mass which agrees with the correlation between massive planet occurrence and host star mass. The second noticeable feature of the data is that there are no AGB engulfs for the  $0.8$  and  $1.0 M_{\odot}$  planet populations, and there is a large jump between the proportions of AGB engulfs between that of the  $1.5 M_{\odot}$  model and the higher masses. The same trend was found with the known exoplanets sample and is due to the large difference in the maximum RGB radius between that reached by the lower mass stars and the higher mass stars. Also worth noting is the difference between the relative number of engulfs between the known exoplanets and the synthetic populations for a given host-star mass. For the known exoplanets, in particular the results displayed in figure 4.5, given that for some host-star masses there are only one or two planets and the fact that they are engulfed on the AGB results in the regression model over-predicting very high probabilities for the AGB engulfment of planets orbiting  $\gtrsim 2 M_{\odot}$ . On the other hand, 38% of the planets from the  $2 M_{\odot}$  and 46% from the  $3 M_{\odot}$  synthetic populations are engulfed on the AGB, which demonstrates the danger of small sample sizes and emphasises why adopting synthetic planet populations in this research was necessary.

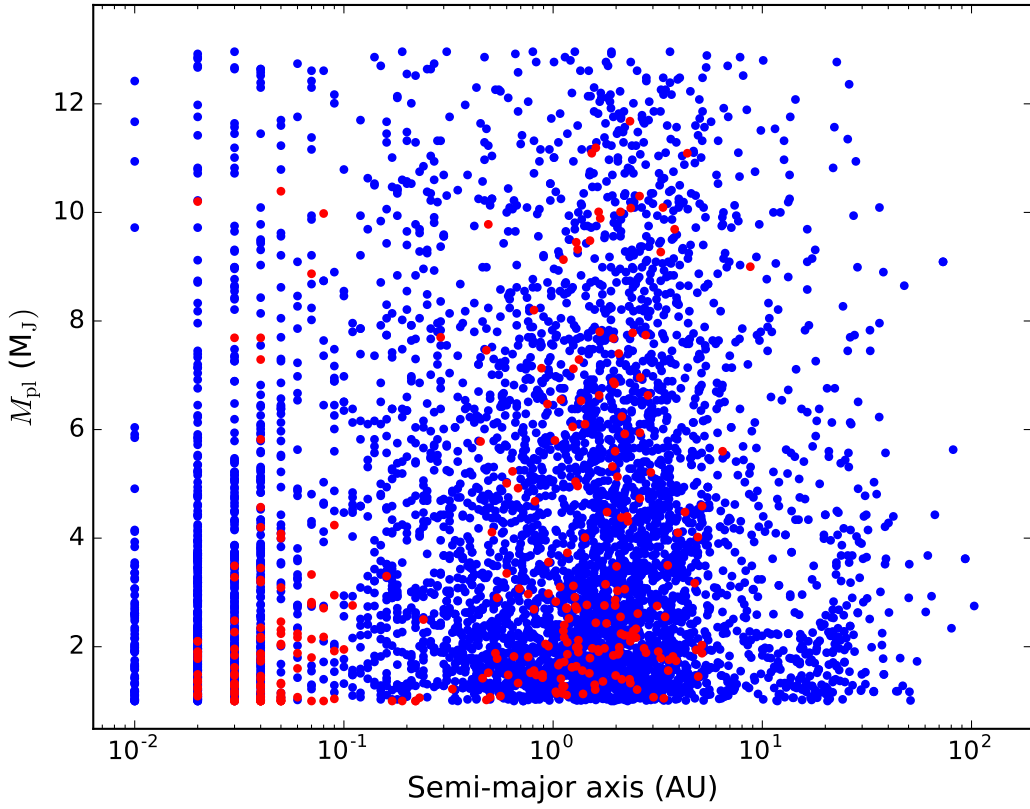


Figure 4.10: Semi-major axis vs. mass scatter plot of the synthetic planet population, after mass cuts were made to the data (plotted in blue). The known exoplanets data are overlaid to illustrate the agreement between the theoretical planet population models and the observational sample (plotted in red).

To compute the probabilities of engulfment on the AGB and RGB, the logistic regression model was first fit to the results of the orbital evolution of the whole synthetic planet population including all star mass populations. However, it was found that by including the  $5 M_\odot$  population model the AGB engulfment probabilities between the two extremes of the star masses were vastly under-predicted. A better fit was found by excluding the  $5 M_\odot$  population from both the RGB and AGB engulfment regressions. In the rest of the analysis, for calculating the planet-fraction, the engulfment probabilities, for both the RGB and AGB, were taken to be that at  $3 M_\odot$ . This is justified since, as was stated earlier in section 4.2.1, the planet formation and evolution models are only well calibrated for up to  $3 M_\odot$  stars (Shigeru Ida, private communication). Also, while the proportion of AGB engulfments in the  $5 M_\odot$  planet population is  $\approx 40\%$  and thus it is over-predicted by the extrapolation from  $3 M_\odot$ , when the planet-fraction was calculated

$M_*$ ( $M_\odot$ )	$N_{\text{SAMPLE}}$	$N_{\text{AGB}}$	$N_{\text{RGB}}$	$N_{\text{SAFE}}$
0.8	92	0	76	16
1.0	172	0	146	26
1.5	508	60	320	128
2.0	722	275	180	267
3.0	858	394	140	324
5.0	1642	649	562	431
Total	3994	1378	1424	1192

Table 4.8: Engulfment results summary for the synthetic planet populations evolved with the reported metallicity of the host-star ( $Z = Z_{\text{host-star}}$ ).

by including the  $5 M_\odot$  planet population there was  $< 0.01$  difference in the probabilities between calculating. The computed probabilities from the regression were then combined with the occurrence rates of massive planets of Gaidos & Mann (2014) to calculate the probabilities of stars having and engulfing massive planets. The computed probabilities for stars engulfing massive planets on the RGB as well as the probabilities of stars both having and engulfing massive planets, as a function of host star mass, obtained from the synthetic populations are plotted in figure 4.11 (the purple and dark blue curves, respectively). There is very little difference in comparison to those obtained from the known exoplanets. For the lower mass stars, the probability of a star engulfing its planet on the RGB is high, but when combined with the probability of the star having a massive planet in the first place the probabilities are lowered due to the dependence of massive planet occurrence on host-star mass.

However, we see that in figure 4.12, the difference between the computed probabilities of stars engulfing planets on the AGB for the synthetic planet populations and that of the known exoplanets is quite stark namely because of the differences in the proportions of engulfments for the stars  $\gtrsim 2 M_\odot$  mentioned already.

The synthetic planet populations were evolved again using the five stellar models with varying metallicity, as in the previous section with the known exoplanets, and the resulting probabilities of having and engulfing massive planets for the five different metallicity models were interpolated to compute a finer grid of models, since the planet-fraction increases with an increase in the mean metallicity, and are plotted in figures 4.13 and

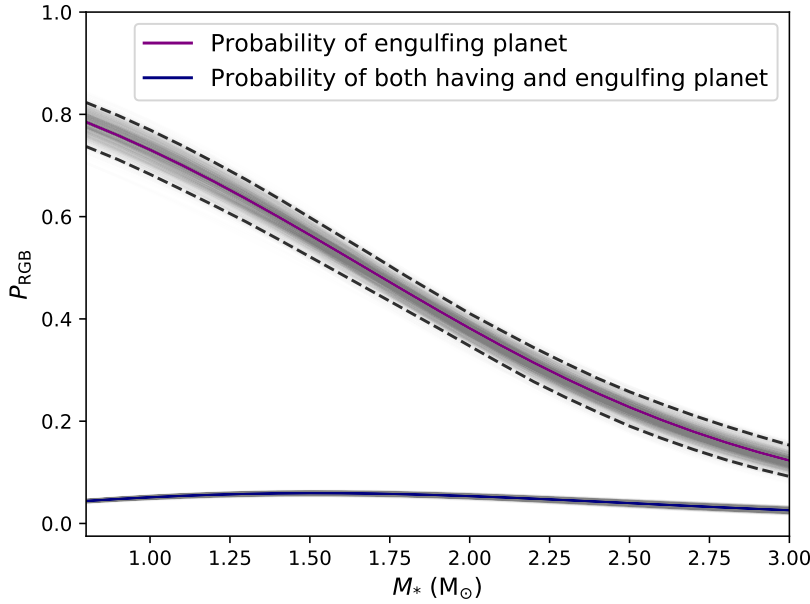


Figure 4.11: The probabilities of massive planet engulfment on the RGB as a function of star mass from the synthetic planet populations and adopting the measured metallicities of the host stars, fit with a logistic regression. The purple curve represents the probability of engulfment of a massive planet assuming the star has a planet in the first place. The dark blue curve represents the combined probability of a star both having and engulfing a planet, by adopting the massive planet occurrence rate of Gaidos & Mann (2014) with a mean metallicity of  $Z_* = 0.014$  in equation 4.2. The grey shaded regions represent the bootstrapped models and the dashed black lines represent the bounds of the 95% confidence limits.

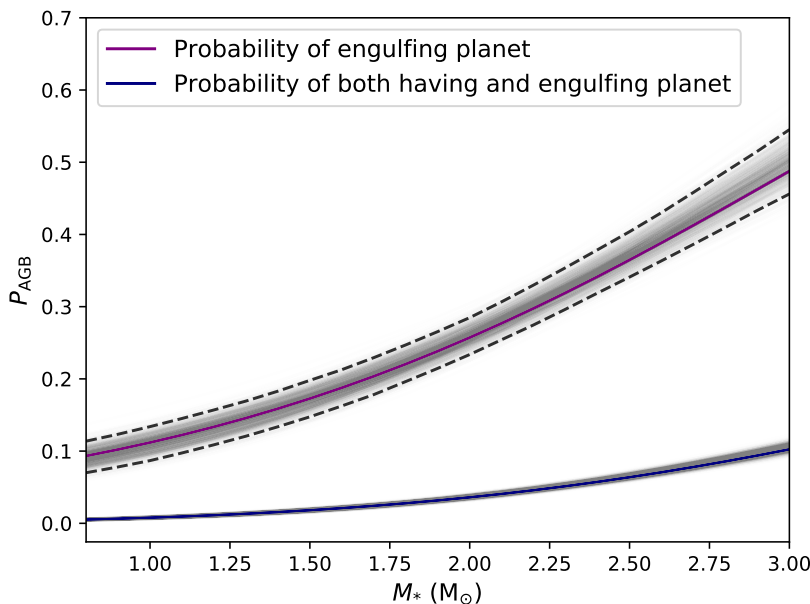


Figure 4.12: Same as figure 4.6, but for the probabilities of engulfment on the AGB.

4.14. While the plots of the interpolated probabilities for the synthetic planet population in comparison to that for the known exoplanets look qualitatively very similar, notice how the colourbar ranges have changed significantly for the probability of having and engulfing massive planets as a function of host-star mass and metallicity.

The PN progenitor populations were calculated using the same method as outlined for the known exoplanets. However it is found that based on the synthetic planet populations, the resulting planet-fractions of PN progenitors are in fact lower than those calculated with the known exoplanets. This is due to the probabilities of AGB engulfs being over-predicted for the higher mass stars in the known exoplanets models because of the small number statistics particularly, for host-stars  $\gtrsim 2 M_{\odot}$ . Tables 4.9 and 4.10 contain a summary of the resulting PN progenitor populations arising from adopting the synthetic planet populations for each metallicity. From this, if we were to make the very simple assumption that the current PN population in the galaxy evolved from a similar population to the current PN progenitor population, the planet-fraction of *all* PNe would be between 2-6%, whereas the fraction of *non-spherical* PNe arising from the engulfment of massive planets on the AGB would be between 10-23%.

$Z_*$	$N_{\text{prog}}$	$\sum_i^k N_{i,\text{Pl(AGB)}}$	$\sum_i^k N_{i,\text{Pl(RGB)}}$	$\sum_i^k N_{i,\text{B(AGB)}}$	$\sum_i^k N_{i,\text{Sph}}$
0.005	$9.0 \times 10^9$	$3.2 \times 10^7$	$3.8 \times 10^7$	$1.7 \times 10^9$	$7.3 \times 10^9$
0.008	$9.0 \times 10^9$	$7.7 \times 10^7$	$8.7 \times 10^7$	$1.7 \times 10^9$	$7.3 \times 10^9$
0.014	$8.9 \times 10^9$	$1.9 \times 10^8$	$2.6 \times 10^8$	$1.7 \times 10^9$	$7.0 \times 10^9$
0.025	$8.4 \times 10^9$	$5.2 \times 10^8$	$7.6 \times 10^8$	$1.7 \times 10^9$	$6.1 \times 10^9$
0.04	$7.4 \times 10^9$	$8.8 \times 10^8$	$1.7 \times 10^9$	$1.7 \times 10^9$	$4.9 \times 10^9$

Table 4.9: The resulting PN progenitor population numbers when adopting the probabilities of engulfment according to the synthetic planet populations evolved with five different metallicity stellar models.

Figure 4.15 displays the resulting number of PN progenitors with RGB and AGB engulfs (plotted in blue and green, respectively) occurring in each mass bin (note that the label for each bin is the *lower limit* of that bin, e.g., 0.8 means the  $0.8 - 0.9 M_{\odot}$  bin) when calculating the PN progenitor population in order to portray that while the relative numbers of PN progenitors with AGB engulfs increases with increasing mass, with respect to PN progenitors engulfing planets on the RGB, the total number from each bin decreases because the decreasing number of stars in the higher mass bins anyway. The

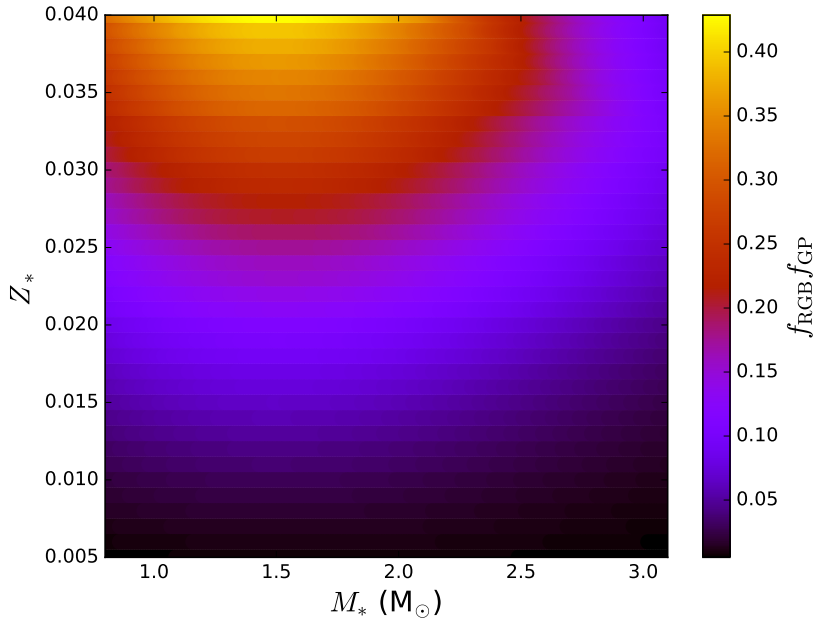


Figure 4.13: The probabilities of a star having and engulfing a massive planet on the RGB as a function of host star mass and metallicity according to the synthetic planet population, interpolated between results from all five metallicity models available in SIMSPLASH.

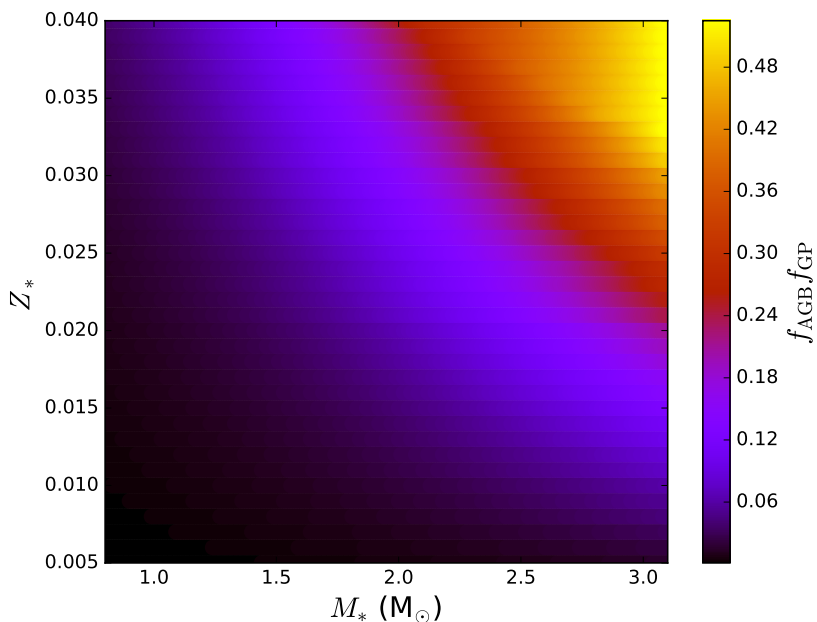


Figure 4.14: The probabilities of a star having and engulfing a massive planet on the AGB as a function of host star mass and metallicity according to the synthetic planet population, interpolated between results from all five metallicity models available in SIMSPLASH.

$Z_*$	$f_{\text{planet}}$	$f_{\text{binary}}$	$f_{\text{single}}$	$f_{\text{NS}}$	$f_{\text{NS(PI)}}$
0.005	<0.01	0.19	0.81	0.19	<0.01
0.008	0.01	0.19	0.80	0.20	0.05
0.014	0.02	0.19	0.78	0.21	0.10
0.025	0.06	0.20	0.73	0.24	0.23
0.04	0.12	0.23	0.65	0.35	0.34

Table 4.10: The resulting PN progenitor population proportions when adopting the probabilities of engulfment according to the synthetic planet population evolved with five different metallicity stellar models.

decrease in numbers of stars in the higher mass bins is a well-known consequence of the initial mass function (e.g., Kroupa 2001). Thus while the probability of PN progenitors engulfing massive planets on the AGB rises with increasing mass, unfortunately the overall numbers from each increasing mass bin diminishes, which keeps the planet-fraction of PN progenitors low. However, it has been assumed throughout this chapter that the current PN progenitor population, along with its population of planets, can be taken as representative of the population from which the current population of PNe arose from. This is not the case, since the timescale of a stars evolution depends strongly on its mass. The current population of PN progenitors is then not a representative population of the population of PNe currently in the galaxy, as it can only represent a single epoch of galactic evolution. The method employed here to calculate the PN progenitor population then is, as such, the method to calculate each epoch in a population synthesis and is the basis for the next chapter, in which the star formation history is traced up to the present-day population of planetary nebulae to determine, from each epoch of star formation, which systems have evolved to the present-day population of PNe. The probabilities of stars having and engulfing massive planets on the RGB and AGB as a function of host star mass and metallicity, presented in this current chapter, will allow the number of PN progenitors in each epoch of the star formation history to be determined as well, and thus arrive at the present-day planet-fraction of planetary nebulae.

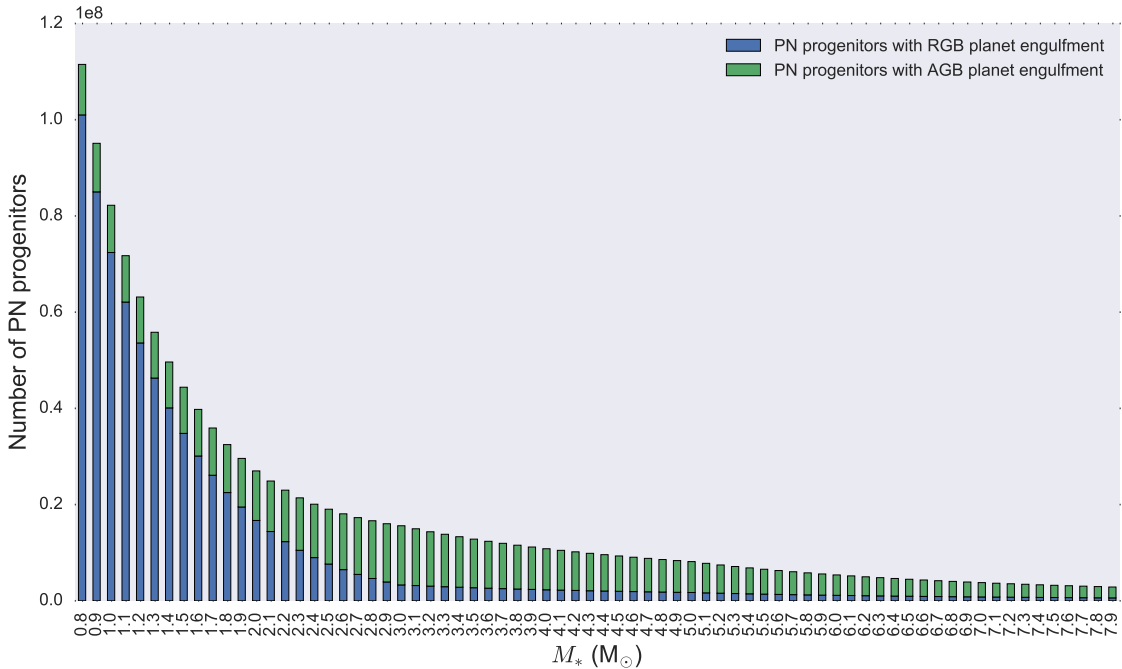


Figure 4.15: Bar plot of the numbers of PN progenitors with RGB and AGB engulfs in each mass bin for the PN progenitor population (calculated with the  $Z_* = 0.025$  stellar models). While the number of progenitors with AGB engulfs increases with increasing mass, the relative number of progenitors with RGB engulfs decreases due to less PN progenitors on the whole in these mass bins. Note that the labels for each bin is the *lower limit* of that bin, e.g., 0.8 means the  $0.8 - 0.9 M_\odot$  bin

## 4.4 Summary and conclusions

In this chapter, the Single-epoch population mode of SIMSPLASH was presented and used to explore planet engulfment in the progenitor populations of planetary nebulae. The Single-epoch population mode of SIMSPLASH contains a method to determine the planet-fraction of planetary nebula progenitors by evolving each system in a sample population of planets, according to the Orbital mode of SIMSPLASH outlined in chapter 3, and perform an analysis on the number of RGB and AGB engulfs and their respective effects on the PN progenitor population. The planet-fraction of planetary nebula progenitors refers to the fraction of planet-hosting planetary nebula progenitors currently in the galaxy which will engulf a massive planet during the AGB phase of its future evolution. It was demonstrated here that by combining the distribution of stellar masses, the distribution of exoplanets, and the conditions for planet engulfment one can calculate the probabilities, and numbers, of stars engulfing massive planets in the PN progenitor population and evolve to

form non-spherical planetary nebulae as a result of that. Two planet populations were investigated here using SIMSPLASH, the known exoplanets obtained from the Exoplanet Orbit Database and a synthetic planet population provided by Shigeru Ida. For the first time, the probabilities of PN progenitor stars having and engulfing massive planets, as a function of mass and metallicity, have been determined. The following is a summary of the main findings presented in this chapter:

- According to the distribution of the known exoplanets, the planet-fraction of planetary nebula progenitors ranges from  $\simeq 3 - 9\%$  depending on the adopted mean metallicity of the sample (between  $Z_* = 0.014$  and  $Z_* = 0.025$ ), which translates to between 14 - 30% when considering the proportion of PN progenitors which would go on to form non-spherical PNe. It was assumed here that the star-planet sample from the Exoplanets Orbit Database is representative of the total population of star-planet systems in the galaxy. Of course, this is likely not the case since the sample is incomplete for intermediate host-star masses and large orbital periods, resulting in large numbers of planets being engulfed on the RGB. However, in chapter 3 we saw that the RGB engulfment zone of a  $1M_\odot$  star is much larger than its AGB engulfment zone suggesting that despite the lack of massive planets with larger semi-major axes in the sample the resulting probabilities for the lower mass stars may be close to the true values.
- The same analysis as applied to the known exoplanets was applied to the synthetic planet populations. The planet fractions calculated for the different metallicity models were lower than those for the known exoplanets in all cases. According to the synthetic planet populations the planet-fraction of planetary nebula progenitors ranges from  $\simeq 2 - 6\%$  depending on the adopted mean metallicity of the sample (between  $Z_* = 0.014$  and  $Z_* = 0.025$ ), translating to between 10-23% of PN progenitors which would evolve to form non-spherical planetary nebulae. While the planet-fraction of PN progenitors may seem low when calculated with both the known exoplanets and the synthetic populations, it is still substantial when considering only systems which will make non-spherical PNe.
- By making the approximation that the present-day population of planetary nebulae evolved from a stellar (and planet) population identical to the present-day stel-

lar population, the planet-fractions of planetary nebulae were estimated using both the known exoplanets and the synthetic planet populations. This assumes that the present-day population evolved from a coeval population, and neglects stellar lifetimes and PN visibility times. Obviously, this is a very simplified approach to determining the distribution of planetary nebulae. A more appropriate analysis would be to follow the star and planet formation history of the Milky Way, which will be addressed in the next chapter, and determine the numbers of planetary nebula progenitors and the respective numbers of stars engulfing planets, and binary systems, for each population of stars forming in each epoch of star formation and then determine the numbers that are visible in the present-day planetary nebula population. In other words a planetary nebula population synthesis calculation which incorporates planet engulfment needs to be performed. In essence the analysis presented in this chapter is an example of the analysis performed for each population of stars formed in each epoch of a star formation history for a population synthesis. Thus the Single-epoch population mode of `SIMSPLASH` serves as a tool to investigate each population in a star formation history individually, just as the Orbital mode of `SIMSPLASH` serves as a tool to investigate each star-planet system individually.

- By using `SIMSPLASH` to analyse the resulting populations depending on the adopted metallicity for the orbital evolution of planets in a population, it was shown that the planet-fraction of planetary nebula progenitors is very sensitive to the adopted metallicity of the host-star population. Population synthesis calculations incorporating a star formation history and the probabilities of stars having and engulfing massive planets must include a metallicity history also.
- `SIMSPLASH` in its Single-epoch population mode is an efficient tool for obtaining, filtering and analysing the known exoplanets from the Exoplanet Orbit Database, as well as synthetic planet populations derived from planet formation and evolution theory, with regards to planet engulfment in the progenitor population of planetary nebulae. It was mentioned above that the current sample of the known exoplanets is biased towards close-in planets and low-mass stars and is thus not likely to be representative of the true population of massive planets orbiting planetary nebula progenitors. However, as the sample becomes more complete in future, the

development of SIMSPLASH and its Single-epoch population mode for this research means that it will be an efficient process to re-calculate and analyse the resulting populations taking into account emerging samples of known exoplanets and also advancements made to planet formation and evolution theories for the generation of synthetic planet populations. Thus SIMSPLASH is a valuable asset in the investigation of the planet-shaping hypothesis.



# Chapter 5

## Population synthesis of planet engulfment by planetary nebula progenitors

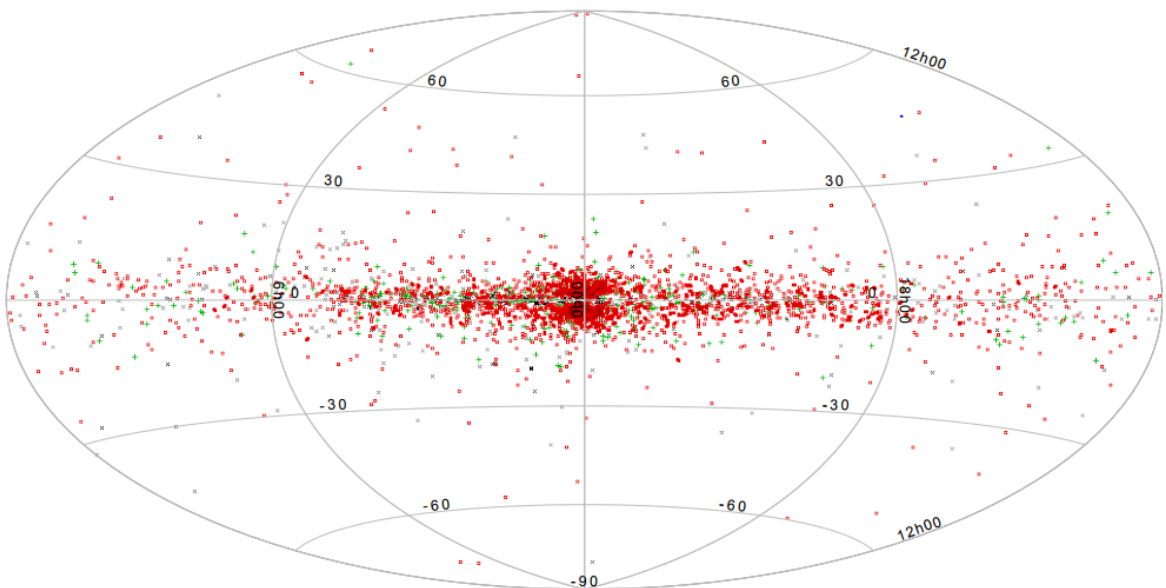


Figure 5.1: Galactic distribution of all currently known PNe (including true (red), likely (green) and possible (black) PNe) in the Hong Kong/AAO/Strasbourg H $\alpha$  (HASH) database. Image credit: Frew (2017).

## 5.1 Introduction

The engulfment of massive planets during the asymptotic giant branch (AGB) phase of planetary nebula (PN) progenitor evolution has been suggested over the past twenty years as a means to explain a proportion of the non-spherical PN population (e.g., Soker 1996b; Nordhaus & Blackman 2006), as a complementary evolutionary channel to the widely accepted binary hypothesis (e.g., De Marco 2009). More recently, this idea has gained momentum with the emergence of hundreds of massive planets being discovered around PN progenitor stars. The aim of this research is to test the hypothesis that the engulfment of massive planets can aid in explaining the lack of binary PN progenitors available to shape the observed population of non-spherical planetary nebulae (PNe). As of yet there is still no substantial observational evidence to support the hypothesis. Thus, there is still no way of knowing what fraction of PNe can be attributed to the engulfment of a planet by an AGB star by any observational means. However, the engulfment of a planet on the AGB has been suggested to explain observed phenomena in a handful of cases of planetary nebula observations, which may aid in the characterisation of planet-shaped planetary nebulae in future. For example, metal-rich components embedded within a planetary nebula have, for some time, been suggested as a resolution for the long-standing abundance discrepancy problem, which describes the discrepancy between abundances measured via optical recombination lines and abundances measured by collisionally excited lines (see, e.g., Liu et al. 2000; Wesson et al. 2005; Yuan et al. 2011). The origin of such metal-rich components is still subject to debate, but one possibility is that it might be due to a destroyed planet (Liu et al. 2006; Corradi et al. 2015). Another interesting observation which adds support to the planet-shaping hypothesis is the recent observations of Kervella et al. (2016), who measured the mass of the companion to the star L<sub>2</sub> Puppis, a nearby AGB star with a dusty circumstellar disk and an emerging bipolar morphology, to be about 1 M<sub>J</sub> providing exciting new support for the planet-shaping hypothesis. But with only one known AGB object of this nature, and just a handful of speculative abundance discrepancy evidence, obtaining an observational *planet-fraction* (the fraction of PNe which have been shaped by the interaction of an AGB star with a planet) to complement the observational binary-fraction is challenging, if not yet impossible. However, by utilising the results in chapters 3 and 4, it is argued here that a theoretical planet-fraction of planetary nebulae,

currently in the galaxy, can be sought and, if substantial, will provide additional support to the hypothesis that the engulfment of planets during the AGB can alter the morphologies of PNe, and may even provide a solution to the mystery behind the discrepancy between the observed non-spherical PN population and the progenitor binary-fraction.

A tractable, yet robust, method for exploring the effects of various stellar evolutionary channels on populations in the Milky Way is to synthesise the expected population in question. Various methods of population synthesis calculations, many of which are concerned with binary evolution, have been reported in the literature. Examples include binary population synthesis to yield the population of subdwarf B stars in the Milky Way to examine the effects of binary evolution on their formation (e.g., Han et al. 2003; Nelemans 2010), while Hurley et al. (2002) employed binary population synthesis to demonstrate the important effects of including tidal evolution when modelling various binary evolution channels. Since the aim of this research is to explore the hypothesis that a subset of non-spherical planetary nebulae may have had their morphologies influenced by the engulfment of a massive planet during the AGB phase of their progenitors evolution, investigating the idea via a population synthesis approach, similar to the aforementioned studies, is appropriate since it will reveal what the PN population would look like when taking planet-shaping into account. Also of interest is the suggestion that a planet engulfment on the red giant branch (RGB) can halt the evolution of a star, preventing the star from evolving to the AGB phase and into a planetary nebula. Such a scenario is thought to result in the formation of the subdwarf B type stars, mentioned above, as a complementary subset to those formed through binary interactions (e.g., Bear & Soker 2011). Such stars will not form a planetary nebula. By incorporating RGB engulfments as a hindrance to the formation of a PN into a population synthesis calculation, the resulting number of PNe can be compared to the observational estimate also. In this chapter, the population synthesis approach is applied in order to explore the effects of planet engulfment on the present-day population of planetary nebulae.

A previous population synthesis study conducted by Moe & De Marco (2006) to calculate the population of planetary nebulae evolving from single and binary star systems revealed yet another mystery pertaining to the origin and evolution of the PNe in the Milky Way. By following the star formation history of PN progenitors through to the present-day PN population, Moe & De Marco (2006) demonstrated that their population synthesis

calculations predicted a theoretical value for the total number of PNe much larger than can be accounted for by observationally based estimates. Their population synthesis calculation yielded a total of  $46,000 \pm 13,000$  galactic PNe with radii  $<0.9$  pc, which was largely discrepant with their adopted observationally based target value of  $8,000 \pm 2,000$  PNe. This led to their conclusion that binarity may not just be responsible for shaping PNe, but is required to form of the majority of them, which had previously been suggested by Soker & Subag (2005).

Considering that with regards to the evolution of planetary nebulae and their shaping mechanisms, that *binary* interactions can include the engulfment of massive planets (Soker 1997), it is interesting to conduct a similar population synthesis study but this time to include the probabilities of planet engulfment derived from the orbital evolution calculations in PN progenitor populations in chapter 4, which to-date has not been performed. It is important to comment on the review of the PN shaping framework of De Marco & Soker (2011), as they provided an estimate on the role of planets in planetary nebulae in terms of the PN population morphologies and predicted that 5% of all stars, and 20% of stars that actually make a PN (based on the idea of Soker & Subag (2005) that only a subset of  $1 - 8 M_{\odot}$  stars actually make PNe), would engulf a planet on the AGB. However, their estimate was wholly based on the observed morphological classes alone and they did not perform a population synthesis calculation nor model the tidal evolution of star-planet systems. Thus a more robust method of determining to what extent planets can explain the population of non-spherical PN morphologies is provided in this work.

In chapter 4, it was demonstrated how to synthesise a single population of planetary nebula progenitors (the PN progenitors currently in the galaxy), and the numbers of which that would evolve through the different evolutionary channels using the known exoplanets, synthetic planet populations and binary star statistics. The aim of this chapter is to apply this treatment in a population synthesis study of planetary nebulae to determine the number of planetary nebulae in the present-day Milky Way which have evolved through an AGB engulfment of a planet. To do this, the Multi-epoch population mode of SIMSPLASH was developed, which utilises an average galactic star formation history to follow the birth and evolution of PN progenitors from each epoch of star formation until their emergence as PNe in the present-day Milky Way. The following sections describe the ingredients of the Multi-epoch population mode of SIMSPLASH.

## 5.2 SIMSPLASH in Multi-epoch population mode: Calculating the planet-fraction by PN population synthesis

Beginning with a star formation history and the associated metallicity history of the Milky Way, the Multi-epoch population mode of SIMSPLASH calculates the number of stars born in each epoch of star formation and the average metallicity of stars at that time. In a similar fashion to Moe & De Marco (2006), the turnoff mass for each population is calculated and the number of stars forming in each epoch, which are visible as planetary nebulae today, is determined from the initial mass function, the progenitor binary-fraction and the average lifetime of a PN. By combining this information with the probabilities of stars having and engulfing massive planets as a function of mass and metallicity, found in chapter 4, SIMSPLASH determines the number of these stars which will engulf a massive planet on the RGB and AGB. Each epoch of star formation can thus be thought of as a simple stellar population, and the present-day galaxy is the composite population resulting from the summation of all populations over time. The present-day population, defined as  $t = 0$ , of planetary nebulae, and the corresponding numbers of those having evolved through planet engulfment, binary interactions and as single stars, is thus determined by the summation of each independently calculated epoch. A schematic representation of the workflow within the Multi-epoch population mode of SIMSPLASH is presented in figure 5.2.

### 5.2.1 Star formation history

The star formation history of the Milky Way is often modelled by a star formation rate (SFR) which decreases with time as a galaxy becomes depleted of gas due to the continuous formation of stars. This is referred to as the Kennicutt-Schmidt law of star formation (Schmidt 1959; Kennicutt 1998). The depletion of gases is then characterised by a depletion timescale,  $\tau$ , which depends on the rate at which the gas is depleted by being converted to stars. Star formation histories modelled in this way are sometimes called *declining-tau models*.

In this work, a typical star formation history of Behroozi et al. (2013) for a Milky Way mass galaxy is adopted<sup>1</sup>. Behroozi et al. (2013) found that a double power law is a

---

<sup>1</sup>Provided by Peter Behroozi, private communication.

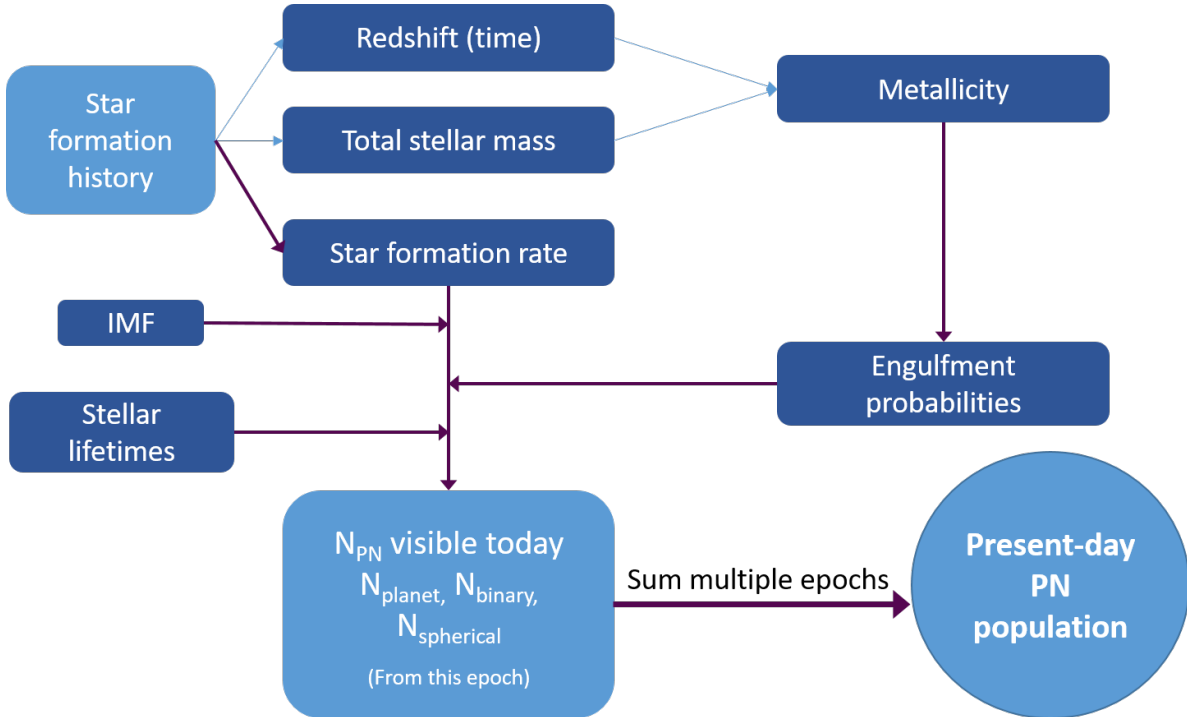


Figure 5.2: Schematic diagram of the Multi-epoch population mode of SIMSPLASH: Beginning with a star formation history and the associated metallicity history of the Milky Way, the Multi-epoch population mode of SIMSPLASH calculates the number of stars born in each epoch of star formation and the average metallicity of stars at that time. The turnoff mass for each population is calculated and the number of stars forming in each epoch, which are visible as planetary nebulae today, is determined from the initial mass function, the progenitor binary-fraction and the average lifetime of a PN. By combining this information with the probabilities of stars having and engulfing massive planets as a function of mass and metallicity, found in chapter 4, SIMSPLASH determines the number of these stars which will engulf a massive planet on the RGB and AGB. Each epoch of star formation can thus be thought of as a simple stellar population, and the present-day galaxy is the composite population resulting from the summation of all populations over time. The present-day population, defined as  $t = 0$ , of planetary nebulae, and the corresponding numbers of those having evolved through planet engulfment, binary interactions and as single stars, is thus determined by the summation of each independently calculated epoch.

better fit than the declining-tau models for the star formation history in Milky Way mass galaxies, by comparing galaxies with equal cumulative number densities, but different redshifts, to determine the build-up of stellar masses as a function of redshift. Thus the star formation history adopted here follows the form

$$SFR_i = A \left[ \left( \frac{t_i}{\tau} \right)^B + \left( \frac{t_i}{\tau} \right)^{-C} \right]^{-1} \quad (5.1)$$

where  $t_i$  is the time at the beginning of the epoch of star formation (i.e., the  $i$ th timebin in the star formation history),  $\tau$  is the star formation rate decay timescale and the constants  $A$ ,  $B$  and  $C$  are the fitting parameters. Behroozi et al. (2013) argue that their method of determination for the star formation histories of galaxies is robust since massive galaxies at early redshifts tend to remain as massive at later redshifts (see also Behroozi & Peebles (2015) for concise a summary of their method).

The raw star formation history data of Behroozi et al. (2013) adopted here contains, for each redshift ( $z_i$ ), the average star formation rate ( $SFR_i$ , in  $\log M_\odot \text{ yr}^{-1}$ ) and the total stellar mass of the galaxy ( $M^*$ , in  $\log M_\odot$ ) at that redshift. The data contains 137 redshift values for the star formation history which determine the discrete star formation epochs. Since stellar lifetimes are important here, the intervals describing each epoch of star formation would be much too large with so few data points and so a linear interpolation is performed between each epoch boundary ( $z_i$  and  $z_{i+1}$ ). SIMSPLASH then converts the redshift to time ( $t_i$ ) by employing the `PYTHON ASTROPY.COSMOLOGY` package from the `ASTROPY` collaboration (Robitaille et al. 2013)<sup>2</sup>.

The total mass of the population of stars born in each epoch,  $M_i$ , is then given by the boundaries of each epoch,  $t_i$  and  $t_{i+1}$ , and the star formation rate

$$M_i = (t_{i+1} - t_i) \times SFR_i. \quad (5.2)$$

The total number of stars born in each epoch is then obtained by normalising the IMF to the total mass of the population.

---

<sup>2</sup>This research made use of Astropy, a community-developed core Python package for Astronomy (Astropy Collaboration, 2013). The Astropy website: <http://www.astropy.org/>.

### 5.2.2 Metallicity evolution of the Milky Way

In earlier chapters it was discussed and demonstrated that stellar metallicity plays an important role in the formation and orbital evolution of planets and the probability of a PN progenitor engulfing a massive planet on both the RGB and AGB. Furthermore metallicity has a large impact on the lifetimes associated with a star of a given mass, which ultimately determines the turnoff mass of a population of stars formed in each epoch. Because of the continuous formation, evolution and destruction of stars throughout the galactic history, the metallicity increases with time, and younger objects will tend to be more metal-rich than older ones. Ejected material from stellar destruction has been nuclear processed, so its composition differs from the primordial galactic gas, resulting in later generations of stars (younger populations) having increasingly larger abundances of metals. For this reason, a population synthesis must account for the metallicity history of the galaxy.

An advantage of adopting the star formation history of Behroozi et al. (2013), described in the previous section, is that their data also contains the evolution of the total stellar mass,  $M^*$ , at each redshift, which takes into account the mass lost from stellar winds and destruction events such as supernovae, throughout the galactic evolution. This allows for the determination of the gas-phase metallicity history by employing a metallicity-stellar-mass-redshift relationship. The adopted relationship used in this work is the following fitting function of Maiolino et al. (2008)

$$12 + \log (\text{O/H}) = -0.0864 (\log M^* - \log M_0)^2 + K_0, \quad (5.3)$$

where the stellar-mass is denoted by  $M^*$ , and the variables  $\log M_0$  and  $K_0$  were determined, by Maiolino et al. (2008), for each redshift and are listed in table 5.1. Note that while values of  $M_0$  and  $K_0$  are determined for redshift  $z < 3.5$ , they have been extrapolated for the range of redshifts applicable for this work (following the Behroozi & Peebles (2015) treatment). The average metallicity of stars in the Milky Way, during each epoch, is then obtained by the relationship between the gas-phase metallicity,  $12 + \log (\text{O/H})$ , and  $[\text{Fe}/\text{H}]$ , with the following analytical fit from Stoll et al. (2013)

$$[\text{Fe}/\text{H}] = -11.2 + 1.25 (12 + \log (\text{O/H})). \quad (5.4)$$

$z$	$\log M_0$	$K_0$
0.07	11.18	9.04
0.7	11.57	9.04
2.2	12.38	8.99
3.5	12.76	8.79
3.5	12.87	8.90

Table 5.1: The best fit parameters determined by Maiolino et al. (2008) for the galactic stellar-mass-metallicity relationship in equation 5.3.

### 5.2.3 The number of visible present-day galactic PNe from each epoch

Moe & De Marco (2006) describe a general prescription to obtain the number of PNe which would have had enough time to evolve to the present-day Milky Way, which is loosely followed in this work. The turnoff masses for the populations of stars formed at times  $t_i$  and  $t_{i+1}$  are calculated using a metallicity dependent relationship between stellar mass and stellar lifetime. The relationship between stellar mass, metallicity and lifetime is modelled here by adopting and rearranging the analytical formula of Raiteri et al. (1996), which was obtained from the Padova group stellar models (e.g., Bertelli et al. 1994),

$$\log(t_*) = a_0(Z_*) + a_1(Z_*) \log M_* + a_2(Z_*) (\log M_*)^2. \quad (5.5)$$

The lifetime,  $t_*$ , is defined as the duration of the combined hydrogen- and helium- burning phases and the corresponding mass in equation 5.5 is thus the turnoff mass of a population with an age equal to  $t_*$ . The coefficients  $a_0(Z_*)$ ,  $a_1(Z_*)$  and  $a_2(Z_*)$  are defined as

$$\begin{aligned} a_0(Z_*) &= 10.13 + 0.07547 \log Z_* - 0.008084 (\log Z_*)^2 \\ a_1(Z_*) &= -4.424 + 0.7939 \log Z_* - 0.1187 (\log Z_*)^2 \\ a_2(Z_*) &= 12662 + 0.3385 \log Z_* - 0.05417 (\log Z_*)^2. \end{aligned} \quad (5.6)$$

In each epoch, the same method as described in chapter 4 (section 4.2.4) for calculating the total number of PN progenitors in a population is then applied, but using the turnoff masses as the limiting star masses which produce the population of PNe which have had enough time to evolve to the PN phase by the present-day Milky Way. The number of stars

engulfing massive planets on the RGB and AGB are then obtained from the probabilities of stars having and engulfing massive planets as a function of mass and metallicity, where the mass and metallicity are taken as the turnoff mass for the population formed at  $t_i$  and the average metallicity of a star at  $t_i$ .

Finally to determine the number of PNe from each evolutionary channel that are currently still *visible* in the Milky Way, the number of PNe produced from each epoch is multiplied by the ratio of the average PN visibility time to the length of time of a given epoch (Moe & De Marco 2006),

$$N_{\text{PN}(t=0)} = N_{\text{PN}} \frac{\tau_{\text{PN}}}{(t_{i+1} - t_i)}, \quad (5.7)$$

where  $\tau_{\text{PN}}$ , is the PN visibility time and the subscript label  $t = 0$  denotes that this is the number of PN visible in the present-day Milky Way from that epoch. To obtain the number of PNe which have evolved through the engulfment of a massive planet on the AGB, and also the numbers evolved through binary interactions and single-star evolution, equation 5.7 is combined with the general methods outlined in chapter 4 (section 4.2.4), although some of the assumptions will vary and are discussed in the next section. From this, the planet-fraction of planetary nebulae currently in the Milky Way can be calculated.

### 5.2.4 Models, assumptions and approximations

In the previous sections, the general galactic model including the star formation history, metallicity evolution and the calculation of stellar lifetimes within the Multi-epoch population mode of SIMSPLASH were described. The population synthesis also depends on a number of approximations and assumptions which must be specified by the user in SIMSPLASH. This allows for the efficient comparison of many models. To arrive at the present-day population of PNe, and the planet-fraction, a number of population synthesis models were run by adopting the following prescriptions.

#### The planetary nebula visibility time

The PN visibility time has been suggested to vary between 20000 - 50000 yrs (Zijlstra & Pottasch 1991; Moe & De Marco 2006). In this work, the PN visibility time, which is also a function of a stars mass and metallicity, is not modelled. Instead, an average PN

visibility time of  $\tau_{\text{PN}} = 26,000$  yrs is adopted in accordance with the average found by Moe & De Marco (2006). The PN visibility time is therefore defined as, as in their paper, the time in which the central star is in excess of the temperature and luminosity required for ionisation ( $T_{\text{eff}} = 25000$  K and  $\log(L_*/L_\odot) = 1.5$ , respectively) which they obtain by interpolating post-AGB evolution tracks Vassiliadis & Wood (1994). It is noted also, that in order to allow for a comparison between the total number of PNe calculated and the observationally based estimates with detection limits corresponding to a maximum PN radius of 0.9 pc, Moe & De Marco (2006) placed an upper limit of  $\tau_{\text{PN}} = 35,000$  yrs in their calculations of the PN visibility times, where the maximum radius limit is based on the average PN expansion velocity of  $25 \text{ km s}^{-1}$  of Phillips (1989). The total number of PNe calculated here then can also be compared to the observationally based estimates of the total number of PNe with radii  $< 0.9$  pc.

### Binary and single star statistics

In all models, a 50% progenitor binary-fraction is assumed as in chapter 4. In chapter 4, the adopted assumption was that (of the 50% progenitor binary-fraction) 28% of binary systems would undergo a common envelope on the RGB and prevent the system from evolving to the AGB phase and subsequently prevent the formation of a PN, and 32% of binary systems would have an interaction (either common envelope or a mild interaction) on the AGB that would shape a PN, and the remaining 40% of binary systems would have separations too large to cause any shaping and so they are considered to evolve as single star systems. As in chapter 4 (section 4.2.5), very wide, but interacting, symbiotic systems are not accounted for in the population synthesis presented here since these objects are treated as *PN mimics* in morphological classification schemes and thus removed from surveys (e.g., Parker et al. 2006). However, the assumption that 28% of binary systems are prevented from evolving to the AGB may be a little speculative in terms of the fact that it doesn't consider the masses of primary or secondary stars in terms of what combination of primary and secondary masses would actually result in such an event. In order to prevent over-estimating the number of systems lost from the total PN count, the estimation of Moe & De Marco (2006) is adopted also, whereby 10% of binary systems are prevented from evolving to the AGB phase.

### The initial mass function

Two forms of the IMF are adopted to model the stellar mass distribution; the broken power-law IMF of Kroupa (2001) and the log-normal function of Chabrier (2003), both of which were defined in chapter 2 (section 2.5.2). The IMF is important here as it ultimately determines the number of stars coming from each epoch, where each epoch is bounded by the turnoff masses of the population forming at that time. Since the probability of a star having and engulfing a massive planet on either the RGB or AGB is very sensitive to stellar mass, the choice of IMF has an influence on the planet-fraction also.

### The probabilities of having and engulfing massive planets

In chapter 4 it was demonstrated that the probability of a star having and engulfing a massive planet on either the RGB or the AGB depends strongly on the stellar mass and metallicity. The importance of this relationship is amplified here since for each epoch the stars which have had enough time to evolve to the PN phase from that epoch is a function of the turnoff masses calculated for the boundaries of that epoch, which in turn depends on the average metallicity during that epoch. The probabilities of stars having and engulfing massive planets, calculated in chapter 4 are therefore utilised to calculate the number of PN progenitors engulfing planets on both the RGB and AGB evolving from each epoch.

The engulfment probabilities were obtained by evolving the synthetic planet populations of Shigeru Ida using the MIST models of Choi et al. (2016), described in chapter 3, which were calculated with a Reimers (1975) RGB mass-loss coefficient of  $\eta_R = 0.1$  and a Bloecker (1995) AGB mass-loss coefficient  $\eta_R = 0.2$ . However, as was demonstrated and discussed in chapter 3, RGB and AGB mass-loss rates are notoriously uncertain, and they also have an effect on the engulfment zones of planets orbiting PN progenitors. Thus, in order to eliminate this uncertainty, a second set of planet engulfment probabilities, calculated in the same way as in chapter 4, but using a set of stellar models calculated by the author using the MESA stellar evolution code, are used to calculate the number of stars engulfing massive planets on the RGB and AGB in each epoch also. The stellar models employed adopt a Reimers (1975) RGB mass-loss coefficient of  $\eta_R = 0.5$  and a Bloecker (1995) AGB mass-loss coefficient of  $\eta_R = 0.1$ , which are generally adopted as the standard mass-loss coefficients in tidal evolution studies (e.g., Madappatt et al. 2016). At

this time, `SIMSPLASH` only contains stellar models using these coefficients for metallicities  $Z_* = 0.01$  and  $Z_* = 0.02$ , and so the probabilities of engulfment can only be calculated and interpolated between these metallicities. However, since the metallicity history in the population synthesis model yields a maximum average stellar metallicity of  $Z_* \simeq 0.017$ , higher metallicities are in fact not needed. With regards to the lower metallicity boundary, at the earliest epochs when the metallicity is very low the turnoff masses are also low which means that very few AGB planet engulfments come from these epochs anyway, so adopting an average metallicity of  $Z_* = 0.01$  for these early epochs should not affect the planet-fraction result.

Finally it is noted that the stellar models adopting the standard mass-loss coefficients are not rotating. However, it was shown in chapter 3 that there was only a small difference between the resulting engulfment zones calculated with the rotating MIST models in comparison to the non-rotating MIST models. From the discussion outlined in chapter 3 it is reasonable to expect that the engulfment zones arising from adopting the rotating Ekström et al. (2012) stellar models might result in different engulfment probabilities and effect the results presented here. However, `SIMSPLASH` is currently built for handling `MESA` stellar model output only. A future update in `SIMSPLASH` will involve the use of any stellar models from any stellar evolution code and thus allow for a comparison between the population synthesis results stemming from the engulfment probabilities calculated with other stellar evolution codes.

### **Planet engulfment on the RGB and PN prevention**

The possibility of a planet engulfment on the RGB preventing a PN progenitor from evolving to the AGB phase was discussed previously (in chapter 1, section 1.6). While it was stated in chapter 4 that including this assumption did not pose much of an effect on the planet-fraction of PN progenitors, it was demonstrated that the total number of PNe is naturally reduced which will have an effect on the total number of PNe calculated in each epoch here, and the total number of PNe currently visible in the Milky Way. However, it is still unknown to what extent this assumption holds true. For this reason, the population synthesis models are calculated both with and without this assumption.

### PN progenitor mass range

The lower mass limit of stars that evolve to form PNe is another subject of debate and uncertainty, and is related to the PN visibility time and so is also stellar model dependent. If the central star does not reach ionisation temperatures before the ejected nebula becomes too dispersed, the nebula will not become ionised and will not be visible as a PN. The typically accepted, textbook, lower-limit for stars becoming PNe is  $0.8 M_{\odot}$ . Moe & De Marco (2006) on the other hand determined a lower-limit of  $0.9 M_{\odot}$  from the post-AGB evolution tracks of Schoenberner (1983), but to circumvent the uncertainty, they calculate their model taking lower limits of  $0.85$  and  $0.95 M_{\odot}$  also. In a similar fashion, the population synthesis in this work is calculated using various lower progenitor mass-limits for the formation of PNe. The populations here are calculated with  $0.8$ ,  $0.9$  and  $1 M_{\odot}$  as the lower mass-limits for stars which evolve to form visible PNe. Stars with initial masses below the adopted lower limit in these models can make a PN only if they undergo a binary interaction or engulf a massive planet on the AGB.

## 5.3 Results: The present-day population of galactic planetary nebulae

To explore the present-day population in terms of the planet-fraction, the steps outlined in the previous sections were carried out to determine the total number of visible PNe in the present-day population, and in particular the number of those which have evolved through the engulfment of a massive planet on the AGB. 48 models were calculated, one for each combination of the assumptions described in section 5.2.4, in an effort to constrain the uncertainty coming from any assumptions or approximations. The 48 models consisted of two mass-loss prescriptions for determining the probability of stars having and engulfing massive planets, two forms of the initial mass function, three lower-limit masses for PN progenitors, two prescriptions for the prevention of a PN by a binary common envelope on the RGB and two prescriptions for the prevention of a PN by planet engulfment on the RGB. The total number of visible PNe was then obtained by taking the mean of the calculations, and the overall uncertainty is obtained from the standard deviation of the calculations.

### 5.3.1 The total number of PNe and the planet-fraction

The resulting PN population consisted of a total of  $16,500 \pm 2,200$  visible PNe in the present-day galactic population. Of these,  $240 \pm 20$  PNe have evolved through the engulfment of a massive planet on the AGB,  $3,300 \pm 200$  PNe have evolved from a binary interaction during the AGB (including mild and severe interactions), and  $13,000 \pm 2,100$  PNe have evolved from either wide binary systems (and thus no interaction) and single stars without a planet engulfment during the AGB. Thus the planet-fraction of planetary nebulae from the models presented here is  $\approx 1.5\%$  and the binary-fraction is  $\approx 20\%$ . These results are summarised in table 5.2. Table 5.3 lists the results from each model which are also illustrated in figure 5.3. Of all calculations, the highest total number of visible PNe is 20,800 PNe (Model 40), and the lowest is 12,300 PNe (Model 21). The higher total is the result of a model calculated with the probabilities of stars having and engulfing massive planets calculated with the MIST models of Choi et al. (2016) with  $\eta_R = 0.1$  and  $\eta_B = 0.2$ , a Chabrier (2003) IMF, adopting a lower mass-limit of  $0.8 M_\odot$  for the formation

of a PN and assuming that 10% of binaries are prevented from evolving to the PN phase by an RGB interaction and that the engulfment of a massive planet on the RGB does not prevent the star from becoming a PN. The planet-fraction in this model is  $\approx 1.2\%$ . On the other hand, the lower total is the result of adopting the standard mass-loss prescriptions for planet engulfment (those calculated by the author with  $\eta_R = 0.5$  and  $\eta_B = 0.1$ ), a Kroupa (2001) IMF, adopting  $1 M_\odot$  as the lower mass-limit for PN formation and assuming that 28% of binaries are prevented from evolving to the PN phase by an RGB interaction and that the engulfment of a massive planet on the RGB does prevent the star from evolving to the PN phase. The planet-fraction in this model was  $\approx 1.9\%$ . The total expected non-spherical PN population was also highest in this model at  $\approx 27\%$  of the total population. Of all models calculated, the planet-fraction never exceeds 2% and the binary-fraction never exceeds 25%.

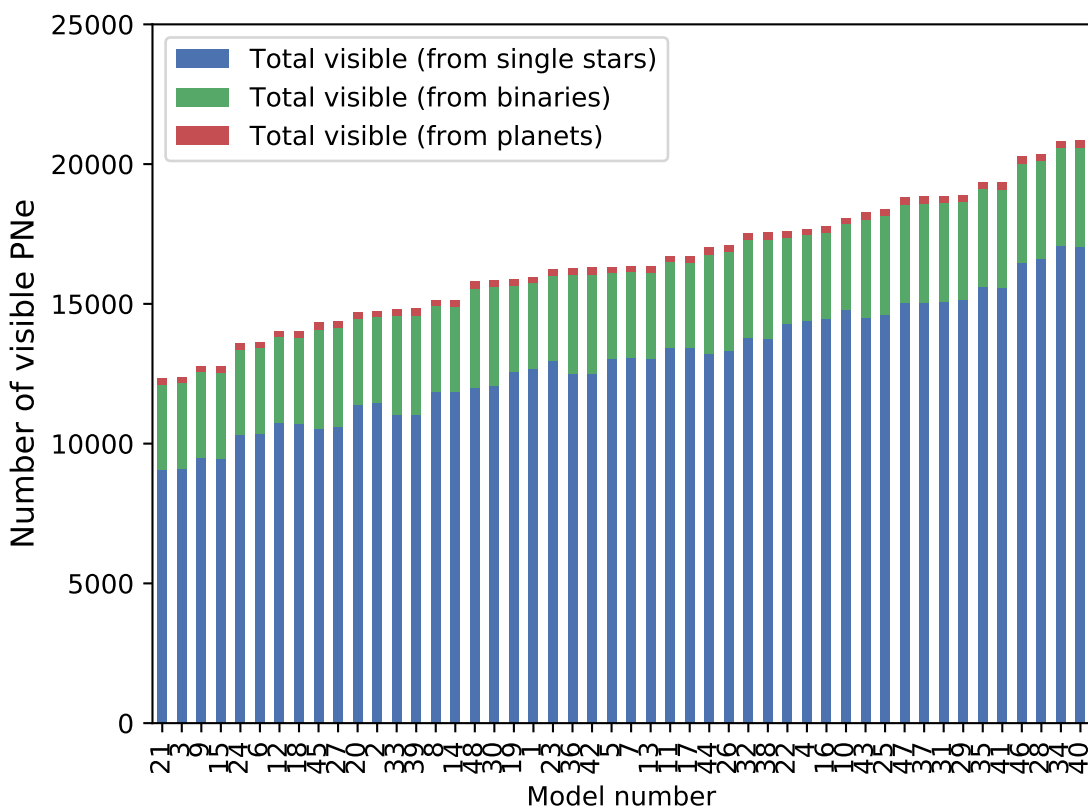


Figure 5.3: Summary plot of the total number of visible PNe resulting from the population synthesis models. Model numbers correspond to those in table 5.2.

### 5.3. RESULTS: THE PRESENT-DAY POPULATION OF GALACTIC PLANETARY NEBULAE

---

$N_{\text{PN}}$	Planet-fraction	Binary-fraction	Single-fraction
16,500	1.5% (240 PNe)	20% (3,300 PNe)	78.5% (13,000 PNe)

Table 5.2: The resulting present-day planetary nebula population from the population synthesis model outlined in this chapter. Values were obtained by taking the mean of all 48 models calculated.

If planet engulfment does result in the formation of non-spherical PNe, and all AGB binary interactions result in non-spherical PNe, then the total fraction of non-spherical PNe from the population synthesis should be  $\approx 21.5\%$ , where 93% of the non-spherical population would be the result of binary interactions and  $\approx 7\%$  would be the result of planet engulfment.

The total number of visible PNe emanating from each epoch for a range of models, some of which have combinations of assumptions and approximations which produce some of the lower and higher total numbers of PNe, are plotted in the bottom panel of figure 5.4, and the corresponding planet fractions are plotted in the top panel. To investigate the reason for such a low expected planet-fraction, the mean progenitor mass of the present-day population of PNe was calculated and found to be  $\approx 1.4 M_{\odot}$ , which corresponds to a population which formed  $\approx 3$  Gyrs ago, according to equation 5.5 (see the shaded region in the bottom panel of figure 5.4). The mean metallicity of stars forming at that time was  $\langle Z_* \rangle \approx 0.016$  (see the shaded region in the top panel of figure 5.4). Given the fact that the probability for stars having and engulfing planets on the AGB based on this mean progenitor mass and metallicity is only 0.019 - 0.025 (depending on the stellar models employed), because of the relatively low -mass progenitors, this result highlights further the necessity of performing the population synthesis here, rather than basing a conclusion off of the current galactic PN progenitor population, as demonstrated for illustration purposes in chapter 4, which would have over-predicted the planet-fraction (as it would have predicted a planet-fraction of between 3-9% for a population evolved with similar mean metallicity). Also evident from figure 5.4, the model plotted in blue in particular (model 15), is the effect of the turnoff masses in a population and also the effect of adopting a higher PN progenitor lower mass limit. This model is the result of calculating the population while adopting the assumption that single stars with masses  $M_* < 1 M_{\odot}$  are not capable of forming a visible PN and so the number of PNe emanating from each

epoch is consistently lower than the other models plotted, which all assume a lower PN progenitor mass limit. In the earliest epochs, the turnoff masses for the populations of stars forming are lower than  $1 M_{\odot}$  and so only stars forming in these epochs which can interact with a planet or binary will form visible PNe, which produces the steep change in the model at the point where the turnoff mass reaches  $1 M_{\odot}$ .

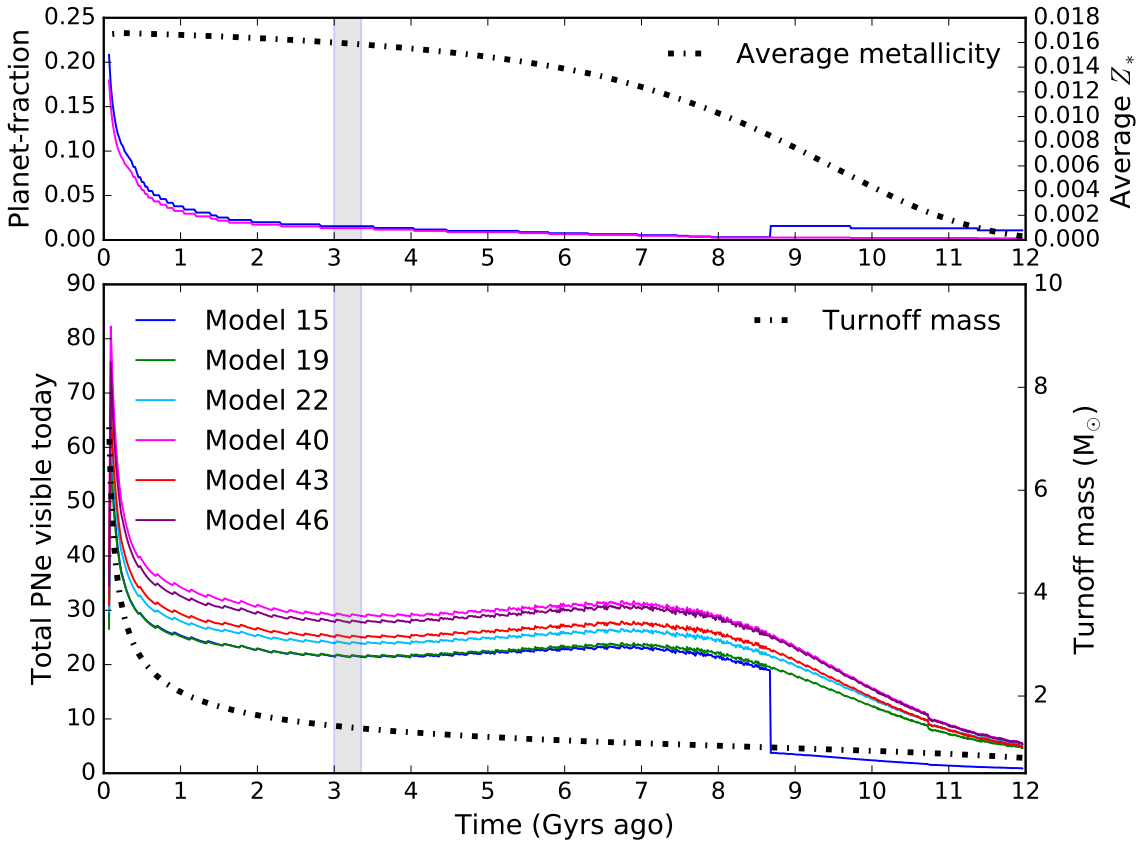


Figure 5.4: The total number of visible PNe emanating from each epoch for a range of models. The top panel displays the planet-fraction of each epoch and the metallicity as a function of time, while the bottom panel displays the total number of visible PNe currently in the galaxy emanating from each epoch. The shaded regions illustrate the epochs corresponding to turnoff masses of  $\approx 1.4 M_{\odot}$ , which is the mean mass of a PN progenitor from the population synthesis models. The mean PN progenitor mass corresponds to populations of stars forming  $\approx 3$  Gyrs ago with an average metallicity of  $\approx 0.016$ . Model numbers correspond to those in table 5.3.

The population synthesis predicts a non-spherical fraction of PNe (that is, the binary-fraction plus the planet-fraction) that is in disagreement with the observed non-spherical population of PNe ( $\approx 80\%$ ). Given that it is widely accepted that a binary interaction is needed to shape a PN (e.g., Garcia-Segura et al. 2014), it was expected that the result of the

population synthesis would be in reasonable agreement with the observed non-spherical population when taking into account both binary statistics and planet engulfment, which was indeed the motivation for this study. However it is apparent that planet engulfment by the AGB progenitors of PNe cannot resolve the mystery of the non-spherical PN population, even though planet engulfment may be likely to be the cause for some of them. The result of the population synthesis calculated here then agrees with suggestions that maybe not all low-mass single-star PN progenitors are capable of producing visible PNe (e.g., Soker & Subag 2005; Moe & De Marco 2006; De Marco & Soker 2011). This is discussed in the next section, where the total number of PNe calculated here is compared with previous theoretical and observational estimates.

### 5.3.2 Comparison with earlier estimates and observations

While the goal of this work was not necessarily to calculate the total number of PNe in the galaxy, it was a necessary requirement to arrive at the planet-fraction of visible PNe. Having arrived at a total number of galactic PNe, though, allows for a comparison to the expected total population of PNe derived from previous population synthesis calculations and, perhaps of most relevance, the expected total derived from observational estimates. This in turn allows for the determination of how well the model fits into the current paradigm for the population of galactic PNe and, in particular, how the planet-fraction fits into this paradigm.

An observational estimate on the total number of galactic PNe, based on extrapolating the column density of PNe in the solar neighbourhood to the whole galaxy, by Frew (2008), which excluded all PNe with radii  $>0.9$  pc, resulted in a total of  $13,000 \pm 2,000$  PNe, which is in agreement with an earlier estimate of Jacoby (1980), who determined a total number of  $10,000 \pm 4,000$  PNe. The total number of PNe calculated by the population synthesis presented here of  $16,500 \pm 2,200$  PNe thus agrees within the error bars of the observationally determined value of Frew (2008), but falls just outside that of Jacoby (1980). The total number of PNe produced in this model, however, appears to be in better agreement with the number of PNe calculated with observational estimates than the theoretical prediction of Moe & De Marco (2006), who calculated a total number of visible galactic PNe of  $46,000 \pm 13,000$  PNe.

Of the most concern is the fact that the resulting expected non-spherical population of PNe calculated here does not mirror that which is observed, which is not entirely unexpected with regards to binary shaping, but means that the engulfment of planets cannot explain a large enough fraction of non-spherical PNe to solve the mystery of PN morphologies. Even the models that assume that the RGB engulfment of planets prevent PNe, which should lower the total number of PNe from single-stars, do not come close to the observed population. This does however, fit into the paradigm that not all single stars are capable of producing luminous, observable PNe. In fact, in an attempt to resolve the discrepancy between their theoretical prediction and their observationally based estimate, Moe & De Marco (2012) updated the theoretical framework of Moe & De Marco (2006) to include only single star evolution for stars with masses  $>2.3 \text{ M}_\odot$ . Their justification for this was that according to the *superwind paradigm* of the interacting winds theory of Kwok (2000), an AGB star must sustain a superwind of at least  $\dot{M}_* = 3 \times 10^{-5} \text{ M}_\odot \text{ yr}^{-1}$  during the time it takes for the envelope mass to decrease from  $\approx 0.3 \text{ M}_\odot$  to  $10^{-3} - 10^{-4} \text{ M}_\odot$ . By adopting various AGB mass-loss prescriptions, and noting that AGB mass-loss is in itself a highly uncertain process, they found that the limiting mass for a single PN progenitor to sustain such a superwind on the AGB to be between  $1.3 - 2.6 \text{ M}_\odot$ . Thus their updated population synthesis model adopted  $2.3 \text{ M}_\odot$  for the lower PN progenitor mass-limit, unless the star experiences a binary interaction on the AGB. This reduced the total number of PNe in their model to  $11,400 \pm 5,000$  PNe and thus resolving the discrepancy between their original observationally based target value, as well as the recent value of Frew (2008), and their theoretical models. However, the assumption that single stars with main-sequence masses below  $2.3 \text{ M}_\odot$  will not make a PN is arguably a rather bold one, and is not generally accepted as the limiting mass for PN production. Nonetheless, this fits into the paradigm that perhaps binary interactions are indeed a precursor for the production of PNe, particularly given the fact that the processes that triggers the onset of the superwind at the end of the AGB are still not well understood (De Marco 2009). Their calculations resulted in a binary-fraction of  $71 \pm 20\%$ , with the remaining 30% of PNe evolving from single stars and wide binaries with primary masses  $>2.3 \text{ M}_\odot$ . Their resulting number of total galactic PNe, as well as the binary-fraction, was indeed in agreement with their observational estimate and the fraction of PNe with non-spherical morphologies, leading them to conclude that not all stars considered to be PN progenitors actually

go on to form PNe.

It is a tempting stance to take here since the planet-fraction would then increase, as would the binary-fraction, and the resulting population would fit the observational population in terms of morphological classes. However, even though the exact processes which lead to ejection of the AGB envelope are still not well understood, there is still no certainty in whether or not a companion (be it a planet or a binary) is indeed needed to form a PN at all. Furthermore, by adopting such a lower mass-limit, the population synthesis model here under-predicts the total number of PNe ( $\approx 5,000$  galactic PNe, however the under-prediction could be explained by the limitations and approximations in the star formation and metallicity history modelling of the galaxy - which is discussed in the next section). Nonetheless, this is not the first time that the possibility of single-stars being unable to produce visible PNe has been suggested to rationalise the lack-of progenitor binaries (e.g., Soker & Subag 2005). Another interesting piece of evidence in the morphological puzzle is the predicted fraction of post-common envelope PNe of Madappatt et al. (2016), which was also surprisingly low at just 2.5% of all PN progenitors which is in stark disagreement with the observed fraction of 15-20% (Miszalski et al. 2009). If it is true that single stars can only produce spherical, sub-luminous PNe that are not readily detected, then the planet-fraction of all visible PNe would be  $\approx 7\%$ , the binary-fraction would be  $\approx 93\%$ , and interestingly the fraction of post-common envelope PNe would be  $\approx 12\%$ , when taking the fraction calculated by Madappatt et al. (2016) into account, which is still too low especially considering that their post-common envelope binary-fraction does not account for the possibility of stellar mergers, but it is in much better agreement with the observed PN population. Considering that the observed population of non-spherical PNe accounts for 80% of the total, and it is predicted here that 7% of non-spherical PNe should be the result of a planet engulfment on the AGB, it can be regarded that  $\approx 6\%$  of all currently visible PNe have been shaped by planets which agrees comfortably with the earlier prediction of De Marco & Soker (2011) which suggested that a  $\approx 5\%$  planet-fraction would be needed alongside the binary-fraction to shape PNe; an estimate which was based entirely off of the fractions of the observed morphological classes.

### 5.3.3 Model limitations

A number of assumptions and approximations made in the population synthesis introduce uncertainty which have not been accounted for in the results presented here. In this section the limitations of the population synthesis model are highlighted.

Firstly the PN visibility times have an effect on the total number of PNe as well as the determination of the number coming from each epoch and most importantly the number of planet-shaped PNe. In order to accurately model the PN visibility time, post-AGB evolution tracks are needed, for example those adopted by Moe & De Marco (2006) of Vassiliadis & Wood (1994), which can then be interpolated to determine the length of time a PN central star with a progenitor of any mass and metallicity retains an effective temperature of  $T_{\text{eff}} > 25000$  K and luminosity  $\log(L_*/L_{\odot}) > 1.5$ . However, recent post-AGB models calculated with updated AGB opacities and mass-loss rates by Miller Bertolami (2016) suggest shorter post-AGB and PN evolution timescales than those predicted by Vassiliadis & Wood (1994). A formation history of the galactic bulge PNe conducted by Gesicki et al. (2017) showed that upon adopting the new post-AGB models of Miller Bertolami (2016) they were able to reproduce the observational distributions of galactic bulge PNe and white dwarfs in contrast to a similar study by Gesicki et al. (2014) which adopted the old models. Thus the adopted post-AGB models for determining the PN visibility times are worth examining more closely in future calculations.

In order to construct the present-day PN population an average star formation history and an average metallicity history was adopted (that is, they vary temporally, but not spatially). These are likely the biggest sources of error in the resulting total number of PNe calculated here, and also the resulting planet-fraction. Moe & De Marco (2006) developed a galactic model in which the galaxy was divided into its four main components (the bulge, thin and thick disks and the spheroid/halo) in order to follow the star formation history, and metallicity evolution, for each component separately. However, their model over-predicts the total number of visible PNe, and it is difficult to determine the reason for this but a possible explanation might be in their modelling of the star formation history. Behroozi et al. (2013) argue that the declining-tau models, which Moe & De Marco (2006) adopt, are only a good fit to the most massive galaxies (that is, more massive than the Milky Way) and thus they may be over-predicting the star formation rate at various

epochs. On the other hand, their approach is arguably more robust for the following reasons. Firstly, adopting an average star formation history in this work is assuming that all components of the galaxy began star formation at the same time, which is not the case (e.g., Idiart et al. 1996; Naab & Ostriker 2006; Bensby et al. 2004, for the bulge, thin disk, thick disk and halo, respectively). Since the star formation rate depends on the total mass of the galaxy (or galactic component), when star formation began, when it ended or whether or not it is ongoing, this will have a substantial impact on the number of stars which have formed in each epoch and have evolved to form PNe in the present-day population. However, star formation history modelling of the various galactic components is, in general, extremely complex. For example, Naab & Ostriker (2006) suggest that the star formation rate of the galactic disk varies as a function of radial distance from the galactic centre. Similarly, adopting an average metallicity across the entire galaxy has an effect on the stellar lifetimes. Each component has a different metallicity distribution (e.g., Bensby et al. 2004). By not accounting for a metallicity distribution across the components of the galaxy, a substantial error has been incurred in the lifetimes of stars, and thus the numbers of stars from each epoch which have evolved to present-day PN population. This of course would also have an impact on the number of PNe evolving from the engulfment of a planet, since the probability of having and engulfing planets depends so strongly on the metallicity of the host-stars. In essence, even though each newly formed population of stars was considered separately, the model presented here still assumes that the galaxy is a coeval population by not considering each galactic component separately. As such, an updated galactic model for the Multi-epoch population mode of SIMSPLASH is suggested for future work.

## 5.4 The consequences of planet engulfment on the evolution of PN progenitors

The vast majority of the observed population of planetary nebulae are non-spherical. The variations in the morphologies of PNe were discussed in chapter 1, where the mystery surrounding their shaping was also introduced. It is clear from the arguments discussed there, many of which are the result of decades of research in the PN community, that the presence of a binary is needed to explain the non-spherical morphologies of PNe (e.g., De Marco 2009; Jones & Boffin 2017). Because the progenitor binary-fraction cannot account for the fraction of non-spherical PNe, the planet-shaping hypothesis was suggested over two decades ago, as a complementary binary channel to that of stellar binaries. Soker (1997) pointed to an interesting theoretical argument in support of the planet-shaping hypothesis, which was perhaps one of the catalysts for the planet-shaping idea in the first place, regarding the work of Chevalier & Soker (1989) on the asymmetrical expansion of the supernova 1987A. Soker (1997) proposed that since the asymmetrical explosion of SN 1987A can be explained by a  $0.5 M_{\odot}$  secondary star, and if the system is scaled down such that the primary is of a PN progenitor mass (a factor of  $\approx 15$ ), the secondary mass is scaled down to that of a brown dwarf, hinting that low-mass companions can indeed produce even some of the most extreme morphologies in PNe. More recently, the idea has gained traction in the community and has become something of a contingency for the lack of binary progenitors. Until now, however, it was unknown to what extent planet engulfment might explain the non-spherical population of PNe.

The planet-fraction of planetary nebulae, according to the population synthesis carried out in this research, suggests a planet-fraction of  $\approx 1.5\%$ . While this fraction may appear unproductively low, when taking into account the binary-fraction from this model and the fact that all non-spherical PNe must come from a binary interaction or the engulfment of a planet, this indicates that  $\approx 7\%$  of the observed non-spherical population of planetary nebulae could have been shaped by planets; which is an observable fraction, given that 80% of observed PNe are non-spherical. If planet engulfment does result in non-spherical PNe morphologies, then this implies that a substantial proportion of the observed non-spherical planetary nebulae have indeed been shaped by planets. In that case, it is perfectly

reasonable to expect that in some of the observed systems there may be evidence of the engulfment and subsequent destruction of massive planets.

Thus, despite the relatively low expected planet-fraction of planetary nebulae calculated here, it is still interesting to consider the supporting theoretical arguments for the events that occur *after* engulfment which can lead to the shaping of PNe, as well as recent observational speculation in favour of the hypothesis. For the much of the following discussion, the reader is reminded of the work of Nordhaus & Blackman (2006) regarding the outcomes of a common envelope or a planet engulfment which was depicted in chapter 1 and reproduced here in figure 5.5. In scenario (a) of figure 5.5, when the planet en-

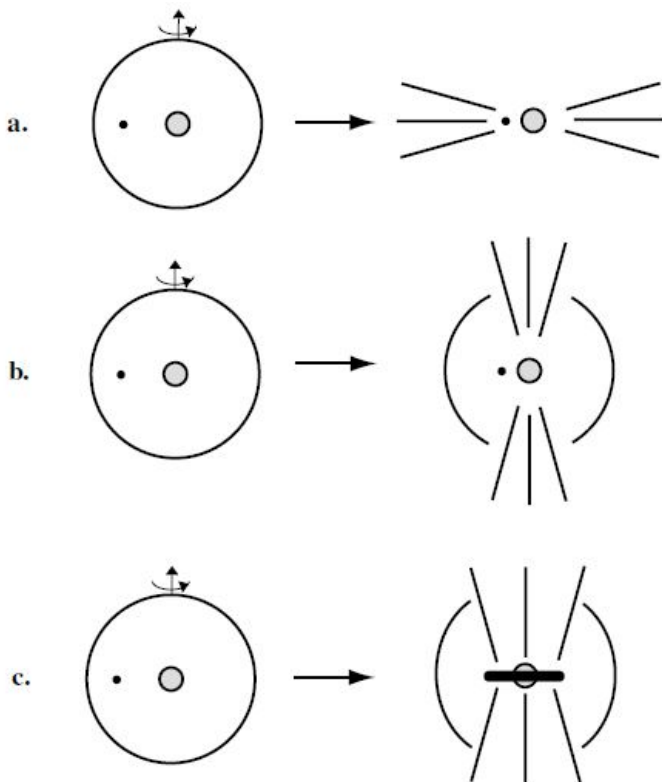


Figure 5.5: Some of the possible outcomes of a binary common envelope scenario, or a planet engulfment, proposed by Nordhaus & Blackman (2006). (a): The removal of mass from the envelope in the orbital plane, or equatorial region, of the system. (b): An alpha-omega dynamo generation of a magnetic field as a result of the differential rotation between the secondary and the AGB envelope. (c): the destruction of the companion near the core of the AGB star, formation of an accretion disk, and a disk-driven outflow.

ters the envelope the injection of orbital energy and angular momentum from this process causes the envelope to become unbound, the planet would therefore survive the process and a non-spherical PN would emerge as a result of the density enhancement due to the

removal of mass in the orbital plane. However, Nordhaus & Blackman (2006) showed that in most cases a planet would not provide enough orbital energy and angular momentum to unbind the envelope. On the other hand, as an alternative to scenario (a), even though the increase of angular momentum cannot unbind the envelope directly, as the planet enters the envelope it is likely to cause the excitation of pressure waves during its in-spiral process (e.g., Soker 1992, 2004). The pressure waves are thought to begin as small-scale oscillations in the orbital plane, which increase in amplitude as they propagate outwards, and increase the mass-loss rate. As the planets orbit decays further, the effect of the pressure waves becomes more pronounced (Soker 1992, 1993).

Scenario (b) in figure 5.5, describes the introduction of external angular momentum from the engulfment of the planet which could be the cause for the generation of an alpha-omega dynamo as a result of the differential rotation introduced by the planet in the convective AGB envelope, and thus shaping by magnetic fields in the form of collimated bipolar outflows. This scenario is unlikely as it would require the planet to survive the entire AGB phase by unbinding the envelope during the in-spiral process (Nordhaus et al. 2011). However, as an alternative to scenario (b), even if the induced differential rotation is not enough to sustain a large-scale dynamo, other magnetic effects have been postulated. Even the small increase in rotation that a planet can introduce (e.g., Carlberg et al. 2009) may promote a modest dynamo in the envelope leading to the formation of cool magnetic spots on the surface of the AGB star, particularly along the equator, facilitating the formation of dust in the region and thus increasing the mass-loss rate in the equatorial plane leading to the formation of an elliptical PN (Soker & Clayton 1999; Nordhaus & Blackman 2006). Thus a combination of both of the alternatives to scenarios (a) and (b) may produce the asymmetrical mass-loss needed to shape a PN. Recently Kervella et al. (2016) measured the mass of the companion to the star L<sub>2</sub> Puppis, a nearby AGB star with a dusty circumstellar disk and an observed bipolar morphology, to be about 1 M<sub>J</sub> providing exciting new support for the planet-shaping hypothesis. In this case, if the planet was the cause of the emerging bipolar morphology, the planet has survived the interaction and the shaping would likely be a result of a combination of the scenarios described thus far.

Scenario (c) in figure 5.5 represents the most extreme consequence of the engulfment of a massive planet by the AGB progenitors of PNe, as discussed most recently by Nordhaus (2017). In this case, the planet cannot unbind the AGB envelope and continues its

in-spiral towards the core of the star until it reaches a critical radius known as the *shredding radius*, which is defined as the radius within which the differential gravitational force across the planet, arising from the AGB core, exceeds the binding force of the planet itself (its self-gravity), at which point the planet will be ripped apart or *shredded* (Nordhaus & Blackman 2006). The material from the now destroyed planet will be colder and denser than the surrounding gas and have enough angular momentum to form an accretion disk around the core of the AGB star (Soker 1996a; Reyes-Ruiz & López 1999; Nordhaus et al. 2011; Nordhaus 2017). Recent ALMA observations by Santander-García et al. (2017) revealed a dense ring of molecular gas near the central star of the bipolar PN NGC 6302, which they speculate might be the remnants of a planet since the mass of the ring has been measured as  $\simeq 3 M_J$ . While they state that more simulations would be needed to form any conclusions on the nature and origin of the material, it is highly appealing to consider it as evidence for the planet-shaping hypothesis in terms of scenario (c). Nordhaus et al. (2011) describes the implications of an accretion disk of planet material forming around the AGB core. They find that even for disks forming from planets with masses as low as  $0.1 M_J$ , the accretion onto the core becomes *hyper-critical*, meaning that the accretion initially exceeds the Eddington accretion limit by a few orders of magnitude due to inefficient photon pressure being unable to slow the accretion. The energy released by such a high accretion rate can be carried away by powerful outflows or jets (e.g., Ohsuga et al. 2005) which can shape the resulting planetary nebula and may even be responsible for secondary morphological features such as ansae (as discussed in sections 1.4.1 and 1.4.2). If planets with masses as low as  $0.1 M_J$  can produce this effect, then the planet-fraction calculated in this chapter needs to be revised, and would likely be much higher. Support for this scenario can be sought by the recent work of Blackman & Lucchini (2014) with regards to the creation of outflows in a sample of PPNe, who found that the kinematical properties of the observed outflows in PPNe were well described by the accretion disks formed inside the envelopes of an AGB star. In this context, another speculative observational clue in favour of the planet shaping hypothesis comes from the long-term radial velocity searches for binary central stars in PPNe of Hrivnak et al. (2017), in which the presence of binaries in their sample remains elusive, leading to the suggestion that the *binaries* are (or rather *were*) in fact planets. Finally Nordhaus et al. (2011) describe how the accretion of material, which presumably contains the gaseous hydrogen envelope of a

Jupiter-like planet, onto the core can be ignited in an unstable, explosive, thermonuclear CNO burning process and, if the material is near the helium burning shell outside the core, it may even be capable of causing a thermonuclear runaway explosion which could potentially completely remove the envelope. Clyne et al. (2014) hypothesised a similar series of events leading to the extreme bipolar morphology of PN MyCn 18, as an alternative to a binary companion which to-date has not been revealed. Since the excitation of pressure waves as the planet enters the envelope is expected to result in massive *clumps* in the stellar winds (e.g., Soker 2017), a combination of the alternative to scenario (a) and the explosions from scenario (c) might explain both the extreme morphology and the hypersonic knotty outflows in PN MyCn 18.

While perhaps not directly linked to shaping, it is worth mentioning recent observational speculation of destroyed planets being connected to the long-standing abundance discrepancy problem (Liu et al. 2006; Corradi et al. 2015; García-Rojas et al. 2016). Recently, García-Rojas et al. (2016) reported, for the first time, direct imaging of a high-metallicity gas component close to the central star of NGC 6778, a PN with a binary central star and an unusually high abundance discrepancy factor (ADF) of around 20 (where the expected value for an ADF should only be between 1-3, e.g., Wesson et al. 2005). While in the case of NGC 6778, and many of the known PNe with a high ADF (e.g., Corradi et al. 2015), the presence of a binary indicates that any shaping is a result of a stellar binary. However, the suggestion that the source of a high ADF may be linked to metal-rich material from the destruction of a planet may provide a means for future characterisation of the shaping of PNe by planet engulfment in non-spherical systems where the presence of a binary has been ruled out. An intriguing example is PN NGC 6153, an elliptical PN with an extreme ADF in which no known binary central star has been found. Yuan et al. (2011) found that a three-dimensional *bi-abundance* photoionisation model consisting of normal warm nebular gas and a small mass of cooler metal-rich inclusions, can produce the observed ADF in this object, leading the authors to suggest that the origin of the metal-rich gas may indeed be a destroyed planet. In this case, with no known binary, the planet could be the source of the elliptical morphology also. With the results presented in this thesis, the idea of planets as an explanation to the abundance discrepancy problem in systems such as this is strengthened. Similar detailed three-dimensional photoionisation models for these systems should be explored in future.

Finally, it is worth mentioning the shaping possibilities of multi-body systems with planets (multiple planet systems orbiting single stars or stellar binary systems with planets). While these systems are not explicitly modelled in this research (but they are implicitly accounted for, since multiple planet systems are assumed to evolve as single systems with one planet and the binary statistics would contain binaries with planets), both the known exoplanets and synthetic planet populations indicate that multiple planet systems are not a rarity, and there are an increasing number of binary systems with planets being added to the Exoplanet Orbit Database. These systems may provide a perfect breeding ground for some of the most perplexing PN morphologies. One example is the model of Manchado et al. (1996) to explain the quadrupolar PNe M 2-46 and M 1-75, in which a binary system provides a disk which collimates the outflow to form one pair of lobes, and then the disk is precessed by an orbiting planet which changes the symmetry axis and forms the second pair of lobes. Santander-García et al. (2010) made the point that the precession of a disk in the case of M 1-75 is unlikely since the kinematical ages of the lobes indicates that each ejection should have happened too rapidly, suggesting instead that a planet engulfment could be the culprit if, for example, the planet itself caused a disk which then becomes warped by radiative instabilities. Nonetheless, both the Manchado et al. (1996) and Santander-García et al. (2010) models provide interesting speculation on the potential role of multiple planets and binary systems with planets in shaping some of the most mysterious PNe. An interesting, related, hypothesis stems from the recent work of Bollen et al. (2017) in which a triple system results in a merger of two components within the envelope of the AGB star resulting in powerful jets which result in messy or irregular PNe. They define that a triple system can either consist of three stellar components or even planets/brown dwarfs. Detailed morpho-kinematic modelling of these types of objects combined with three-dimensional photoionisation models discussed earlier might uncover interesting results on their shaping mechanisms.

## 5.5 Summary and conclusions

In this chapter, the SIMSPLASH Multi-epoch population mode was introduced and used to calculate the present-day population of planetary nebulae in the galaxy, with the particular aim of determining the planet-fraction of planetary nebulae; the fraction of planetary nebulae which are shaped by the engulfment of a planet during the AGB phase of their progenitors evolution. The Multi-epoch population mode performs a population synthesis by utilising an average galactic star formation history and associated galactic metallicity evolution relationship combined with the probabilities of planet engulfment on the RGB and AGB derived in chapter 4 of this thesis and also the probabilities of same when calculated using the standard mass-loss prescriptions.

This is the first time a population synthesis of planets and planetary nebulae has been attempted with the thorough treatment of tides and also adopting synthetic planet populations to circumvent the observational bias in the known exoplanets. Because of the growing support for the planet-hypothesis in planetary nebulae, one can expect that population synthesis of planets around evolving stars in the context of PNe will soon be of utmost interest. The ways in which the engulfment of a massive planet during the AGB phase can alter the morphology of the subsequent PNe was discussed.

It was found that despite the fact that the models here predict that an observable proportion of non-spherical PNe would have evolved through the engulfment of a planet on the AGB, shaping by planets is unable to account for the remaining population of non-spherical PNe that the progenitor binary-fraction also fails to account for. These results therefore add support to the suggestion that not all low-to-intermediate mass single stars can form visible PNe. Nonetheless, the Multi-epoch population mode of SIMSPLASH is a useful tool in predicting the PN population from the engulfment of planets. A summary of the main conclusions from this chapter is as follows:

- The total number of visible galactic PNe predicted from the population synthesis here is  $16,500 \pm 2,200$  PNe, of which  $240 \pm 20$  PNe evolved through a planet engulfment on the AGB, resulting in a planet-fraction of  $\simeq 1.5\%$ . The total number of binary PNe (stemming from both mild and severe binary interactions) is  $3,300 \pm 200$  PNe. The binary-fraction is thus  $\simeq 20\%$ . Together, the binary-fraction

and the planet-fraction yield an expected non-spherical PN fraction of just  $\simeq 21.5\%$ , which is in disagreement with the observed non-spherical population of  $\simeq 80\%$  of all PNe. This result supports the argument that not all single stars can make visible PNe. If it is true that low-mass single stars cannot form a visible PN, then the expected planet-fraction of observable PNe in the present-day galaxy would be  $\simeq 7\%$ .

- It was demonstrated that the planet-fraction varies between 1-2% across all 48 population synthesis models calculated, depending on the assumptions adopted. Furthermore, from this it is evident that the variation between the resulting planet-fractions when adopting the engulfment probabilities with the stellar models that employ standard mass-loss coefficients and the MIST stellar models, is negligible. Hence, while the mass-loss prescriptions employed in the stellar models here effected the engulfment zones of individual systems as demonstrated in chapter 3, the effect was not substantial when averaged over an entire population.
- Even though the expected planet-fraction is relatively low, since 80% of the observed population of PNe are non-spherical, there are some observational hints of the engulfment of planets in an observable proportion of non-spherical PNe. Future observational work on individual PNe in which there is a lack of evidence for binarity should consider this.

Table 5.3: The resulting PN progenitor populations from the 48 population synthesis models. Each model represents a combination of the assumptions and approximations outlined in section 5.2.4. Where  $\text{RGB}_B$  refers to the fraction of binary systems that are prevented from becoming PNe due to an interaction on the RGB,  $\text{RGB}_{\text{pl}}$  refers to whether or not it is assumed that the engulfment of a planet on the RGB prevents the formation of a PN (the number of such are obtained from the RGB engulfment probabilities),  $\dot{M}$  represents the mass-loss prescription used in calculating the probabilities of stars engulfing planets and is either low (using the MIST models of Choi et al. 2016) or standard (calculated by the author with MESA),  $M_{\text{low}}$  refers to the lower mass-limit of stars which can form PNe, the IMF is the initial mass function which is either a Kroupa (2001) (denoted as K01 in table) IMF or a Chabrier (2003) (denoted as C03 in table) IMF. The resulting numbers of PNe in the population, as well as the number of those coming from planets, binaries and single star evolution are denoted as  $N_{\text{PN}}$ ,  $N_{\text{pl}}$ ,  $N_B$  and  $N_S$ , respectively.

Model	$\text{RGB}_B$	$\text{RGB}_{\text{pl}}$	$\dot{M}_*$	$M_{\text{low}}(\text{M}_\odot)$	IMF	$N_{\text{PN}}$	$N_B$	$N_{\text{pl}}$	$N_S$
1	0.28	yes	low	0.8	K01	15947	3068	209	12670
2	0.28	yes	low	0.9	K01	14750	3068	209	11473
3	0.28	yes	low	1	K01	12381	3068	209	9104
4	0.1	yes	low	0.8	K01	17673	3068	209	14396
5	0.1	yes	low	0.9	K01	16320	3068	209	13042
6	0.1	yes	low	1	K01	13640	3068	209	10362
7	0.28	no	low	0.8	K01	16348	3068	209	13070
8	0.28	no	low	0.9	K01	15145	3068	209	11868
9	0.28	no	low	1	K01	12759	3068	209	9482
10	0.1	no	low	0.8	K01	18073	3068	209	14796
11	0.1	no	low	0.9	K01	16715	3068	209	13438
12	0.1	no	low	1	K01	14018	3068	209	10741
13	0.28	no	standard	0.8	K01	16348	3068	235	13044
14	0.28	no	standard	0.9	K01	15148	3068	235	11844
15	0.28	no	standard	1	K01	12766	3068	235	9462
16	0.1	no	standard	0.8	K01	18073	3068	235	14470
17	0.1	no	standard	0.9	K01	16717	3068	235	13414
18	0.1	no	standard	1	K01	14025	3068	235	10721
19	0.28	yes	standard	0.8	K01	15866	3068	235	12562
20	0.28	yes	standard	0.9	K01	14686	3068	235	11382
21	0.28	yes	standard	1	K01	12346	3068	235	9043

Table 5.3 Continued:

Model	RGB <sub>B</sub>	RGB <sub>pl</sub>	$\dot{M}_*$	$M_{\text{low}}(\text{M}_\odot)$	IMF	$N_{\text{PN}}$	$N_{\text{B}}$	$N_{\text{pl}}$	$N_{\text{S}}$
22	0.1	yes	standard	0.8	K01	17592	3068	235	14288
23	0.1	yes	standard	0.9	K01	16255	3068	235	12952
24	0.1	yes	standard	1	K01	13605	3068	235	10302
25	0.28	yes	low	0.8	C03	18385	3537	243	14604
26	0.28	yes	low	0.9	C03	17089	3537	243	13308
27	0.28	yes	low	1	C03	14383	3537	243	10602
28	0.1	yes	low	0.8	C03	20375	3537	243	16594
29	0.1	yes	low	0.9	C03	18910	3537	243	15129
30	0.1	yes	low	1	C03	15849	3537	243	12068
31	0.28	no	low	0.8	C03	18851	3537	243	15070
32	0.28	no	low	0.9	C03	17549	3537	243	13768
33	0.28	no	low	1	C03	14824	3537	243	11042
34	0.1	no	low	0.8	C03	20841	3537	243	17060
35	0.1	no	low	0.9	C03	19370	3537	243	15589
36	0.1	no	low	1	C03	16290	3537	243	12508
37	0.28	no	standard	0.8	C03	18851	3537	273	15039
38	0.28	no	standard	0.9	C03	17552	3537	273	13740
39	0.28	no	standard	1	C03	14831	3537	273	11020
40	0.1	no	standard	0.8	C03	20841	3537	273	17029
41	0.1	no	standard	0.9	C03	19372	3537	273	15561
42	0.1	no	standard	1	C03	16297	3537	273	12486
43	0.28	yes	standard	0.8	C03	18293	3537	273	14481
44	0.28	yes	standard	0.9	C03	17015	3537	273	13203
45	0.28	yes	standard	1	C03	14343	3537	273	10531
46	0.1	yes	standard	0.8	C03	20283	3537	273	16471
47	0.1	yes	standard	0.9	C03	18835	3537	273	15024
48	0.1	yes	standard	1	C03	15809	3537	273	11997



# Chapter 6

## Summary and conclusions

### 6.1 Introduction

The objective of the research presented in this thesis was to test the hypothesis that planet engulfment on the asymptotic giant branch is responsible for the shaping of a subset of planetary nebulae by exploring the orbital evolution of star-planet systems, determining the probabilities of stars engulfing massive planets and applying this information in a planetary nebula population synthesis. The novelty of this research can be attributed, in part, to the application of tidal evolution modelling of star-planet systems to planet populations derived from planet formation and evolution theories to determine the probability of a star having and engulfing a massive planet as a function of the stellar mass and metallicity. The planet population models adopted here are based on the current theories of planet formation and have not been employed in this type of study before, and were adopted since they provide the mass and semi-major axis distributions of exoplanets, which cannot yet be deduced from exoplanet observations. Another novel aspect of this research is the inclusion of the aforementioned results in a planetary nebula population synthesis study to determine, for the first time, the expected planet-fraction of PNe. Finally, the development of the new tool, `SIMSPLASH`, to perform this study provides a means for future experiments on the topic.

The most important result from this research is the finding that the planet-fraction of planetary nebulae in the present-day galaxy should fall between 1-2%, depending on the stellar models employed to evolve the star-planet systems as well as assumptions under-

taken about the stellar populations from which they form. From this it can be concluded that the planet-fraction, combined with the binary-fraction, cannot explain the observed non-spherical majority of planetary nebulae. The following sections provide a summary of the work, as well as the conclusions arising from each chapter, that led to this result.

## 6.2 Summary

### 6.2.1 SIMSPLASH: A new tool for exploring the effect of planet engulfment on the PN population

The work required to obtain the results presented in this thesis was made possible through the development of a new tool, SIMSPLASH, which consists of three modes of operation to explore the orbital evolution and engulfment of planets orbiting PN progenitors as well as calculating the present-day population of PNe. SIMSPLASH, in its Orbital mode allows the user to explore and experiment with the conditions for engulfment of individual star-planet systems; its Single-epoch population mode allows the user to explore the probabilities of engulfment in PN progenitor populations; and its Multi-epoch population mode allows the user to conduct a population synthesis in order to construct the full present-day population of PNe and the fraction of which were shaped via a planet engulfment. SIMSPLASH currently contains a database of pre-calculate stellar tracks between  $0.8$  and  $8.0 M_{\odot}$  in increments of  $0.1 M_{\odot}$  for a range of metallicities between  $Z_* = 0.005$  and  $Z_* = 0.025$ . Such a range of stellar masses in the database may seem redundant regarding the fact that the planet populations adopted in this research consist of synthetic models for six specific star masses, and the known exoplanets data does not contain systems with host star masses larger than  $\approx 3 M_{\odot}$ . However, these stellar tracks will become more useful as more exoplanet discoveries are made, particularly with the forecasted potential of the ongoing Gaia mission, since the known exoplanets are expected to become more complete in terms of host star masses above  $1.5 M_{\odot}$  (Winn & Fabrycky 2015).

SIMSPLASH is a valuable tool for the planet shaping hypothesis since it allows for an efficient exploration of planet engulfment in planetary nebula progenitor populations and also the quick calculation of a planetary nebula population synthesis, including the effects of planet engulfment on the present-day population. As exoplanets become more com-

plete and knowledge on planet formation theory advances, the results can be re-calculated following the methods presented in this thesis using `SIMSPLASH`.

### 6.2.2 Exploring the engulfment zones of planetary nebula progenitors

In chapter 3, the `SIMSPLASH` Orbital mode was introduced and used to explore the conditions for engulfment by PN progenitors. The RGB and AGB engulfment zones were then demonstrated for various star-planet systems with various stellar properties. The semi-major axis evolution models calculated with `SIMSPLASH` were shown to agree well with orbital evolution models in the literature in terms of sensitivity to stellar mass, particularly around the masses marking the transition from those stars which develop electron degenerate helium cores and those that do not (e.g., Villaver et al. 2014). Generally, a star which reaches degeneracy has a much more extended envelope on the RGB, and so the AGB engulfment zone width tends to be smaller. Also in general agreement with the orbital evolution models from the literature was the sensitivity to planet-mass (e.g., Villaver & Livio 2009; Kunitomo et al. 2011). While the width of the AGB engulfment zone tends to remain constant, both the RGB and AGB engulfment zone boundaries are shifted upwards with increasing planet mass.

The semi-major axis evolution as a result of mass-loss and tides that is implemented in `SIMSPLASH` was tested for star-planet systems using the MIST stellar evolution tracks of Choi et al. (2016), which have a lower RGB Reimers mass-loss coefficient than the typical value adopted in orbital evolution models across the literature. The result of employing a modest mass-loss on the RGB is that the semi-major axis evolution due to the tides can more easily dominate over mass-loss, extending the RGB engulfment zone boundary. The AGB engulfment zone is also extended since less mass is ejected on the RGB, allowing the core to grow to larger masses and extending the lifetime and maximum radius reached on the AGB. It was discussed that a modest prescription for mass-loss on the RGB may indeed be appropriate as it reproduces the initial-to-final mass ratios in clusters (e.g., Miglio et al. 2012), and that there has also been recent speculation that the higher mass-loss rates observed on the RGB may only be appropriate in a binary system, or after a planet has been engulfed but not before any engulfment has occurred (Sabach &

Soker 2018). The effects of including and neglecting rotation in the stellar models was also presented. It was demonstrated that a stellar model calculated with rotation turned on results in an increase in the RGB engulfment zone boundaries and a decrease in the AGB engulfment zone boundaries, such that the width of the AGB engulfment zone decreases by  $\simeq 5\%$ , in contrast to the decreasing RGB engulfment zone boundary found by Privitera et al. (2016). Such a result has revealed another source of uncertainty in tidal evolution modelling with regards to rotational mixing during the main sequence and its effect on the post main sequence evolution. Finally, it was suggested that the effect of initial composition on the semi-major axis evolution is an important consideration for population synthesis since there is a strong correlation between the formation of planets and host-star metallicity. Thus the engulfment zones calculated using stellar models with a range of metallicities in SIMSPLASH were presented.

### **6.2.3 The planet-fractions of planetary nebula progenitor populations**

In chapter 4, the SIMSPLASH Single-epoch population mode was introduced and used to calculate, for the first time, the probabilities of PN progenitor stars having and engulfing massive planets, as a function of mass and metallicity and apply this information to the current PN progenitor population to calculate the planet-fraction of planetary nebula progenitors. The planet-fraction of planetary nebula progenitors refers to the fraction of planet-hosting planetary nebula progenitors currently in the galaxy which will engulf a massive planet during the AGB phase of its future evolution and go on to form a non-spherical PN as a result. This was performed considering two independent planet samples. One of these was the sample of the currently known exoplanets from the Exoplanet Orbit Database, and the other was a sample of massive planets derived from adopting a synthetic planet population generated from the planet formation and evolution models of Ida and Lin (provided by Shigeru Ida for this work) (Ida & Lin 2004a,b, 2005, 2008a,b, 2010; Ida et al. 2013). Each sample was evolved using the Single-epoch population mode of SIMSPLASH, which determines the number of RGB and AGB engulfs in a given input sample, and determines the probabilities of stars engulfing massive planets as a function of host-star mass and metallicity. This was achieved by adopting the five different sets of

stellar models available in `SIMSPLASH`, each with a different stellar metallicity, to determine the probabilities of massive planet engulfment as a function of host star mass for a given metallicity. The probabilities were then interpolated with respect to metallicity in order to compute a fine grid of engulfment probabilities as a function of host-star mass and metallicity. The probabilities of planet engulfment were then combined with the occurrence rates of massive planets as a function of host-star mass and metallicity to determine the probability of stars having and engulfing massive planets which was then used to calculate the present-day planetary nebula progenitor population in terms of total number of PN progenitors, the total number of which will undergo a binary interaction and most importantly the total number of which will engulf massive planets on the AGB.

It was demonstrated that the planet-fraction of all PN progenitors, depending on the adopted mean metallicity (between  $Z_* = 0.014$  and  $Z_* = 0.025$ ) of planet-hosting stars for the Milky Way, can range from 3% - 9% or 2% - 6% when adopting the distribution of the known exoplanets or the synthetic planet populations, respectively . The fractions, respectively, translate to 15%-30% and 10%-23% of the population which would evolve to form non-spherical PNe. However, it was noted that the current population of PN progenitors is not representative of the current population of PNe so estimating the planet-fraction from these results is not an adequate approach. However the results presented in this chapter, namely the computed probabilities of stars having and engulfing planets as a function of star mass and metallicity, are an imperative ingredient in the population synthesis calculations presented in chapter 5.

### 6.2.4 The planet-fraction of planetary nebulae in the Milky Way

In chapter 5, the `SIMSPLASH` Multi-epoch population mode was introduced and used to calculate, for the first time, the planet-fraction of planetary nebulae currently in the Milky Way by conducting a population synthesis including the probabilities of stars having and engulfing planets as a function of mass and metallicity. The results presented in this chapter have demonstrated that the planet-fraction of planetary nebulae in the present-day galaxy should fall between 1-2%, depending on the stellar models employed to evolve the star-planet systems as well as assumptions undertaken about the stellar populations from which they form. From this it can be deduced that, if planet engulfment on the AGB

can indeed shape a PN, then  $\simeq 7\%$  of the observed non-spherical PN population are the result of planet shaping. This is an observable fraction of PNe, particularly given that  $\simeq 80\%$  of observed PNe are non-spherical. However, the combined fraction of all PNe which should have evolved through either a planet engulfment or a binary interaction is only  $\simeq 22\%$ , which means that the mystery still remains as to why the vast majority of observed PNe are non-spherical. The results here demonstrate that planets are unlikely to increase the fraction of expected non-spherical PNe enough to resolve the mystery and so provides support to the argument put forward by Soker & Subag (2005) that perhaps not all single stars can actually evolve to form a visible planetary nebula.

The limiting approximations contained within the population synthesis in `SIMSPLASH` were highlighted, with the approximation of an average star formation history and galactic metallicity being the two most important sources of error in these calculations. Finally, given that the planet-fraction of non-spherical PNe should be an observable proportion if planet engulfment does influence a PN morphology, the ways in which a planet can shape a PN was revisited as well as recent observational evidence pointing to the planet-shaping hypothesis. Future plans to update the Multi-epoch population mode of `SIMSPLASH` are outlined in the next section.

## 6.3 Future work

### 6.3.1 The future of the known exoplanets: Re-calculating the planet-fraction with discoveries from Gaia

For the research presented in this thesis, since the orbital evolution of the star-planet systems depended on the host-star masses and the planet masses and semi-major axes, the data which made up the sample from which the engulfment probabilities were calculated were those discovered via the radial velocity method. While the radial velocity method has arguably been the most successful detection method with regards to advancing our knowledge of exoplanets, it does have its limitations in that it is sensitive to low mass stars with close-in planets. As we saw in chapter 4, most of these planets will be within the RGB engulfment zones of their hosts.

Astrometric methods, on the other hand, have the potential to detect and deduce the properties of exoplanet systems with wider orbits, since the amplitude of the displacement of the centre of mass increases with increasing orbital period (Fischer et al. 2014). However, despite astrometry being the oldest exoplanet search method (Jacob 1855), astrometric searches have not been fruitful for discoveries with only a handful to date (Perryman et al. 2014; Winn & Fabrycky 2015). The European Space Agency (ESA) Gaia mission promises to change this. Gaia began its 5 year observational period in 2014. During this time it has been (and continues to) monitor, through repeated measurements, the positions, distances and change in brightness of around a thousand million stars, of magnitude as low as 20 to extreme accuracy ( $\simeq 10 - 20\mu\text{as}$ ). It is expected that data from the Gaia mission will lead to the discovery of  $\simeq 70,000$  planets,  $\simeq 21,000$  of which with masses between  $1-15 M_J$  (Perryman et al. 2014), around stars of all ages and masses. Thousands of these are expected to have semi-major axes out to 3-4 AU (Winn & Fabrycky 2015). For this reason, the future Gaia results are extremely exciting for determining exoplanet statistics, and in particular for this research, the planet-fraction of planetary nebulae. Indeed, central stars of planetary nebula observations with Gaia may possibly reveal planets which were engulfed by the progenitor orbiting within the nebula, if the planet has not been destroyed. Future work will then involve employing the eventual exoplanet samples from Gaia to improve on the results presented here already.

### 6.3.2 Proposed updates to SIMSPLASH

A new tool, `SIMSPLASH`, was developed specifically to carry out the research in this thesis. While it is the first of its kind in terms of combining orbital evolution modelling of star-planet systems, synthetic planet populations stemming from current planet formation theories and planetary nebula population synthesis techniques, there are some assumptions embedded within the framework which lead to uncertainty in the resulting planet-fractions, in particular those which were discussed in chapter 5. Future work will involve building upon each working mode in `SIMSPLASH` and also eliminating the aforementioned uncertainties.

Firstly, the Orbital mode and Single-epoch population mode of `SIMSPLASH`, in which the orbital evolution is calculated for star-planet systems, consists of a database of stellar evolution tracks all calculated with the `MESA` stellar evolution code (Paxton et al. 2011, 2013, 2015) and is thus currently only capable of handling `MESA` stellar model output files. Other stellar evolution codes may have a different file format, however, so in order to be fully capable of evolving star-planet systems with *any* stellar evolution track from any stellar evolution code, the handling of the output from stellar evolution codes needs to be updated within `SIMSPLASH`. With regards to eliminating the uncertainties in the population synthesis calculations presented in chapter 5. It is envisioned that the Multi-epoch population mode of `SIMSPLASH` will be updated to calculate the planetary nebula visibility time as a function of progenitor mass and metallicity, rather than assuming an average visibility time. Finally, it is clear that adopting an average galactic star formation history, and average galactic metallicity evolution is a rather rudimentary approach and is likely the biggest source of uncertainty in the population synthesis presented in this thesis, since it assumes that the galaxy is *spatially* coeval, which is indeed not the case. Each principle galactic component began, and in some components has already ended, star formation at different epochs and thus the star formation rates are not constant across all components. Furthermore, since the stellar metallicity is not only important for the probability of a star having and engulfing a massive planet, but also for the stellar lifetimes and PN visibility times, computing a galactic model with a star formation history and metallicity evolution which varies spatially across the galaxy will greatly improve upon the results presented here.

### 6.3.3 PN MyCn 18: A planet-shaped planetary nebula?

PN MyCn 18, also known as the *Etched Hourglass Nebula*, is a striking example of a young, compact, planetary nebula displaying extreme bipolarity, made famous by the striking WFPC2 narrowband images of Sahai et al. (1999). Like many planetary nebulae, the origin of its morphology is a mystery. The high speed knots ( $\simeq 500$  km/s) discovered by Bryce et al. (1997), located outside the main nebula, which cannot be explained by the generalised interacting stellar winds model are particularly troublesome to explain.

Despite attempts, a binary companion has not been observed in MyCn 18 (e.g., Clyne et al. 2014), and so the cause of its morphology is still unclear. It is therefore reasonable to assume, in the apparent absence of a stellar companion, that the engulfment of a planet during the AGB phase may have led to an accretion disk of destroyed planet material around the stellar core leading to powerful outflows (Nordhaus et al. 2011; Clyne et al. 2014), as discussed in section 5.5. Evidence of this is expected to be found within the rarely studied high speed knots. Thus a future investigation for exploring the planet shaping hypothesis would involve a deep spectroscopic study of MyCn 18, in which emission line strengths of both the knotty structures and the main nebula are measured, to allow for a comparison of their compositions. This would also allow for the measurement of the abundance discrepancy factor (ADF) of the nebula. Furthermore, by adopting the 3-D density distribution of MyCn 18 (as computed by Clyne et al. 2014) one can compute a 3-D photoionisation model of the nebula using, for example, the PYCLOUDY code (Morisset 2013; Ferland et al. 2017). Such a technique was introduced by Akras et al. (2016) for modelling PN Abell 14. If the nebula is found to have an abnormal ADF, it should then be determined whether the 3-D photoionisation model can produce the ADF when modelled with clumps of the same composition as the knotty outflows, providing a link between the source of the outflows and the source of the ADF.

It is unclear, as of yet, the exact elemental enrichment/depletion that should be expected from a planet destruction event. However, by quantifying the composition of the nebula and the knots it should be possible to model the knots in terms of either a nova-like event, a destroyed planet, or a binary star interaction, to determine the most plausible scenario.



# Appendix A

## Deterministic models of planet formation

The following is a summary of the typical ingredients in a planet formation and evolution model outlined in a recent review by Benz et al. (2014), along with the description of initial conditions and method followed by the Ida & Lin models which produced the planet populations adopted in this research:

- **Structure and evolution of the proto-planetary disk**

When producing a planet population from a planet formation model, it is assumed that the observed distributions of exoplanets must be correlated with the observed distributions of the proto-planetary disks from which they formed. Thus the initial conditions for the disks are drawn from probability distributions derived from proto-planetary disk observations using Monte Carlo techniques. The disk properties needed for a planet formation model are the total disk mass, the initial radial profiles of the gas and solids surface densities in the disk, and the disk lifetime. Ida & Lin follow a log-normal distribution for the mass of the disk with a median value of  $0.01 M_*$  and a dispersion of 10 ( $0.001 - 0.1 M_\odot$ ). The disk lifetime is also modelled as a log-normal distribution with a median value of 3 Myrs/ ( $M_*/M_\odot$ ) and a dispersion of 3 [ $(1 - 10)$  Myrs/ ( $M_*/M_\odot$ )]. For the densities of gasses and solids, they adopt the minimum-mass solar nebula model of Hayashi (1981) for their initial conditions and introduce scaling factors,  $f_d$  and  $f_g$ , to scale the disk surface densities of gas and planetesimals, where  $f_d$  is given by  $f_{g,0} 10^{[\text{Fe}/\text{H}]}$  and  $f_g$  decreases

exponentially as a function of the disk lifetime ( $f_{g,0}$  is the initial gas-fraction of the disk and [fe/H] is the stellar metallicity).

- **Structure and evolution of the disk of planetesimals**

Ida & Lin model the distribution of planetesimals within the disk as  $(0.035 - 10) \times (M_*/M_\odot)^2$  AU. Planetesimals are defined as rocky or icy by their initial position in the disk, where those which form within the ice line are rocky and those outside are icy (the ice line is defined as the position in the disk outside of which the temperature of the gas is below the ice condensation temperature. The ice line is given by  $2.77(M_*/M_\odot)^2$  AU in their models. The motion and dynamics of the planetesimals within the disk are important as the growth rate of planets will be influenced by the collision rates of the planetesimals. Ida & Lin model the growth rate of a proto-planet by the spatial mass density of the planetesimals and relative velocity between a proto-planet and planetesimals, where the velocity dispersion of the planetesimals is determined by the balance between gravitational interactions with proto-planets and damping due to gas-drag.

- **Accretion of solids and gases**

In a planet formation model proto-planets are first seeded by very small masses which then grow by the accretion of planetesimals and gas. Ida & Lin model the growth of the proto-planets by a timescale defined by the mass and semi-major axis of the proto-planet seed and the local gas density.

If the proto-planetary core reaches a sufficient mass, known as the critical core mass, it can begin to accrete the surrounding gas, provided it has been capable of cooling. Fitting formulae derived by calculations of envelope structure and heat transfer are typically used to determine the critical core mass. Once the critical core mass is reached by the proto-planet, the accretion of gas continues and is governed by the subsequent envelope contraction which determines whether the proto-planet evolves to a gas giant or not.

- **N-body interactions among proto-planets/planets**

After their growth, the proto-planets tend to be in isolated and almost circular orbits until such time that the disk gas is depleted leading to perturbations in the orbits

---

and hence an increase in eccentricities, orbit crossing and subsequently collisions between proto-planets. Collisions act to increase the mass of the proto-planets but also contribute to planet scattering and possible ejection from the disk which results in the planets left behind being in highly eccentric orbits which may alter the orbital evolution of the entire system. Because they are computationally expensive, N-body simulations in the Ida & Lin planet formation models are computed via semi-analytic Monte-Carlo methods to compute the outcomes of such interactions from statistical distributions.

- **Planet-disk interactions**

There are two types of interactions between a resulting planet and the disk: migration and gap formation. Planet migration is a result of the exchange of angular momentum between the disk and the newly formed planet. Planet migration depends on the mass of the planet, where the lower mass planets follow what is known as *type I migration* and the higher mass planets follow *type II migration*. Type I migration occurs due to an imbalance between the different torques exerted by the inner and outer regions of the disk, whereas type II migration occurs due to the fact that a high mass planet is more capable of creating a gap in the disk which it is then confined to. The rate of migration is determined from numerical calculations and the local viscous evolution of the disk for type I and type II migration, respectively. The Ida & Lin models adopt isothermal type I migration with 10× reduced speed because non-isothermal type I migration is not clear for large mass stars. Gravitational torques exerted on the disk by the planet facilitates the formation of a gap in the disk. Once formed, the gap reduces the flow of gas to the planet, and so accretion either slows or discontinues completely.



# Bibliography

- Adamów, M., Niedzielski, A., Villaver, E., Nowak, G., & Wolszczan, A. 2012, ApJL, 754, L15
- Akras, S., Clyne, N., Boumis, P., et al. 2016, MNRAS, 457, 3409
- Amiri, N., Vlemmings, W., & van Langevelde, H. J. 2011, A&A, 532, A149
- Balick, B. 1987, AJ, 94, 671
- Balick, B., Alexander, J., Hajian, A. R., et al. 1998, AJ, 116, 360
- Balick, B. & Frank, A. 2002, ARA&A, 40, 439
- Balick, B., Rugers, M., Terzian, Y., & Chengalur, J. N. 1993, ApJ, 411, 778
- Bear, E. & Soker, N. 2011, MNRAS, 411, 1792
- Behroozi, P. & Peeples, M. S. 2015, MNRAS, 454, 1811
- Behroozi, P. S., Wechsler, R. H., & Conroy, C. 2013, ApJ, 770, 57
- Bensby, T., Feltzing, S., & Lundström, I. 2004, A&A, 421, 969
- Benz, W., Ida, S., Alibert, Y., Lin, D., & Mordasini, C. 2014, Protostars and Planets VI, 691
- Bertelli, G., Bressan, A., Chiosi, C., Fagotto, F., & Nasi, E. 1994, A&AS, 106
- Bjorkman, J. E. & Cassinelli, J. P. 1993, ApJ, 409, 429
- Blackman, E. G., Frank, A., Markiel, J. A., Thomas, J. H., & Van Horn, H. M. 2001a, Nature, 409, 485

## BIBLIOGRAPHY

---

- Blackman, E. G., Frank, A., & Welch, C. 2001b, ApJ, 546, 288
- Blackman, E. G. & Lucchini, S. 2014, MNRAS, 440, L16
- Bloecker, T. 1995, A&A, 297, 727
- Boffin, H. M. J. 2015, in Ecology of Blue Straggler Stars, 153
- Boffin, H. M. J., Miszalski, B., Rauch, T., et al. 2012, Science, 338, 773
- Bollen, D., Van Winckel, H., & Kamath, D. 2017, A&A, 607, A60
- Bond, H. E. 1976, PASP, 88, 192
- Boss, A. P., Butler, R. P., Hubbard, W. B., et al. 2007, Transactions of the International Astronomical Union, Series A, 26, 183
- Bowen, I. S. 1928, ApJ, 67
- Bowler, B. P., Johnson, J. A., Marcy, G. W., et al. 2010, ApJ, 709, 396
- Boyle, L. A. & Redman, M. P. 2017, in IAU Symposium, Vol. 323, Planetary Nebulae: Multi-Wavelength Probes of Stellar and Galactic Evolution, ed. X. Liu, L. Stanghellini, & A. Karakas, 193–196
- Bryce, M., López, J. A., Holloway, A. J., & Meaburn, J. 1997, ApJL, 487, L161
- Bujarrabal, V. 2016, in Journal of Physics Conference Series, Vol. 728, Journal of Physics Conference Series, 032010
- Bujarrabal, V., Castro-Carrizo, A., Alcolea, J., & Sánchez Contreras, C. 2001, A&A, 377, 868
- Butler, R. P., Marcy, G. W., Vogt, S. S., et al. 2002, ApJ, 578, 565
- Caffau, E., Ludwig, H.-G., Steffen, M., Freytag, B., & Bonifacio, P. 2011, Sol. Phys., 268, 255
- Capriotti, E. 1971, ApJ, 166, 563
- Capriotti, E. R. 1973, ApJ, 179, 495

- Carlberg, J. K., Majewski, S. R., & Arras, P. 2009, *ApJ*, 700, 832
- Chabrier, G. 2003, *PASP*, 115, 763
- Charpinet, S., Fontaine, G., Brassard, P., et al. 2011, *Nature*, 480, 496
- Chevalier, R. A. & Luo, D. 1994, *ApJ*, 421, 225
- Chevalier, R. A. & Soker, N. 1989, *ApJ*, 341, 867
- Choi, J., Dotter, A., Conroy, C., et al. 2016, *ApJ*, 823, 102
- Chu, Y.-H., Jacoby, G. H., & Arendt, R. 1987, *ApJS*, 64, 529
- Clyne, N., Akras, S., Steffen, W., et al. 2015, *A&A*, 582, A60
- Clyne, N., Redman, M. P., Lloyd, M., et al. 2014, *A&A*, 569, A50
- Conroy, C. 2013, *ARA&A*, 51, 393
- Corradi, R. L. M., García-Rojas, J., Jones, D., & Rodríguez-Gil, P. 2015, *ApJ*, 803, 99
- Corradi, R. L. M., Rodríguez-Gil, P., Jones, D., et al. 2014, *MNRAS*, 441, 2799
- Corradi, R. L. M. & Schwarz, H. E. 1995, *A&A*, 293, 871
- Curtis, H. D. 1918, *Publications of Lick Observatory*, 13, 55
- Darwin, G. H. 1879, *The Observatory*, 3, 79
- De Marco, O. 2009, *PASP*, 121, 316
- De Marco, O., Bond, H. E., Harmer, D., & Fleming, A. J. 2004, *ApJL*, 602, L93
- De Marco, O. & Izzard, R. G. 2017, *PASA*, 34
- De Marco, O. & Soker, N. 2011, *PASP*, 123, 402
- de Souza, R. S., Dantas, M. L. L., Krone-Martins, A., et al. 2016, *MNRAS*, 461, 2115
- Dehnen, W. & Binney, J. 1998, *MNRAS*, 294, 429
- Delfosse, X., Kahane, C., & Forveille, T. 1997, *A&A*, 320, 249

## BIBLIOGRAPHY

---

- Deutsch, A. J. 1956, ApJ, 123, 210
- Dorman, B., Rood, R. T., & O'Connell, R. W. 1993, ApJ, 419, 596
- Dotter, A. 2016, ApJS, 222, 8
- Dyson, J. E., Hartquist, T. W., Pettini, M., & Smith, L. J. 1989, MNRAS, 241, 625
- Ekström, S., Georgy, C., Eggenberger, P., et al. 2012, A&A, 537, A146
- Etoka, S. & Diamond, P. 2004, MNRAS, 348, 34
- Ferland, G. J., Chatzikos, M., Guzmán, F., et al. 2017, RMxAA, 53, 385
- Fischer, D. A., Howard, A. W., Laughlin, G. P., et al. 2014, Protostars and Planets VI, 715
- Fischer, D. A. & Valenti, J. 2005, ApJ, 622, 1102
- Frank, A., Balick, B., Icke, V., & Mellemma, G. 1993, ApJL, 404, L25
- Frank, A., Balick, B., & Riley, J. 1990, AJ, 100, 1903
- Frew, D. J. 2008, Ph.D. Thesis
- Frew, D. J. 2017, in IAU Symposium, Vol. 323, Planetary Nebulae: Multi-Wavelength Probes of Stellar and Galactic Evolution, ed. X. Liu, L. Stanghellini, & A. Karakas, 11–19
- Gaidos, E. & Mann, A. W. 2014, ApJ, 791, 54
- García-Rojas, J., Corradi, R. L. M., Monteiro, H., et al. 2016, ApJL, 824, L27
- García-Segura, G., Langer, N., Różyczka, M., & Franco, J. 1999, ApJ, 517, 767
- García-Segura, G., López, J. A., & Franco, J. 2005, ApJ, 618, 919
- García-Segura, G., Villaver, E., Langer, N., Yoon, S.-C., & Manchado, A. 2014, ApJ, 783, 74
- Geier, S., Edelmann, H., Heber, U., & Morales-Rueda, L. 2009, ApJL, 702, L96
- Gesicki, K., Zijlstra, A. A., Hajduk, M., & Szyszka, C. 2014, A&A, 566, A48

- Gesicki, K., Zijlstra, A. A., & Miller Bertolami, M. M. 2017, in Astronomical Society of the Pacific Conference Series, Vol. 509, 20th European White Dwarf Workshop, ed. P.-E. Tremblay, B. Gaensicke, & T. Marsh, 457
- Goldreich, P. & Nicholson, P. D. 1977, in *baas*, Vol. 9, Bulletin of the American Astronomical Society, 474
- Gonçalves, D. R., Corradi, R. L. M., & Mampaso, A. 2001, *ApJ*, 547, 302
- Greaves, J. S. 2002, *A&A*, 392, L1
- Guerrero, M. A., Chu, Y.-H., & Miranda, L. F. 2004, *AJ*, 128, 1694
- Han, E., Wang, S. X., Wright, J. T., et al. 2014, *PASP*, 126, 827
- Han, Z., Podsiadlowski, P., Maxted, P. F. L., & Marsh, T. R. 2003, *MNRAS*, 341, 669
- Han, Z., Podsiadlowski, P., Maxted, P. F. L., Marsh, T. R., & Ivanova, N. 2002, *MNRAS*, 336, 449
- Hayashi, C. 1981, *Progress of Theoretical Physics Supplement*, 70, 35
- Henyey, L., Vardya, M. S., & Bodenheimer, P. 1965, *ApJ*, 142, 841
- Herschel, W. 1791, *Philosophical Transactions of the Royal Society of London*, 81, 71
- Herwig, F. 2000, *A&A*, 360, 952
- Herwig, F. 2005, *ARA&A*, 43, 435
- Hillwig, T. C., Jones, D., De Marco, O., et al. 2016, *ApJ*, 832, 125
- Hrivnak, B. J., Van de Steene, G., Van Winckel, H., et al. 2017, *ApJ*, 846, 96
- Huggins, W. & Miller, W. A. 1864, *Philosophical Transactions of the Royal Society of London Series I*, 154, 437
- Hurley, J. R., Tout, C. A., & Pols, O. R. 2002, *MNRAS*, 329, 897
- Iaconi, R., De Marco, O., Passy, J.-C., & Staff, J. 2017, ArXiv e-prints, 1706, arXiv:1706.09786

## BIBLIOGRAPHY

---

- Iaconi, R., Reichardt, T., Staff, J., et al. 2017, MNRAS, 464, 4028
- Iben, Jr., I. & Livio, M. 1993, PASP, 105, 1373
- Icke, V. 1988, A&A, 202, 177
- Icke, V., Preston, H. L., & Balick, B. 1989, AJ, 97, 462
- Ida, S. & Lin, D. N. C. 2004a, ApJ, 604, 388
- Ida, S. & Lin, D. N. C. 2004b, ApJ, 616, 567
- Ida, S. & Lin, D. N. C. 2005, ApJ, 626, 1045
- Ida, S. & Lin, D. N. C. 2008a, ApJ, 673, 487
- Ida, S. & Lin, D. N. C. 2008b, ApJ, 685, 584
- Ida, S. & Lin, D. N. C. 2010, ApJ, 719, 810
- Ida, S., Lin, D. N. C., & Nagasawa, M. 2013, ApJ, 775, 42
- Idiart, T. P., de Freitas Pacheco, J. A., & Costa, R. D. D. 1996, AJ, 111, 1169
- Ignace, R. 1996, PASP, 108, 1142
- Ivanova, N., Justham, S., Chen, X., et al. 2013, A&AR, 21, 59
- Jacob, W. S. 1855, MNRAS, 15, 228
- Jacoby, G. H. 1980, ApJS, 42, 1
- Johnson, J. A., Aller, K. M., Howard, A. W., & Crepp, J. R. 2010a, PASP, 122, 905
- Johnson, J. A., Butler, R. P., Marcy, G. W., et al. 2007, ApJ, 670, 833
- Johnson, J. A., Howard, A. W., Bowler, B. P., et al. 2010b, PASP, 122, 701
- Jones, D. & Boffin, H. M. J. 2017, Nature Astronomy, 1, 0117
- Jones, D., Boffin, H. M. J., Miszalski, B., et al. 2014, A&A, 562, A89
- Jones, D., Boffin, H. M. J., Rodríguez-Gil, P., et al. 2015, A&A, 580, A19

- Jones, D., Lloyd, M., Mitchell, D. L., et al. 2010, MNRAS, 401, 405
- Jordan, S., Werner, K., & O'Toole, S. J. 2005, A&A, 432, 273
- Kahn, F. D. & West, K. A. 1985, MNRAS, 212, 837
- Kaler, J. B. 1974, AJ, 79, 594
- Karakas, A. I. & Lattanzio, J. C. 2014, PASA, 31, e030
- Kennicutt, Jr., R. C. 1998, ApJ, 498, 541
- Kervella, P., Homan, W., Richards, A. M. S., et al. 2016, A&A, 596, A92
- Kroupa, P. 2001, MNRAS, 322, 231
- Kunitomo, M., Ikoma, M., Sato, B., Katsuta, Y., & Ida, S. 2011, ApJ, 737, 66
- Kwok, S. 2000, Cambridge Astrophysics Series, 33
- Kwok, S. 2007, in Asymmetrical Planetary Nebulae IV
- Kwok, S. 2010, PASA, 27, 174
- Kwok, S., Chong, S.-N., Koning, N., Hua, T., & Yan, C.-H. 2008, ApJ, 689, 219
- Kwok, S., Purton, C. R., & Fitzgerald, P. M. 1978, ApJL, 219, L125
- Liu, X.-W., Barlow, M. J., Zhang, Y., Bastin, R. J., & Storey, P. J. 2006, MNRAS, 368, 1959
- Liu, X.-W., Storey, P. J., Barlow, M. J., et al. 2000, MNRAS, 312, 585
- Lloyd, J. P. 2013, ApJL, 774, L2
- Madappatt, N., De Marco, O., & Villaver, E. 2016, MNRAS, 463, 1040
- Maercker, M., Mohamed, S., Vlemmings, W. H. T., et al. 2012, Nature, 490, 232
- Maiolino, R., Nagao, T., Grazian, A., et al. 2008, A&A, 488, 463
- Maldonado, J., Villaver, E., & Eiroa, C. 2013, A&A, 554, A84

## BIBLIOGRAPHY

---

- Manchado, A. 2004, in Astronomical Society of the Pacific Conference Series, Vol. 313, Asymmetrical Planetary Nebulae III: Winds, Structure and the Thunderbird, ed. M. Meixner, J. H. Kastner, B. Balick, & N. Soker, 3
- Manchado, A., Stanghellini, L., & Guerrero, M. A. 1996, ApJL, 466, L95
- Marigo, P. 2001, A&A, 370, 194
- Matsuura, M., Speck, A. K., McHunu, B. M., et al. 2009, ApJ, 700, 1067
- Mayor, M. & Queloz, D. 1995, Nature, 378, 355
- McDonald, I. & Zijlstra, A. A. 2015, MNRAS, 448, 502
- Mellema, G. & Frank, A. 1995, MNRAS, 273, 401
- Miglio, A., Brogaard, K., Stello, D., et al. 2012, MNRAS, 419, 2077
- Miller Bertolami, M. M. 2016, A&A, 588, A25
- Miszalski, B., Acker, A., Parker, Q. A., & Moffat, A. F. J. 2009, A&A, 505, 249
- Moe, M. & De Marco, O. 2006, ApJ, 650, 916
- Moe, M. & De Marco, O. 2012, in IAU Symposium, Vol. 283, IAU Symposium, 111–114
- Mohamed, S. & Podsiadlowski, P. 2012, Baltic Astronomy, 21, 88
- Monteiro, H., Morisset, C., Gruenwald, R., & Viegas, S. M. 2000, ApJ, 537, 853
- Mordasini, C., Mollière, P., Dittkrist, K.-M., Jin, S., & Alibert, Y. 2015, IJAsB, 14, 201
- Morisset, C. 2013, Astrophysics Source Code Library, ascl:1304.020
- Murray, C. D. & Dermott, S. F. 2000, Solar System Dynamics
- Mustill, A. J. & Villaver, E. 2012, ApJ, 761, 121
- Naab, T. & Ostriker, J. P. 2006, MNRAS, 366, 899
- Nandez, J. L. A. & Ivanova, N. 2016, MNRAS, 460, 3992
- Nelemans, G. 2010, AP&SS, 329, 25

- Nelemans, G. & Tauris, T. M. 1998, A&A, 335, L85
- Nordhaus, J. 2017, in IAU Symposium, Vol. 323, Planetary Nebulae: Multi-Wavelength Probes of Stellar and Galactic Evolution, ed. X. Liu, L. Stanghellini, & A. Karakas, 207–212
- Nordhaus, J. & Blackman, E. G. 2006, MNRAS, 370, 2004
- Nordhaus, J., Blackman, E. G., & Frank, A. 2007, MNRAS, 376, 599
- Nordhaus, J. & Spiegel, D. S. 2013, MNRAS, 432, 500
- Nordhaus, J., Spiegel, D. S., Ibgui, L., Goodman, J., & Burrows, A. 2010, MNRAS, 408, 631
- Nordhaus, J., Wellons, S., Spiegel, D. S., Metzger, B. D., & Blackman, E. G. 2011, Proceedings of the National Academy of Science, 108, 3135
- O'Dell, C. R. & Handron, K. D. 1996, AJ, 111, 1630
- O'Dell, C. R., Henney, W. J., & Burkert, A. 2000, AJ, 119, 2910
- Ohsuga, K., Mori, M., Nakamoto, T., & Mineshige, S. 2005, ApJ, 628, 368
- Paczynski, B. 1976, in IAU Symposium, Vol. 73, Structure and Evolution of Close Binary Systems, ed. P. Eggleton, S. Mitton, & J. Whelan, 75
- Parker, Q. A., Acker, A., Frew, D. J., et al. 2006, MNRAS, 373, 79
- Parker, Q. A., Bojićić, I. S., & Frew, D. J. 2016, in Journal of Physics Conference Series, Vol. 728, Journal of Physics Conference Series, 032008
- Pascoli, G. 1987, A&A, 180, 191
- Passy, J.-C., De Marco, O., Fryer, C. L., et al. 2012, ApJ, 744, 52
- Paxton, B., Bildsten, L., Dotter, A., et al. 2011, ApJS, 192, 3
- Paxton, B., Cantiello, M., Arras, P., et al. 2013, ApJS, 208, 4
- Paxton, B., Marchant, P., Schwab, J., et al. 2015, ApJS, 220, 15

## BIBLIOGRAPHY

---

- Penev, K., Zhang, M., & Jackson, B. 2014, PASP, 126, 553
- Peretto, N., Fuller, G., Zijlstra, A., & Patel, N. 2007, aap, 473, 207
- Perrine, C. D. 1929, Astron. Nachr., 237, 89
- Perryman, M., Hartman, J., Bakos, G., & Lindegren, L. 2014, ApJ, 797, 14
- Pfleiderer-Altenburg, J. & Kroupa, P. 2006, MNRAS, 373, 295
- Phillips, J. P. 1989, in IAU Symposium, Vol. 131, Planetary Nebulae, ed. S. Torres-Peimbert, 425–442
- Pollack, J. B., Hubickyj, O., Bodenheimer, P., et al. 1996, Icarus, 124, 62
- Prialnik, D. 2009, An Introduction to the Theory of Stellar Structure and Evolution
- Privitera, G., Meynet, G., Eggenberger, P., et al. 2016, A&A, 591, A45
- Raghavan, D., McAlister, H. A., Henry, T. J., et al. 2010, ApJS, 190, 1
- Raiteri, C. M., Villata, M., & Navarro, J. F. 1996, A&A, 315, 105
- Rasio, F. A. & Livio, M. 1996, ApJ, 471, 366
- Rasio, F. A., Tout, C. A., Lubow, S. H., & Livio, M. 1996, ApJ, 470, 1187
- Reddy, A. B. S. & Lambert, D. L. 2016, A&A, 589, A57
- Redman, M. P., O'Connor, J. A., Holloway, A. J., Bryce, M., & Meaburn, J. 2000, MNRAS, 312, L23
- Reimers, D. 1975, in Problems in stellar atmospheres and envelopes., 229–256
- Reyes-Ruiz, M. & López, J. A. 1999, ApJ, 524, 952
- Robitaille, T. P., Tollerud, E. J., Greenfield, P., et al. 2013, A&A, 558, A33
- Sabach, E., Hillel, S., Schreier, R., & Soker, N. 2017, MNRAS, 472, 4361
- Sabach, E. & Soker, N. 2018, MNRAS, 473, 286
- Sabin, L., Zhang, Q., Zijlstra, A. A., et al. 2014, MNRAS, 438, 1794

- Sabin, L., Zijlstra, A. A., & Greaves, J. S. 2007, MNRAS, 376, 378
- Sackmann, I.-J., Boothroyd, A. I., & Kraemer, K. E. 1993, ApJ, 418, 457
- Sahai, R. 2002, in Revista Mexicana de Astronomia y Astrofisica Conference Series, Vol. 13, Revista Mexicana de Astronomia y Astrofisica Conference Series, ed. W. J. Henney, W. Steffen, L. Binette, & A. Raga, 133–138
- Sahai, R., Claussen, M., Sánchez Contreras, C., Morris, M., & Sarkar, G. 2008, apj, 680, 483
- Sahai, R., Dayal, A., Watson, A. M., et al. 1999, AJ, 118, 468
- Sahai, R., Morris, M. R., & Villar, G. G. 2011, AJ, 141, 134
- Salpeter, E. E. 1955, ApJ, 121, 161
- Santander-García, M., Bujarrabal, V., Alcolea, J., et al. 2017, A&A, 597, A27
- Santander-García, M., Bujarrabal, V., Koning, N., & Steffen, W. 2015, A&A, 573, A56
- Santander-García, M., Corradi, R. L. M., Balick, B., & Mampaso, A. 2004, A&A, 426, 185
- Santander-García, M., Rodríguez-Gil, P., Hernandez, O., et al. 2010, A&A, 519, A54
- Santander-García, M., Corradi, R. L. M., Mampaso, A., et al. 2008, aap, 485, 117
- Schmidt, M. 1959, ApJ, 129, 243
- Schoenberner, D. 1983, ApJ, 272, 708
- Shaw, R. A. 2012, in IAU Symposium, Vol. 283, IAU Symposium, 156–163
- Shklovsky, I. S. 1957, in IAU Symposium, Vol. 3, Non-stable stars, ed. G. H. Herbig, 83
- Siess, L. & Livio, M. 1999, MNRAS, 308, 1133
- Soker, N. 1990, AJ, 99, 1869
- Soker, N. 1992, ApJ, 399, 185

## BIBLIOGRAPHY

---

- Soker, N. 1993, ApJ, 417, 347
- Soker, N. 1995, MNRAS, 274, 147
- Soker, N. 1996a, ApJ, 468, 774
- Soker, N. 1996b, ApJL, 460, L53
- Soker, N. 1997, ApJS, 112, 487
- Soker, N. 1998a, ApJ, 496, 833
- Soker, N. 1998b, AJ, 116, 1308
- Soker, N. 1998c, MNRAS, 299, 1242
- Soker, N. 2004, New Astronomy, 9, 399
- Soker, N. 2004, in IAU Symposium, Vol. 219, Stars as Suns : Activity, Evolution and Planets, ed. A. K. Dupree & A. O. Benz, 323
- Soker, N. 2006, PASP, 118, 260
- Soker, N. 2017, MNRAS, 471, 4839
- Soker, N. & Clayton, G. C. 1999, MNRAS, 307, 993
- Soker, N. & Livio, M. 1994, ApJ, 421, 219
- Soker, N., Rappaport, S., & Harpaz, A. 1998, ApJ, 496, 842
- Soker, N. & Subag, E. 2005, AJ, 130, 2717
- Sowicka, P., Jones, D., Corradi, R. L. M., et al. 2017, MNRAS, 471, 3529
- Staff, J. E., De Marco, O., Wood, P., Galaviz, P., & Passy, J.-C. 2016, MNRAS, 458, 832
- Stanghellini, L., Corradi, R. L. M., & Schwarz, H. E. 1993, A&A, 276, 463
- Steffen, M. 1990, A&A, 239, 443
- Stoll, R., Prieto, J. L., Stanek, K. Z., & Pogge, R. W. 2013, ApJ, 773, 12

- Terzian, Y. & Hajian, A. R. 2000, in Astronomical Society of the Pacific Conference Series, Vol. 199, Asymmetrical Planetary Nebulae II: From Origins to Microstructures, ed. J. H. Kastner, N. Soker, & S. Rappaport, 33
- Tout, C. A. & Eggleton, P. P. 1988, MNRAS, 231, 823
- Vassiliadis, E. & Wood, P. R. 1994, ApJS, 92, 125
- Verbunt, F. & Phinney, E. S. 1995, A&A, 296, 709
- Vila, S. C. 1984, Earth Moon and Planets, 31, 313
- Villaver, E. & Livio, M. 2007, ApJ, 661, 1192
- Villaver, E. & Livio, M. 2009, ApJL, 705, L81
- Villaver, E., Livio, M., Mustill, A. J., & Siess, L. 2014, ApJ, 794, 3
- Vishniac, E. T. 1994, ApJ, 428, 186
- Vlemmings, W., Diamond, P. J., & van Langevelde, H. J. 2001, A&A, 375, L1
- Vlemmings, W. H. T., Diamond, P. J., & Imai, H. 2006, Nature, 440, 58
- Vlemmings, W. H. T., Diamond, P. J., & van Langevelde, H. J. 2002, A&A, 394, 589
- Vlemmings, W. H. T., van Langevelde, H. J., & Diamond, P. J. 2005, A&A, 434, 1029
- Werner, K. 2012, in IAU Symposium, Vol. 283, IAU Symposium, 196–203
- Wesson, R., Liu, X.-W., & Barlow, M. J. 2005, MNRAS, 362, 424
- Winn, J. N. & Fabrycky, D. C. 2015, ARA&A, 53, 409
- Wood, P. R. & Faulkner, D. J. 1986, ApJ, 307, 659
- Wright, J. T., Fakhouri, O., Marcy, G. W., et al. 2011, PASP, 123, 412
- Yuan, H.-B., Liu, X.-W., Péquignot, D., et al. 2011, MNRAS, 411, 1035
- Zahn, J. P. 1966, Annales d’Astrophysique, 29, 565
- Zahn, J.-P. 1977, A&A, 57, 383

## BIBLIOGRAPHY

---

Zahn, J.-P. 1989, A&A, 220, 112

Zahn, J.-P. 2008, EAS Publications Series, 29, 67

Zijlstra, A. A. & Pottasch, S. R. 1991, A&A, 243, 478